ANHYDROUS PHOSPHATES OF MOLYBDENUM AND RHENIUM
SYNTHESIS, CRYSTALLIZATION, CRYSTAL STRUCTURES, AND SPECTROSCOPIC INVESTIGATIONS

Dissertation
zur
Erlangung des Doktorgrades (Dr. rer. nat.)
der
Mathematisch-Naturwissenschaftlichen Fakultät
der
Rheinischen Friedrich-Wilhelms-Universität Bonn

vorgelegt von

Master of Science in Chemistry

Muhammad Saiful Islam
aus Munshigonj / Bangladesch

Bonn, 2011

Angefertigt mit Genehmigung der Mathematisch-Naturwissenschaftlichen Fakultät der
Rheinischen Friedrich-Wilhelms-Universität Bonn

1. Gutachter: Prof. Dr. R. Glaum
2. Gutachter: Prof. Dr. J. Beck
Tag der Promotion: 06.12.2011
Erscheinungsjahr: 2012
Diese Dissertation ist auf dem Hochschulschriftenserver der ULB Bonn
http://hss.ulb.uni-bonn.de/diss_online elektronisch publiziert.

Dedicated to my parents, wife Rony Akhter and daughter Tanihsa Islam

1 Introduction

Up to now crystalline, anhydrous phosphates have been structurally characterized for all transition metals with the only exception of radioactive technetium [1, 2, 3]. The *Inorganic Crystal Structures Database* (version 2011/01) lists some 300 entries for anhydrous phosphates of transition metals containing just one metal [4, 5]. The driving forces for the formation of a plethora of transition metal phosphates are the stabilization of several oxidation states for a given transition metal, the compositional variability *n*(metal oxide) : *n*(phosphorus oxide), and the ability of transition metals to form various co-ordination polyhedra. In addition to the crystal chemistry, for more than forty years the interest in this family of compounds is driven by its fascinating applications. Anhydrous phosphates are used as heterogeneous catalysts for selective oxidation of light hydrocarbons (e. g. $(VO)_2P_2O_7$ [6]), ionic conductors (NASICON and related compounds [7]), crystalline non-linear optical materials (e. g. $KTiOPO_4$ [8]), cathode materials for rechargeable batteries (e. g. $LiFePO_4$ [9]), fuel cell (e. g. a hybrid PEM of $Zr(HPO_4)_2$ and Nafion [10]), and hydrogen storage (e. g. nanoporous nickel(II) phosphate [11]). Most of these applications are related to the redox properties of transition metals in a phosphate matrix. Systematic studies on the redox behaviour of titanium [12, 13, 14], vanadium [15, 16], niobium [17], chromium [18], molybdenum [19], tungsten [20], manganese [21], iron [22], and copper [23] have been undertaken during the last twenty years. A review of the various phase diagrams *M* / P / O (*M* = Ti, V, Cr, Mn, Fe, Co, Ni, Cu, Zn, Zr, Nb, Mo, W) has been given recently [2].

In 1995 LENZ [19] carried out a systematic search for new molybdenum phosphates by Chemical Vapor Transport (CVT) and found the metastable molybdenyl(V) pyrophosphate $(Mo^{V}O)_4(P_2O_7)_3$. He developed the ternary phase diagram of Mo / P / O [19] which contains eight phosphates {$(Mo^{VI}O_2)_2(P_2O_7)$ [24, 25], $(Mo^{VI}O_2)(PO_3)_2$ [26], $Mo^{V}OPO_4$ [27], $(Mo^{V}O)_4(P_2O_7)_3$ [19], $(Mo^{V}O)_2P_4O_{13}$ [28, 29], $Mo^{\sim V}_{1.3}O(P_2O_7)$ [30], $Mo^{IV}P_2O_7$ [31], and $Mo^{III}(PO_3)_3$ [32]}. According to LENZ the crystal structure of $(Mo^{V}O)_4(P_2O_7)_3$ is closely related to TiP_2O_7 [33]. Formally, the structure of $(Mo^{V}O)_4(P_2O_7)_3$ can be derived from that of pyrophosphates $M^{IV}P_2O_7$. Despite this formal understanding the detailed crystal structure of $(Mo^{V}O)_4(P_2O_7)_3$ was not refined. The inability to refine the crystal structure of $(Mo^{V}O)_4(P_2O_7)_3$ might have been a consequence of the lack of a suitable crystal for X-ray single-crystal investigation as well as its very complex crystal structure. In the present work, in addition to a nicely reproducible procedure for the crystallization of $(Mo^{V}O)_4(P_2O_7)_3$, a crystal structure model will be presented.

Table 1 Crystallographically characterized rhenium oxides, halides and rhenates.

type of compound	oxidation state of rhenium			
	IV	V	VI	VII
oxides	$Re^{IV}O_2$ [34]	$Re^{\sim V}{}_{1\,16}O_3$ [35]	$Re^{VI}O_3$ [36], $Re^{VII}{}_2Re^{VI}O_{10}$ [37]	$Re^{VII}{}_2O_7$ [38]
oxide halides	---	---	$Re^{VI}OX_4$ X = F [39], Cl [40]	$Re^{VII}O_2X_3$ (X = F, Cl) [41, 42]
rhenates	$M^{III}{}_2(Re^{IV}O_5)$ M^{III} = Eu [43], Gd [44] $Li_2Re^{IV}O_3$ [45]	$M^{III}Re^{V}O_4$ M^{III} = Cr [46], Co [47], Bi [48] $M^{III}{}_3Re^{V}O_7$ M^{III} = (Sm, Eu, Ho) [49] $LiRe^{V}O_3$ [50] $Cd_2Re^{V}{}_2O_7$ [51]	$Mn^{II}Re^{VI}O_4$ [52] $Cr^{III}{}_2Re^{VI}O_6$ [46] $Ba^{II}{}_2Re^{VI}O_5$ [53]	$M^{I}Re^{VII}O_4$ M^{I} = NH_4 [54], Li [55], Na [56], K [57], Rb [58], Cs [59], Cu [60], Tl [61], Ag [62] $M^{II}(Re^{VII}O_4)_2$ M^{II} = (Mn, Co, Ni, Zn) [63], Pb [64] $M^{II}{}_5Re^{VII}{}_2O_{12}$ M^{II} = (Ca, Sr) [65] $M^{III}{}_3Re^{VII}O_8$ M^{III} = La [66], Pr [67], Sm [68], Gd [69] $VO(Re^{VII}O_4)_2$ [70, 71]

For rhenium, despite its diagonal relationship to molybdenum and its neighbourhood to tungsten, that exhibits an enormous number of anhydrous phosphates such as $W^{VI}{}_2O_3(PO_4)_2$ [72, 73, 74, 75], $W^{VI}OP_2O_7$ [76], $W^{V}OPO_4$ [77], $W^{V}{}_2O_3(P_2O_7)$ [78], $W^{IV}P_2O_7$ [79] and monophosphate tungsten bronzes, with general formula $(PO_2)_4(WO_3)_{2m}$ ($2 \leq m \leq 14$) [80], at the beginning of this PhD work just one phosphate, namely $Re^{IV}P_2O_7$, has been reported in literature [81, 82, 83]. Due to the stability of various oxidation states of rhenium in its binary oxides, oxide halides as well as ternary oxides (rhenates, see Table 1), one may envisage a comprehensive redox chemistry of rhenium in a phosphate matrix. Consequently, a great motivation was felt to dedicate the system Re / P / O to a closer inspection.

During the last two decades, Chemical Vapour Transport (CVT) became an efficient tool for the synthesis and crystallization of transition metal phosphates. A survey on synthesis and crystallization of anhydrous phosphates of transition metals has already been presented by GLAUM [2]. The effectiveness of chemical vapour transport for crystallization of rhenium oxides was reported by SCHÄFER [84] in 1973. Its implementation on the synthesis and crystallization of anhydrous phosphates of rhenium was however not examined. Therefore, in the present work CVT experiments are introduced to synthesize and crystallize new anhydrous phosphates of rhenium. In addition to the characterization of new rhenium

phosphates, it might be interesting to compare the redox behaviour of rhenium phosphates to its neighbour elements i.e, V, Nb, Mo, and W phosphates.

Apart from crystallographic and chemical aspects of molybdenum and rhenium phosphates, it is worth to investigate the electronic structure of these metals in phosphates. Thus, more detailed information about the chemical composition, crystal structure, and bonding might be obtained. To understand the structure-property-relationship it is more demanding to synthesize new phosphates of molybdenum and rhenium of suitable optical quality. In addition to electronic absorption spectra, studies on magnetic behaviour are valuable in order to gain precise knowledge on the electronic state of the transition metal. Furthermore, vibrational (IR and Raman) spectroscopic investigations are introduced for the study of the bonding phenomena in molybdenum and rhenium phosphates.

^{31}P- and ^{29}Si-MAS-NMR investigations have already shown its tremendous success for the characterization of the bonding situation of these elements in solids. In addition to knowledge of the individual sites of the respective elements in the crystal structure, the chemical shift parameters obtained from ^{31}P- and ^{29}Si-MAS-NMR provide more detailed knowledge on chemical bonding of the phosphate or the silicate groups and their chemical environment. In the present work, ^{31}P- and ^{29}Si-MAS-NMR investigations were included for the anhydrous phosphates of rhenium.

2 Chemical Vapour Transport

A fascinating and prospectively useful preparative method has been developed in particular by SCHÄFER [85], is the method of Chemical Vapour Transport (CVT) in a temperature gradient. This method proved to be very convenient for the syntheses of new compounds (even metastable ones), the growth of single-crystals as well as the purification of the solids. CVT requires the reversible conversion of nonvolatile solids (or liquids) into volatile derivatives according to equation 2.1.

$$a\,A_{s,l} + b\,B_s = c\,C_g + d\,D_g \qquad (2.1)$$

The transport of substance A is attained by a difference in partial pressures of the gaseous species C, D, …. between the source region (side of dissolution of the condensed phase in gas phase) and the sink region (side of deposition of the condensed phase from the gas phase; crystallization zone). The CVT experiments are generally carried out in evacuated glass tubes heated in a two zone furnace. Typically a temperature gradient $50 < \Delta T < 150$ K is applied. While a physical transport (sublimation, distillation) always leads to the migration of the condensed phase from the higher to lower temperature, the direction in CVT depends on the

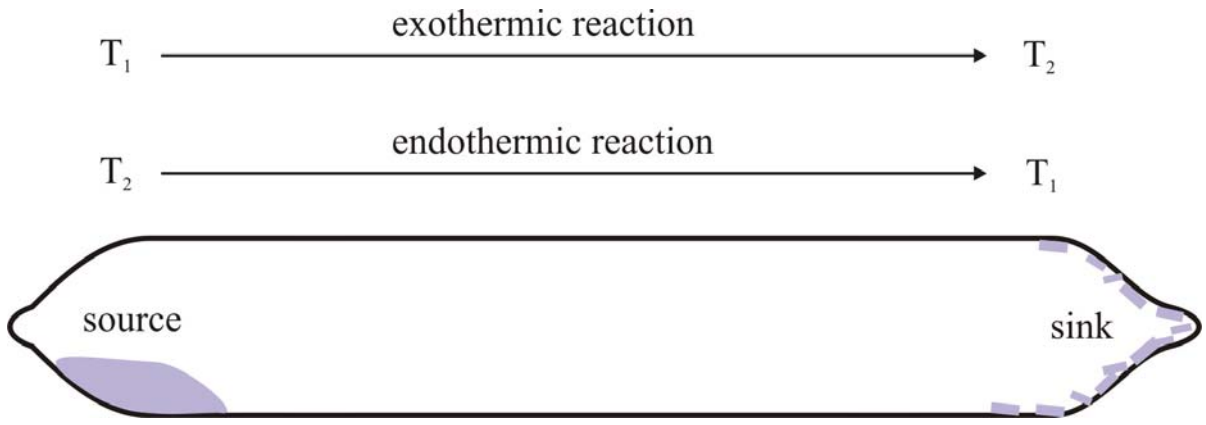

Figure 1.1 Schematic representation of chemical transport, $T_2 > T_1$.

the sign of the heat of reaction $\Delta_R H°$. In case of an endothermic reaction ($\Delta_R H° > 0$), migration proceeds to the lower temperature region ($T_2 \rightarrow T_1$, $T_2 > T_1$) while for an exothermic reaction ($\Delta_R H° < 0$) it is just reverse ($T_1 \rightarrow T_2$, $T_2 > T_1$).

With the help of GIBBS HELMHOLTZ'S and VAN'T HOFFS equation [86] (see Equations 2.2-2.4) the temperature dependent equilibrium pressures and hence the partial pressure gradient can be obtained.

$$\Delta_R G_T = \Delta_R H_T - \Delta_R S_T \cdot T \tag{2.2}$$

$$\log K_p = \frac{\Delta_R H_T}{4.567 \cdot T} + \frac{\Delta_R S_T}{4.567} \tag{2.3}$$

$$K_p = \frac{P(C) \cdot P(D)}{P(B)} \tag{2.4}$$

For endothermic reactions, the partial pressure of gaseous species C increases with the increase of temperature. At the higher temperature region a larger amount of C is dissolved than at the cooler region. C diffuses into the lower temperature region where the products deposit from a supersaturated gas phase and A is deposited. The reverse situation can be observed for an exothermic reaction. A sufficiently large amount of mass transfer from the source to the sink is only achieved for the transport reaction when the value of the free reaction enthalpy $\Delta_R G$ becomes close to zero (±30 kcal/mol). Otherwise, either forward or backward reaction becomes unfavourable and the reversibility of the whole reaction is not given.

Equation 2.2 expresses that only the existence of a larger entropy difference leads to an adequate transport which is obtained when both $\Delta_R H$ and $\Delta_R S$ are of same sign. If $\Delta_R H$ is positive, successful transport will be observed with the increase of entropy. This occurs in the transport reaction as at higher entropy more molecules come into the gas phase. On the other hand, if $\Delta_R H$ is negative, negative entropy is necessary for an effective transport reaction.

Since, according to GIBBS-HELMHOLTZ equation entropy depends on temperature, so the temperature aiming for a successful transport reaction can be chosen in such a way that free reaction enthalpy remains approximately zero.

As we know that reaction enthalpy and entropy are temperature dependent, any change of them with respect to temperature can be calculated according to KIRCHHOFF'S law (see Equation 2.5).

$$\Delta_R H_T = \Delta_R H_{298} + \int_{298}^{T} \Delta C_P(T)\, dT\,; \qquad S_T = S_{298} + \int_{298}^{T} \frac{\Delta C_P(T)}{T}\, dT \tag{2.5}$$

VAN'T HOFF shows that $\Delta_R H$ depends on temperature but can be set $\Delta_R H_T \approx \Delta_R H_{298}$ to a first approximation. This is permissible because the temperature dependence of $\Delta_R C_p$ is not much smaller than that of C_p. SCHÄFER [85] obtained an equation (2.6) in order to determine the migration rate caused by diffusion in a sealed tube. In such a system it is assumed that diffusion only proceeds along the long axis of the ampoule. Provided that the gas phase as a whole does not move from the source to the sink, the amount of transported solid A (mole) can be calculated according to equation 2.6 (convection and thermal diffusion are neglected).

$$\dot{n}_A = \frac{i}{j} \cdot \frac{\Delta p(c)}{\Sigma p} \cdot \frac{D^\circ \cdot \overline{T}^{0\,75} \cdot q}{s} \cdot 2.4 \cdot 10^{-3} \ (\text{mol}\cdot\text{h}^{-1}) \qquad (2.6)$$

i, j = stoichiometric reaction coefficients
Σp = total pressure in the ampoule (atm)
n_A = transport rate (mol·h^{-1})

Δp_c = partial pressure difference (atm)
q = diffusion cross section (cm^2)
s = length of diffusion path (cm)

$\overline{T} = \frac{T_1 + T_2}{2}$ in (K)

D° = diffusion coefficient (cm^2·s^{-1})

The transport rate is inversely proportional to the diffusion path length and total pressure inside the ampoule. But it is proportional to the cross section of the ampoule, experimental time, average temperature and difference of partial pressure of C at temperature T_1 and T_2. Diffusion is accelerated by increasing the temperature as the speed of the particles increase with the rise of temperature.

Nevertheless, phenomenology of CVT process is very complex, as it involves in principle non-equilibrium thermodynamics, kinetics of both heterogeneous and homogeneous chemical reactions, as well as mass, and heat transfer via the phases. This process might become more complex when several solid phases constitute the source and the sink region.

3 Three Component Systems

Apart from achievement of rapid equilibria between solids and gas phases, better crystallinity of the compounds can be obtained by chemical vapour transport. Furthermore, different distribution of temperature in sink and source side of the ampoule frequently leads to different phases. Such information facilitates to developoment of a phase diagram at a particular temperature. In this work, a ternary phase diagram of Re / P / O has been developed at 500 and 800°C.

Based on thermodynamics, GIBBS' Phase Rule [87] provides the theoretical foundation for the characterization of the chemical state of a system and predicting the equilibrium relations of the phases present as a function of physical conditions (for exmple pressure and temperature). It also allows constructing of a phase diagram, to represent and to interpret the results of equilibrium experiments in heterogeneous systems. In straightforward, the phase rule (see equation 3.1) shows a general relationship among the number of degrees of freedom F, number of the components C and the number of co-existing phases P of a system for a given parameters (generally pressure and temperature).

$$P + F = C + 2 \tag{3.1}$$

For example, in a three component ($C = 3$) system, $F = 5 - P$, or 4 degrees of freedom are possible, i.e., temperature, pressure and the composition of the two components. If the composition or concentration of the two components in a phase is fixed, the third is automatically fixed by difference. In order to represent the dependence of the phase equilibria on the composition of such systems, one uses GIBBS' phase triangles. The mathematical relations among the molar fractions x_A, x_B and x_C in a ternary system $A_aB_bC_c$ (see Equations 3.2-3.5) can be plotted by a phase diagram in order to form of an equilateral triangle.

$$x_A + x_B + x_C = 1 \tag{3.2}$$

$$x_A = \frac{n_A}{n_A + n_B + n_C} = \frac{n_A}{\Sigma n_i} \tag{3.3}$$

$$x_B = \frac{n_B}{n_A + n_B + n_C} = \frac{n_B}{\Sigma n_i} \tag{3.4}$$

$$x_C = \frac{n_C}{n_A + n_B + n_C} = \frac{n_C}{\Sigma n_i} \tag{3.5}$$

n_A, n_B, n_C, n_i amount substance (mol)
x_A, x_B, x_C mole fraction

Ternary compositions within equilateral triangles are given by reference to grid (see Figure 3.1). Each of the three binary edges is divided into a hundred divisions (only ten are shown for clarity of the diagram). For example point A corresponds to 100% A; the edge BC corresponds to 0 % A and the line PQ to 15% A.

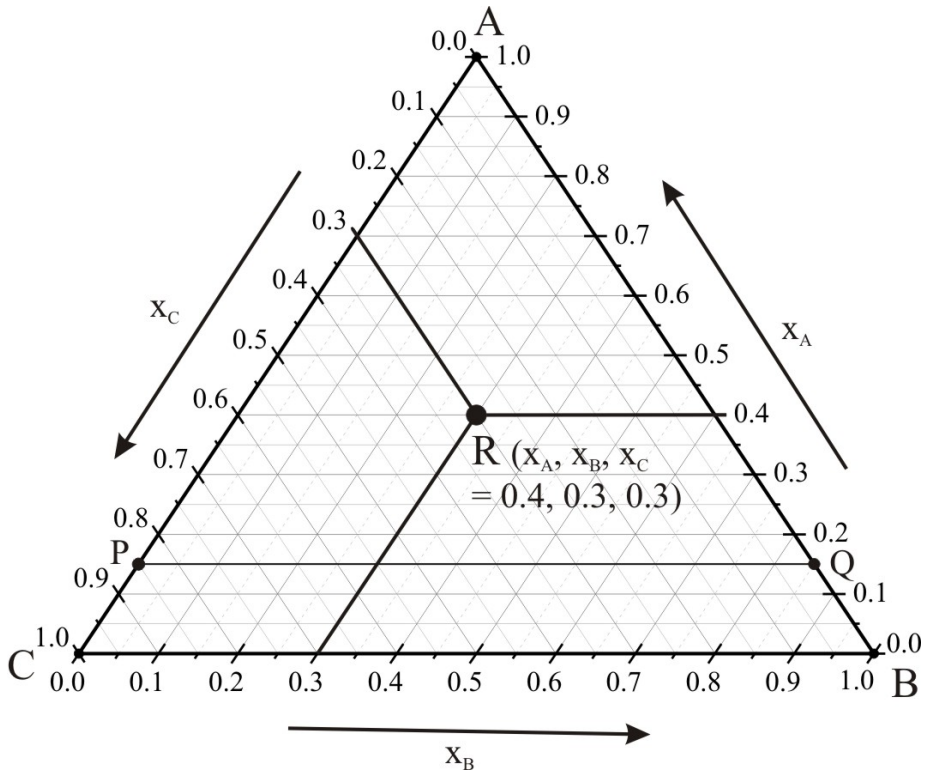

Figure 3.1 Triangular grid for representing compounds and equilibrium relations in the sub solidious of a three component systems.

Thus the A content of any ternary composition is given by drawing a line through that composition and parallel to the BC edge. The A content is then read off from the intersection of this line with either the AB or AC edges. The contents of B and C are given similarly by drawing lines parallel to the AC and AB edges, respectively. The point R in the Figure 3.1 has a composition 40% A, 30% B and 30% C, or a molar fraction $x_A = 0.4$, $x_B = 0.3$ and $x_C = 0.3$. Straight inter-connection between two phases in the phase triangle represents a quasi-binary system.

4 Ligand Field Theory

In the present work compounds of 4- and 5*d*-transition metal ions coordinated by oxygen ligands have been investigated. The metal ions in these compounds attain independent crystallographic sites. The influence of the ligands on the electronic structure of the central ions can be described nicely with in the ligand field theory. The ligand field theory is an advanced development of the crystal field theory, which considers the symmetry, strength of the electrostatic crystal field and the electronic structure of free ions of the transition metals. The disadvantage of the crystal field theory is the view of purely electrostatic interaction. Covalent interactions between the central metal atom and the ligands are completely ignored. A more detailed description of bonding in coordination compounds is provided by Ligand Field Theory. The principle of Ligand Field Theory is similar to those of Molecular Orbital Theory. The following list summarizes the key concepts of Ligand Field Theory.

- One or more orbitals of the ligand overlap with one or more atomic orbitals of the metal.
- If the metal- and ligand-based orbitals have compatible symmetries, a net interaction exists.
- These interactions lead to stabilization / destabilization of the interacting orbitals (formation of bonding and anti-bonding orbitals).
- The amount of stabilization / destabilization depends on the overlap integral of two orbitals and their absolute energy.
- The net interaction produces a new set of orbitals, one bonding and the other anti-bonding in nature.
- Where no net interaction exists, the original atomic and molecular orbitals are unaffected and are nonbonding in nature as regards the metal-ligand interaction.
- Bonding and anti-bonding orbitals are of sigma (σ) or pi (π) character, depending upon whether the bonding or anti-bonding interaction lies along the line connecting the metal and the ligand. Delta (δ) bonding is also possible, but it is unusual and is generally rather weak.

In the free transition metal ion the *d*-orbitals are five-fold degenerated (see Figure 4.1) and the electron density is symmetrically distributed on a spherical surface. With the approach of the ligands to the free ion the energy of the *d*-orbitals is raised by electrostatic repulsion. Since

the total charge of the ligands is not distributed uniformly on the spherical surface, the degeneracy of the *d*-orbitals of the central metal ion is in parts or even completely removed.

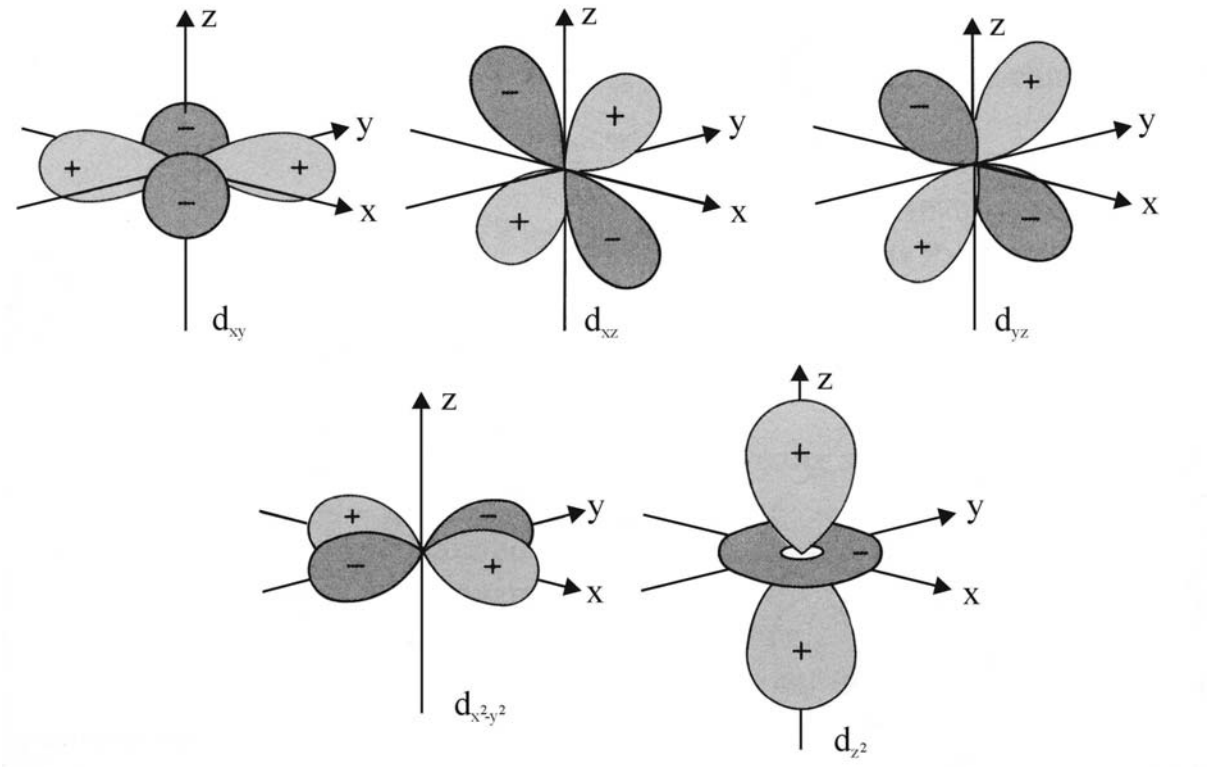

Figure 4.1 Representation of the 5 3*d*-orbitals.

The most common geometric structure of a complex is that of an octahedron. Here six ligands are arranged in an octahedral fashion around the metal ion. In octahedral symmetry the *d*-orbitals split into two sets with an energy difference Δ_{oct} (the crystal-field splitting parameter) where the *d*(*xy*), *d*(*xz*), and *d*(yz) orbitals will be lower in energy than the $d(z^2)$ and $d(x^2\text{-}y^2)$ because the former group are farther from the negative charged ligands than the latter and therefore experience less repulsion. The three lower-energy orbitals are collectively referred to as t_{2g}, and the two higher-energy orbitals as e_g. These labels are based on the theory of molecular symmetry. Further splitting of the energy levels can result from the transition from octahedral (O_h) to tetragonal symmetry (D_{4h}), e.g. by elongation or compression of the octahedron along along *z*-direction. The energy of the *d*-orbitals of the free ion, in the spherically symmetric, octahedral (O_h) and pseudo-octahedral (D_{4h}) ligand field is compared in figure 4.2.

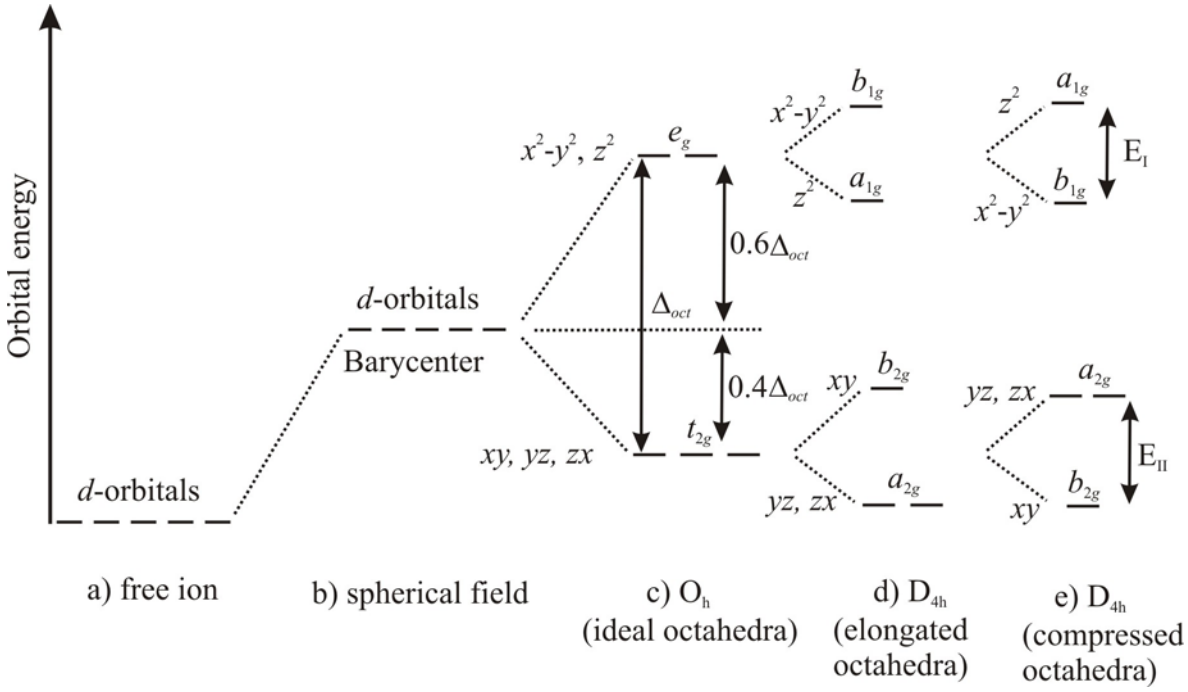

Figure 4.2 Energy diagram of the *d*-orbitals for ligand fields of different symmetry. Energy states of the orbitals are represented for free ion (a), spherical symmetry (b), octahedron (O_h) (c), distortions along *z*-axis so called pseudo octahedra (D_{4h}), while elongation (d) and compression (e) along *z*-axis.

In case of octahedral symmetry the energy difference between the t_{2g} and e_g orbitals is regarded as Δ_{oct} = 10Dq. 10Dq (in cm^{-1}) is regarded as ligand field strength parameter. It depends on the strength of the ligands, geometry of the complex and the oxidation state of the central metal ion. The field strength parameter for the transition metal complexes lies in the range between $7000 \leq \Delta_o \leq 30000$ cm^{-1}.

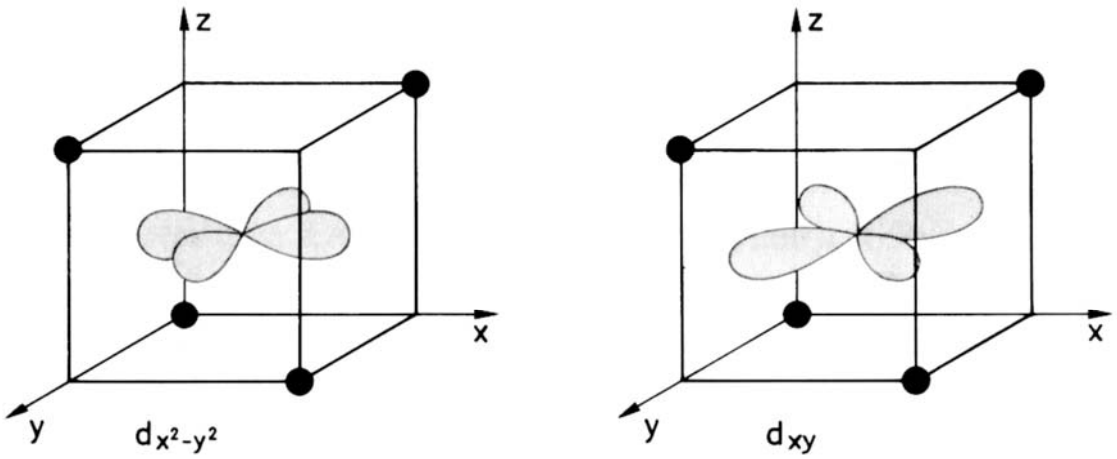

Figure 4.3 Orientation of the *d*-orbitals towards the tetrahedral coordinated ligands.

Tetrahedral complexes are the second most common type. Here four ligands form a tetrahedron around the metal ion. In a tetrahedral crystal field the *d*-orbitals again split into two groups. The energy difference between the two groups is Δ_{tet} where the lower energy orbitals are d_z^2 and $d_{x^2-y^2}$, consequently, d_{xy}, d_{xz} and d_{yz} the higher energy orbitals, as the latter point close to the direction in which ligands approach (see Figure 4.3). Furthermore, since the ligand electrons in tetrahedral symmetry are not oriented directly towards the *d*-orbitals, the energy splitting will be lower than in the octahedral case, $\Delta_{tetr.} = 4/9\ \Delta_{oct}$. Further, *d*-orbital splitting can also be deduced for trigonal bipyramidal, square-planar and other complexes.

5 Experimental

5.1 Preparation of Silica Ampoules

In the present work chemical vapour transports as well as isothermal heating experiments were carried out exclusively in evacuated sealed silica tubes. These were made from silica tubes (Ø: 12-18 mm, thickness of the wall: 0.8 - 1.8 mm, length: 150 cm, company GVB, Aachen). With the help of glass cutter they were at first divided into three pieces of about 50 cm in lengths and then melted in the middle of the already obtained pieces with the help of an oxygen / hydrogen burner**.** Thus two half ampoules of about 25 cm in lengths were achieved. At the open end of the half tubes a ground glass joint (NS 19.5) was attached in order to connect it to vacuum line.

The ampoules were cleaned thoroughly with customarily used cleaning agents and then rinsed with demineralised water and acetone respectively. Afterwards these tubes were dried at 105°C overnight in a drying oven. The dried raw ampoules were heated at last in a tube furnace for about four hours at 800°C under vacuum (10^{-3} – 10^{-4} atm) as silica has strong ability to bind a significant amount of water reversibly [88]. Thus any influence of water on the experiments should be avoided. Once the ampoules are cooled down to ambient temperature, they were filled with argon as inert gas and removed from the vacuum line. The prepared reactants were put in a small sample holder which was attached to a long glass stick to place the reactants in the tube (e.g. Re_2O_7, P_4O_{10}, I_2). Thus contamination on the wall of tube was avoided. Reactants containing end of the ampoule was cooled with a wet paper or with liquid nitrogen in order to prevent the vaporization of reactants. Finally a capillary was made (preferably ~ 10 cm away from the closed end of the half ampoules) with the help of a oxygen / hydrogen burner and then connected to the vacuum line. If the test of evacuation by a ionization source (Spark tester, Edwards company) shows a significant amount of evacuation, the capillary was sealed. This new end of the ampoule is rounded carefully using a burner. Prior to putting the ampoule into the furnace its surface was cleaned by washing agents and rinse with acetone and demineralised water to prevent recrystallization of the silica during annealing.

5.2 Vacuum Line

Figure 5.1 represents a combination of the heating furnace and a vacuum pump that allows the preparation of silica ampoules for the isothermal and chemical vapour transport experiments. This combination lets simultaneous drying and evacuation of the ampoule. At the final stage the half ampoule were filled with dry argon. For evacuating an oil pump (BS5000, Edwards company) was used.

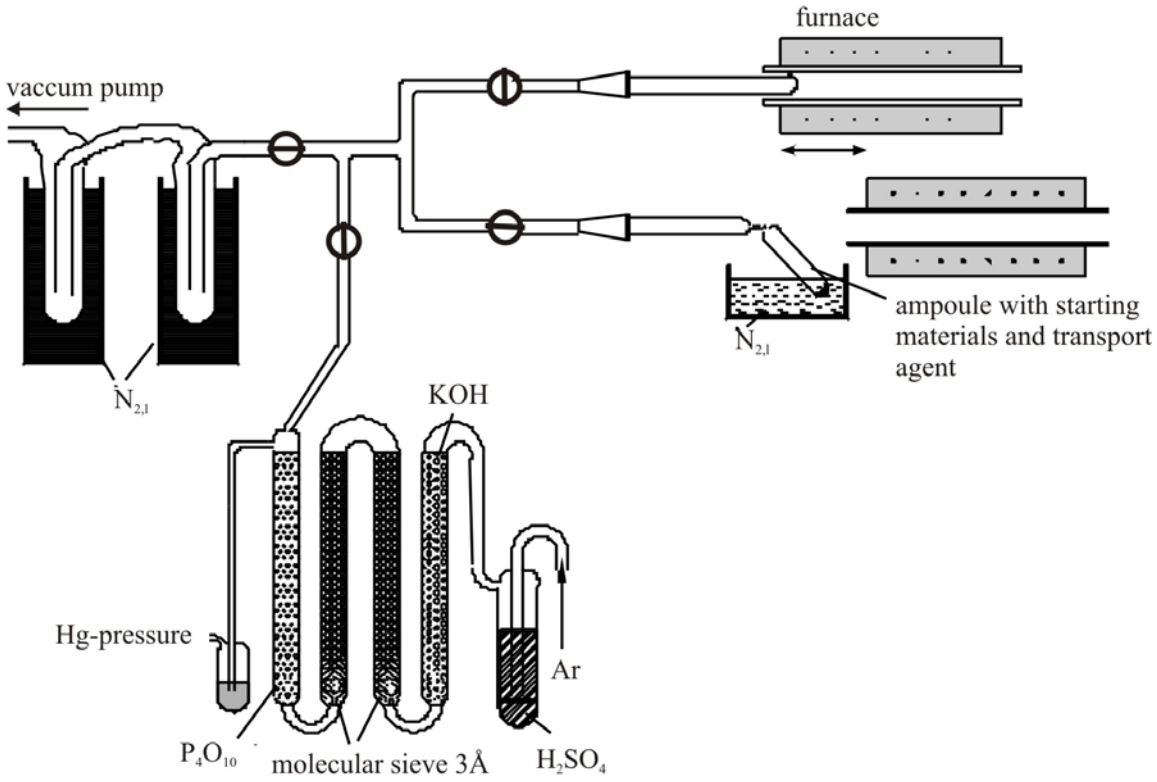

Figure 5.1 Lay out of the vacuum line [18].

5.3 Furnaces

For the synthesis and crystallization experiments different types of furnaces were used. A single zone tube furnace was used to heat the ampoules during the evacuation. It consists of a ceramic tube which is made of pythagorasmass with an inner diameter of 4 cm. A heating coil made of Kanthal wire (Kanthal A-1: 22% Cr, 5.8% Al, 72.2% Fe) attach just to the outer surface of the tube which is then surrounded by an insulator to prevent the loss of heat.
Chemical Vapour Transport was carried out in a two zone tube furnace so called "transport furnace". It consists of two independent heating coils. Thus the two sides of the tube furnace can be heated to different temperatures. This furnace can work up to 1100°C. A continuous temperature gradient is always established between the defined temperatures. The temperature drops significantly at the ends of the furnace (see Figure 5.2). Both ends of the furnace are closed with ceramic stoppers in order to stabilize the temperature and to reduce thermal convection. The temperature of the furnace is controlled either by Pt/Pt-Rh or Ni/Cr-thermo couples.

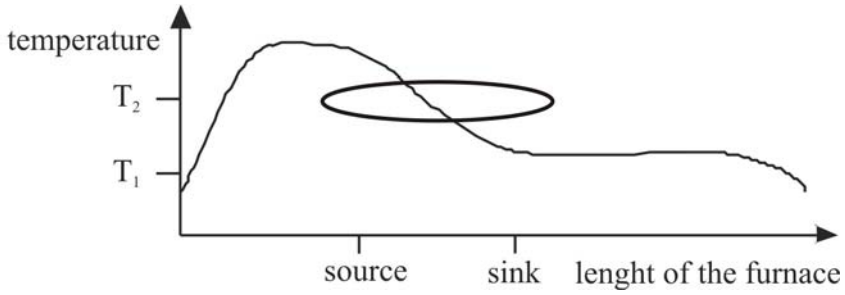

Figure 5.2 Temperature profile of a two zone furnace. T_{max} ~ 1100°C, ΔT: 50 – 150°C, thermocouple at the ends of the ampoule.

Isothermal experiments were carried out in sealed ampoules. In some cases the reactants were heated in half ampoules in muffle furnaces (Type Le16 7PS from Lenton Furnaces or type B170 from Nabertherm) in order to release water or other volatile substances.

5.4 Solid-state Reactions

In most cases solid state reactions exhibit a very slow reaction rate which is due to the very slow diffusion of the reactants into each other. Therefore, mineralizers are used sometimes to speed up the reaction rate. The use of some mineralizers, for example chlorine, however may dissolve a significant amount of SiO_2 from the wall of the silica tube. Another approach to speed up the reaction rate is to reduce the length of the diffusion path among the reactants. This can be achieved through a homogeneous mixture of finely ground reactants. The homogeneity of the mixture can be achieved by mixing the reactants thoroughly in an agate mortar and a pellet can be prepared by applying a pressure on the mixture. About 200 mg of the homogeneously ground mixture were introduced into the slot of the powder compaction tool (see Figure 5.3a) with the help of a funnel. It is then inserted in the hydraulic press (see Figure 5.3b) and the pellet is obtained by a force of 20 kN for about 20 minutes. Finally, the pressure is relaxed carefully and the pellet is taken from the tool. In this way, rectangular pellets with dimensions of about $12\times2\times2$ mm^3 were prepared. This sample was then transferred into the silica tube according to section 5.1 and heated in the furnace. An important advantage of the pellet is its low contact with the ampoule wall by which reaction between the sample and the silica wall can be minimized.

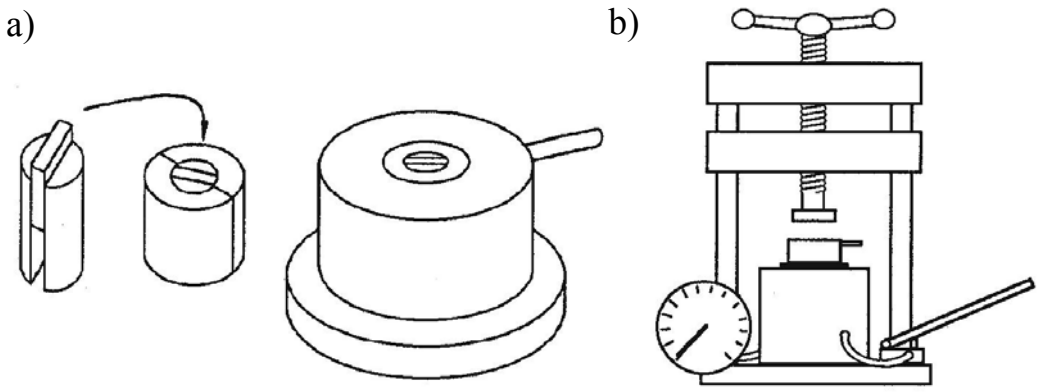

Figure 5.3 Lay out of the sample holder (a) and Hydraulic Press (b).

5.5 Chemical Vapour Transport Experiments

At the very beginning furnace zones are set to the desired temperatures. The already prepared ampoule (see. Sect. 5.1) is brought into the transport furnace in such a way so that about ⅔ of the ampoule remain at the source temperature and ⅓ at the sink temperature. Thus, a small crystallization zone can be ensured. The ampoule is at first held in a reverse temperature gradient for about 24 hours which is in opposite to the actual transport direction (reverse transport). Consequently, the sink end of the ampoule can be cleaned by removing unwanted crystal seeds. At the end of the transport experiment the source side of the ampoule is removed at first so that all the unwanted gaseous species are condensed. The hot ampoule is put on a curved gauge and the source end is sunk down in cold water or liquid nitrogen so that condensation of the equilibrium gas phase occurs rapidly. Thus, contamination of the crystals grown in the sink region can be avoided. The tube was cut into two approximately equal parts by a diamond saw. The crystals or the solid substances are taken out from the ampoule very carefully. If they are attached firmly to the ampoule wall, the half ampoule is filled with 5% hydrofluoric acid. After couple of hours, the crystals separated from the wall can be collected. The solid substances are filtered and then washed by distilled water. Subsequently, they are dried in the drying oven for about one hour and then examined under the microscope.

6 Characterization Methods

In the present work all the solid compounds were identified by X-ray powder diffraction. Crystals of unknown substances were structurally characterized by X-ray single-crystal studies as well. Elemental analyses were carried out with the help of energy-dispersive X-ray fluorescence (EDX). In addition, selected compounds have been investigated by spectroscopic techniques such as Solid-state MAS-NMR, UV/Vis/NIR, Infrared, and Raman. Magnetic behaviour was also studied for some molybdenum- and rhenium-phosphates.

6.1 X-ray Diffraction Techniques

X-ray scattering is used in a family of non-destructive analytical techniques which provides information about the crystallographic structure and chemical composition of solids. These techniques are based on the scattering X-rays hitting a crystalline substance. X-ray wavelengths are comparable with inter-atomic distances (~1Å). Therefore, it is regarded an excellent means of crystal diffraction study for this length scale. Atoms scatter X-ray waves, primarily through the atoms' electrons that can emanate secondary spherical waves. This phenomenon is known as elastic scattering, and the electron shell is known as the scatterer. A regular array of scatterers produces a regular array of spherical waves. Although these waves cancel one another out for most of the directions through destructive interference, they add constructively in a few specific directions, determined by BRAGG'S law [89] (see Equation 6.1.1).

$$n \cdot \lambda = 2 \cdot d \cdot \sin\theta \qquad (6.1.1)$$

where n is an integer determined by the order given, λ is the wavelength of the X-rays , d is the spacing between the planes in the atomic lattice, and θ is the angle between the incident ray and the scattering planes.

6.1.1 X-ray Powder Diffraction

6.1.1.1 The Guinier Method

Powder diffraction for this work was carried out using a Guinier camera (see Figure 6.1.1) of type FR-552, manufactured by Enraf-Nonius (Delft). This camera uses Cu-$K\alpha_1$ radiation, λ = 1.54052 Å.

For the X-ray generation a focused electron beam is accelerated towards a copper anode at a very high voltage of 40 kV with 25 mA. The electrons decelerate as they plunge into the metal and generate radiation with a continuous range of wavelengths called "Bremsstrahlung" or white radiation. A few highly intense very sharp peaks are superimposed onto the continuum. These peaks arise from collision of the incoming electrons with electrons of the inner shell of the anode's atoms. A collision expels an electron from an inner shell (1*s* for Cu-$K\alpha$)**,** and an electron of higher energy (outer shell, 2*p* or 3*p*) drops into the vacancy, emitting the excess energy as radiation. The $2p \rightarrow 1s$ transition called $K\alpha$*,* has a wavelength of 1.5418 Å while $3p \rightarrow 1s$ transition is known as $K\beta$ and λ = 1.3922 Å. The $K\alpha$ transition occurs more

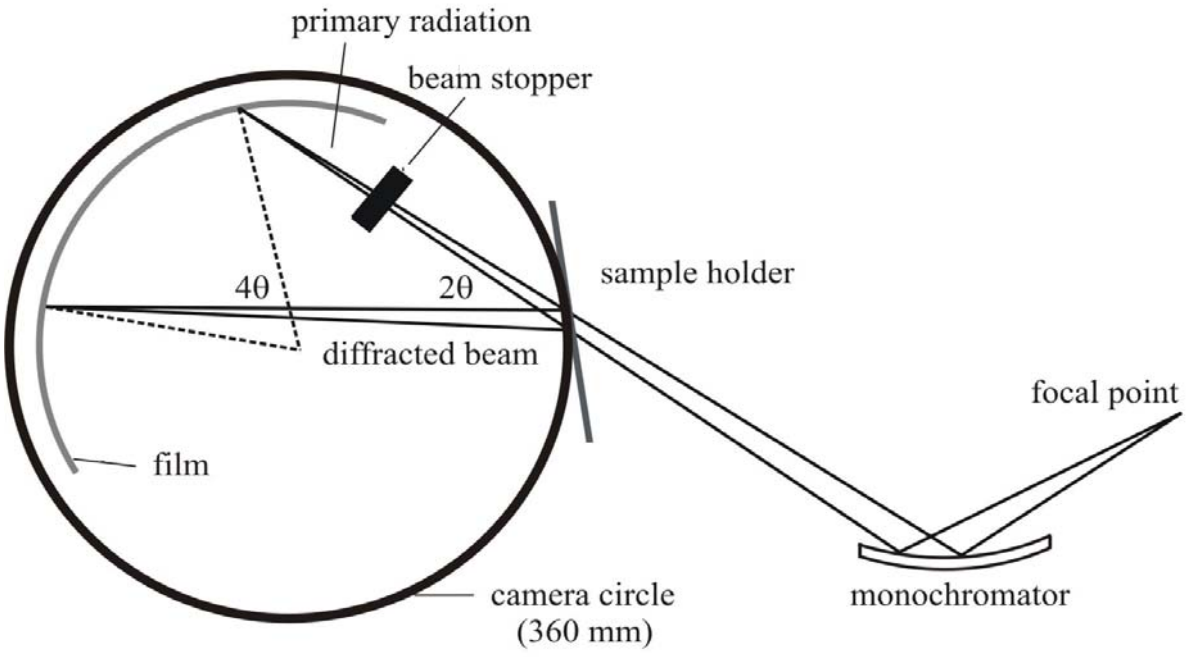

Figure 6.1.1 Optical path of the Guinier camera [18]

frequently than $K\beta$ and it is more intense, too. In fact, the $K\alpha$ radiation is a doublet, $K\alpha_1$ = 1.54051 Å and $K\alpha_2$ = 1.54433 Å, because the transition has slightly different energies for the two possible spin states of the 2*p* electron. A bent crystal monochromator is added to the

Guinier focusing camera that allows the separation of the $K\alpha_1$ (used for the X-ray diffraction) from the rest and also to produce an intense convergent X-ray beam. The crystal monochromator consists of a large (1-2 cm) bent single-crystal of quartz (α-SiO_2), orientated such that by the (101) plane strongly monochromatic X-ray beam is diffracted. The monochromatic beam strikes a finely powdered sample that, ideally, has crystals randomly arranged in every possible orientation. In such a powder sample, the various lattice planes are also present in every possible orientation. For each set of planes, at least some crystals must be orientated at the Bragg angle θ, to the incident beam. Thus, diffraction occurs for these crystalites. The sample and the diffracted beams are arranged to focus at the surface of the film. Radiation that is not diffracted is stopped by a beam stopper, placed in front of the photographic film to prevent its blackening.

For the present work, a non-conventional film, so called image plate (*IP*) film of type BAS-*IP* MS 2325 manufactured by Fuji was used. The chosen geometry results from the inter relation between diffraction angle, 4θ, and the distance of the reflection position from the primary beam on the film. 1 mm distance corresponds exactly to 1° (in 4θ). The *IP* is approximately 0.5 mm in thickness, and is composed of a flexible plastic coated with fine X-ray sensitive phosphor crystals of $BaFBr:Eu^{2+}$ combined with an organic layer. The *IP* technology is based on "*photo stimulated luminescence*" (PSL) [90]. When the image plate is bit by incoming X-rays, some of the Eu^{2+} is oxidized to Eu^{3+} liberating electrons to the conduction band of the crystal. The electrons are trapped in bromine vacancies, forming a color centre. These are called F-centres and store information. This latent diffraction pattern is scanned afterwards with a laser scanner. For this work an instrument BAS-1800 II manufactured by Fuji was used. By stimulation of laser (λ = 632.8 nm) the stored information is released as light of wavelength λ = 390 nm, where the intensity of the luminescence UV-radiation is proportional to the intensity of absorbed X-ray.

Prior to take a Guinier photograph one has to prepare the powder sample on a holder (see Figure 6.1.2). A few mg of the substances are ground finely in an agate mortar, so that microcrystals develop. The fine powder is then placed as a thin layer on an X-ray-amorphous adhesive strip (Scotch Magic transparent film) on window **b** of the holder. Finely powdered α-quartz (α-SiO_2) is placed on window **a** as an internal standard. Window **c** contains a mixture of the sample and α-quartz.

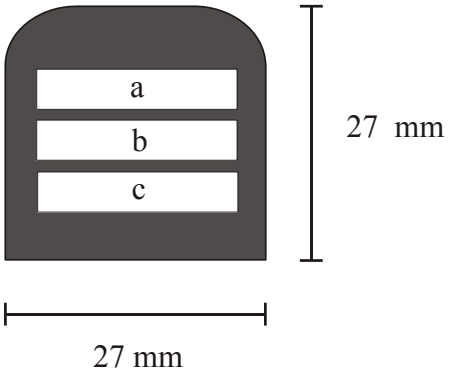

Figure 6.1.2 Sample holder for Guinier photographs. a: window contains internal standard, b: window containing sample of investigation, and c: window containing a mixture of sample and internal standard.

The reflection positions of α-quartz are well-known. On the basis the reflections of α-quartz, the diffraction angles of the investigated phases can be examined and corrected. The evaluation takes place by a computer. The *IP* is then loaded by the laser scanner and subsequently the intensities are measured from different strength of blackening on the film with the help of the program AIDA [91]. The *x*,*y*-data are obtained as ASCII format, in which the absolute intensities against the 4θ values are recorded. The *x*,*y*-data are imported into a computer program (ORIGIN 6.1) [92] and a diffraction pattern (called Guinier photograph) of absolute intensity versus diffraction angle can be evaluated.

6.1.1.2 Simulations and Analyses of X-ray Powder Diffraction

In order to identify the investigated compounds already obtained powder diffraction patterns were compared with the simulation of the diffraction patterns of already known compounds from the *Inorganic Crystal System Database* (ICSD) [93]. With the help of the computer program LAZY PULVERIX [94] the integrated intensity (I_c) of each powder diffraction peak can be calculated according to equation 6.1.2.

$$I_c = \left|F_c\right|^2 \cdot PLG \cdot H \cdot T \cdot A \qquad (6.1.2)$$

F_c Calculated structure factor
PLG Polarization-, Lorentz- und Geometric factor
H Multiplicity factor
T Temperature factor
A Absorption factor

The computer program SOS [95] allows the determination of the cell parameters on the basis of the diffraction angles, obtained from Guinier photographs. SOS1 accomplishes a correction of reflection positions with the help of an internal standard (α-SiO_2). The error like an incorrect positioning of the film in the camera's film holder can be corrected. This correction of the reflection position is attained by the corresponding polynomial regression of the fourth order using the program SOS1. From the accurate position of the reflections SOS2 determines the cell parameters with the help of the principle of "*least square errors*", whereby the indexing of the reflections has to be known. In case of new compounds the indexing can either be achieved from single crystal data or from indexing by "*Trial and Error*" [96] or with computer programs like TREOR-90 [97], DICVOL [98] or VISSER [99] (in Program packet WinPLOTR [100]). All these programs are using to the de Wolff algorithm [101].

6.1.2 Single-crystal Investigations

Single-crystal X-ray diffraction is a powerful analytical technique which provides detailed information about the structure of crystalline substances, including unit cell dimensions, bond-lengths, bond-angles, and on site-ordering.

6.1.2.1 Selection and Mounting of a Single-crystal

In order to carry out an X-ray single-crystal investigation, a selected crystal must meet some important criteria such as (1) uniform internal structure and (2) proper size and shape. This can be determined conveniently by selecting the crystals under a cross polarizing microscope. The ideal size of the preferred crystal should be in the range of 0.1 to 0.2 mm so that absorption and extinction effects can be kept to a minimum. The selected crystal is mounted on the tip of a thin glass fiber (20-70 μm) using an adhesive. Before mounting of the crystal the glass fiber must be fastened with sealing wax on a metallic support that is suitable for insertion into the goniometer head (Figure 6.1.3).

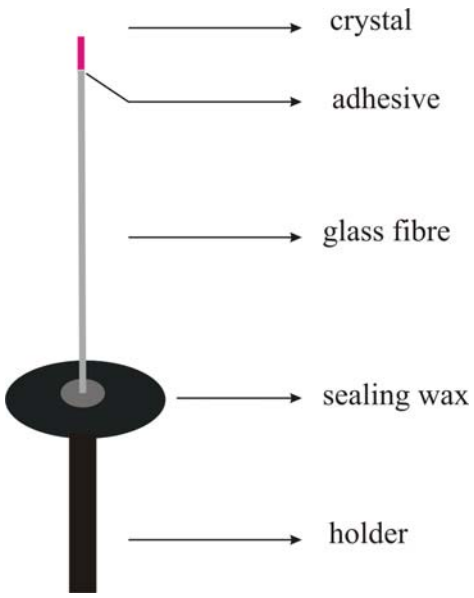

Figure 6.1.3 Pictorial representation of a crystal mounted for X-ray single-crystal investigation.

6.1.2.2 Intensity Data Collection Using a κ-CCD Diffractometer

A charge-coupled device (CCD) is a detector that is based on a method of electronic imaging, which employs an X-ray sensitive layer of fluorescent material such as gadolinium oxide. Reflections can be recorded very fast by the CCD detector. A disadvantage is the level of background noise which is problematic especially for weakly scattering materials or the crystals containing weak superstructure reflections. After the precise centering of the crystal on the goniometer a few orientation photographs are taken which provide information about the quality, diffracting power of the crystal and a tentative unit cell. The crystal is rotated over an angular range of 0.3-1.0° about the vertical axis so that reciprocal lattice points can be brought to coincide with the surface of the Ewald sphere (see Figure 6.1. 4).

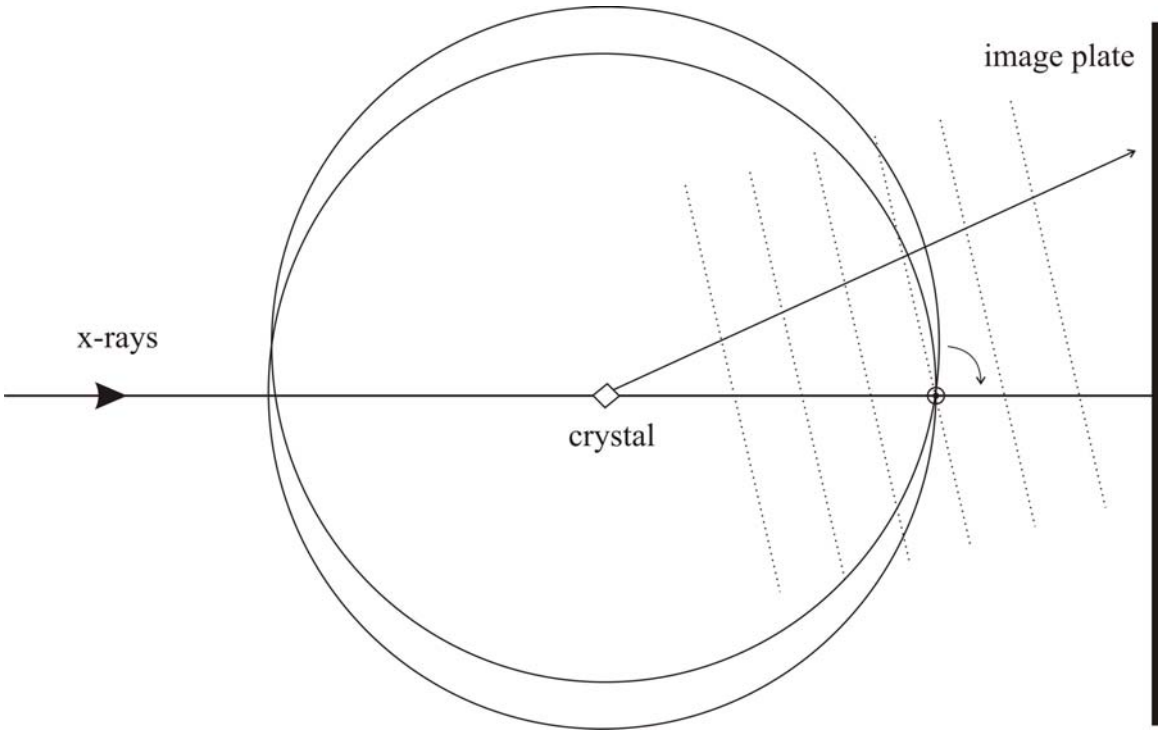

Figure 6.1.4 Principle of an area detector system in terms of Ewald construction [102].

An advantage of area detectors is the recording of the entire diffraction properties of a crystal. A complete image of the diffraction intensity for the reciprocal lattice appears from the different photographs. Information on symmetry, extinction conditions, twinning, foreign reflections, satellite and diffuse reflection streaks can be obtained from the photographs. The actual intensity measurement based on the integration of diffraction spots can be started once

no anomalies in the data were found. The initial step is to determine a more accurate orientation matrix by selecting a range of spot positions throughout the data. Then a computer-assisted program can determine the angle dependent reflection profiles. From the matrix of this profile information, the software can refine the exposures and the positions to search for components of each reflection *hkl*. Around the calculated positions a circular area is scanned with an area determined by a profile-function. The pixel intensities inside the circle are summed to yield the raw intensity. The intensities around the edge are used to estimate the background. These are then scaled and subtracted from the raw intensities to acquire a net intensity. After the data collection and reduction, the corrected intensities can be converted into the structure factors F_o, which are directly comparable with the calculated values F_c. From the corrected data, the starting positional parameters are obtained by the program with the help of *Direct Methods* (SHELXS-97 [103]) or C*harge Flipping* (SUPERFLIP [104]). Finally, the crystal structure is refined using the program SHELX-97 [105].

6.1.2.3 Evaluation of the Results

From X-ray single crystal investigation intensity data, unit cell parameters, and space group can be achieved directly. In order to reach the ultimate goal, determination of the crystal structure, it is necessary to know the location of the atoms in the unit cell. The diffraction phenomena of the coherent X-ray beam from a crystal can be converted by the periodic array of the electron density into the individual structure factors $F_o(hkl)$ by a process of Fourier transformation. In straightforward, if all the individual waves, that is the structure factors and their phases, are known, a Fourier synthesis will give the electron density, and hence the crystal structure. The basic equation of the Fourier summation is given in equation 6.1.3.

$$\rho(x,y,z) = \frac{1}{V} \sum_{h,k,l=-\infty}^{+\infty} F_{hkl} \cdot e^{[-i2\pi(hx+ky+lz)]} \tag{6.1.3}$$

$\rho(x,y,z)$	electron density function in the unit cell
V	volume of the unit cell
x, y, z	coordination of the atoms in the unit cell
h, k, l	miller indices

Light detectors (IP or CCDs) measure the intensity of the light that hits them but not the phase. Therefore the measurement become incomplete as a light wave has not only an amplitude (related to the intensity, $I \alpha |F_{hkl}|^2$), but also a phase, which is systematically lost during the diffraction procedure. The inability to determine the phase is commonly known as "*phase problem*" or "*lost phases*" and can be overcome by utilizing a number of methods. There are three main methods to recover the lost phases from the corresponding diffraction amplitudes obtained by X-ray single crystal experiments.

Patterson Methods. The principle of the Patterson method [106, 107] is based on the utilization of Fourier synthesis for the determination of a structural model. This method is widely used for crystal structures of small inorganic molecules and for organic molecules containing a small number of heavy atoms. The Patterson Function or Patterson Map resembles a map of electron density with positive electron density peaks in various positions that can be defined according to equation 6.1.4.

$$P_{u,v,w} = \frac{1}{V} \cdot \sum_h \sum_k \sum_l \left|F_{hkl}\right|^2 \cdot e^{-2i\pi(hu+kv+lw)} \tag{6.1.4}$$

$P_{u,\,v,\,w}$	patterson-fuction
V	volume of the unit cell
$u,\ v,\ w$	coordinates in Patterson-space
$\lvert F_{hkl}\rvert^2$	structure factor
$h,\ k,\ l$	miller indices

The positions of these peaks are not the positions of the atoms in the structure but a function of vectors between pairs of atoms in the unit cell. Thus, if atom A is at coordination (x_A, y_A, z_A) and atom B is at (x_B, y_B, z_B), there will be a peak at (x_A-x_B, y_A-y_B, z_A-z_B) in the Patterson map. There will also be a peak at the negative coordinates because there is also a vector from B to A. The height of the peak in the Patterson map is proportional to the product of the atomic number of the two atoms, Z_AZ_B. The location of the heavy atoms can be deduced quite readily from their dominating scattering efficiency. The sign of F_{hkl} can be calculated from the location of the heavy atoms in the unit cell, and to a high probability the phase calculated for them will be the same phase for the whole unit cell.

Direct Methods. It is a numeric method [108, 109, 110] that is typically applied if the crystal structure is lacking of heavy atoms. To solve the phase problem Direct Methods make use of a relationship between the measured intensities and the associated phases of certain groups of reflections. Direct Methods started its journey in 1948, when HARKER and KRESPER found that because of symmetry elements, special relationships arise between the amplitudes of specific pairs of reflections. Based on the assumptions: "*electron density in the crystal structure can never have a negative value, and it is concentrated in well defined maxima*" SAYRE developed a very important relationship (see Equation 6.1.5)

$$F_{hkl} = k\sum\nolimits_{h'k'l'}(F_{h'k'l'} \cdot F_{h-h',k-k',l-l'}) \tag{6.1.5}$$

This equation states that the structure factor F_{hkl} is determined by the products of all other pairs of structure factors whose miller indices add to (*hkl*). All the products $F_{h'k'l'} \cdot F_{h-h',k-k',l-l'}$ which have minimum one weak reflection provide, in practical, no contributions to the structure amplitude, while the products of two strong reflections exert a high probability to contribute to the phase of F_{hkl}. The triplet relations (see Equation 6.1.6, 6.1.7) derived by KARLÉ and CAPTAIN [109, 110] for the signs S_{hkl} of three strong reflections and their phase angle, Φ_{hkl}, closely resembles to SAYRE'S equation (6.1.5).

$$S_{hkl} \approx S_{h'k'l'} \cdot S_{h-h',k-k',l-l'} \tag{6.1.6}$$

$$\Phi_{hkl} \approx \Phi_{h'k'l'} \cdot \Phi_{h-h',k-k',l-l'} \tag{6.1.7}$$

Thus obtained statements about the relation between the phases can be formulated with certain probabilities. In order to obtain a final structure model, on the basis of a starting set from well-known or arbitrarily specified phases solutions can be computed, which can be examined with the assistance of higher members of the SAYRE equation (quartet and quintet relations) for their plausibility.

Charge flipping. It is a simple structure determination method [111, 112, 113] that shows a decisive contribution to the solution of structure that are very difficult or impossible to solve by Direct Methods or related techniques. The charge flipping algorithm works iteratively in the manner of Fourier recycling. This iterative algorithm reconstructs approximate electron densities from structure factor amplitudes. The advantage of this method is that it does not require a prior knowledge of either the space-group symmetry, or chemical composition and does not depend on probabilistic phase relations. This makes it particularly suitable for the structure solution of modulated structures, structures with pseudo symmetry, and quasicrystals, where the atoms form continuous domains in a (3+*d*)-dimensional space. Incommensurately modulated structures can be solved by this method without determining the average structure (subcell structure) which is sometimes very difficult or impossible by using classical methods.
The name SUPERFLIP stands for charge *flipping* in *superspace.* It is a computer program [114] and provides an effective tool for the application of the charge flipping algorithm.

6.1.2.4 Structure Solution and Refinement

The Difference Fourier Syntheses. Using the starting atomic positions obtained by methdods described in section 6.1.2.3 Difference Fourier Syntheses (program SHELXL-97 [105]) can calculate the atomic positions as well as anisotropic displacement parameters for all the atoms. However, the resulting structural model contains still errors, which are due to the shortcoming of the solution methods or the calculation of electron density maxima from Fourier syntheses, and errors within the recorded data set. Therefore, the calculated structure factors F_c for the reflection *hkl* do not match with the observed F_o-values. For this discrepancy Difference Fourier Syntheses are necessary to obtain FOURIER-coefficients (F_o-F_c) (see Equation 6.1.8).

$$\Delta\rho = \rho_{obs} - \rho_{calc} = \frac{1}{V} \cdot \sum_h \sum_k \sum_l (F_o - F_c) \cdot e^{-2i\pi(hx+ky+lz)} \tag{6.1.8}$$

$\Delta\rho$ difference of the electron density
$\rho_{obs.}$ observed electron density
$\rho_{calc.}$ calculated electron density
V volume of the unit cell
F_o observed structure amplitude
F_c calculated structure amplitude
hkl miller indices
x, y, z positional parameter of the atoms

The Difference Fourier Syntheses describe the difference between the electron density of the real structure and the incompletely determined structural model. Therefore for the structural model, where the atoms are missing considerable electron density maxima arise, which must be assigned to appropriate atoms in the next step of the refinement. The closer the structural model approaches the actual crystal structure, the less is the difference of the electron density. Difference Fourier Syntheses has several valuable properties which are as following:

(1) Incorrectly placed atoms correspond to the regions of high electron density in $\rho_{calc}(x,y,z)$ and low density in $\rho_o(x,y,z)$, $\Delta\rho(x,y,z)$ is therefore negative in this regions.

(2) A correctly placed atom with either too small atomic number or too high temperature factor, shows up as a small positive area in $\Delta\rho$. The converse situations produce negative peaks in $\Delta\rho$.

(3) An atom that requires a small positional correction tends to lie in a negative area at the side of a small positive peak. The correction is applied by moving the atom into the positive area.

(4) Very light atoms, such as hydrogen, may be revealed by a $\Delta\rho$ synthesis when the places are essentially correct, after least squares refinement has been carried out.

Least Square Refinement. It is a method used to compare experimental data with calculated data to obtain a degree of similarity between them. For crystal structure refinement the similarities between the experimental (observed) structural factor, F_o, and calculated structural factor, F_c is compared in term of the *residual index* or *R-factor* by equation 6.1.9.

$$R = \frac{\sum_{hkl} \left| |F_o| - |F_c| \right|}{\sum_{hkl} |F_o|} \tag{6.1.9}$$

R residual value (R_1 value)
$|F_0|$ observed structure factor
$|F_c|$ calculated structure factor

Ideal solutions would have R-values of 0, however, due to random errors, this is never achieved. R-values (listed as percents) of less than 5% are considered good solutions; high quality refinements often result in R-values lower than 2.5%. wR_2 is similar to R_1, but refers to squared F-values. This results in wR_2 always higher than R_1 (about twice as high).

$$wR_2 = \sqrt{\frac{\sum_{hkl} w \cdot (F_o^2 - F_c^2)^2}{\sum_{hkl} w \cdot (F_o^2)^2}} \tag{6.1.10}$$

$$\text{with } w = \frac{1}{\sigma^2(F_o^2) + (u \cdot P)^2 + v \cdot P} \tag{6.1.10a}$$

$$\text{and } \sigma(F_o^2) = \frac{\sigma(I)}{\sqrt{P \cdot L}} \tag{6.1.10b}$$

wR_2 weighted R-value
w weighting factor
$\sigma(F_o^2)$ standard deviation from F_o^2
$\sigma(I)$ standard deviation of the intensity
F_o^2 observed structure factor
P polarization factor ($P = (F_o^2 + 2F_c^2)/3$)
F_c^2 calculated structure factor
L Lorentz-Factor
u, v balancing factor

The final value, GooF, refers to the "goodness of fit" of the solution. In addition to the difference in F values, the GooF also takes into account the number of observed reflections and the parameters used (see Equation 6.1.11). At the end of refinement, the GooF should approach 1.

$$GooF = \sqrt{\frac{\sum_{hkl} w \cdot (F_o^{\,2} - F_c^{\,2})^2}{(n-p)}} \tag{6.1.11}$$

n / p number of reflection / number of parameter

Displacement parameters. Atoms execute more or less substantial vibrations about their mean positions. Therefore, in order to obtain a realistic structure model, the vibrational behaviour of the atoms should be considered. This behaviour is described by six parameters, known as anisotropic displacement coefficients. With these vibrational ellipsoids can be drawn, which represent the spatial propagation and the direction of the oscillations. The consideration of this anisotropic displacement for the calculation of the structure amplitude $F_c(hkl)$ of a reflection *hkl* (equation 6.1.12) takes place via introduction of an anisotropic temperature factor *Tj* (*hkl*) for each atom *j* (Equation 6.1.12a).

$$F_c(hkl) = \sum_{j=1}^{n} f_i \cdot T_j(hkl) \cdot e^{[2i\pi \cdot (hx_j + ky_j + lz_j)]} \qquad 6.1.12)$$

With $T_j(hkl) = e^{-2\pi^2 \cdot [U_{11}(ha^*)^2 + U_{22}(kb^*)^2 + U_{33}(lc^*)^2 + 2U_{12}(hka^*b^*) + 2U_{23}(klb^*c^*) + 2U_{13}(lhc^*a^*)}$ (6.1.12a)

$T_j(hkl)$	anisotropic temperature factor
a^*, b^*, c^*	reciprocal lattice constant
h, k, l	miller indices
U_{ij}	coefficient of thermal ellipsoids of an atoms *j* /Å^2.

The shape and orientation of the vibration can be given by six parameters U_{ij} (equation 6.12a). In orthogonal system, the diagonal components U_{11}, U_{22} and U_{33} are mutually perpendicular like principle axes of the vibration ellipsoid U_1, U_2 and U_3, and represent the extend of vibration along *a*, *b*, *c* respectively. The "off diagonal term" U_{ij} refers to the orientation of the ellipsoid to that of the reciprocal axes. In non orthogonal systems, they also have the components related to the length of the principle axes. With an isotropic refinement (direction-independent vibration behaviour) there is only one parameter, so called "*isotropic vibrational coefficient*" U*eq* which is almost equal to 1/3(U_{11} + U_{22} + U_{33}). In drawings of the structure, atoms are often very effectively represented as thermal ellipsoids. For this purpose, the principle axes *U1, U2* and *U3* are scaled in such a way that the ellipsoid represents the space in which the centre of the electron density can be localized with a specific probability (normally 50%).

Extinction correction. An additional effect must be taken into account in the final stage of the refinement that reveals its presence when the reflection of high intensity and low scattering angle systematically give $|F_o| < |F_c|$. This is usually due to extinction, divided into primary and secondary extinction. Primary extinction occurs when a strong diffracted ray functions significantly as primary beam and is thus weakened by further diffraction.

Secondary extinction arises when the primary beam proceeds through the crystal; a significant fraction is diffracted by the first layers encountered. This means that planes further into the crystal experience a reduced primary beam, and the overall effect is that the reflection is weakened. In an ideally imperfect crystal the intensity of the primary beam is little affected by the scattering (less than 1%) and is neglected. Secondary extinction, however, is more common than the primary extinction.

Absorption correction. When X-rays pass through a crystal different physical processes such as elastic (Rayleigh) or inelastic (Compton) scattering or ionization reduce its strength. These effects increase with the fourth power of the atomic number Z of the scattering atoms and with third power of the wavelength λ of the used X-radiation. With the help of equation 6.1.13, these can be recapitulated in terms of the *linear absorption coefficient*, μ.

$$I = I_0 \cdot e^{-\mu x} \qquad (6.1.13)$$

I Intensity of the X-ray beam before striking the crystal
I_0 Intensity of the X-ray beam after passing through the crystal
μ linear absorption coefficient / mm^{-1}
x thickness of the crystal that is travelled by the X-ray

Whether an absorption correction is necessary, depends on the shape of the crystal and the atomic number of the elements. Correction becomes very important if the crystal is very anisotropic (thin plate, needle). In such a case, depending on the orientation of the crystal, there may be very big differences in the length of the path of X-ray beam through the crystal. Therefore a large error may arise during the measuring of the relative intensities. Different absorption correction methods are available. In this work *semi empirical absorption corrections based on equivalent reflections* [115] were applied. For different orientations of the crystal to the X-ray many equivalent reflections appear several times when the data are collected with the help of an area detector. It models the absorption surface using a spherical harmonic series based on differences between equivalent reflections.

6.1.3 EDX Analysis

EDX stands for **E**nergy **D**ispersive **X**-ray analysis. Sometimes, it is however, referred to as EDS or EDAX analysis. It is a technique used for identifying the elemental composition of the specimen. The EDX [116, 117, 118] analysis system works as an integrated feature of a scanning electron microscope (SEM).

During EDX analysis, the specimen is bombarded with an electron beam inside the scanning electron microscope. The bombarding electrons collide with the electrons of the atoms of the specimen, knocking some of them off in the process. A position is thus vacated by an ejected inner shell electron which is then eventually occupied by a higher-energy electron from an outer shell. On the way of this occupancy, the transferring outer electron must give up some of its energy by emitting an X-ray.

The amount of energy released by the transferring electron obviously depends on which shell it is transferring from, as well as which shell it is transferring to. Furthermore, every element releases X-rays with unique amounts of energy during the relaxation process. Thus, by measuring the energy of X-rays being released by a specimen the identity of the atom from which the X-ray was emitted can be established.

The output of an EDX analysis is an EDX spectrum. The EDX spectrum is just a plot of how frequently an X-ray is received for each energy level. An EDX spectrum normally displays peaks corresponding to the energy levels for which the most X-rays had been received. Each of these peaks is unique to an atom, and therefore corresponds to a single element. The higher is a peak in the spectrum, the more concentrated the element is in the specimen.

6.2 Spectroscopic Investigations

6.2.1 Solid-sate MAS-NMR Spectroscopy

Over the last decades, NMR spectroscopy has grown into an indispensable tool for chemical analyses and structure determination in organic, inorganic, and biological systems. The NMR phenomenon is based on the fact that nuclei of atoms have magnetic properties that can be utilized to yield chemical information. Quantum mechanical subatomic particles (protons, neutron, electrons) have spin. In some atoms (for example ^{12}C, ^{14}N, ^{16}O) these spins are paired and cancel each other so that the nucleus of the atom has no overall spin. However, in many isotopes (^{1}H, ^{13}C, ^{19}F, ^{29}Si, ^{31}P etc) the nucleus does possess an overall spin, I. Quantum mechanics tells us that a nucleus of spin I will have $2I + 1$ possible orientations. A nucleus with spin 1/2 will have 2 possible orientations. In the absence of an external magnetic field, these orientations are of equal energy. If a magnetic field is applied, then the energy levels split. For each level there is a magnetic quantum number, m. Since the nucleus is positively charged and spinning, it generates its own magnetic field. This implies a magnetic moment (μ) which is proportional to its spin (I) as in equation 6.2.1.

$$\mu = \frac{\gamma I h}{2\pi} \tag{6.2.1}$$

The constant, γ, is called the gyromagnetic ratio and is defined as a fundamental nuclear constant of proportionality between nuclear angular momentum and magnetic moment. For a proton, $\gamma = 2.674 \times 10^4$ gauss^{-1} sec^{-1}. This precession process generates an electric field with frequency ω_o. If we irradiate the sample with radio waves (in MHz frequency range), the proton will absorb the energy and be promoted to the less favorable higher energy state. This absorption is called resonance because the frequency of the applied radiation and the precession coincide or resonate. Since constant γ attains a constant value for each nucleus, consequently it is logical that all atoms of the same type would always experience the same energy from the applied magnetic field and thus all show up on a spectrum as a singular peak denoting that specific atom. This is however not the case due to the principle of nuclear shielding. This aspect of NMR is due to the fact that the electronic effects of some nuclei, generally nuclei with excess electron density, affects the effect of the external magnetic field by shielding them from the full effect of the external force. The inverse of this, is deshielding, which entails the removal of electron density from another nuclei by some electron poor nucleus. If the nucleus is more shielded, then its NMR signal will be shifted upfield (lower

chemical shift). If it is more deshielded, then the signal will be shifted downfield (higher chemical shift). Depending on the local symmetry at the nuclear site, the magnitude of the chemical shift varies as a function of the orientation of the molecule with respect to the external magnetic field. This orientation dependence of the chemical shift is referred to as chemical shift anisotropy. Mathematically, the chemical shift anisotropy is described by a second-rank tensor (a 3 × 3 matrix), which in the case of the symmetric part of the chemical shift tensor consists of six independent components. Generally, one is able to express the chemical shift tensor in a coordinate frame where all off-diagonal elements vanish. In this principal axis system, the chemical shift tensor is fully described by the three diagonal elements - the principal components - and the three eigenvectors or Euler angles describing the orientation of the principal axes with respect to an arbitrary frame. In addition, various combinations of the principal components (and their orientations) are in use to describe the chemical shift tensor. Chemical shift can be classified as isotropic and anisotropic. In contrast to the anisotropic chemical shift δ_{aniso}, the isotropic chemical shift δ_{iso} is independent of the orientation of the molecule towards the magnetic field. While anisotropic chemical shifts δ_{aniso} are observed exclusively in Solid-State NMR, isotropic chemical shifts δ_{iso} appear for the NMR investigation in solution, where the molecule rotates so strongly by Brownian's molecular motion that all the direction orientated interactions becomes average. In contrast to this the line-width, for the Solid-State NMR experiments can be often up to kilohertz (kHz). An excellent example is provided by water whose proton NMR line-width at room temperature is 0.1 Hz, while for ice it becomes 10^5 Hz, six orders of magnitude broader [119]. This broadening is the result of the presence of the anisotropic chemical shift as well as the Dipole-Dipole interactions between the spinning nuclei. In order to reduce the line-widths of a solid sample, a technique so called **M**agic **A**ngle **S**pinning (MAS) [120] is applied. By spinning the sample (usually at a frequency of 1 to 70 kHz) at the magic angle θ_m (θ_m = 54.74°) with respect to the direction of the magnetic field the orientation dependence averages to zero. The angle θ_m = 54.74°, results for the contribution of the chemical shift to the Hamilton operator H_{cs} (Equation 6.2.2).

$$\hat{H}_{cs} = \delta_{iso} \cdot \gamma B_0 \cdot \hat{I}_z + (1\text{-}3\cos^2\theta) \cdot \delta_{aniso} \qquad (6.2.2)$$

γ = gyromagentic constant
B_o = strength of external magnetic field
$\hat{I}_z$ = operator of the z-component

Other problems which arise in solid-state NMR spectroscopy are related to the strong heteronuclear interactions and to the existence of very long spin-lattice relaxation times T_1 of the order of minutes to hours. These can be solved in the **C**ross **P**olarization (CP) technique. The chemical shift of a molecule with arbitrary orientation to the magnetic field can be described generally by six parameters, with three center lines δ_{11}, δ_{22}, δ_{33} (tensor principal values) and the three angles $\Theta = \{\alpha, \beta, \gamma\}$, which describe orientation relative to the magnetic field axis. The three principle axes can take very different values, as a consequence of that, the observed chemical shift of the measured NMR signal depends on the orientation of the molecule relative to the applied magnetic field. In contrast to liquid NMR spectroscopy, all six components play an important role in Solid-State NMR spectroscopy which reveal useful correlations with the structure. Both orientation and the size of the principal tensor adopt values for specific building groups and are therefore suitable for the characterization of structural properties of inorganic samples. Since during the measurement of a powder sample the orientation of the chemical shift is statistically distributed with respect to the *Z*-axis, orientation dependence is lost and only the three principal tensor values δ_{11}, δ_{22}, δ_{33} can be determined. For the correlation with the structure the three principal values are represented favorably into another form. One transforms $\{\delta_{11}, \delta_{22}, \delta_{33}\}$ to $\{\delta_{iso}, \delta_{aniso}, \eta\}$ so that both representations possess the same content. The representation with isotropic chemical shift δ_{iso}, anisotropy δ_{aniso}, and asymmetry parameters η can be brought however more easily into a chemical composition, than those of the tensor principal values. The chemical shift δ is defined in accordance with equation 6.2.3.

$$\delta = \frac{(\nu - \nu_{ref})}{\nu_{ref}} \tag{6.2.3}$$

δ chemical shift / ppm
ν resonance frequency of the sample / Hz
ν_{ref} resonance frequency of the standard sample with chemical shift $\delta = 0$ / Hz

The axial values of the chemical shifts can be arranged according to the resonance frequency (Equation 6.2.4). δ_{11} corresponds to the direction of least shielding, with the highest frequency, while δ_{33} corresponds to the direction of highest shielding, with the lowest frequency.

$$\delta_{11} \geq \delta_{22} \geq \delta_{33} \tag{6.2.4}$$

The isotropic values, δ_{iso}, are the average values of the principal components, and correspond to the center of gravity of the line shape. The isotropic chemical shift δ_{iso} can be defined as equation 6.2.5.

$$\delta_{iso} = \frac{(\delta_{11} + \delta_{22} + \delta_{33})}{3} \tag{6.2.5}$$

One can sort the differences concerning the isotropic chemical shift as in eqaution 6.2.6.

$$|\delta_{cc} - \delta_{iso}| \geq |\delta_{bb} - \delta_{iso}| \geq |\delta_{aa} - \delta_{iso}| \tag{6.2.6}$$

The anisotropic chemical shift δ_{aniso} describes the largest separation from the centre of gravity. The sign of the anisotropy indicates on which side of the isotropic value one can find the largest separation. It can be defined as in equation 6.2.7.

$$\delta_{aniso} = \delta_{cc} - \delta_{iso} \tag{6.2.7}$$

The asymmetry parameter η, indicates how much the line shape deviates from that of an axially symmetric tensor. It can be calculated according to equation 6.2.8.

$$\eta = \frac{\delta_{bb} - \delta_{aa}}{\delta_{aniso}}, \ \eta \in [0, 1] \tag{6.2.8}$$

It is worth mentioning that, both ^{31}P (100% natural abundance) and ^{29}Si (4.7% natural abundance) nuclei have spin I = ½, thus don't suffer from quadrupolar peak broadening and distortion. Thus, they are particularly attractive nuclei for Solid-State NMR measurements. In the present work, ^{31}P- and ^{29}Si-MAS-NMR spectra were recorded and analyzed in order to attain a correlation with the crystal structure determined by X-ray single crystal investigations.

6.2.2 Single-crystal UV/Vis/NIR Spectroscopy

The colour of transition metal complexes is caused by electronic transitions through the absorption of light in the UV/Vis region, 400-800 nm; 25000-12500 cm^{-1}. With the help of the UV/Vis absorption spectroscopy electronic transition of transition metal complexes are investigated in order to determine the symmetry of the chromophore as well as the oxidation state of the transition metal ion. However, the investigations of the following two kinds of transitions in UV/Vis/NIR spectroscopy are of special importance:

(i) The transition of an electron from one orbital to another at a higher energy state of the same atom. This type of transition is known as *d-d* electron transition, observed in transition metal complexes. These transitions in centrosymmetric chromophores are Laporte-forbidden. However, it is sometimes observed (example in ideal octahedrons) where the intensity is comparatively low.

(ii) Charge transfer spectra reflect a redistribution of the electron density in a complex. This transition is either from a filled ligand orbital to a partly filled or empty *d* orbital on the metal or from a filled or partly filled metal *d* orbital to a vacant ligand orbital. These are termed as ligand → metal (L → M) and metal → ligand (M → L) charge transfer transitions, respectively. Apart from this electronic transition along M → M is known as intervalent charge transfer transition.

With these processes parts of the electromagnetic radiation are absorbed. The measurements were accomplished at a single-crystal spectrometer CARY 17, which was developed in the Research School of Chemistry (Canberra, Australia) [121, 122]. The schematic diagram of the spectrometer is represented in Figure 6.2.1.

A halogen lamp is introduced as a light source and a photomultiplier is used as a detector for the measurement at the UV/Vis range (12000-30000 cm^{-1}). For measurement in the near infrared (6000-16000 cm^{-1}) region, a germanium semiconductor detector is used, which was cooled in liquid nitrogen. A polarization filter allows measurements at horizontal as well as vertical polarization of the incident light beam.

A small transparent single-crystal is selected under a microscope. Subsequently, an aluminum foil is attached on a sample holder so that the holes of the sample holder are masked. Under the microscope two equally large holes (sample hole and reference hole) are made into the foil with the help of pin. The holes should be some what smaller than the selected crystals.

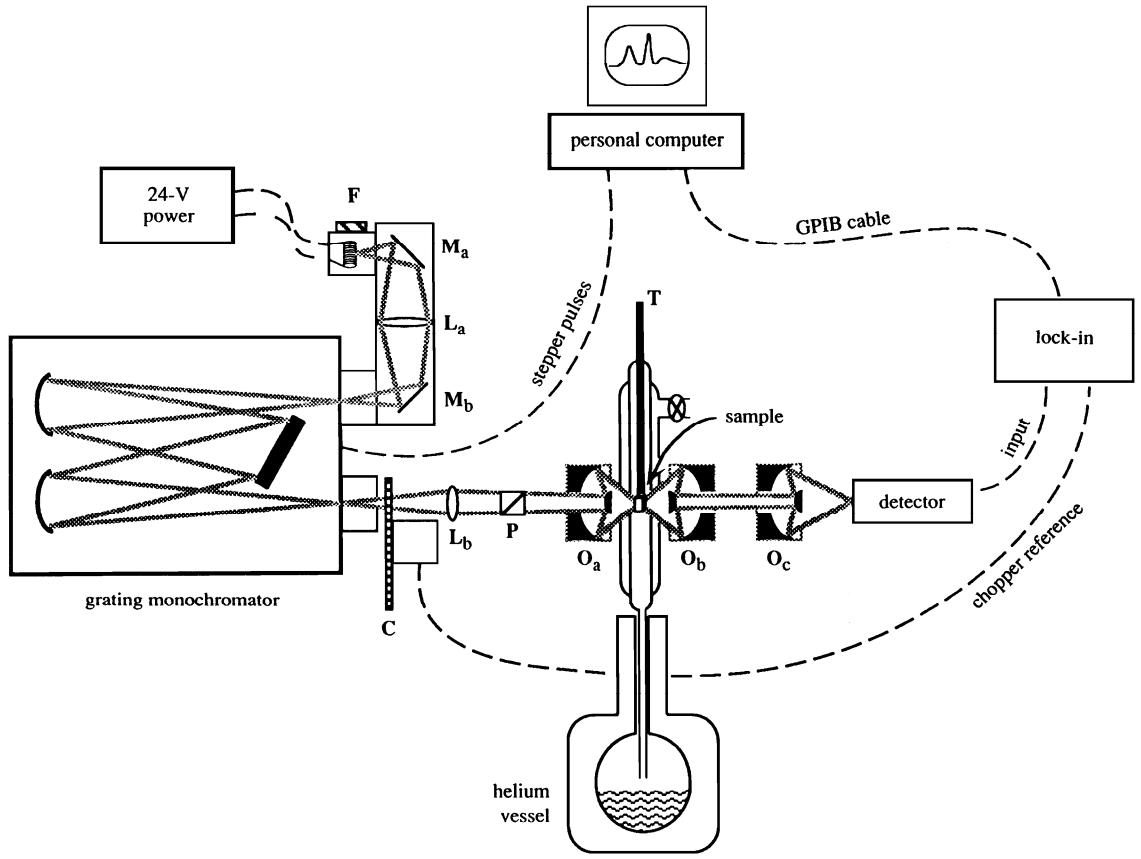

Figure 6.2.1 Schematic of microcrystal UV/Vis/NIR spectrphotometer CARY 17 [122].

The crystal is then carefully placed on the grease at the sample hole under the microscope. Grease has been introduced before to attach the crystal. The sample holder is then placed to the spectrophotometer for the measurement of the absorption spectra of the crystal. It is necessary to mention that a base line measurement with the reference hole is necessary for each measurement. Measurement of (I) and baseline (I_o) for every wavelength can be achieved through Beer-Lambert law (see Equation 6.2.9).

$$A = -\log\frac{I}{I_o} = \varepsilon \cdot c \cdot l \tag{6.2.9}$$

I_o intensity of the incident radiation
I intensity of the transmitted radiation
c concentration of the metal cations
ε molar absorption coefficient
l thickness of the crystal

The dimensionless relationship I/I_o is called transmission. The negative logarithm of transmission is known as absorbance or optical density and is represented by A.

6.2.3 Vibrational Spectroscopy

Infrared spectroscopy [123, 124] utilizes the fact that molecules (having a permanent dipole moment) absorb specific frequencies as light quanta in the range 10 to 14000 cm^{-1}. These absorptions are obviously resonance frequencies, i.e. the frequency of the absorbed radiation matches the frequency of the bond or group that vibrates. The energies are determined by the shape of the molecular potential energy surfaces, the masses of the atoms, and the associated vibronic coupling that can be expressed in terms of equation (6.2.10)

$$E = (v + ½)\cdot h\cdot v \tag{6.2.10}$$

v vibrational quantum number (selection rule: $\Delta v = \pm 1$)
h Planck's constant / $6.626\cdot 10^{-34}$ J·s
v frequency / s^{-1}

The natural frequencies of vibration of a bond are given by equation 6.2.11. According to this equation frequency depends upon force constant K, and reduced mass μ of the vibrating atoms.

$$\nu = \frac{1}{2\pi}\sqrt{\frac{k}{\mu}} \tag{6.2.11}$$

K = force constant / $N.m^{-1}$
μ = reduced mass / kg

This expression immediately meets the following two concepts.

(i) Stronger bonds have larger force constant K and vibrate at higher frequencies than weaker bonds. Force constants vary from one bond to another.

(ii) Bonds between atoms of higher masses (larger reduced mass, μ) vibrate at lower frequencies than that of lighter atoms.

For this work on molybdenum and rhenium phosphates, it was rather interesting to characterize [MO_6] (M = Mo, Re), [PO_4] and [P_2O_7] groups with the help of infrared spectroscopy. The infrared spectra of a few selected crystals of the phosphates were measured using mainly a NICOLET 380 FT-IR spectrometer (SMART ORBIT).

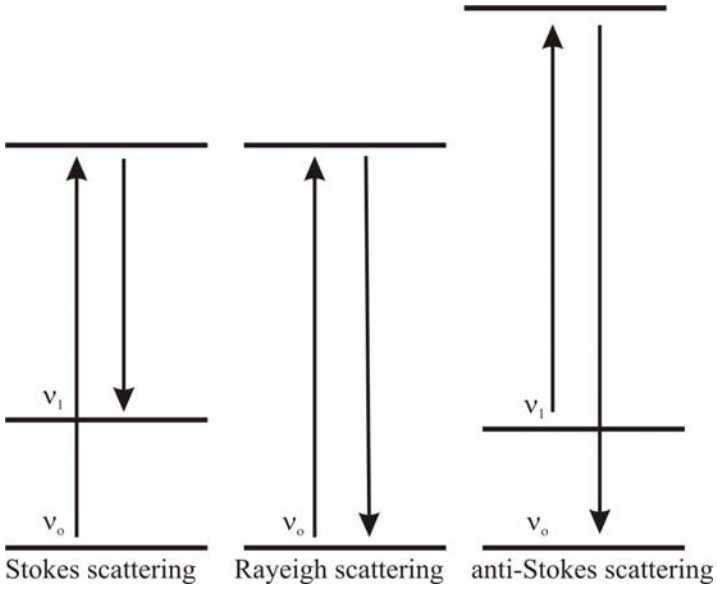

Figure 6.2.2 Energy level diagram showing the states involved in Raman signal.

In **Raman Spectroscopy** [123, 124] a highly intensed monochromatic light beam (LASER; λ = 1064 nm) strikes the molecule and interacts with the electron cloud as well as bonds that leads to the excitation of the molecule from the ground state to a higher energy state. During the relaxation of the molecule, it emits a photon and returns to a different vibrational or rotational energy state (see Figure 6.2.2). The difference in energy between this new state and the original state leads to a shift in the emitted photon's frequency away from the excitation wavelength. Radiation scattered with a frequency lower than that of the incident beam is referred to as Stokes' radiation, while at higher frequency is regarded as anti-Stokes radiation. The former is accompanied by an increase in energy while the latter involves a decrease. Stoke's radiation is generally more intense than that of anti-Stokes'. A change in the molecular polarization potential or amount of deformation of the electron cloud with respect to the vibrational coordinate is required for a molecule to exhibit a Raman effect. The intensity of the Raman scattering depends on the change of the polarizibility. As a lot of i.r. inactive modes may be observed as Raman active or vise versa, a combination of both techniques is therefore demanded for a clear understanding of the molecule. The samples for the present work were investigated by using a *FT*-Raman Spectrometer RFS 100 (Brucker). The samples were placed in a one end sealed capillary and then directly placed into the monochromatic radiation from a Neodymium-YAG-Laser. Scattered radiation (Raman scattering) was recorded with the help of liquid nitrogen cooled germanium detector.

6.2.4 Magnetic Measurements

Inorganic solids exhibit magnetic properties which are due to the presence of unpaired electrons centered usually at the metal cations. Therefore, magnetic behaviour is generally restricted to compounds of transition metals and lanthanides, which posses unpaired *d* or *f* electrons, respectively. Electrons moving in a circular path in an atom or molecule are constantly undergoing acceleration and therefore, generate a magnetic field perpendicular to their direction of motion, the orbital magnetic moment. Electrons also spin around their own axis, which produces a magnetic spin moment. If the electrons are paired in a wave function, their spin magnetic fields are equal and opposite (spin paired). If these moving electrons are placed into a large external magnetic field, then the external field induces an additional current that causes a magnetic field by itself. The induced magnetic field is opposite to the external magnetic field (LENZ law). As a consequence, the magnetic field (*B* is the magnetic flux density) inside the sample $B_{internal} < B_{external}$, and the sample is repelled by the applied field. This phenomenon is known as diamagnetism. $B_{internal} > B_{external}$ is called paramagnetism (Equation 6.2.12). Every electron contributes to the diamagnetism of a substance, consequently diamagnetism is present in every matter. Equation 6.2.12, can be written in two different ways (Equations 6.2.12a and b).

$$B_{internal} = B_{external} + B' \tag{6.2.12}$$

$$B_{internal} = \mu_r B_{external} \tag{6.2.12a}$$

$$B_{internal} = (1 + \chi_v)\, B_{external} \tag{6.2.12b}$$

μ_r = relative magnetic permeability
$B' = \chi_v B_{external}$
χ_v = magnetic susceptibility (volume susceptibility)

For a diamagnetic substance B' is negative and $\mu_r < 1$. The substance may be paramagnetic, ferromagnetic, ferrimagnetic, or antiferromagnetic if B' is positive and $\mu_r > 1$. Generally, susceptibility is referred to the number of moles. With the help of the molar volume V_{mol}, the molar susceptibility χ_{mol} of one mole of substance can be determined according to equation 6.2.13.

$$\chi_{mol} = \chi_v \cdot V_{mol} \quad (\mathrm{cm^3 \cdot mol^{-1}}) \tag{6.2.13}$$

The total magnetic susceptibility χ_{mol} of one mole of a substance is the sum of all the diamagnetic and paramagnetic contributions from all the electrons in the sample (see Equation 6.2.14).

$$\chi_{mol} = \chi_{mol}^{dia} + \chi_{mol}^{para} \tag{6.2.14}$$

On the basis of the LANGEVIN equation the diamagnetic fraction can be obtained as

$$\chi_{mol}^{dia} = -\frac{e^2 \cdot N_L}{6 \cdot m_e} \sum_{i=1}^{n} \overline{R_i}^2 \tag{6.2.15}$$

χ_{mol}^{dia} diamagnetic fraction of the molar susceptibility ($cm^{3} \cdot mol^{-1}$)
e elementary charge $[\sqrt{dyn}.s] = [\sqrt{g.cm.s^{-2}}.s]$
N_L avogadro constant (mol^{-1})
m_e rest mass of electron (g)
n number of electron
R_i distance between the electron and nucleus (cm)

While the core electrons are responsible for the diamagnetic susceptibility, paramagnetic susceptibility results from the unpaired electrons of the valence shell. Paramagnetic susceptibility can be calculated on the basis of the consideration of the influence of orbital- and spin angular momentum of the electrons (*Russel-Saunders*- or L. S. coupling) of the atoms or ions of the transition metals (see Equation 6.2.16).

$$\chi_{mol}^{para} = \frac{(N_L \cdot \mu_B)^2}{3 \cdot R \cdot T} \cdot [L(L+1) + 4S(S+1)] \tag{6.2.16}$$

Effective magnetic moments μ_{LS} arise on the basis of the spin orbital coupling according to the equation 6.2.17.

$$\mu_{eff} = \mu_{LS} = \mu_B \cdot \sqrt{L(L+1) + 4S(S+1)} \tag{6.2.17}$$

L total angular momentum quantum number
S total spin quantum number
μ_B Bohr magneton, 9.27×10^{-21} ($erg \cdot Oe^{-1}$)
T temperature (K)
R gas constant, 8.3144×10^{7} ($erg \cdot K^{-1} \cdot mol^{-1}$)

If L is dropped from equation 6.2.17, an expression is obtained where spin angular momentum alone is the basis of the magnetic behaviour of an ion. This expression is known as spin only formula for magnetic moment (Equation 6.2.18)

$$\mu_{eff} = \mu_{SO} = \mu_B \cdot \sqrt{4S(S+1)} = 2\mu_B \cdot \sqrt{S(S+1)} \tag{6.2.18}$$

The relation between temperature and susceptibility can be achieved from the well known Curie-Weiss relation (Equation 6.2.19).

$$\chi_m = C/(T-\theta) \tag{6.2.19}$$

C is called Curie constant, whereas θ is the Curie Weiss constant, has a fundamental significance.

In the present work, effective magnetic moment was calculated based on of the equation 6.2.20.

$$\mu_{eff} = .\sqrt{\frac{C}{n \cdot 0.12505}}.\mu_B = \sqrt{\frac{\chi.(T-\theta)}{n \cdot 0.12505}} \cdot \mu_B \tag{6.2.20}$$

Here n is the number of paramagnetic center per formula unit and the value of χ and T were obtained from the graphical representation of $1/\chi$ vs T.

7 Chemicals Used Throughout This Thesis

7.1 Purchasable Chemicals

Chemical used during the present work are listed in Table 7.1. Due to its hygroscopic behaviour, Re_2O_7 was protected in a argon atmosphere in sealed silica tubes. Argon was used as an inert gas during preparation of the quartz glass ampoules.

Table 7.1 Purchasable chemicals

substance	**company**	**purity**
Aceton	Merck, Darmstadt	99%
Argon	Air Products, Hattingen	99.996%
Rehenuim(VII) oxide	ABCR	99.99%
Rhenium	Chempur	99.99%
Molybdenum(VI) oxide	RdH	99%
Diammonium hydrogen phosphate	Riedel de Haën	p. A.
Vanadum(V) oxide	Acros	98%
Phosphorus(V) oxide	KMF Laborchemie	97%
Phosphorus, red	Knapsack Electronic	Electronic grade 6N
Sodium iodide	Applichem	99%
Iodine	Grüssing GmbH	99.5%
Ammonium chloride	Geyer, Gehalt	99.50%
Platinum(II) chloride	ChemPur, Karlsruhe	p.A.
Barium sulphate	Merck, Darmstadt	p.A.
Hydrofluoric acids	Merck, Darmstadt	38-40%; reinst
Quartz glass	GVB, Aachen	
Oxygen	Praxair	99,9 %
α-quartz	Merck, Darmstadt	p. A.
Hydrogen	Air Products, Hattingen	99.9%
Silver(I) oxide	Sigma Aldrich	99.99%

7.2 Chemicals Synthesized

7.2.1 Molybdenyl(VI) oxidepyrophosphate

A microcrystalline powder of $(MoO_2)_2P_2O_7$ was prepared by heating a mixture of MoO_3 and $(NH_4)_2HPO_4$ in an open silica tube according to equation 7.2.1. The heating was conducted initially at 250 (2 days) and 400°C (2 days) in order to remove volatile gaseous species from $(NH_4)_2HPO_4$, followed by a subsequent heating at 600°C.

$$MoO_3 + (NH_4)_2HPO_4 \rightarrow \tfrac{1}{2}\,(MoO_2)_2P_2O_7 + 2\,NH_3 + 3/2\,H_2O \qquad (7.2.1)$$

7.2.2 Rhenium(VI) oxide

Rhenium(VI) oxide was synthesized by reduction of Re_2O_7 by metallic rhenium according to equation 7.2.2 [84, 125]. A red powder of ReO_3 was obtained when a stoichiometric mixture of Re_2O_7 and metallic rhenium was heated isothermally at 300°C for three days in an evacuated sealed silica tube ($l \approx 11$ cm, $d \approx 1.5$ cm, $V \approx 20$ cm^3). About 40 mg of iodine was used as a mineralizer.

$$3\,Re_2O_7 + Re \rightarrow 7\,ReO_3 \qquad (7.2.2)$$

7.2.3 Rhenium(IV) oxide

A microcrystalline grey powder of rhenium(IV) oxide was synthesized by the reduction of Re_2O_7 by metallic rhenium according to equation 7.2.3. ReO_2 was obtained when a stoichiometric mixture of Re_2O_7 and metallic rhenium was heated isothermally at 300°C for three days in an evacuated sealed silica tube ($l \approx 11$ cm, $d \approx 1.5$ cm, $V \approx 20$ cm^3). About 50 mg of iodine was used as a mineralizer.

$$2\,Re_2O_7 + 3\,Re \rightarrow 7\,ReO_2 \qquad (7.2.3)$$

8 Molybdenyl(V) oxidepyrophosphate

8.1 Introduction

Dealing with synthesis, crystallization, purification and thermochemical characterization of solids Chemical Vapour Transport (CVT) has become a valuable tool [85, 126]. The potential applicability of CVT for synthesis and crystallization of transition metal phosphates has been already discussed in detail [2].

Anhydrous phosphates of molybdenum at oxidation states +III, +IV, +V, and +VI have been synthesized and characterized. The comparable stability of various oxidation states of molybdenum is the key to formation of several thermodynamically stable phosphates. The ratio *n*(molybdenum oxide) : *n*(phosphorus oxide) in ternary molybdenum phosphates covers a range form 1/3 in $Mo(PO_3)_3$ [32] to 1 in $MoO(PO_4)$ [27]. Molybdenum phosphates show a large structural diversity. Corner sharing between $[MoO_6]$ octahedra and a variety of phosphate anions (PO_4^{3-}, $P_2O_7^{4-}$, $P_4O_{13}^{6-}$, PO_3^-) is the main structural feature.

The crystal structure of $(Mo^{VI}O_2)_2(P_2O_7)$ [24, 25, this work] consists of $[Mo^{VI}O_6]$ octahedra and $[P_2O_7]$ groups. $[Mo^{VI}O_6]$ octahedra form zigzag chains by sharing their corners. Two successive chains are connected to each other by $[P_2O_7]$ groups. Conversely, $Mo^{VI}O_2(PO_3)_2$ [26] is built up of $[Mo^{VI}O_6]$ octahedra connected by metaphosphate chains. In this way, two oxygen atoms in each $[Mo^{VI}O_6]$ octahedron are bound only to molybdenum and the remaining four oxygen atoms are shared with (PO_3) chains. Thus infinite wavelike layers of the composition $Mo^{VI}O_2(PO_3)_2$ are formed. Up to date, two phosphates of molybdenum in its pentavalent state, $MoO(PO_4)$ [27] and $(MoO)_2P_4O_{13}$) [28, 29], are structurally characterized. The framework of molybdenyl(V) oxide phosphate, $MoO(PO_4)$ is built up from $[Mo^VO_6]$ octahedra and $[PO_4]$ tetrahedra. The $[Mo^VO_6]$ octahedra share opposite corners to form infinite chains (O=Mo···O=Mo···O) along the *c*-axis of the tetragonal structure. These chains are interconnected to each other by corner sharing $[PO_4]$ tetrahedra. The crystal structure of $(MoO)_2P_4O_{13}$ consists of $[Mo^VO_6]$ octahedra sharing five of their corners with $P_4O_{13}^{6-}$ groups. The sixth one corresponds to a molybdenyl group. The original framework of $Mo^{\sim V}{}_{1.3}O(P_2O_7)$ is built up from $[(Mo^{\sim V}{=}O)O_5]$ octahedra, $[P_2O_7]$ groups and also from $[MoO_4]$, $[Mo_2O_4]$ and $[Mo_3O_8]$ units containing Mo_2 and Mo_3 clusters [30]. MoP_2O_7 [31] is isotypic to the cubic modification of ZrP_2O_7 [127] and built up by corner sharing of $[Mo^{IV}O_6]$ octahedra and $[P_2O_7]$ groups. Interestingly, this pyrophosphate shows a 3·3·3 superstructure of the subcell [128]. The structure of $Mo(PO_3)_3$ [32] consists of infinite chains $^1_\infty(PO_3)^-$ bridged by isolated

[$Mo^{III}O_6$] octahedra. Each of the octahedra shares its six apices with six different phosphate tetrahedra. It is appealing to see that molybdenum adopts a very simple structure with only 4 atoms in the asymmetric unit in $MoO(PO_4)$ [27], whereas a very complex structure with 441 atoms in the asymmetric unit of $(MoO)_2P_4O_{13}$ (space group *Pn*) [29] is observed. Crystallographic properties of the already known molybdenum phosphates are summarized in Table 8.1.

Table 8.1 Summary of the crystallographic properties of anhydrous molybdenum phosphates.

phosphates	**space group**	***Z***	**unit cell parameters (Å,°)**	**ref.**
α-$(Mo^{VI}O_2)_2P_2O_7$	*P2/c*	16	17.8161(1), 10.3672(5), 17.8089(1) 90.2009(2)	[25, this work]
γ-$(Mo^{VI}O_2)_2P_2O_7$	*Pnma*	4	12.58(1), 6.338(5), 10.38(1)	[24, 25]
δ-$(Mo^{VI}O_2)_2P_2O_7$	$C222_1$	2	16.2213(11), 3.8936(3), 6.2772(4) 90.2009(2)	[129]
$(Mo^{VI}O_2)(PO_3)_2$	*Pbcm*	2	7.683(5), 7.426(5), 4.889(3)	[26]
$Mo^{V}OPO_4$	*P4/n*	2	6.1768(3), 4.2932(3)	[27]
β-$Mo^{V}OPO_4$	*Cc*	4	7.4043(3), 7.2128(3), 7.2876(3) 118.346(2)	[129]
β_1-$Mo^{V}OPO_4$	*Pnma*	4	7.704(2), 6.301(2), 7.080(2)	[this work]
$(Mo^{V}O)_4(P_2O_7)_3$	$P2_12_12_1$	36	23.514(1), 23.514(1), 31.912(5)	[19, this work]
Phase X1	---	---	7.8887(5), 7.8887(5), 15.778(19)	[this work]
$(Mo^{V}O)_2P_4O_{13}$	$P2_1/c$	2	8.3068(8), 6.5262(6), 10.718(1) 106.705(8)	[28]
	Pn	42	24.133(2), 19.579(1), 25.109(2) 99.962(3)	[29]
	$P\bar{1}$	24	17.947(3), 19.864(3), 21.899(3) 72.421(3), 78.174(4), 68.315(4)	[29]
$Mo^{\sim V}{}_{1.3}O(P_2O_7)$	*I2/a*	16	22.88(1), 22.94(2), 4.83(1) 90.36(5)	[30]
$Mo^{IV}P_2O_7$ [a)]	$Pa\bar{3}$	4	7.944(1)	[31]
$Mo^{III}(PO_3)_3$	*Ia*	12	10.819(1), 19.515(3), 9.609(1) 97.74(1)	[32]

[a)] Exhibits a 3·3·3 superstructure ($a' = 3a$) of the subcell [128].

Despite the wealth of molybdenum phosphates with such interesting structural variations, prior to the work of LENZ [19] there was no systematic investigation at the ternary system Mo / P / O in order to search for new phosphates. On the way to develop the ternary phase diagram Mo / P / O (see Figure 8.1), LENZ [19] found a new metastable molybdenyl(V) oxidepyrophosphate, $(MoO)_4(P_2O_7)_3$. Despite some efforts at that time neither a detailed structural description nor reproducible experimental conditions for the synthesis of this

compound could be obtained. This inadequate results gave inspiration for the reinvestigation of molybdenyl(V) oxidepyrophosphate.

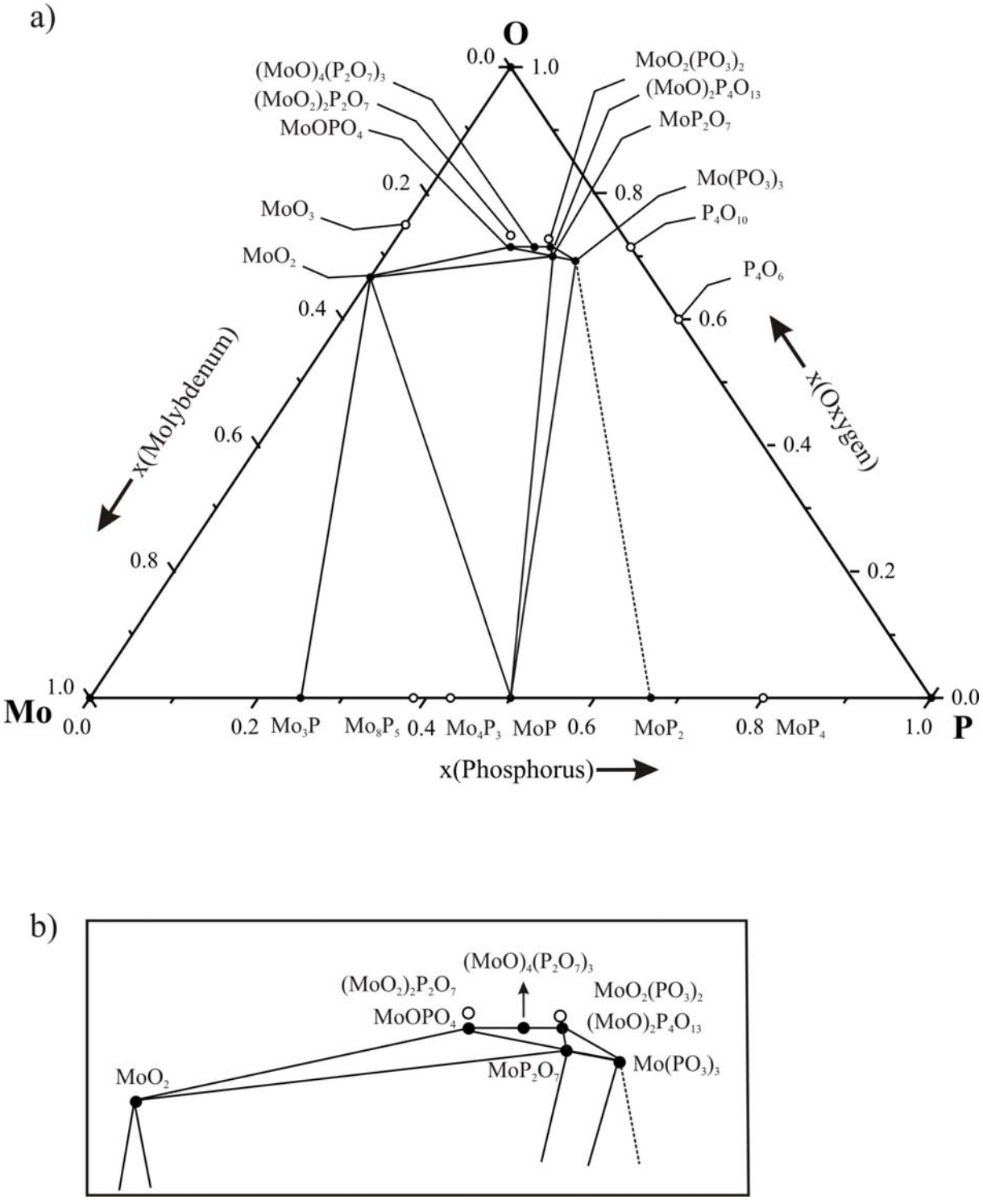

Figure 8.1 Ternary phase diagram Mo / P / O at 800°C [19]. Solid lines indicate solid-solid equilibria. Open circles indicate the compounds those do not exist as solid at this temperature.

In the present work, in addition to a clear synthetic pathway to this pyrophosphate, a reliable structual model was developed. In addition, adequate evidence for the pentavalent state of

molybdenum (d^1 electronic configuration) was obtained by using UV/Vis spectroscopy and magnetic measurements. Apart from this, evidence for the presence of molybdenyl $(Mo{=}O)^{3+}$ and $[P_2O_7]$ groups will be discussed based on i.r. spectroscopy.

8.2 Syntheses and Crystallization of Molybdenyl(V) phosphates

Molybdenyl(V) phosphates $(MoO)_4(P_2O_7)_3$, $MoOPO_4$, β_I-$MoOPO_4$, and $(MoO)_2P_4O_{13}$ were synthesized (see Figure 8.2) reducing $Mo^{VI}{}_2P_2O_{11}$ by red phosphorus followed by chemical vapour transport. About 30 mg of iodine were used as transport agent.

For the synthesis of phosphates containing pentavalent molybdenum, a homogeneous mixture of $Mo_2P_2O_{11}$ and red phosphorus (~200.5 and ~5.75 mg respectively) was prepared by careful grinding in an agate mortar. A pellet was prepared with the help of a hydraulic press by applying a pressure of ~25 kN for about 20 minutes. This pellet was then transferred into evacuated sealed silica tubes ($l \approx 11$ cm, $d \approx 1.5$ cm, $V \approx 20$ cm^3) along with iodine (transport agent) and heated isothermally (400 or 800°C, 4 days) and subsequently in a temperature gradient (800 → 650°C, 6 days). After heating, the ampoules were removed from the furnace in such a way that led to the condensation of the equilibrium gas phase in the source region in order to avoid contamination of the crystals of molybdenum phosphates which were grown at the sink. Details on various experiments are summarized in table 8.2.

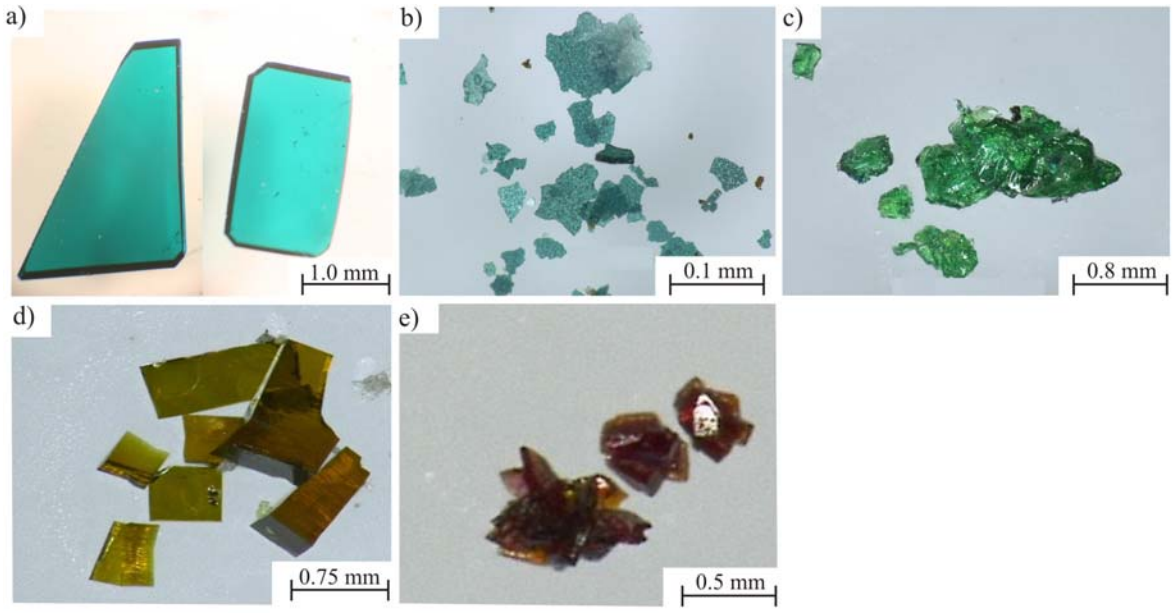

Figure 8.2 Crystals of molybdenyl(V) phosphates obtained by CVT. $(Mo^VO)_4(P_2O_7)_3$ (a), Phase X1 (b), $(Mo^VO)_2P_4O_{13}$ (c), α-Mo^VOPO_4 (d) and β_I-Mo^VOPO_4 (e).

Table 8.2 Experiments for synthesis and crystallization of $(MoO)_4(P_2O_7)_3$

starting solids / mg		$n(Mo_2P_2O_{11})$ / n(P)	I_2 / mg	temperature[a] / °C	time / d	products (source) (according to *IP* Guinier photographs)	products (sink)
$Mo_2P_2O_{11}$	390.12	5.26	40	800 → 650	5	amorphous solids	$MoPO_5$, amorphous solids
P	5.35						
$Mo_2P_2O_{11}$	195.30	2.81	31	800 → 700	1		
P	5.02			850 → 700	6	$MoPO_5$, $Mo_2P_4O_{15}$ (-)	----
$Mo_2P_2O_{11}$	195.13	2.75	98	500	1		
P	5.10			800 → 650	6	$MoPO_5$, $Mo_2P_4O_{15}$ (-)	$MoPO_5$, $Mo_2P_4O_{15}$ (-)
$Mo_2P_2O_{11}$	194.20	2.74	41	800 → 650	6	$MoPO_5$	$MoPO_5$, $Mo_2P_4O_{15}$ (-)
P	5.10						
$Mo_2P_2O_{11}$	200.71	2.54	----	800	7		
P	5.70			800 → 650	7		
				800 → 650	5	$MoPO_5$	**Phase X1,** $MoPO_5$
$Mo_2P_2O_{11}$	200.52	2.51	32	400	4		
P	5.75			820 → 650	6	$MoPO_5$, $Mo_2P_4O_{15}$ (--)	**$Mo_4P_6O_{25}$**[b]
$Mo_2P_2O_{11}$	200.50	2.51	32	400	4		
P	5.75			820 → 650	7	$MoPO_5$	**$Mo_4P_6O_{25}$**[b], $MoPO_5$ (-)
$Mo_2P_2O_{11}$	200.51	2.51	28	400	4		
P	5.75			800 → 650	6	$MoPO_5$	**$Mo_4P_6O_{25}$**[b], **(--)**
$Mo_2P_2O_{11}$	200.51	2.51	32	800	7		
P	5.75			800 → 650	7	$MoPO_5$	**Phase X1**
$Mo_2P_2O_{11}$	200.50	2.51	32	400	8		
P	5.75			820 → 650	9	$MoPO_5$	**$Mo_4P_6O_{25}$**[b], **Phase X1 (-),** $MoPO_5$ (-)
$Mo_2P_2O_{11}$	200.51	2.51	32	400	8		
P	5.75			810 → 650	9	$MoPO_5$	**$Mo_4P_6O_{25}$**[b], **Phase X1 (-),** $MoPO_5$ (-)
$Mo_2P_2O_{11}$	200.52	2.51	32	400	4		
P	5.75			800→ 810	7	$MoPO_5$, $Mo_2P_4O_{15}$	----
$Mo_2P_2O_{11}$	200.50	2.51	30	400	4		
P	5.75			650→ 660	6	$Mo_2P_4O_{15}$ / $MoPO_5$ (-)	----
$Mo_2P_2O_{11}$	200.51	2.51	30	650	7	$Mo_2P_4O_{15}$ / $MoPO_5$ (-)	----
P	5.75						
$Mo_2P_2O_{11}$	200.52	2.51	30	850	7	$MoPO_5$	----
P	5.75						
$Mo_2P_2O_{11}$	200.50	2.51	30	400	8		
P	5.75			805→ 650	9	$MoPO_5$	**$Mo_4P_6O_{25}$**[b], **Phase X1 (-),** $MoPO_5$ (-)
$Mo_2P_2O_{11}$	200.51	2.51	39	400	7		
P	5.75			805→650	7	$MoPO_5$	**Phase X1**, $MoPO_5$ (-), **β_1-$MoPO_5$** (--)
$Mo_2P_2O_{11}$	200.51	2.51	38	800	3		
P	5.75			800→650	4	$MoPO_5$	**$Mo_4P_6O_{25}$**[b], $MoPO_5$ (-)
$Mo_2P_2O_{11}$	200.03	2.50	40	750→600	7		
P	5.77			800→650	4	$MoPO_5$	$MoPO_5$, $Mo_2P_4O_{15}$ (-)
$Mo_2P_2O_{11}$	200.57	2.49	39	800	6		
P	5.80			800 → 650	4	$MoPO_5$	$MoPO_5$, **$Mo_4P_6O_{25}$**[b] (-)
$Mo_2P_2O_{11}$	200.70	2.49	30	780 → 800	6		
P	5.80			800 → 650	7	$MoPO_5$	**Phase X1**
$Mo_2P_2O_{11}$	200.68	2.49	71	790 → 650	6	$MoPO_5$ / $Mo_2P_4O_{15}$	$MoPO_5$
P	5.80						

$Mo_2P_2O_{11}$	199.90	2.48	38	800	6		
P	5.79			800 → 650	6	$MoPO_5$, $Mo_2P_4O_{15}$ (-)	$MoPO_5$, $Mo_2P_4O_{15}$ (-)
$Mo_2P_2O_{11}$	200.72	2.48	41	800	6		
P	5.84			800 → 650	2	$MoPO_5$	$MoPO_5$, $Mo_2P_4O_{15}$ (-)
$Mo_2P_2O_{11}$	200.15	2.46	70	760 → 610	7	$MoPO_5$	$MoPO_5$, $Mo_2P_4O_{15}$ (-)
P	5.87						
$Mo_2P_2O_{11}$	193.20	2.13	40	800 → 650	4	$MoPO_5$, MoP_2O_7 (-)	MoP_2O_7, (--)
P	6.54						
MoO_3	211.39	----	30	650	7	$Mo_2P_4O_{15}$ / $MoPO_5$ (-)	----
P	9.13						
P_4O_{10}	136.00						
$Mo_4P_6O_{25}$ Phase X1	~80	----	32	800 → 810	7	**$Mo_4P_6O_{25}$, Phase X1** (-), $MoPO_5$(--)	----
$Mo_4P_6O_{25}$	~100	----	----	800[c)]	12	**$Mo_4P_6O_{25}$, Phase X1**[c)] (-)	----

a) given are the various heating periods for an ampoule. Starting solids were always at the temperature at the left side of the arrow. Solid reaction products were characterized by their XRPD pattern after the final heating period, only.
b) amorphous blue lamella.
c) formation at a few centimeters away from the source containing $Mo_4P_6O_{25}$.
(-) minor component.
(--) trace or a few crystals.

The formation of molybdenyl(V) pyrophosphate, $(MoO)_4(P_2O_7)_3$, is rather sensitive to the starting solids ($Mo_2P_2O_{11}$ and red phosphorus), molar ratio of the starting materials, temperature, and crystallization via vapour phase transport.

Dark green rectangular crystals of $(MoO)_4(P_2O_7)_3$ (see Figure 8.2a) up to 2.5 mm in length were obtained only at a molar ratio of $n(Mo_2P_2O_{11}) : n(P) = 2.5$ by chemical vapour transport (400 or 800°C, 4 days; 800 → 650°C, 6 days) in the sink of the ampoule according to equation 8.1. Isothermal heating of $Mo_2P_2O_{11}$ and red phosphorus ($n(Mo_2P_2O_{11}) : n(P) = 2.5$) at 650°C produced $MoOPO_4$ and $(MoO)_2P_4O_{13}$ instead of $(MoO)_4(P_2O_7)_3$ (see Equation 8.2). An attempt to prepare $(MoO)_4(P_2O_7)_3$ by isothermal heating of a stoichiometric mixture of MoO_3, P_4O_{10} and red phosphorus (see Equation 8.3) at 650°C failed and thereby led to the formation of $(MoO)_2P_4O_{13}$ and $MoOPO_4$.

It is worth mentioning that a thin layer of blue amorphous material is being formed together with the crystals of $(MoO)_4(P_2O_7)_3$ at the sink side of the ampoule. Though we observed no amorphous mass in the immediate vicinity of the crystals of $(MoO)_4(P_2O_7)_3$ (see Figure 8.3). This might point to the fact that crystals of $(MoO)_4(P_2O_7)_3$ form instead of deposition of the blue amorphous mass. This observation is further backed by the result of EDX analyses (see Table 8.3) of $(MoO)_4(P_2O_7)_3$ and the blue amorphous mass that show close compositional ratio with respect to molybdenum and phosphorus.

$$5Mo_2P_2O_{11} + 2P \rightarrow 6MoOPO_4 + (MoO)_4(P_2O_7)_3 \quad (8.1)$$

$$5Mo_2P_2O_{11} + 2P \rightarrow 8MoOPO_4 + (MoO)_2P_4O_{13} \quad (8.2)$$

$$40MoO_3 + 8P + 13P_4O_{10} \rightarrow 10(MoO)_4(P_2O_7)_3 \quad (8.3)$$

Apart from $(MoO)_4(P_2O_7)_3$, often the new phase called phase X1 (see Figure 8.2b) was obtained by heating a pellet of a mixture of $Mo_2P_2O_{11}$ and red phosphorus at previously specified molar ratio ($n(Mo_2P_2O_{11})$: $n(P)$ = 2.5) isothermally at 800°C for 7 days. Subsequently a temperature gradient from 800 → 650°C for 7 days was applied. In addition to this, $(MoO)_4(P_2O_7)_3$ along with phase X1 and $MoOPO_4$ were also obtained when the same starting solids of aforementioned molar ratio were heated isothermally at 400°C and subsequently in a temperature gradient 820-805 → 650°C for 8, 9 days respectively. Apart from this, the simultaneous formation of $(MoO)_4(P_2O_7)_3$ and phase X1 clearly represent that these two phases are also thermodynamically closely related to each other. There might be a very narrow thermal boundary between these two phases that we were not able to detect from our experimental conditions.

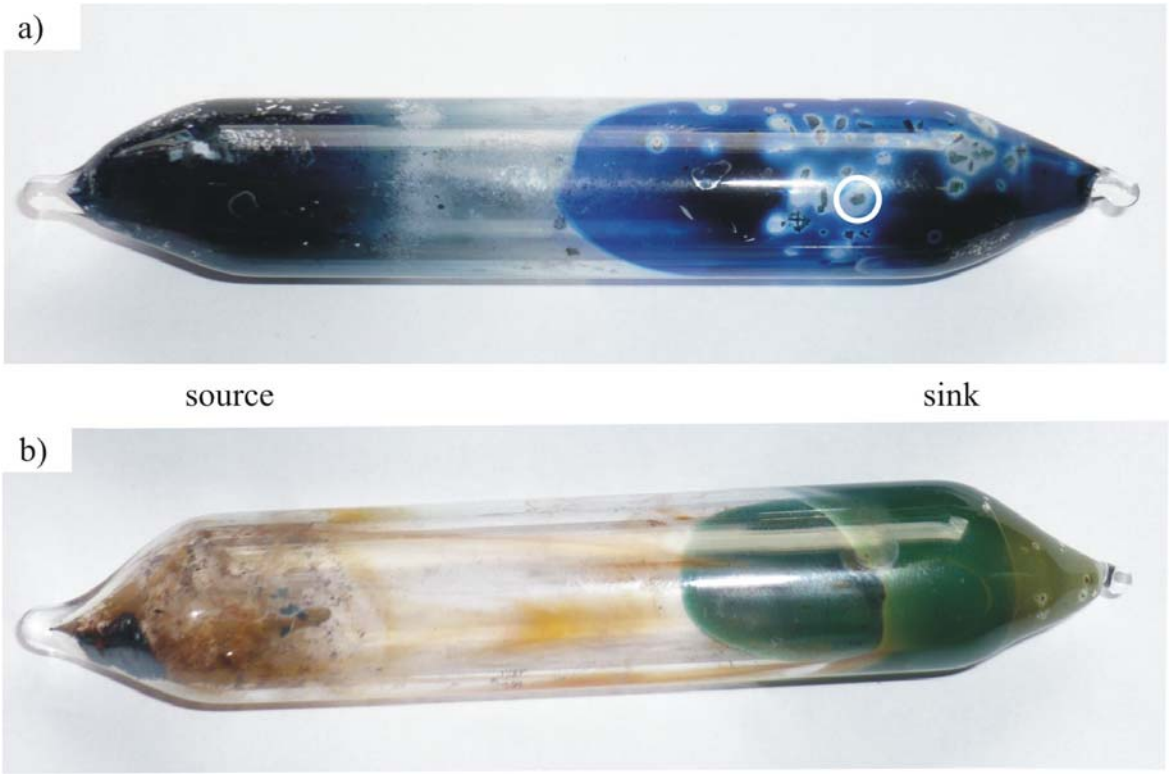

Figure 8.3 Formation of $(MoO)_4(P_2O_7)_3$ (a) and phase X1 (b) at the sink of an ampoule.

In addition, one experiment led to the formation of a few red crystals (see Figure 8.2) of a new modification of $MoOPO_4$ (isotypic to β-$VOPO_4$ [130]) called β_1-$MoOPO_4$, $MoOPO_4$ as well as phase X1 by CVT ($n(Mo_2P_2O_{11})$: n(P) = 2.5, 400, 805 → 650°C for 7 and 7 days). So far it was not possible to reproduce this result.

The CVT experiments allow simultaneous crystallization of other molybdenyl(V)-phosphates such as $MoOPO_4$ and $(MoO)_2P_4O_{13}$ at the same temperature but at a slightly different molar ratio of the starting solids, ($n(Mo_2P_2O_{11})$: n(P) = 2.48 (see Table 8.1). In all the experiments, $MoOPO_4$, occasionally with $(MoO)_2P_4O_{13}$ was obtained in the source region of the ampoule. $MoOPO_4$ frequently transported along with $(MoO)_4(P_2O_7)_3$ and the Phase X1 but $(MoO)_2P_4O_{13}$ was never found.

Increasing of the phosphorus contents along the quasibinary section of $Mo_2P_2O_{11}$ and P led to the formation of $Mo^{IV}P_2O_7$, $Mo^{IV}O_2$, $Mo^{III}P_3O_9$ and MoP (see Equations 8.4-8.7).

$$10Mo_2P_2O_{11} + 5P \rightarrow 15MoOPO_5 + 5MoP_2O_7 \quad (8.4)$$

$$5Mo_2P_2O_{11} + 4P \rightarrow 3MoO_2 + 7MoP_2O_7 \quad (8.5)$$

$$7Mo_2P_2O_{11} + 11P \rightarrow 11MoP_2O_7 + 3MoP \quad (8.6)$$

$$9Mo_2P_2O_{11} + 22P \rightarrow 11MoP_3O_9 + 7MoP \quad (8.7)$$

Molybdenyl(V) pyrophosphate, $(MoO)_4(P_2O_7)_3$, can only be obtained by chemical vapour transport (CVT). Migration of molybdenum phosphates always proceeds from higher to lower temperature ($T_2 \rightarrow T_1$, ΔT = 150 K) due to endothermic reactions. $(MoO)_4(P_2O_7)_3$ was only obtained at crystallization conditions that might favour a supersaturated gas phase. For CVT, iodine was used as a transport agent. The dominance of gaseous MoO_2I_2 as molybdenum carrier under such conditions has already been discussed in detail for the CVT of MoO_2 [131, 132]. In addition to P_4O_{10}(g) and P_4O_6(g), also PO(g), PO_2(g) and P_4O_n(g), $7 \leq n \leq 9$ are known as gaseous phosphorus oxides [133]. The stability of P_4O_{10}(g) and P_4O_6(g) as phosphorus carrier has been already discussed [2, 134]. In addition, we assume that under such mild reducing conditions a mixture of P_4O_{10}(g) and P_4O_6(g) is present in the gas phase. We assume that the deposition of molybdenyl(V) phosphates, $MoOPO_4$, $(MoO)_4(P_2O_7)_3$, and $(MoO)_2P_4O_{13}$ in the sink of the ampoule is achieved by transport via MoO_2I_2(g), P_4O_{10}(g) and P_4O_6(g).

8.3 EDX Analyses of Molybdenyl(V) phosphates

Energy-dispersive X-ray fluorescence analyses [116, 117, 118] (EDX system, scanning microscope DMS 940, Zeiss) of crystals of $(MoO)_4(P_2O_7)_3$, blue amorphous lamella, phase X1 and β_I-$MoPO_5$ showed the presence of molybdenum, phosphorus and oxygen. Experimentally obtained compositions are given in table 8.3.

Table 8.3 EDX analyses of molybdenyl(V) phosphates.

Phosphates	Mo [%]	P [%]	O [%]	n(Mo) / n(P)
$(MoO)_4(P_2O_7)_3$				
crystal 1	2.72	6.0	91.28	0.45
crystal 2	4.98	10.3	84.72	0.49
average	3.85	8.3	87.85	0.47[a)]
blue amorphous lamella				
sample 1	2.77	6.37	90.86	0.43
sample 2	2.67	6.00	91.33	0.45
average	2.72	6.19	91.09	0.44
phase X1				
crystal 1	15.53	27.34	57.13	0.56
crystal 2	16.29	27.16	56.58	0.60
crystal 3	20.88	31.46	47.66	0.66
crystal 4	22.02	31.27	46.71	0.70
average	18.67	29.31	52.02	0.64
$MoOPO_4$				
crystal 1	3.86	5.47	90.67	0.71
crystal 2	4.94	6.58	88.48	0.75
average	4.40	6.03	89.57	0.73
β_I-$MoOPO_4$				
crystal 1	28.54	28.08	43.38	1.02
crystal 2	29.22	26.0	54.78	1.12
average	28.88	27.4	43.72	1.07
$(MoO)_2P_4O_{13}$				
crystal 1	4.89	13.77	81.34	0.35
crystal 2	2.95	8.09	88.96	0.36
average	3.92	10.93	85.15	0.35

[a)] n(Mo) / n(P) = 0.667 theoritical value for $(MoO)_4(P_2O_7)_3$

8.4 X-ray Single-crystal Study of Molybdenyl(V) phosphates

$(MoO)_4(P_2O_7)_3$. Intensity data were measured on a κ-CCD diffractometer (Enraf-Nonius Inc.) at ambient temperature. In agreement with LENZ [19], the subcell of $(MoO)_4(P_2O_7)_3$ was obtained with the cell parameters, a = 7.8674(1) Å, b = 7.8674(1) Å, c = 31.9457(5) Å. The present study confirms a 3×3×1 supercell which is clearly visible in figure 8.4. The cell parameters of the supercell derived from X-ray single-crystal measurements are a = 23.60670(3) Å, b = 23.60670(3) Å, c = 31.94660(4) Å.

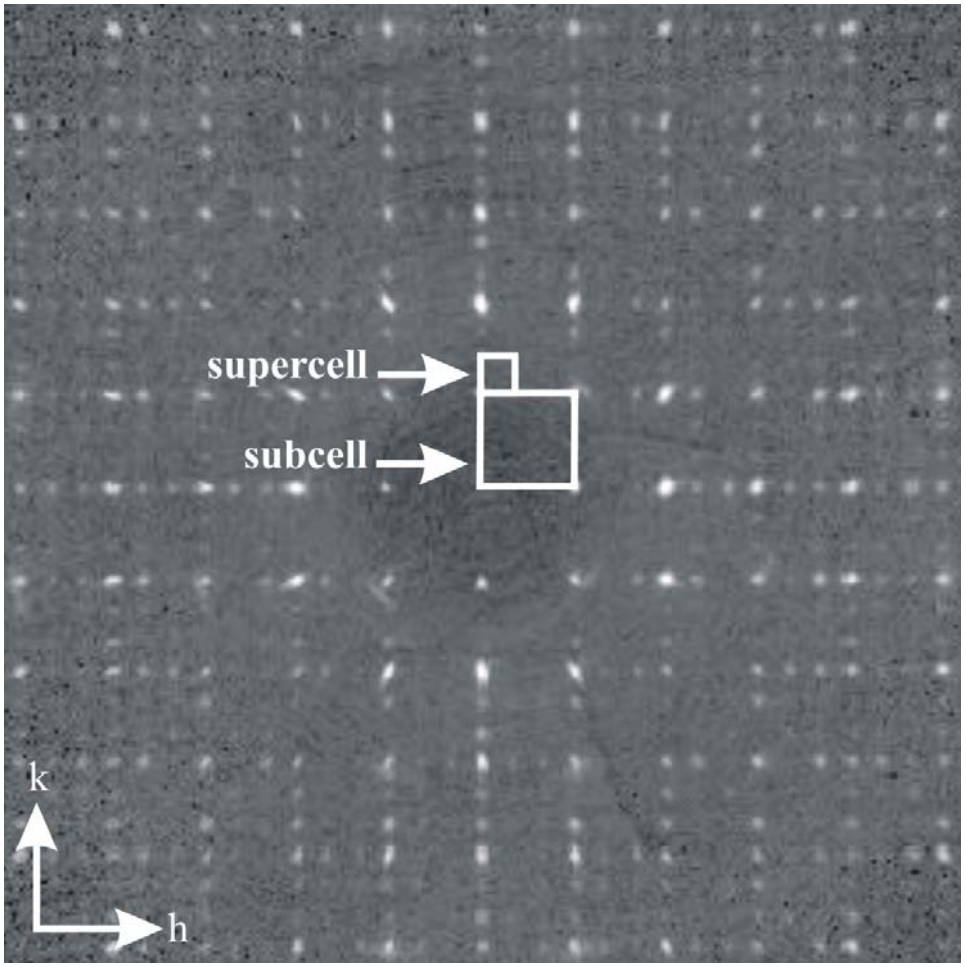

Figure 8.4 A section of single-crystal X-ray diffraction of *hk*3 plane showing the presence of the 3×3 superstructure.

Structure determination and refinement of $(MoO)_4(P_2O_7)_3$ were performed using the SHELX-97 [105] suite in the WinGX [135] framework. At first the crystal structure of the subcell of $(MoO)_4(P_2O_7)_3$ was refined. The symmetry $P2_12_12_1$ for this refinement was obtained from the symmetry search routine in program KPLOT [136]. This refinement converged to residuals R_1 = 0.069 and wR_2 = 0.22 for all atoms, suggesting the splitting of a large number of oxygen atoms. It simply illustrates the necessity of the refinement of the superstructure. Due to the

presence of a large number of very weak reflections in the superstructure of $(MoO)_4(P_2O_7)_3$, no reliable space group determination was possible on the basis of systematic absences and of statistic intensity distributions. Therefore, the structure refinement of the superstructure was carried out in space group $P2_12_12_1$ obtained from the isomorphic transition of index 3 in space group $P2_12_12_1$ found for the subcell $(MoO)_4(P_2O_7)_3$. Starting parameters were obtained by Direct Methods in SHELXS [137]. Thus molybdenum and phosphorus atoms were revealed. Subsequent Δ-Fourier syntheses allowed localization of most of the oxygen atoms. The missing oxygen atoms were determined assuming oxygen atoms required for the completion of the coordination polyhedra around molybdenum and phosphorus. Therefore two oxygen atoms O531 and b27 were introduced for the completion of the coordination of P54 and P53. Apart from these, 18 oxygen sites (from O19A, O19B to O27A, O27B) were introduced in the Z = 1/8 layer found as phosphorus and oxygen deficient layer in the crystal structure (see detail in section 8.5). At this stage the model refinement gave a residual R_1 = 0.159 and wR_2 = 0.47. The refinement of the crystal structure allowing for a two-fold axis along [1 1 0] as twin element $0\ 1\ 0\ \ 1\ 0\ 0\ \ 0\ 0\ \bar{1}$ converged at R_1 = 0.128, wR_2 = 0.401. Only eighteen molybdenum atoms were refined allowing anisotropic displacement parameters while for other atoms the refinement is blocked due to too small *array B*. Introduction of restrains for the split molybdenum atoms (EXYZ or EADP) as well as for distances d(Mo-O) and d(P-O) (DFIX) revealed the refinement to be unstable. We can relate these problems to the large number of parameters involved in the refinement of the superstructure of $(MoO)_4(P_2O_7)_3$.

Details on X-ray single crystal data collections as well as structural refinements are given in table 8.4. Atomic coordinates, anisotropic displacement parameters are given in Appendix A1 (Table A1.1 to Table A1.5).

Table 8.4 Details concerning data collection, structure solution and refinement of $(MoO)_4(P_2O_7)_3$.

crystal data	
chemical formula	$(MoO)_4(P_2O_7)_3$ (supercell)
crystal system	orthorhombic
space group	$P2_12_12_1$ (No. 19)
a / Å	23.60670 (3)
b / Å	23.60670 (3)
c / Å	31.94660 (4)
V / Å^3	17803.76(3)
Z	36
μ / mm^{-1}	3.09
$D_{X\text{-}ray}$ / g·cm^{-3}	3.26
colour	dark green
crystal shape	rectangular
size /mm^3	0.2·0.1·0.02
molecular weight / g·mol^{-1}	1150.58
F(000)	16481
data collection	
Nonius κ-CCD diffractometer; Mo-Kα radiation, λ = 0.71073Å, graphite-monochromator	
temperature / K	293
scan range θ / °	$1.27 \le \theta \le 30.04$
	$-33 \le h \le 33$
	$-23 \le k \le 23$
	$-45 \le l \le 45$
structure refinement	
software	SHELX97 [105]
measured reflections	52026
independent reflections	14250; 5654 with $\lvert F_o \rvert > 2\sigma(F_o)$
parameter; Goof	1478; 1.12
residuals	
R_{int}	0.081
R_1[a)]	0.128
wR_2[b)]	0.405
weighting scheme	A = 0.20; B = 0.0
residual electron density	
$\Delta\rho_{max}$ / Å^{-3}	3.79 (close to Mo29A)
$\Delta\rho_{min}$ / Å^{-3}	-2.60 (close to Mo34A)

[a)] $R_1 = \Sigma||F_o| - |F_c|| / |F_o|$, $F_o^2 \ge 2\sigma(F_o^2)$

[b)] $w = 1 / [\sigma^2(F_o^2) + (A \cdot P)^2 + B \cdot P]$; $P = (F_o^2 + 2F_c^2) / 3$

Phase X1. Intensity data of a very small (0.04·0.03·0.01 mm^3) rectangular crystal of the Phase X1 have been measured on a κ-CCD diffractometer at ambient temperature. A full sphere in the range of $2.91 \leq \theta \leq 34.97°$ was measured (2358 independent reflections from 16034). The cell parameters $a = b$ =7.8887(5) Å, c = 15.778(19) Å obtained from the single-crystal investigation are in agreement with those from the indexing of the powder diffraction pattern using the program DICVOL ($a = b$ = 7.897 Å, c = 15.778 Å) [98]. All the attempts for structure determination and refinement using the SHELX-97 [105] (Direct Methods and SUPERFLIP) suite in the WinGx [135] framework failed. This failure in structural refinement might be due to the bad quality of the crystal used for the single-crystal investigation. The crystals of Phase X1 so far obtained by CVT, are not suitable for the crystal structure refinement from X-ray single crystal investigations.

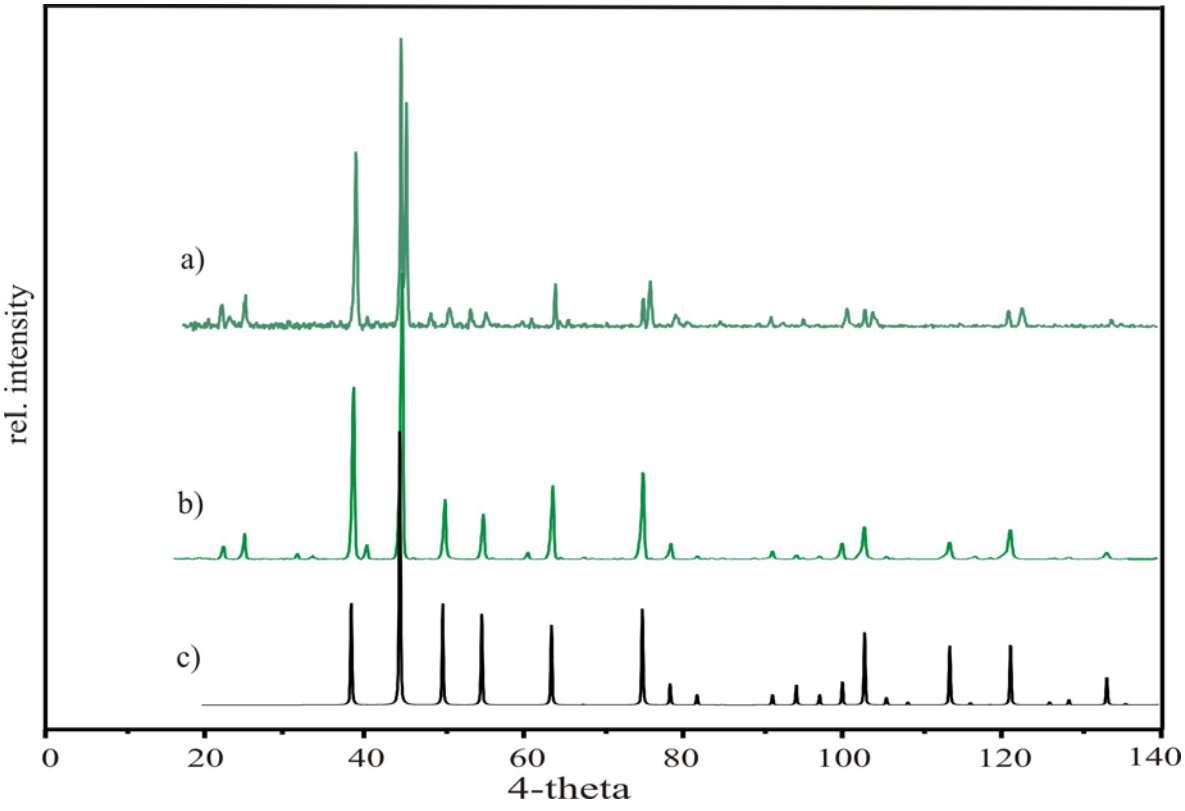

Figure 8.5 Comparison of the experimental Guinier photograph of $(MoO)_4(P_2O_7)_3$ (a), Phase X1 (b), and MoP_2O_7 (c).

X-ray powder difrraction patterns of $(MoO)_4(P_2O_7)_3$ and Phase X1 are very similar to each other (see Figure 8.5). The a and b parameters of the subcell of $(MoO)_4(P_2O_7)_3$ and of the Phase X1 are almost identical. However, the c parameter is just one half to that of $(MoO)_4(P_2O_7)_3$. This, in addition to the closely related X-ray powder pattern provides significant information of their close crystallographic relationship. Apart from this, EDX

analyses show the ratio Mo : P = 1:1.5. Therefore, it might be reasonable to state that the Phase X1 is a second polymorph of $(MoO)_4(P_2O_7)_3$.

β_I-$MoOPO_4$. In the course of this investigation (Table 8.2) a few reddish crystals of the new polymorph of molybdenyl(V)-orthophosphate were obtained. We call this β_I-$MoOPO_4$ in accordance with the isotypic β-$VOPO_4$ [130].

Single-crystal intensity data of a small ($0.04 \cdot 0.03 \cdot 0.02$ mm^3) rectangular red crystal of β_I-$MoOPO_4$ have been measured on a κ-CCD diffractometer at ambient temperature. Structure determination and refinement were performed using the SHELX-97 [105] suite in the WinGx [135] framework. Despite the reasonable bond-lengths and angles, the refinement of β_I-$MoOPO_4$ converged to the rather high residuals of $R_1 = 0.1005$ and $wR_2 = 0.2838$. We relate these high residuals to the poor quality of the crystal used for X-ray single-crystal experiment. Details on this compound are given as Appendix A2 (see Table A2.1 to A2.4, Figiure A2.1).

8.5 Description and Discussion of the Crystal structures of Molybdenyl(V) phosphates

The structural relationship of $M^{II}P_2O_7$ to the rock salt type via the pyrite type is visualized in figure 8.6. In the $M^{II}P_2O_7$ structure the arrangement of the metal cations and pyrophosphate anions are similar to pyrite and thus to the NaCl type structure. Metal atoms are situated at the corners and at the face centers of the unit cell while the centers of the pyrophosphate anions lie on the oxygen atoms bridging the phosphorus atoms (P-O_b-P). These bridging oxygen atoms are located at the middle points at the edges and at the body centers. Phosphorus atoms are located on the three-fold axis running along the direction of the body diagonals. Thus the structure of $M^{II}P_2O_7$ is related to that of pyrite, in that the P-O-P vectors show the same orientation as $[S\text{-}S]^{2-}$ groups and in consequence the space group $Pa\bar{3}$ persists as in pyrite [128].

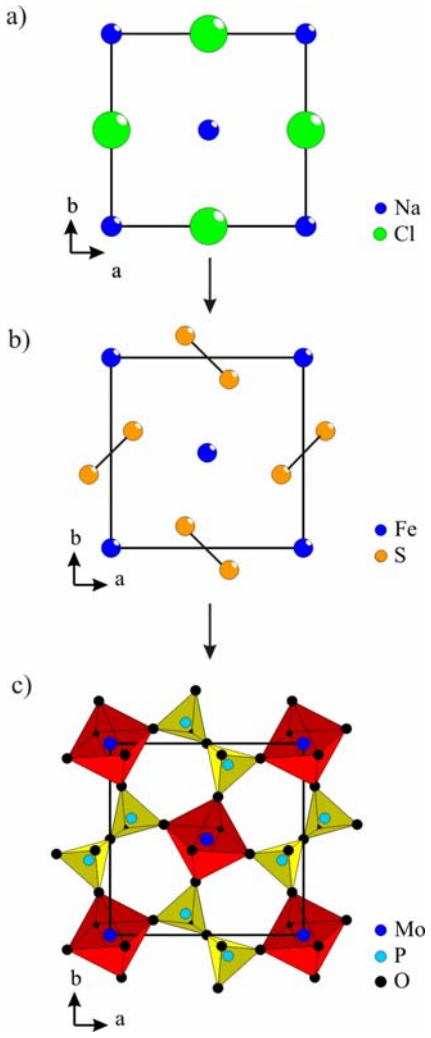

Figure 8.6 Structural relationship between NaCl (a), FeS_2 (b) and $M^{II}P_2O_7$ (c). Diamond version 3.2c [138].

The crystal structure of MP_2O_7 is built up from alternating corner sharing of [MO_6] octahedra to [P_2O_7] groups. This class of compound shows generally a weak superstructure with $a' = 3a_o$ (~24 Å). The superstructures of ZrP_2O_7 and HfP_2O_7 were refined in symmetry *Pbca* avoiding unrealistic ∠(P,O,P = 180° [139, 140] which we assume the consequence for the formation of the superstructure.

The crystal structure of $(MoO)_4(P_2O_7)_3$ can be derived from that of MoP_2O_7 according to the scheme $(Mo^{V}O)_4(P_2O_7)_3 = 4Mo^{IV}P_2O_7$ - "P_2O_3". Thus, a very complicated structure can be derived from a rather simple one according to the relationship, NaCl → FeS_2 → $M^{IV}P_2O_7$ → $(Mo^{V}O)_4(P_2O_7)_3$. This relationship can be based on group-subgroup relations (see Figure 8.7). The structural relationship between $Mo^{IV}P_2O_7$ and $(Mo^{V}O)_4(P_2O_7)_3$ is immediately recognized from *IP*-Guinier photographs (see Figure 8.5).

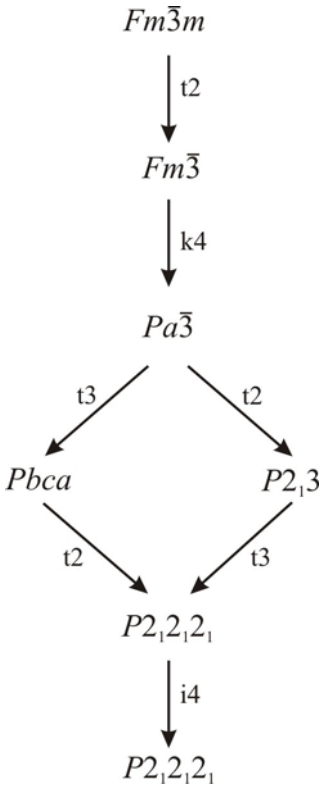

Figure 8.7 Group-subgroup relation between NaCl and $(MoO)_4(P_2O_7)_3$.

The crystal chemical transition from $Mo^{IV}P_2O_7$ to $(Mo^{V}O)_4(P_2O_7)_3$ can be described by the stacking of four MoP_2O_7 unit cell along the crystallographic *c*-axis followed by the loss of "P_2O_3" groups from every second layer and thereby the remaining 4 oxygen atoms displace to the close vicinity of the molybdenum atoms forming molybdenyl groups as well as Mo-O_b-Mo bridges (see Figure 8.8). A careful analysis shows that from the remaining 4-oxygen

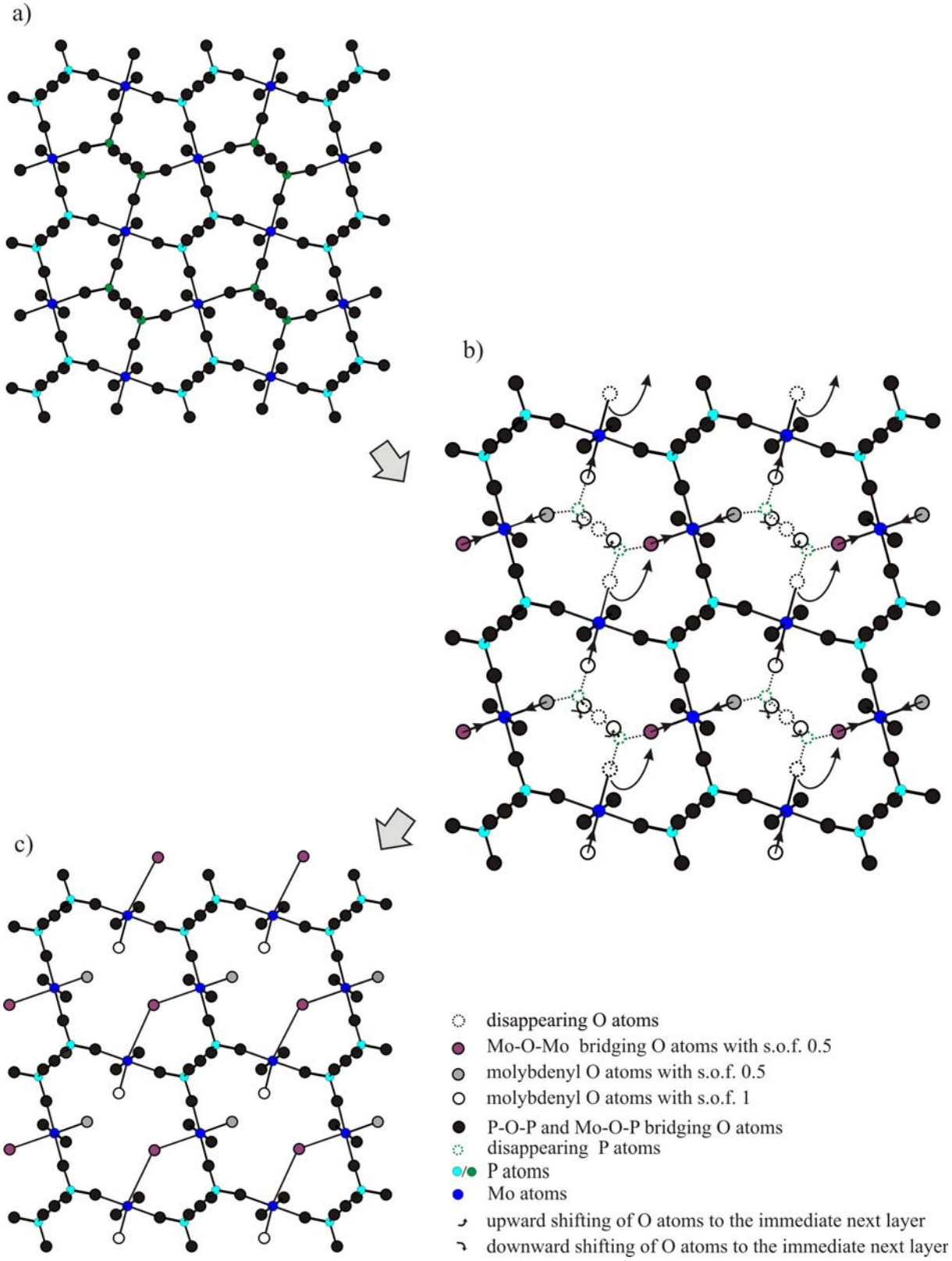

Figure 8.8 Pictorial representations of the crystal chemical transitions from the MP_2O_7 structure (a) to z = 1/8 layer of $(MoO)_4(P_2O_7)_3$ (c). Changing of angular orientations of O,Mo/P,O; P/Mo,O,P/Mo, Mo,O,P were not considered.

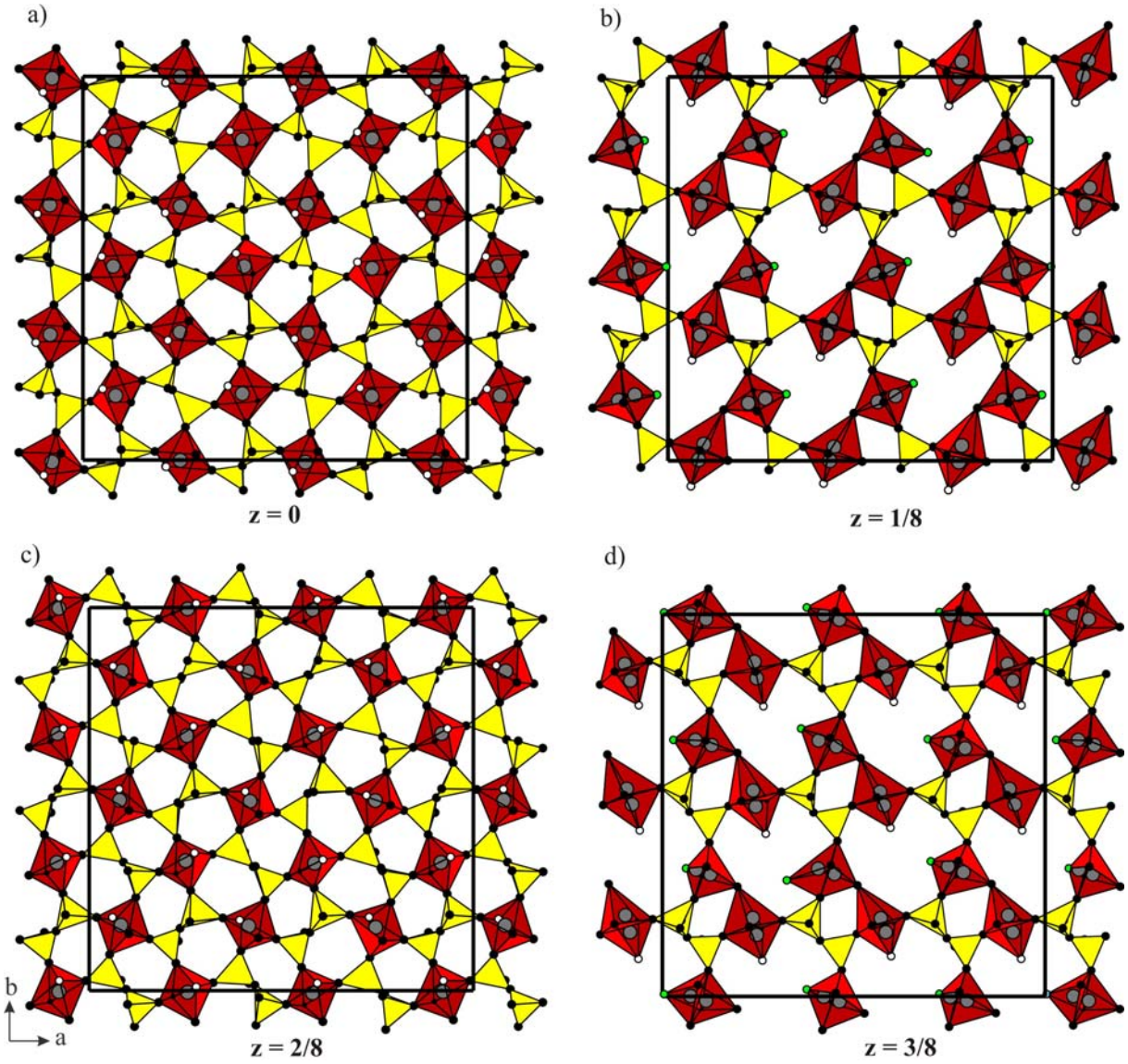

Figure 8.9 Layers of z = 0, 1/8, 2/8, 3/8 (a, b, c, d respectively) in the crystal structure of $(MoO)_4(P_2O_7)_3$; $[MoO_6]$, $[Mo_2O_{11}]$ groups (red), $[P_2O_7]$ groups (yellow). Open and green circles indicate terminal oxygen atoms with site occupancy factor 1 and 0.5, respectively (Diamond version 3.2c [138]).

atoms, three displace appropriately to the close vicinity of three molybdenum ions. Among these three, one lying in the same plane (z = 1/8), whereas the other two displace to its adjacent layer just below z = 0 and above z = 2/8. Apart from this, two oxygen atoms exhibit a site occupancy factor of 0.5. One of them exists as terminal oxygen atom and the other is being a Mo-O_b-Mo bridging one exists in $[Mo_2O_{11}]$ groups in z = 1/8 layer. Thus this layer, z = 1/8 (Figure 8.9b), is being a defect structure of first layer (z = 0, Figure 8.9a), build up by loss of phosphorus and oxygen atoms. In this way, a large empty eight-membered ring is revealed instead of five-membered ring that we observe in the z = 0 and 2/8 layers. As a consequence the crystal structure of $(MoO)_4(P_2O_7)_3$ is built up by alternating stacking of the

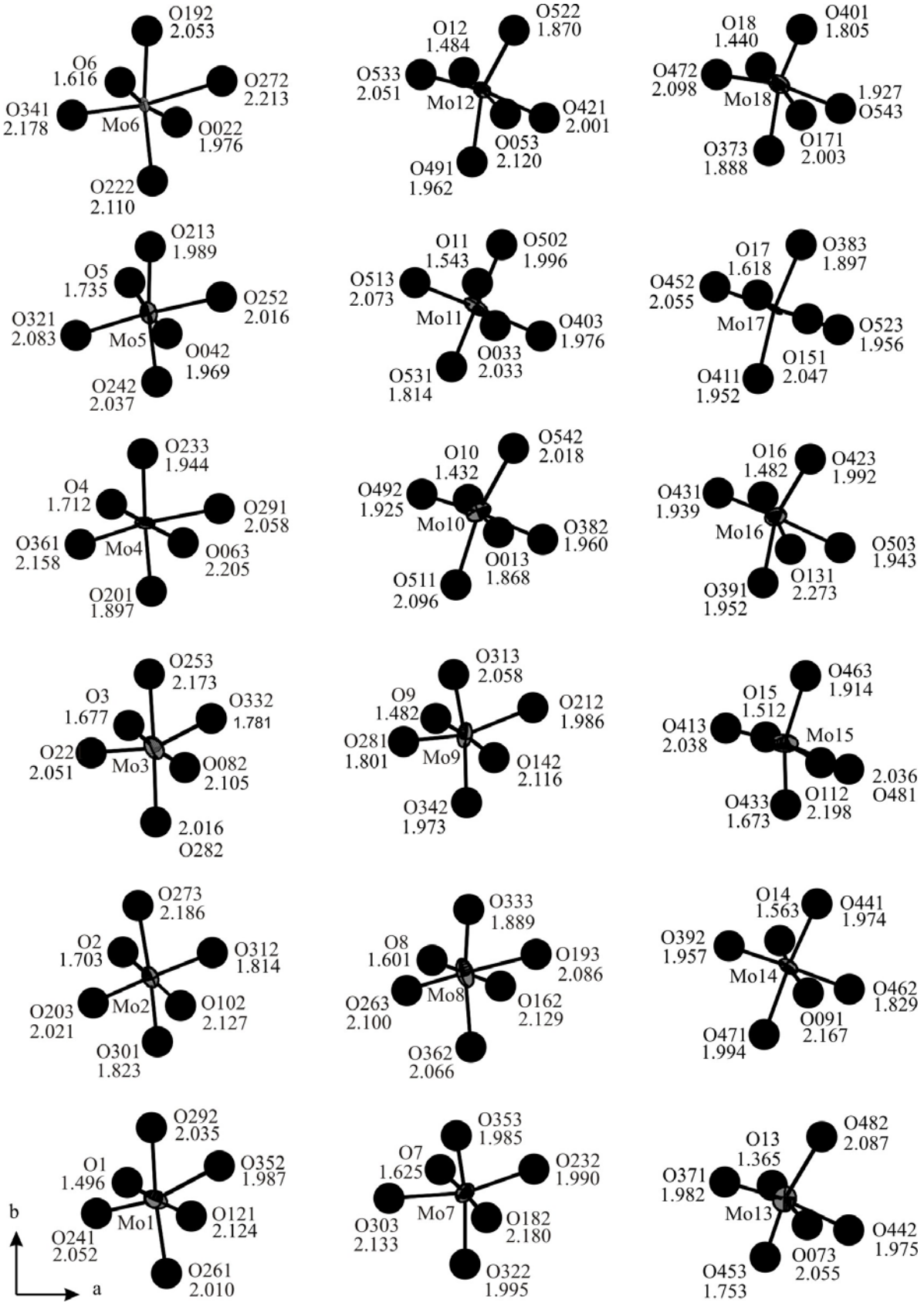

Figure 8.10 Polyhedral representation of $[MoO_6]$ octahedra in $(MoO)_4(P_2O_7)_3$. 50% probability of molybdenum atoms (ORTEP in Diamond version 3.2c [138]).

non-defect (A) and defect (B) layers forming ABA´B´AB…. pattern along the crystallographic *c*-axis (see Figure 8.9). The crystal structure is stabilized by alternating P-O-Mo bridging of two successive layers.

In the crystal structure of MoP_2O_7 all the six oxygen atoms of the [MoO_6] octahedra bridge to six phosphorus atoms, provided by six [P_2O_7] groups. Whereas, the ground level (z = 0) of $(MoO)_4(P_2O_7)_3$ is built up by the alternating corner sharing of [MoO_6] octahedra to five [P_2O_7] groups, and the sixth one is being a terminal oxygen atom, (molybdenyl group, (Mo^V=O)O_5). Thus pentagonal windows as in the crystal structure of MoP_2O_7 are formed. Despite different atomic sites, analogous structural building pattern of the first (z = 0) and the third (z = 2/8) layer is observed (Figures 8.9a, 8.9c). The other layers z = 4/8 and 6/8 are related by symmetry to z = 0 and 2/8, respectively. According to our structural model, the asymmetric unit of $(MoO)_4(P_2O_7)_3$ is built up by 36 crystallographically independent Mo atoms. Out of 36 molybdenum, 18 atoms possess unique sites, forming z = 0 and 2/8 layers (non-defect layer A, A´) of the structure. Conversely, the remaining 18 molybdenum atoms are split, build up z = 1/8 and 3/8 layers (B, B´) so called defect layers (see Figures 8.9b, 8.9d). Representive polyhedra of [MoO_6] and [Mo_2O_{11}] are given in figures 8.10 and 8.11, respectively.

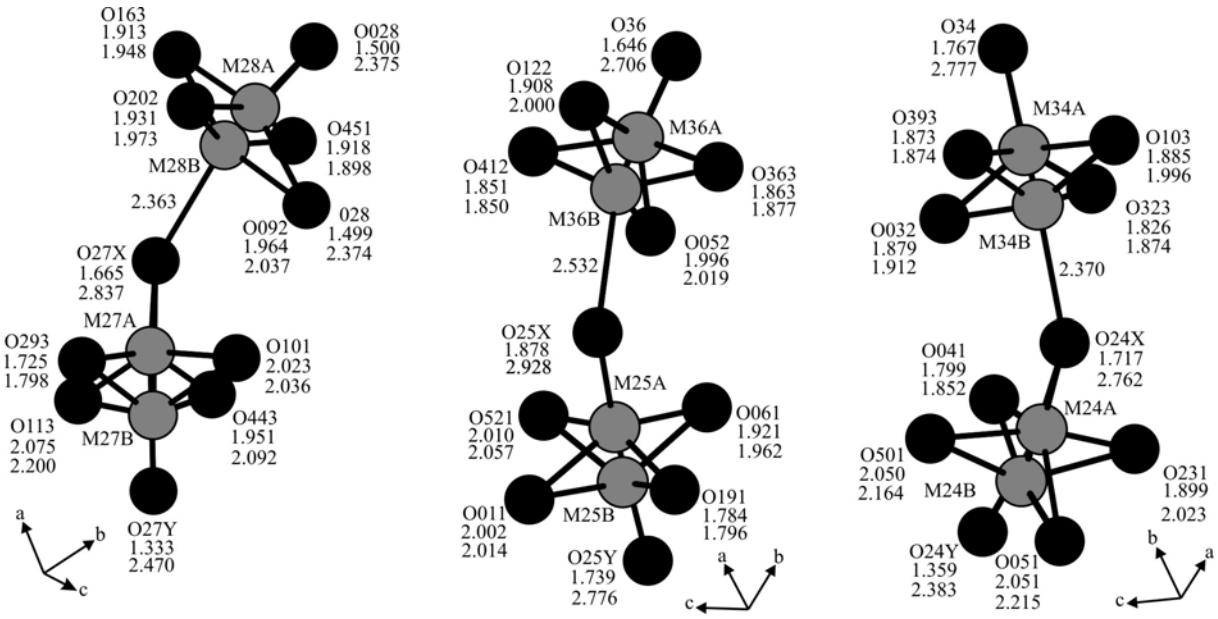

Figure 8.11 Representive polyhedra of [Mo_2O_{11}] di-octahedra in the crystal structure of $(MoO)_4(P_2O_7)_3$ (Diamond version 3.2c [138]).

In contrast to the existence of the [MoO_6] groups (formed by unsplit Mo atoms) in the non-defect layers at z = 0 and 2/8, the split molybdenum atoms form the [Mo_2O_{11}] groups in the

defect layer (z = 1/8, and 3/8). The current structural model shows that molybdenum atoms of layer z = 1/8, and 3/8 form the $[Mo_2O_{11}]$ groups. However, the existence of the five-fold coordination instead of $[Mo_2O_{11}]$ groups can not be completely ruled out. The existence of $[Mo_2O_{11}]$ groups is found in the crystal structure of $A^{I}_2Mo^{V}_2P_2O_{11}$ (A^{I} = Rb [141], Tl [142]). We noticed that in $[Mo_2O_{11}]$ di-octahedra, the terminal oxygen atoms persist trans conformation with the site occupancy factor of 1 and 0.5, respectively. Half occupancy of the oxygen atoms can also be observed for the bridging oxygen atoms of the Mo-O-Mo linkage in $[Mo_2O_{11}]$ di-octahedra.

The crystal structure of $(Mo^{V}O)_4(P_2O_7)_3$ is a hybrid of a non-defect like MP_2O_7 and "P_2O_3" defect structure. This structure model for $(Mo^{V}O)_4(P_2O_7)_3$ i.e. "$Mo^{V}P_{1.5}O_{6.25}$" is distinctly different to that of $Nb^{V}P_{1.8}O_7$ [143], another variation of the $M^{IV}P_2O_7$ structure type. In the niobium(V)-phosphate, charge balance does not occur by the occupation of M^{IV} positions in MP_2O_7, but by the occupation of the phosphorus positions [143], apparently by the building of $(NbO)^{3+}$ groups and orthophosphate unit. In $(MoO)_4(P_2O_7)_3$, Mo^{V+} is attained due to "P_2O_3" deficiency following by the formation of molybdenyl groups, $(MoO)^{4+}$.

Despite our detailed knowledge on the structural model of the pyrophosphate, $(MoO)_4(P_2O_7)_3$, structural refinement in many cases gave physically meaningless distances d(P-O) and d(Mo-O). In addition to this, splitting of half of the molybdenum atoms (18) in the z = 1/8 and 3/8 layer appeared. These observations might indicate that the true cell is even larger which we were unable to identify from X-ray single-crystal investigations or the symmetry is even lower.

8.6 UV/Vis/NIR Investigations of Molybdenyl(V) phosphates

Molybdenum(V) ions exhibit d^1 electronic configuration. The colours of the corresponding phosphates $MoOPO_4$ (yellow), $(MoO)_2P_4O_{13}$ (green), and $(MoO)_4(P_2O_7)_3$ (dark green) vary significantly. This variation in colours is clearly visualized in the electronic spectra (see Figure 8.12) from the position of absorption minima 17250 cm^{-1}, 19100 cm^{-1}, 20150 cm^{-1} for $MoOPO_4$, $(MoO)_2P_4O_{13}$, and $(MoO)_4(P_2O_7)_3$, respectively.

The single-crystal electronic absorption spectrum of each molybdenyl(V) phosphate shows two strong absorption bands. These are at $\tilde{\nu}_1 \approx 12650$ and $\tilde{\nu}_2 \approx 20800$ cm^{-1} for $MoOPO_4$, $\tilde{\nu}_1$

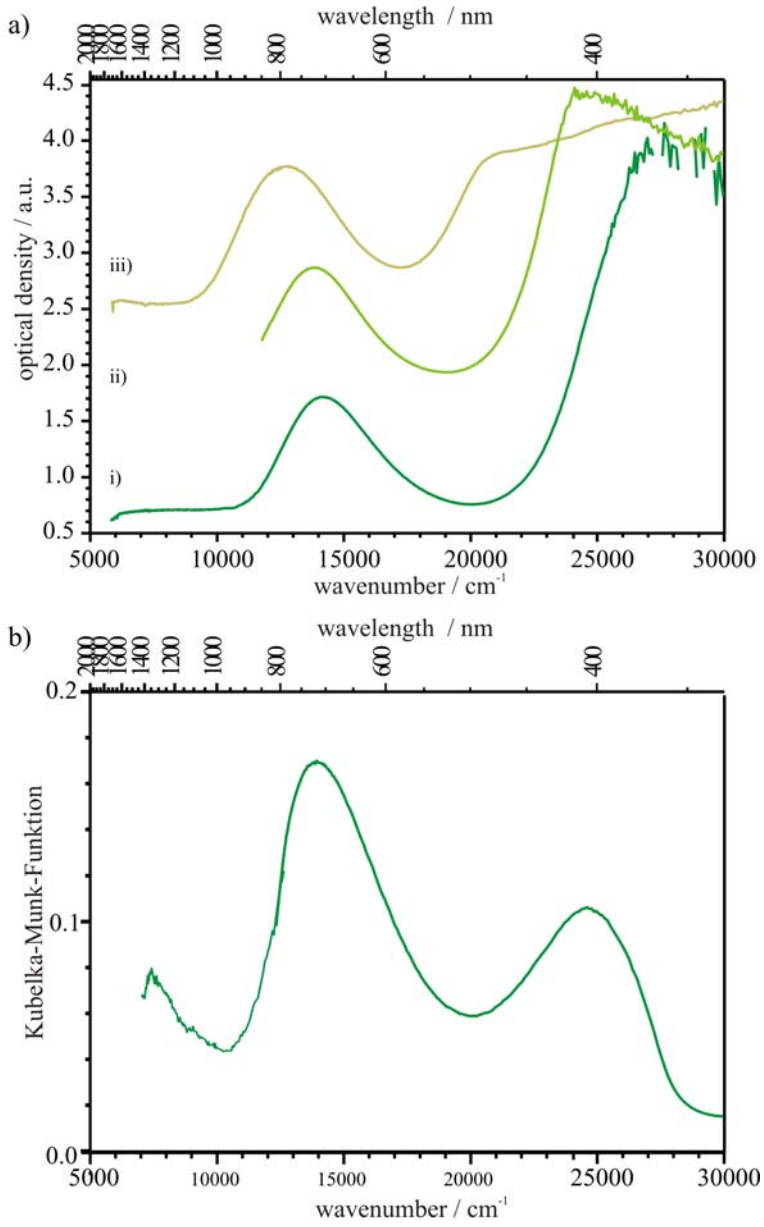

Figure 8.12 (a) Single-crystal electronic absorption spectra of $(MoO)_4(P_2O_7)_3$ (i), $(MoO)_2P_4O_{13}$ (ii) and $MoOPO_4$ (iii). (b) Powder reflectance spectrum of Phase X1.

≈ 13800 and $\tilde{\nu}_2$ ≈ 24200 cm^{-1} for $(MoO)_2P_4O_{13}$, and $\tilde{\nu}_1$ ≈ 14250 and $\tilde{\nu}_2$ ≈ 26100 cm^{-1} for $(MoO)_4(P_2O_7)_3$. Aside from this, the powder reflectance spectrum of Phase X1 (see Figure 8.12b) shows two strong bands centered at $\tilde{\nu}_1$ ≈ 13490 and $\tilde{\nu}_2$ ≈ 24600 cm^{-1}. The intensities as well as the energies of the two bands in Phase X1 are in agreement with the 5+ oxidation state of molybdenum as in the phosphates of other pentavalent molybdenum.

The crystal structures of molybdenyl(V) phosphates consist of $[MoO_6]$ octahedra and phosphate groups. Each of the $[MoO_6]$ contains a notably short Mo-O bond (d(Mo-O) ~ 1.65 Å) forming the $Mo{=}O^{3+}$ oxycation, four medium Mo-O bonds (d(Mo-O) ~ 2.0 Å) and a long bond trans to molybdenyl oxygen atom. A typical example of the geometric structure of the $(Mo{=}O)O_5$ chromophore is given in figure 8.13a. Due to the large deviation of the Mo-O bond lengths the $[MoO_6]$ octahedra becomes extremely distorted which leads to a large splitting between t_{2g} and e_g orbitals (see Figure 8.13b). This results the lowering from O_h symmetry to C_{4V}.

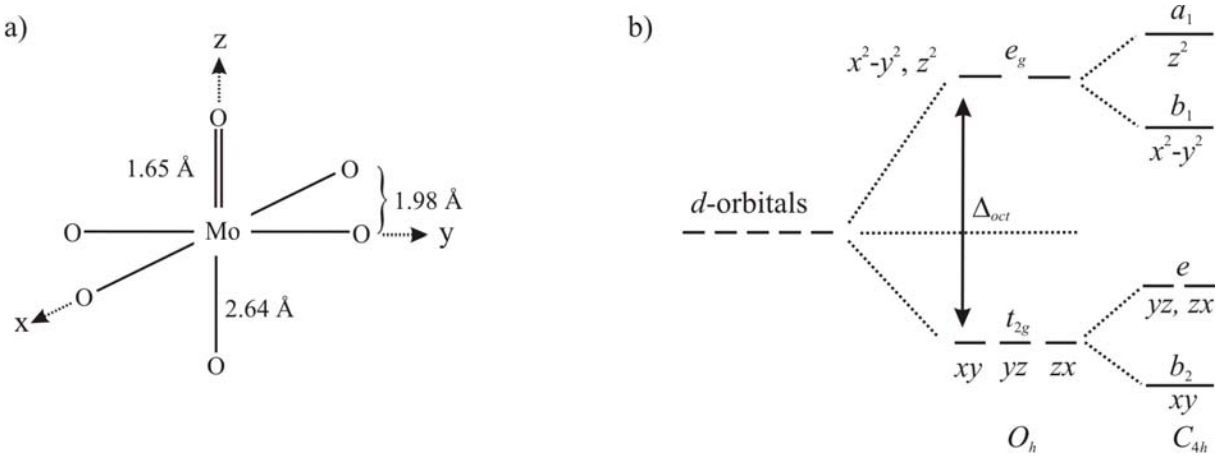

Figure 8.13 Schematic lay out of the distorted $(Mo{=}O)O_5$ octahedra in $MoOPO_4$ [27] (a), lowering the symmetry from O_h to C_{4V} (b).

In the diffuse reflectance spectra, LEZAMA *et al*. [144] observed three signals at 12000, 23000, and 31000 cm^{-1} for $MoOPO_4$; two at 13900 and 25000 cm^{-1} for $(MoO)_2P_4O_{13}$. Despite a slight shift of absorption maxima, our observations agree to these results [144]. On the basis of the empierical molecular orbital diagram proposed by GRAY and HARE [145] for the $[MoOCl_5]^{2-}$ ion which is backed by the pioneer work of BALLHAUSEN and GRAY for the $VO(H_2O)_5^{2+}$ ion [146] (see Figure 8.14), the absorption band with the lowest energy correspond to the $^2B_2(dxy) \rightarrow {}^2E(dxz, dyz)$ transition, while the band at higher energy correspond to $^2B_2(dxy) \rightarrow {}^2B_1(dx^2\text{-}y^2)$. The high energy band in the $MoOPO_4$ spectrum (31000 cm^{-1}) was assigned to

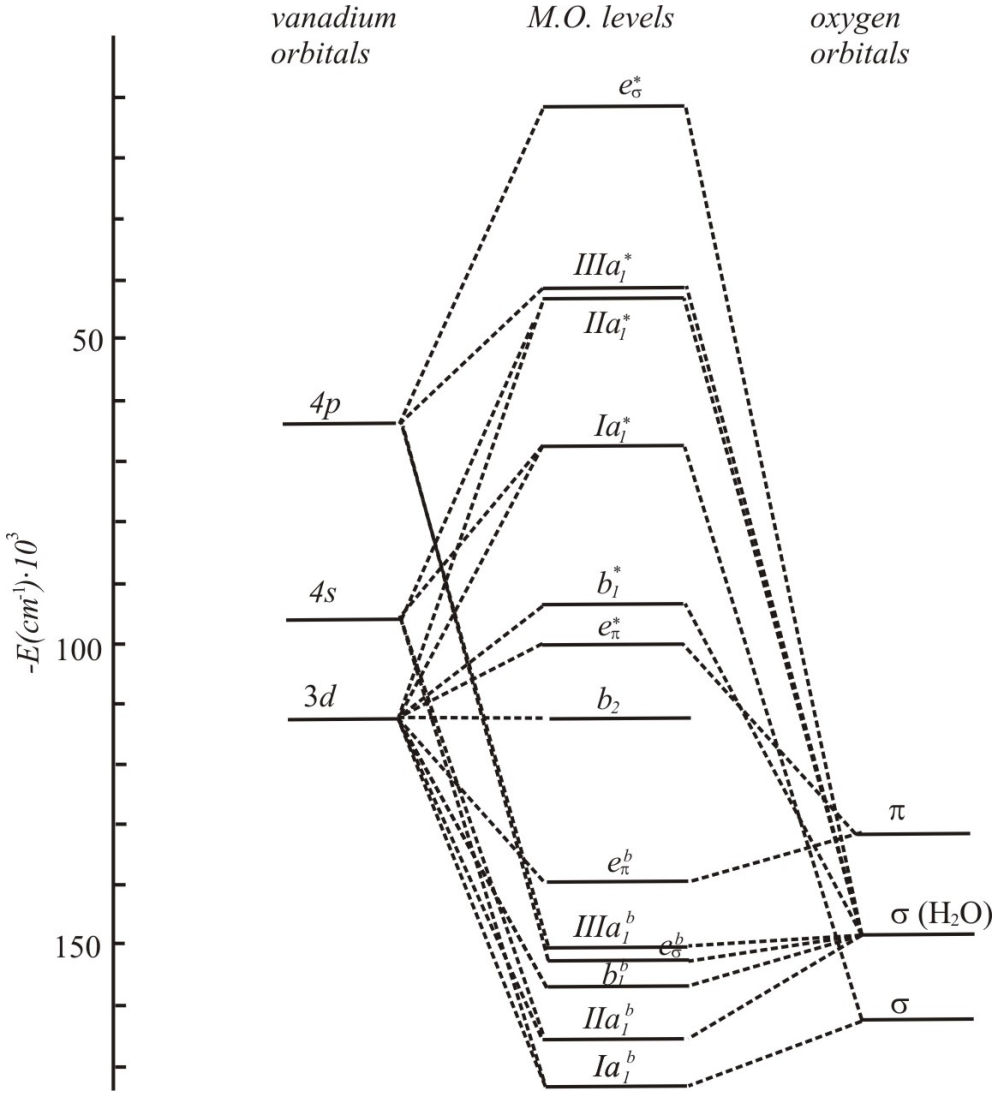

Figure 8.14 MO-schema for [V=O(H_2O)$_5$] chromophore [146].

a charge transfer transition. In agreement to these authors [144, 145] our results obtained for (Mo^VO)$_4$(P_2O_7)$_3$ and the new phase Phase X1 can be assigned due to the electronic transitions $^2B_2(dxy) \rightarrow {}^2E(dxz, dyz)$ and $^2B_2(dxy) \rightarrow {}^2B_1(dx^2\text{-}y^2)$. Apart from this, for an extremely distorted octahedron the last transition $^2B_2(dxy) \rightarrow {}^2A_1(dz^2)$ requires a significantly large amount of energy. As a result, this transition is often obscured by low lying charge transfer transition.

8.7 Magnetic Behaviour of Molybdenyl(V) phosphates

Magnetic measurements were carried out for the samples of the selected crystals of $MoOPO_4$, $(MoO)_4(P_2O_7)_3$ and $(MoO)_2P_4O_{13}$ with a "SQUID magnetometer (MPMS, Quantum design)" at Max-Planck-Institute for Solid-state Research (MPIFKT Stuttgart; Dr. Kremer).

The evaluation of the reciprocal susceptibility versus temperature, χ^{-1} vs T (see Figure 8.15), confirms the phosphates, $Mo^{V}O(PO_4)$, $(Mo^{V}O)_4(P_2O_7)_3$, and $(Mo^{V}O)_2P_4O_{13}$ to be paramagnetic. Our results are in agreement to those obtained by LENZ [19].

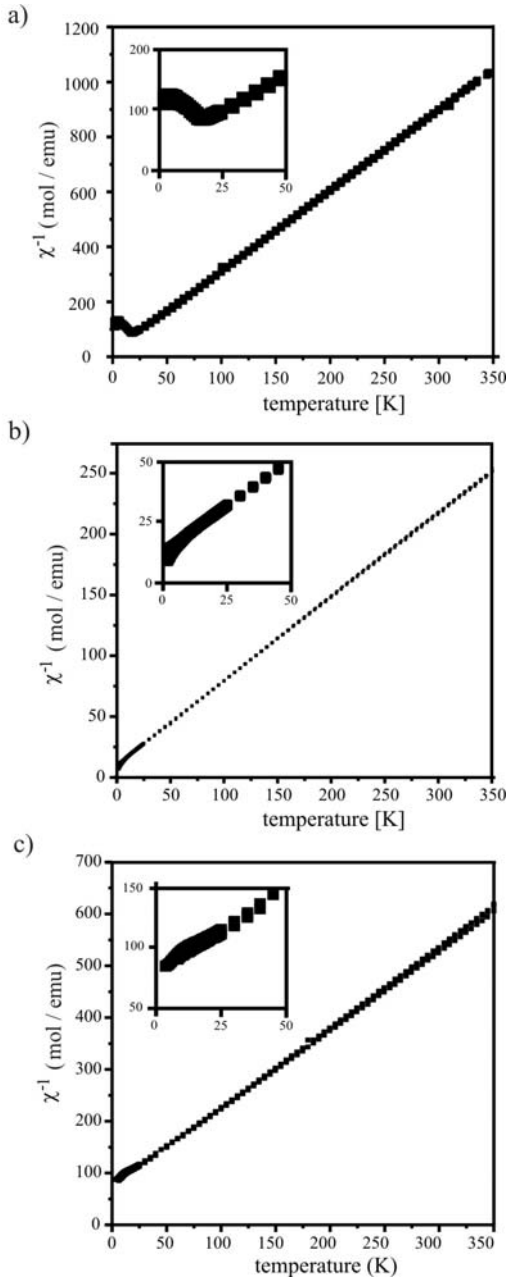

Figure 8.15 Magnetic behaviour of $Mo^{V}O(PO_4)$ (a), $(Mo^{V}O)_4(P_2O_7)_3$ (b), and $(Mo^{V}O)_2P_4O_{13}$ (c).

A maximum observed at about 10K indicates the existence of antiferromagnetic interaction in $Mo^{V}O(PO_4)$. This observation for $Mo^{V}O(PO_4)$ is in contrast to $(Mo^{V}O)_4(P_2O_7)_3$, and $(Mo^{V}O)_2P_4O_{13}$. While the crystal structure of $(MoO)_2P_4O_{13}$ consists of isolated $[(Mo^{V}=O)O_5]$ octahedra, an infinite chain of $[(Mo^{V}=O)O_5]$ octahedra (O=Mo····O=Mo····O) exhibits in the crystal structure of $MoO(PO_4)$. This structural feature might be a reason for the antiferromagnetic interaction in $MoO(PO_4)$. This observation might indicate that instead of $[Mo_2O_{11}]$ groups isolated square pyramids $[(Mo=O)O_4]$ occur in the crystal structure of $(Mo^{V}O)_4(P_2O_7)_3$.

It is important to note that Curie and Curie-Weiss constants for $Mo^{V}O(PO_4)$, $(Mo^{V}O)_4(P_2O_7)_3$, and $(Mo^{V}O)_2P_4O_{13}$ are found to be $C \sim 0.34$, 1.47, 0.66 emu · K · mol^{-1} and $\theta \sim$ -19.4, -14.7 and -27.7 K. However, the negative values of θ indicate that the main interactions are antiferromagnetic in these phosphates. The observed effective magnetic moment, μ_{eff}, is 1.65 μ_B for $Mo^{V}O(PO_4)$, 1.71 μ_B for $(Mo^{V}O)_4(P_2O_7)_3$, and 1.62 μ_B for $(Mo^{V}O)_2P_4O_{13}$. These values of μ_{eff} are close to the spin only value of 1.73 μ_B for d^1 systems. The slight reduction of the effective magnetic moment might be due to the presence of weak spin-orbit interactions.

However, the observed effective magnetic moments give clear evidence for the pentavalent oxidation state of molybdenum in $Mo^{V}O(PO_4)$, $(Mo^{V}O)_2P_4O_{13}$, and $(Mo^{V}O)_4(P_2O_7)_3$.

8.8 Infrared Spectra of $(MoO)_4(P_2O_7)_3$ and Phase X1

The infrared spectra of a few selected crystals of $(MoO)_4(P_2O_7)_3$ and Phase X1 were measured using a NICOLET 380 FT-IR spectrometer (SMART ORBIT).

Closely comparable band shapes and energies in the infrared spectra of $(MoO)_4(P_2O_7)_3$ and Phase X1 are visible in figure 8.16 and table 8.5. The very similar spectra obviously point to a very close crystal chemical relationship.

A tentative assignment of the IR spectra of reduced molybdenum phosphates $Mo^{V}O(PO_4)$, $(Mo^{V}O)_2P_4O_{13}$, $Mo^{IV}P_2O_7$, and $Mo^{III}(PO_3)_3$ has been discussed by LEZAMA *et al*. [144]. Bands within the range of 1258 to 1018 cm^{-1} (grey region in Figure 8.16) in the i. r. spectra of $(MoO)_4(P_2O_7)_3$ and the Phase X1 can be assigned as symmetric and asymmetric vibrations of $P\text{-}O_{ext}$ in PO_3 groups accordingly. Conversely, a strong band at 940 cm^{-1} and a weak band at 750 cm^{-1} (grey shaded area in Figure 8.16) correspond to the asymmetric and symmetric stretching vibration of the P-O-P bridge of the diphosphate [144], respectively. These

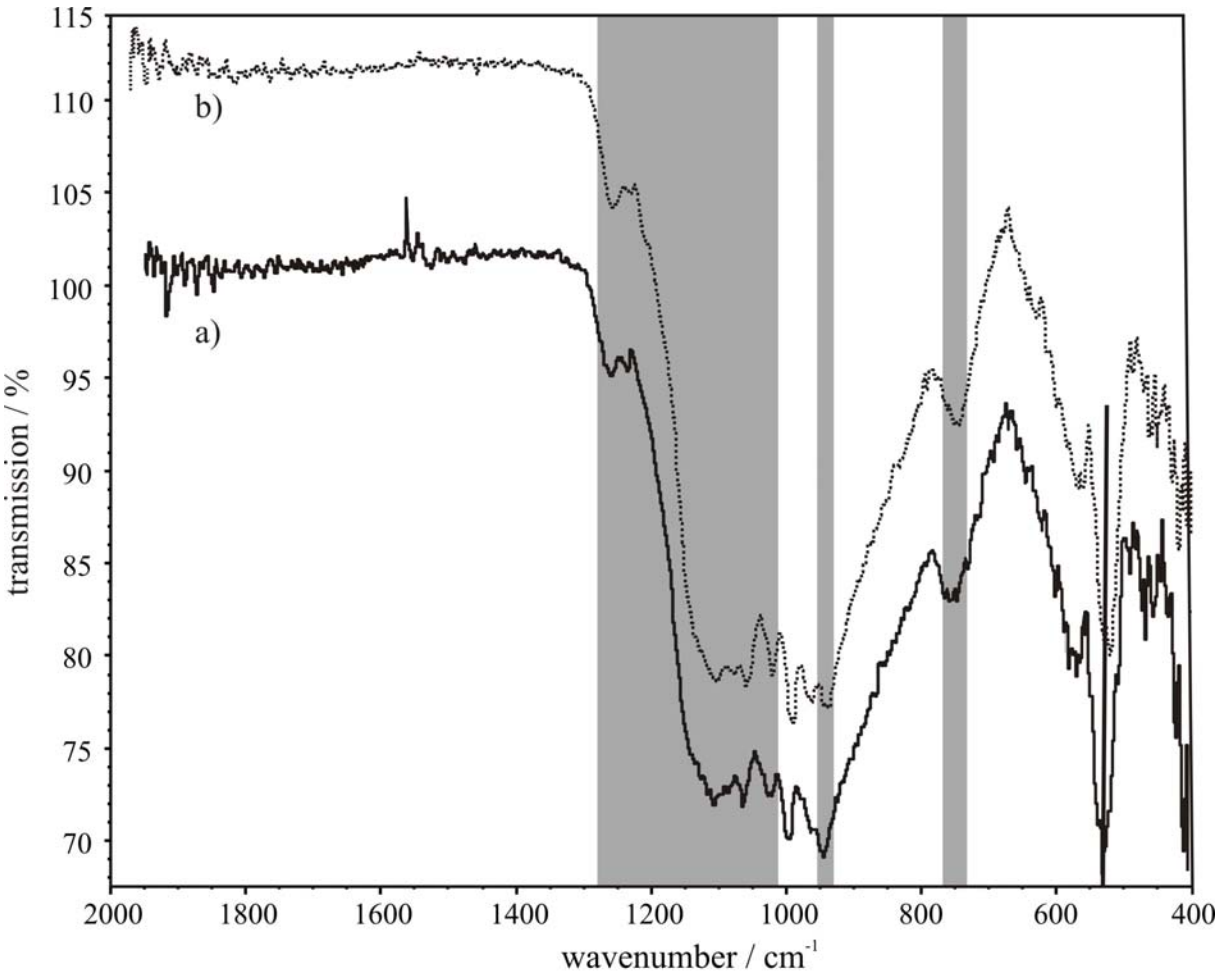

Figure 8.16 Infrared spectra of $(MoO)_4(P_2O_7)_3$ (a) and Phase X1 (b).

Table 8.5. IR spectra of $(MoO)_4(P_2O_7)_3$ and Phase X1. Vibrational transitions and their tentative assignments.

$(MoO)_4(P_2O_7)_3$		**Phase X1**		**vibrational modes**
wavenumber	intensity	wavenumber	intensity	
1258	w, sharp	1256	w, sharp	
1135	w, sharp	1128	w, shoulder	
1100	vs, sharp	1082	m, shoulder	ν_{asy}(P-O_{ext}) and
1059	vs, sharp	1060	s, sharp	ν_{sym}(P-O_{ext})
1020	vs, sharp	1018	vs, sharp	
990	vs, sharp	898	vs, sharp	ν_{asy}(Mo=O) and
965	vs, sharp	962	vs, sharp	ν_{sym}(Mo=O)
942	vs, sharp	940	vs, sharp	ν_{asy}(P-O_{int}) and
751	m, sharp	748	m, sharp	ν_{sym}(P-O_{int})
580	w, sharp	566	w, sharp	
572	w, sharp	560	w, sharp	
525	s, sharp	519	s, sharp	δ(O-P-O)
408	m, sharp	417	m, sharp	

w: weak intensity
m: medium intensity
s: strong intensity
vs: very strong intensity

vibrations are typical for many diphosphates. In addition to the evidence of the diphosphate groups in the IR spectra for both phosphates, strong bands at about 990 and 965 cm^{-1} clearly represent the presence of the molybdenyl group in $(Mo=O)O_5$ octahedra. Bands in between 580 and 400 cm^{-1} can be assigned to the deformation bands δ(O-P-O).

However, owing to the high valency of the cation (Mo^{5+}), extremely high distortion of $[MoO_6]$ octahedra as well as the complex three dimensional crystal structure of $(MoO)_4(P_2O_7)_3$, it becomes extremely difficult to interpret all the vibrational bands unambiguously.

9 Molybdenyl(VI) oxidepyrophosphate ($Mo^{VI}O_2)_2(P_2O_7$)

9.1 Introduction

As already mentioned in the preceding sections, in the ternary system Mo / P / O up to now two fully oxidized molybdenum phosphates ($Mo^{VI}O_2)_2(P_2O_7$) [24, 25] and $Mo^{VI}O_2(PO_3)_2$ [26] have been characterized. LENZ has given in his PhD thesis [19] a survey on the crystallization of only reduced molybdenum phosphates by Chemical Vapour Transport (CVT). The crystal structure of $(MoO_2)_2(P_2O_7)$ derived by KIERKEGAARD [24] converged at a rather high residual (R_1 = 0.18) along with crystal chemically dobious interatomic distances and angles. This author also reported a four times superstructure of its sublattice cell that forms along the crystallographic *b*-axis. In contrast to two phosphorus sites in structure refinement of the $(MoO_2)_2(P_2O_7)$ subcell by KIERKEGAARD [24] the ^{31}P-MAS-NMR spectrum shows four resonance peaks with an approximate integrals of 2:1:1:1:3 [147]. This observation is also agreement to structural complexity which was reported by KIERKEGAARD [24]. These results inspired us to reinvestigate this compound.

During our study LISTER *et al.* [25] reported in detail on this compound in 2010. LISTER *et al.* [25], have refined the crystal structure of $(MoO_2)_2(P_2O_7)$ from X-ray and neutron powder diffraction at 423 K and 500 K, respectively. These authors reported the subcell as *γ*-phase (space group *Pnma*). In addition to this, LISTER *et al.* indexed the room temperature phase, called *α*-phase (space group $P2_1/c$) from electron diffraction. The structure of the *α*-$(MoO_2)_2(P_2O_7)$ was determined and refined, from X-ray and neutron powder diffraction at 250 K. It was assumed that the intermediate *β*-phase adopts an incommensurately modulated structure. Apart from this, a fourth modification *δ*-$(MoO_2)_2(P_2O_7)$ is also reported [129]. LISTER *et al.* [25] have excellently shown from variable temperature ^{31}P-Solid-state NMR that the high temperature (419 K) *γ*-phase contains two phosphorus sites which is in agreement to the structural model derived by KIERKEGAARD [24]. These authors have also shown that at 277 K, the appearance of the five signals with a ratio of intensity of 2:1:1:1:3 is in agreement to the structure model at room temperature *α*-phase.

In the present work, $(MoO_2)_2P_2O_7$ was synthesized and crystallized by CVT. The crystal structure of the *α*-$(MoO_2)_2P_2O_7$ was determined and refined for the first time from X-ray single-crystal diffraction data collected at 293 K.

9.2 Syntheses and Crystallization

A microcrystalline powder of $(MoO_2)_2P_2O_7$ was prepared by heating a mixture of MoO_3 and $(NH_4)_2HPO_4$ which is described in detail in section 7.2.1.

With the colour ranging from light blue to colourless crystals of $(MoO_2)_2P_2O_7$ (Figure 9.1) were grown by chemical vapour transport starting from a stoichiometric mixture of MoO_3 and P_4O_{10} (see Equation 9.1). The starting materials were carefully transferred in evacuated silica tubes ($l \approx 11$ cm, $d \approx 1.5$ cm, $V \approx 20$ cm^3) and a prereaction was carried out at 500 → 600°C for 3 days (reactants containing region of the ampoule was placed at 500°C). The prereacted mixture was subsequently heated in a temperature gradient 600 → 500°C for about 7 days. Due to its extreme hygroscopic nature P_4O_{10} was handled in a glove bag. Details on various experimental results are summarized in table 9.1.

$$2MoO_3 + 1/2P_4O_{10} \rightarrow (MoO_2)_2P_2O_7 \qquad (9.1)$$

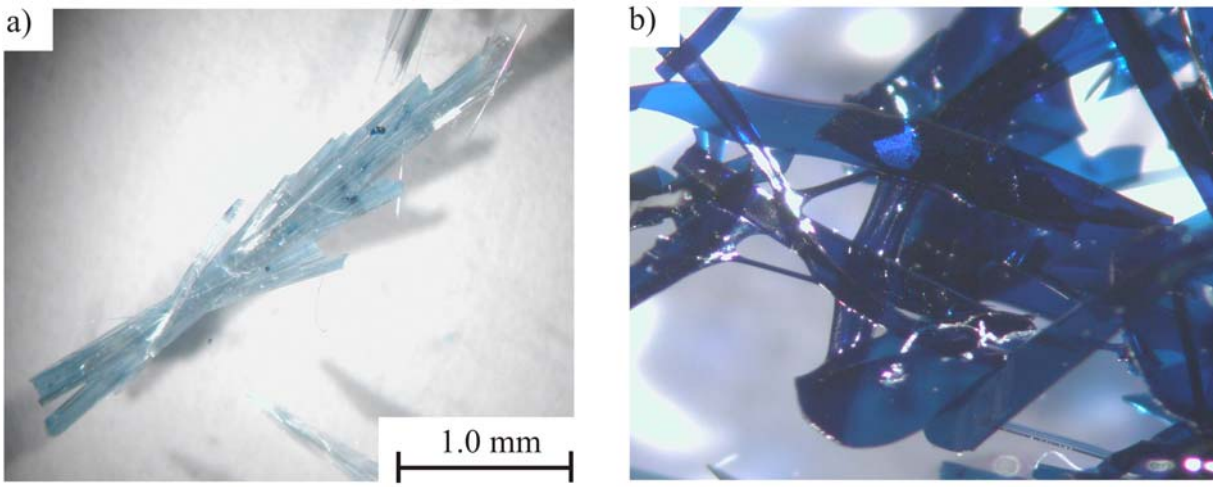

Figure 9.1 Crystals of $(MoO_2)_2P_2O_7$ grown by CVT (a); amorphous blue lamella formed along with the crystal of $(MoO_2)_2P_2O_7$ at the sink region of the tube (b).

Light blue needlelike crystals of $(MoO_2)_2P_2O_7$ up to 3.0 mm were deposited in the lower temperature region of the ampoule due to endothermic transport reactions. In contrast to reduced molybdenum phosphates [19], H_2O plays the vital role for the crystallization of $(MoO_2)_2P_2O_7$ by CVT even though water was not intentionally added as transport agent. Owing to the hygroscopic nature of P_4O_{10}, some water is expected in the system. The migration of molybdenum from higher to lower temperature via the formation of gaseous $MoO_2(OH)_2$ has already been reported by SCHÄFER *et al*. [148]. Depending on H_2O content in

the ampoule, the migration of phosphorus can proceed via formation of gaseous polymeric meta phosphoric acid $(HPO_3)_n$ (n = 3,4) and even by gaseous H_3PO_4 [149]. In accordance with this scenario, the crystallization of $(MoO_2)_2P_2O_7$ occurs in the sink end of the ampoule via decomposition of gaseous $MoO_2(OH)_2$, $(HPO_3)_n$ and H_3PO_4 (Equations 9.2, 9.3). It is interesting to mention that crystallization of $(MoO_2)_2P_2O_7$ at the sink end was always accompanied by the deposition of amorphous blue lamella (see Figure 9.1b).

$$(MoO_2)_2P_2O_7(s) + 3H_2O(g) = 2MoO_2(OH)_2(g) + 2(HPO_3)_n(g), \quad n = 3,4 \qquad (9.2)$$

$$(MoO_2)_2P_2O_7(s) + 5H_2O(g) = 2MoO_2(OH)_2(g) + 2H_3PO_4(g) \qquad (9.3)$$

In addition, the already prepared powder of $(MoO_2)_2P_2O_7$ was taken as starting materials along with various transport agents such as iodine, water or $PtCl_2$. In no case migration of $(MoO_2)_2P_2O_7$ from the source to the sink was observed. Instead we observed that at about 700°C, $(MoO_2)_2P_2O_7$ starts melting, thereby leading to the formation of a dark blue melt which is in accordance with the observation of KIERKEGAARD [150]. Upon cooling no recrystallization of the melt was observed.

Table 9.1 Experiments for synthesis and chemical vapour transport of $(MoO_2)_2P_2O_7$.

starting materials / mg		**TA / mg**	**Temperature[a] / °C**	**time / d**	**products (source)** (according to Guinier photographs)	**products (sink)** (according to Guinier photographs)
MoO_3	204.3	---	500 → 600[b]	3		
P_4O_{10}	100.7		600 → 500	7	$(MoO_2)_2P_2O_7$	$(MoO_2)_2P_2O_7$ / amorphous blue lamella
MoO_3	144.8	---	500 → 600[b]	3		
P_4O_{10}	74.7		600 → 500	9	$(MoO_2)_2P_2O_7$	$(MoO_2)_2P_2O_7$ / amorphous blue lamella
MoO_3	275.0	I_2 = 43.0	500 → 600[b]	1		
P_4O_{10}	142.5		560 → 480	4		no transport
			580 → 430	2	$(MoO_2)_2P_2O_7$	no transport
$Mo_2P_2O_{11}$	200.0	H_2O	600 → 500	5	$(MoO_2)_2P_2O_7$	no transport
$Mo_2P_2O_{11}$	200.0	H_2O	500 → 600[b]	4		
			600 → 500	7	$(MoO_2)_2P_2O_7$	amourphous substances
$Mo_2P_2O_{11}$	200.0	H_2O + I_2 (30.0)	600 → 500	5	$(MoO_2)_2P_2O_7$	no transport
$Mo_2P_2O_{11}$	200.0	$PtCl_2$ = 26	500 → 400	5	$(MoO_2)_2P_2O_7$	no transport
		NH_4Cl = 3	600 → 500	5		

a) Given are the various heating temperatures for each experiment. Starting solids were always at the left side of the arrow. Solid reaction products were characterized by their XRPD pattern after the final heating period, only.
b) Prereaction.

9.3 X-ray Investigations

Energy-dispersive X-ray fluorescence analyses [116, 117, 118] (EDAX system, scanning microscope DMS 940, Zeiss) showed the presence of molybdenum and phosphorus. Oxygen was not considered during the investigation.

X-ray powder diffraction. For identification, examination of the purity and for determination of the lattice parameters of α-$(MoO_2)_2P_2O_7$ image-plate (*IP*) Guinier photographs (Guinier camera FR-552 Enraf-Nonius, quartz-monochromator, Cu-Kα_1 radiation, λ = 1.54052 Å, BAS-TR 2025 image plate film (Fuji), BAS-1800 scanner (Fuji), software: BASREADER, [151], AIDA [91] (for digitization)) were used. Details on this method were already reported in literature [90, 152, 153]. Assignment of 37 reflections of the powder pattern (see Figure 9.2) in the angular range 22.04° ≤ 4θ ≤ 117.03° led to a = 17.808(3) Å, b = 10.370(2) Å, c = 17.814(2) Å and β = 90.12(1)° in agreement with the superstructure proposed by LISTER *et al.*

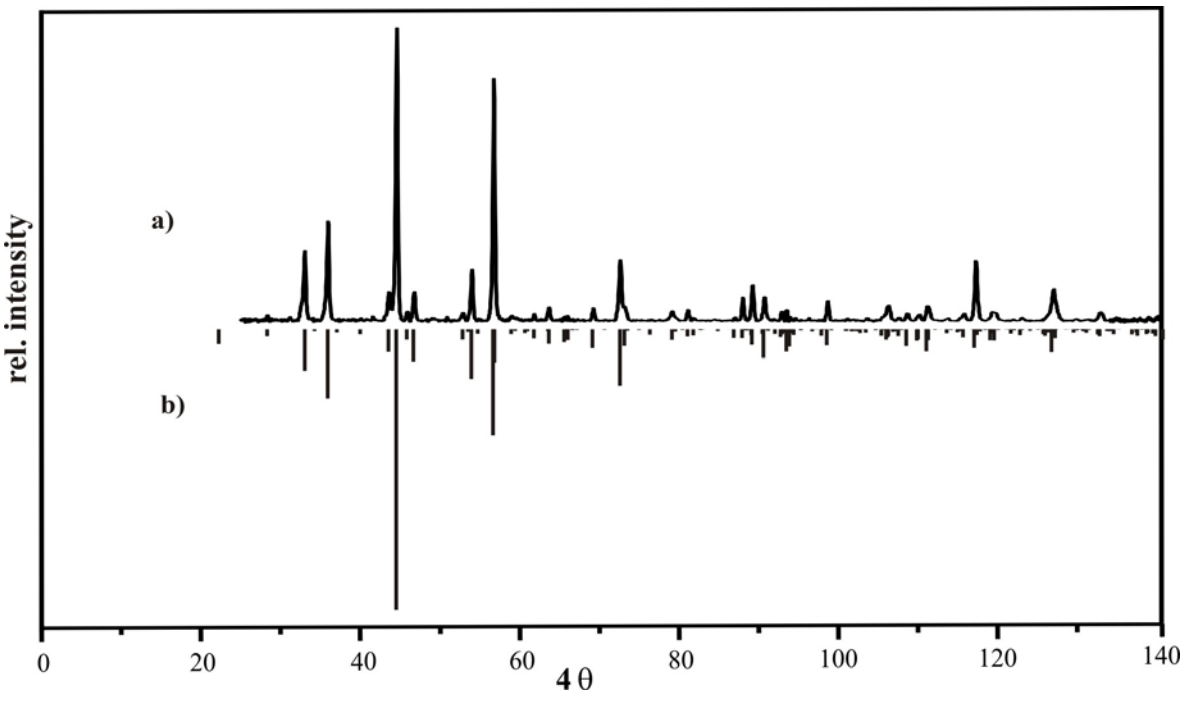

Figure 9.2 *IP*-Guinier photograph of α-$(MoO_2)_2P_2O_7$ (a) and the simulation of α-$(MoO_2)_2P_2O_7$ on basis of the X-ray single-crystal data (b).

Single-crystal X-ray study. For the X-ray investigation, a well-shaped single-crystal of α-$(MoO_2)_2P_2O_7$ was selected under the polarizing microscope and then fixed at the top of a glass

fibre. Intensity data were measured by a κ-CCD diffractometer (Enraf-Nonius Inc.) at ambient temperature.

Structure determination and refinement were performed using the SHELX-97 [105] suite in the WinGX framework [135]. Starting parameters were obtained by Direct Methods in SHELXS [137]. Thus, molybdenum and phosphorus atoms in agreement to the model of LISTER *et al.* were located. Subsequent Δ-Fourier syntheses allowed localization of oxygen atoms. An empirical absorption correction was made by using equivalent reflections (multi-scans) [115]. Despite reasonable bond-lengths and -angles, the refinement of the crystal structure allowing for anisotropic displacement parameters converged at residuals of R_1 = 0.128 and wR_2 = 0.226 along with a large number of "*non positive definite*" atoms. These high residuals are the consequence of twinning which is clearly visible in figure 9.3.

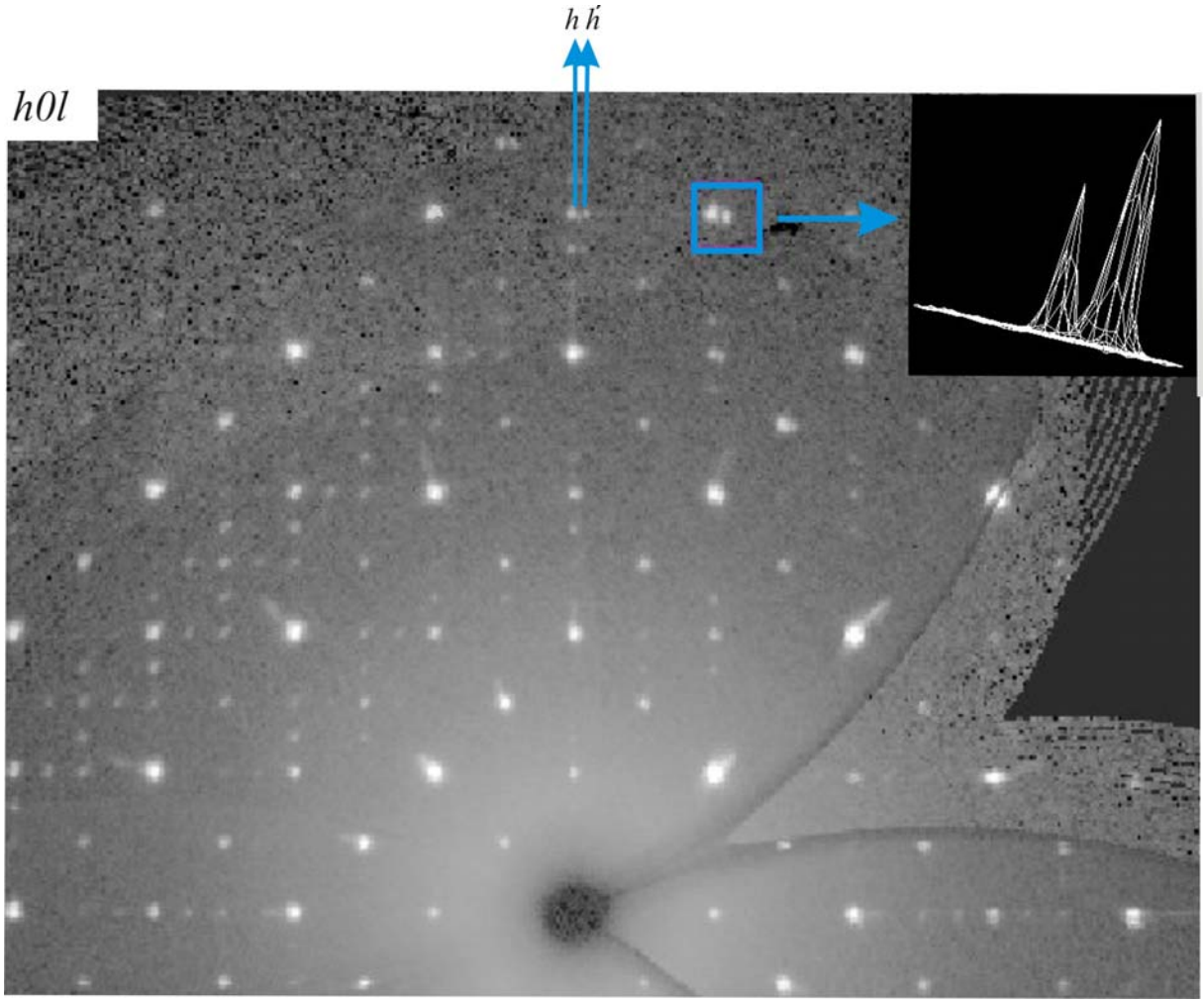

Figure 9.3 Calculated precession photograph of the *h0l* plane showing the twinning of α-$(MoO_2)_2P_2O_7$. The Inset shows the intensities of two reflections from the twinned domains.

The assumption of the loss of a mirror plane perpendicular to the *b*-axis of α-$(MoO_2)_2P_2O_7$ as twin element 0 0 1 0 1 0 1 0 0 gave an immediate improvement in the refinement of the crystal structure. It avoided all the "*non posite definite*" and led to residuals of $R_1 = 0.039$, $wR_2 = 0.079$.

Details concerning data collection, structure solution and refinement of α-$(MoO_2)_2P_2O_7$ are summarized in table 9.2. Final atomic coordinates are listed in table 9.3. A complete list of interatomic distances, indexing of the cell parameters and anisotropic displacement parameters are given in Appendix A3 (Table A3.1 to Table A3.3).

Table 9.2 Crystallographic data, structure solution and refinement of α-$(MoO_2)_2P_2O_7$.

crystal data	
chemical formula	α-$(MoO_2)_2P_2O_7$
formula weight (g/mol)	429.82
crystal system	monoclinic (14)
space group	$P2_1/c$ (no. 62)
a / Å	17.808(3)
b / Å	10.370(2)
c / Å	17.814(2)
β / °	90.12(1)
V / Å^3	3289.7(9)
Z	16
D_{calc} / g·cm^{-3})	3.471
μ / mm^{-1}	3.49
colour	light blue crystals, colourless powder
data collection	
diffractometer	κ-CCD (NONIUS)
radiation, wavelength, monochromator	Mo-$K\alpha$ (λ = 0.71073 Å), graphite
crystal size / mm^3	0.22×0.03×0.03
F(000)	3232
temperature	293 K
theta range / ^{o}	$2.91 \le \theta \le 30.03$
index ranges	$-25 \le h \le 25$
(whole sphere)	$-14 \le k \le 14$
	$-25 \le l \le 25$
structure refinement	
software	SHELX97 [105]
absorption correction	multi-scans [115]
collected reflections	128749
indipendent reflections	9875, 6519 with $\lvert F_o \rvert > 4\sigma(F_o)$
no. of parameters used, Goof	543, 1.036
residuals	
R_{int}	0.066
R_1	0.039
R_1 (all)	0.079
wR_2 (for all data)	0.1010
BASF	0.662
extinction coefficient	0.000189
weighting scheme	A = 0.0395; B = 6.9985
residual electron density	
$\Delta\rho_{max}$ / Å^{-3}	1.87 (close to O17)
$\Delta\rho_{min}$ / Å^{-3}	-1.28 (close to Mo7)

[a] $R_1 = \Sigma||F_o| - |F_c|| / |F_o|$, $F_o^2 \ge 2\sigma(F_o^2)$

[b] $wR_2 = 1 / [\sigma^2(F_o^2) + (A \cdot P)^2 + B \cdot P]$; $P = (F_o^2 + 2F_c^2) / 3$

Table 9.3 Atomic coordinates and isotropic displacement parameters for α-$(MoO_2)_2P_2O_7$.

atom	*x*	*y*	*z*	U_{eq} /Å$^{2\ a)}$
Mo1	0.06702(3)	0.77553(5)	0.94116(3)	0.0109(1)
Mo2	0.31168(3)	0.76967(5)	0.68693(3)	0.0114(1)
Mo3	0.56185(3)	0.77846(5)	0.43960(3)	0.0104(1)
Mo4	0.81567(3)	0.78101(5)	0.18952(3)	0.0106(1)
Mo5	0.93436(3)	-0.02250(5)	0.81259(3)	0.0120(1)
Mo6	0.18684(3)	-0.00237(5)	0.56234(3)	0.0126(1)
Mo7	0.44157(3)	-0.01146(5)	0.31607(3)	0.0119(1)
Mo8	0.68664(3)	-0.02307(5)	0.05961(3)	0.0122(1)
P1	0.23535(9)	0.01201(13)	0.10960(9)	0.0109(3)
P2	0.48375(9)	0.00867(14)	0.85778(9)	0.0107(3)
P3	0.73214(9)	0.00431(13)	0.60903(9)	0.0100(3)
P4	-0.01625(9)	0.00714(14)	0.35682(9)	0.0104(3)
P5	0.07424(9)	0.30900(14)	0.94914(9)	0.0112(3)
P6	0.33081(9)	0.30608(14)	0.70479(9)	0.0120(3)
P7	0.57697(9)	0.31470(14)	0.45119(9)	0.0115(3)
P8	0.82480(9)	0.31415(14)	0.20041(9)	0.0111(3)
O1	0.7468(3)	-0.0567(6)	-0.0312(3)	0.0309(14)
O2	0.0043(3)	-0.0147(5)	0.7269(2)	0.0191(11)
O3	0.2520(3)	-0.0135(5)	0.4742(3)	0.0239(12)
O4	0.5045(3)	-0.0228(5)	0.2258(3)	0.0182(11)
O5	0.8420(3)	0.5596(5)	0.3703(3)	0.0310(14)
O6	0.0998(3)	0.5215(5)	0.1282(3)	0.0228(12)
O7	0.3520(2)	0.5164(5)	0.8799(3)	0.0212(11)
O8	0.5996(3)	0.5154(5)	0.6275(3)	0.0207(11)
O9	0.8721(3)	0.7774(5)	0.0936(3)	0.0184(11)
O10	0.1241(3)	0.7706(5)	0.8463(3)	0.0177(11)
O11	0.3702(3)	0.7709(5)	0.5930(3)	0.0183(11)
O12	0.6286(3)	0.7781(5)	0.3517(3)	0.0207(11)
O13	-0.0269(2)	0.7258(5)	0.5000(3)	0.0158(10)
O14	0.2188(3)	0.7282(5)	0.2471(3)	0.0175(10)
O15	0.4647(3)	0.7316(5)	-0.0064(3)	0.0165(10)
O16	0.7266(3)	0.7246(5)	0.7562(3)	0.0215(11)
O17	0.1106(2)	0.4213(4)	-0.0126(3)	0.0205(9)
O18	0.3839(3)	0.3693(5)	0.7586(3)	0.0341(12)
O19	0.6138(3)	0.4311(4)	0.4849(2)	0.0193(9)
O20	0.8611(3)	0.4268(4)	0.2378(3)	0.0258(10)
O21	0.2472(3)	0.8745(4)	0.1234(3)	0.026(1)
O22	0.5232(3)	0.8978(4)	0.8921(3)	0.0192(9)
O23	0.7666(3)	0.8926(4)	0.6472(3)	0.0221(9)
O24	0.0187(3)	0.8956(4)	0.3950(3)	0.0199(9)
O25	0.0185(3)	0.3635(4)	0.8876(3)	0.0229(10)
O26	0.2921(3)	0.4165(5)	0.6626(3)	0.0515(15)
O27	0.5158(3)	0.3619(4)	0.3928(3)	0.0209(9)
O28	0.7645(3)	0.3672(4)	0.1425(3)	0.0266(10)
O29	-.0165(3)	0.8586(4)	0.8582(3)	0.0195(9)
O30	0.2366(3)	0.8841(4)	0.6115(3)	0.0232(10)
O31	0.4781(3)	0.8481(4)	0.3532(3)	0.0187(9)

O32	0.7296(3)	0.8565(4)	0.1100(3)	0.0197(9)
O33	0.8781(3)	0.8044(4)	0.7437(3)	0.0258(11)
O34	0.1236(3)	0.8141(4)	0.4983(3)	0.0221(9)
O35	0.3604(3)	0.8457(5)	0.2361(3)	0.0304(11)
O36	0.6162(3)	0.8036(4)	0.0027(3)	0.0221(10)
O37	-0.0398(3)	0.1085(5)	0.8571(3)	0.0400(15)
O38	0.2179(3)	0.1373(5)	0.5963(3)	0.0352(12)
O39	0.4905(3)	0.0973(4)	0.3643(3)	0.0313(11)
O40	0.7297(3)	0.1067(5)	0.0893(3)	0.0382(14)
O41	0.8366(3)	0.5656(4)	0.7104(3)	0.0235(10)
O42	0.0913(3)	0.5726(4)	0.4635(3)	0.025(1)
O43	0.3449(3)	0.5915(5)	0.2201(3)	0.0292(10)
O44	0.5783(3)	0.5669(4)	-0.0386(3)	0.0233(10)

[a] $U_{eq} = (⅓)\Sigma_i\Sigma_j U_{ij} a_i^* a_j^* \mathbf{a}_i \cdot \mathbf{a}_j$

9.4 Description and Discussion of the Crystal structure

The crystal structure of $(MoO_2)_2P_2O_7$ shows several phase transitions [25]. At ambient temperature this pyrophosphate forms the α-phase whereas at 423 K γ-phase exists. α-$(MoO_2)_2P_2O_7$ can be derived from the γ-phase by the transformation matrix (see Equations 9.4 - 9.6) that can be described according to figure 9.4. According to LISTER *et al.* [25] this pyrophosphate reveals a series of phase transitions on cooling at temperatures 377 and 325 K. These authors assumed an incommensurately modulated structure, described as β-phase, that forms within the range of 340 - 360 K. In addition to this, a fourth modification δ-$(MoO_2)_2(P_2O_7)$ is also reported [129] that forms on slowly heating the precursor materials $MoO_2PO_3OH.H_2O$ at 793 K.

$$a_{mono} = 1\,a_{ortho} + 2\,b_{ortho} + 0\,c_{ortho} \quad (9.4)$$

$$b_{mono} = 0\,a_{ortho} + 0\,b_{ortho} + 1\,c_{ortho} \quad (9.5)$$

$$c_{mono} = 1\,a_{ortho} - 2\,b_{ortho} + 0\,c_{ortho} \quad (9.6)$$

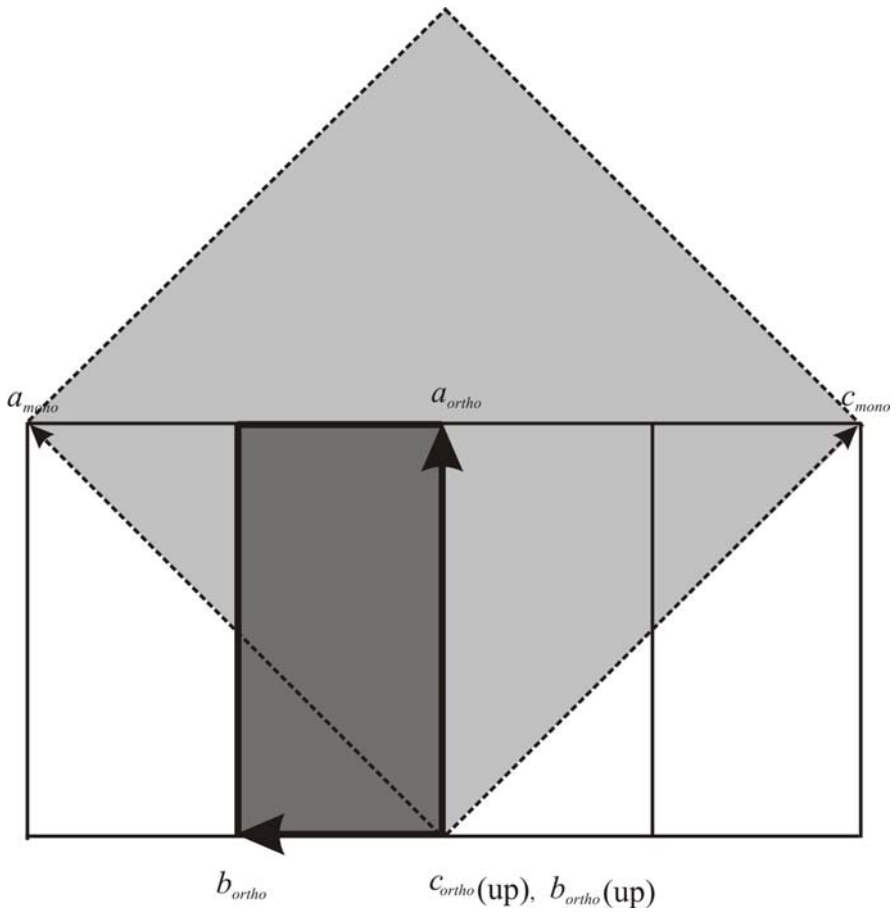

Figure 9.4 Pictorial representation for the transformation of γ- to α-$(MoO_2)_2P_2O_7$. Dark and light grey region represent the γ- and α-$(MoO_2)_2P_2O_7$, respectively.

The crystal structure of α-$(MoO_2)_2P_2O_7$ consists of eight crystallographically independent sites for molybdenum and phosphorus, each of them coordinated by oxygen atoms forming $[MoO_6]$ octahedra and $[P_2O_7]$ groups, respectively (Figure 9.5a). The $[Mo^{VI}O_6]$ octahedra share their corners to form infinite zigzag chains (O_t=(O_b=)Mo─O_t=(O_b=)Mo─O_t) (see Figure 9.6a). Two successive chains are connected by P_2O_7 groups. This building pattern can be

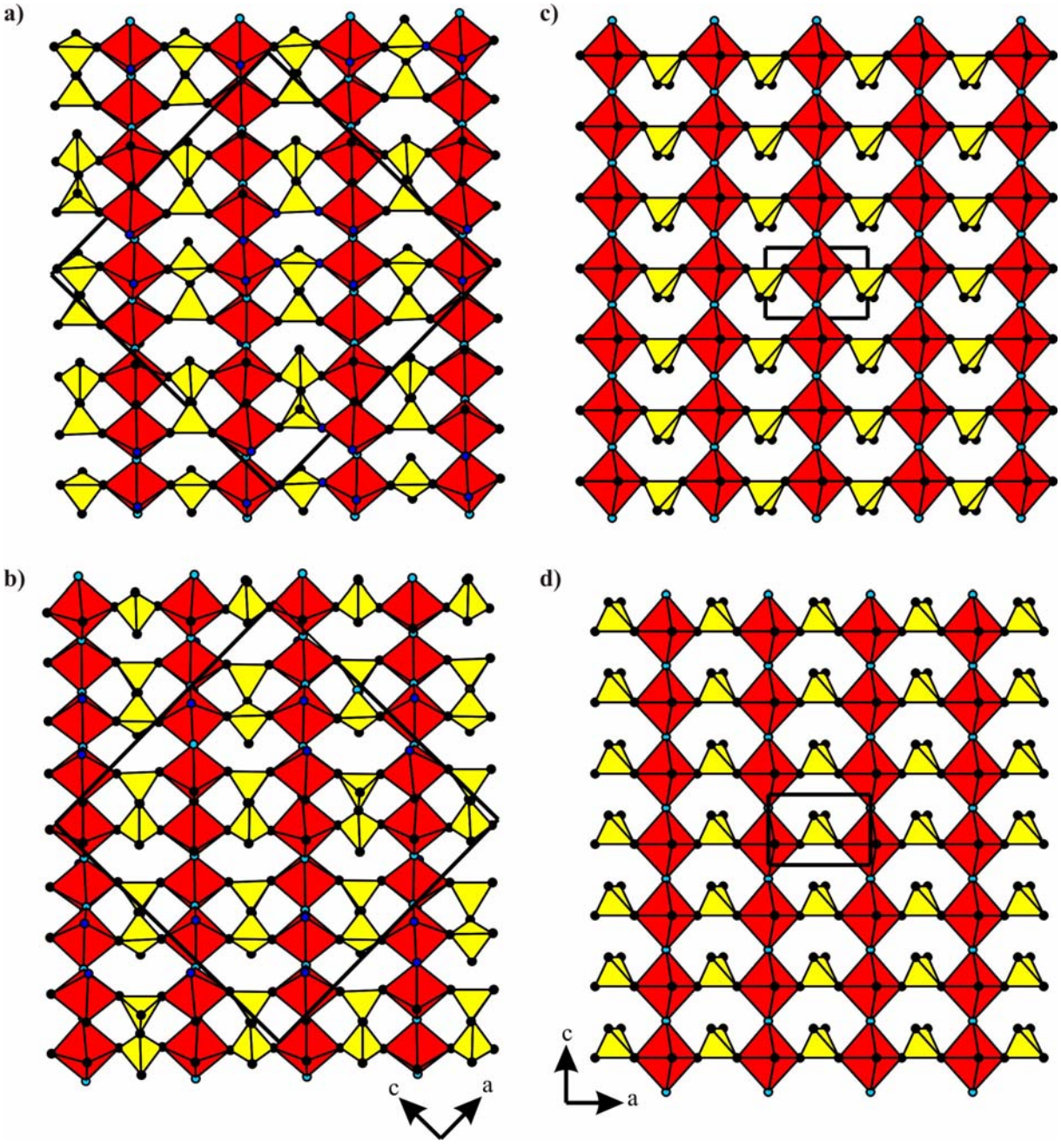

Figure 9.5 Crystal structures of α-$(MoO_2)_2P_2O_7$ (a, b) and $MoOPO_4$ [27] (c, d) with $[MoO_6]$ groups (red), $[P_2O_7]$ and $[PO_4]$ (yellow). Figures a and b represent $y \approx 0$ and $y \approx 1/4$ layers and c and d represent $y = 0$ and $y = 1/2$ layers. Black circles represent oxygen atoms that connect either only P or Mo and P atoms. Dark blue and light blue circles represent molybdenyl(VI) oxygen atoms where the former is bonded only to molybdenum; the latter connect two molybdenum atoms (Diamond version 3.2c [138]).

correlated to that of $MoOPO_4$ [27]. The crystal structure of $MoOPO_4$ is built up by infinite chains of distorted $[Mo^{V}O_6]$ octahedra, linked together by molybdenyl(V) oxygen atoms according to the scheme $Mo(O_5)=O\cdots Mo(O_5)=O\cdots Mo(O_5)=O\cdots$. One may describe molybdenum as five-fold coordinated, the sixth atom being at a very long Mo-O distance. In the crystal structure of $MoOPO_4$ two chains of the octahedra are bridged by $[PO_4]$ tetrahedra instead of $[P_2O_7]$ group that we have already seen for α-$(MoO_2)_2P_2O_7$. It is worth to mention that the combination of two $[PO_4]$ tetrahedra leads to the formation of $[P_2O_7]$ by the loss of one oxygen atom. This lost oxygen atom appropriately displaces to the close vicinity of the molybdenum atom. Thus the formation of $[P_2O_7]^{4-}$ and MoO_2^{2+} ions occur which are present in the crystal structure of α-$(MoO_2)_2P_2O_7$.

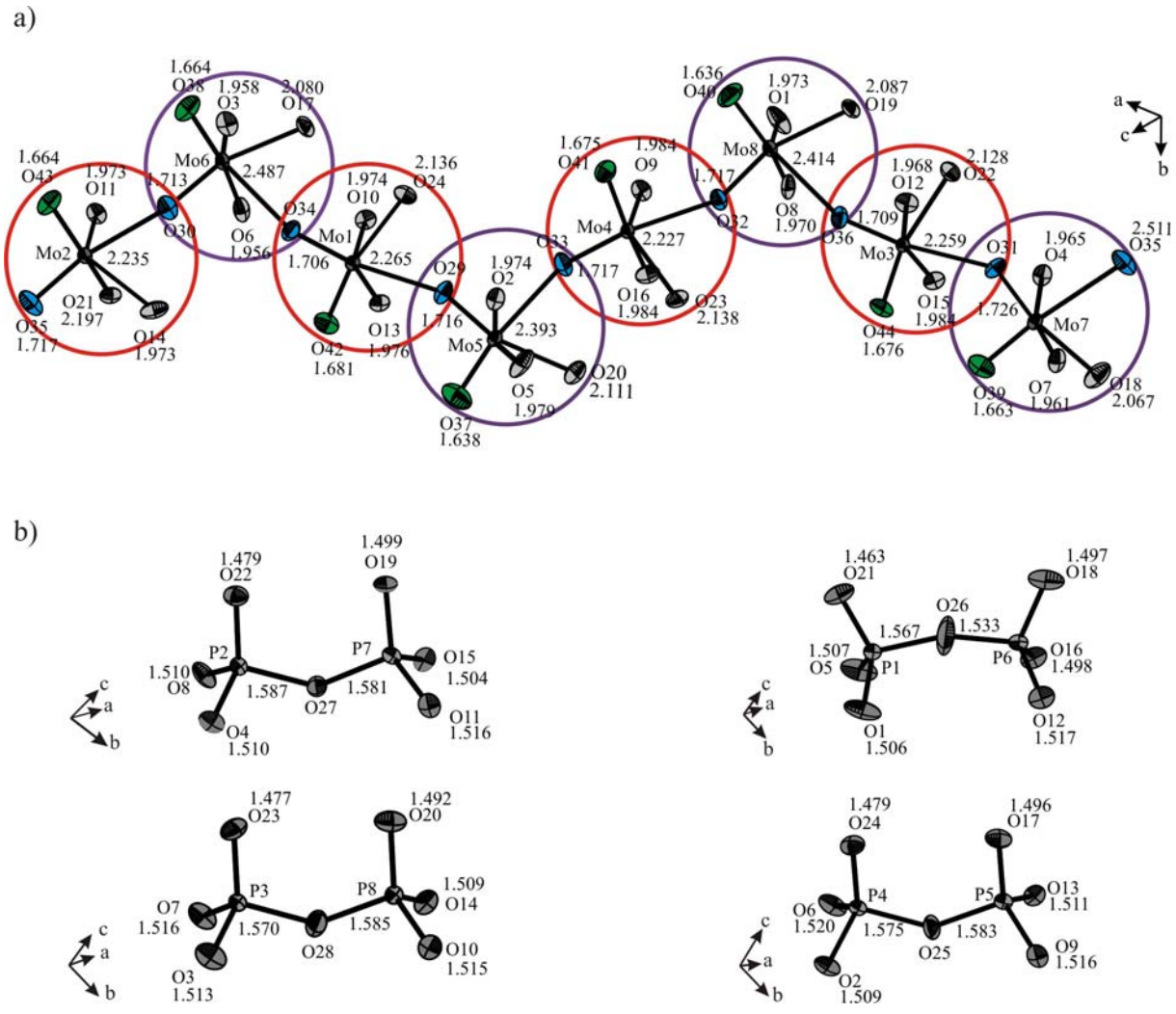

Figure 9.6 ORTEP of $[MoO_6]$ octahedra (a) and $[P_2O_7]$ groups (b) in α-$(MoO_2)_2P_2O_7$. Green and blue ellipsoids represent molybdenyl(VI) oxygen atoms where the former is bound only to molybdenum; the latter connect two molybdenum atoms. Ellipsoids with 50% probability (Diamond version 3.2c [138]).

The coordination polyhedra [MoO_6] (1.63 Å ≤ *d*(Mo-O) ≤ 2.511 Å) (Figure 9.6a, Table A3.1 in Appendix) deviate strongly from an ideal octahedron. Three pairs of Mo-O bond-lengths can be easily distinguished, e. g. long (2.08 Å ≤ *d*(Mo-O) ≤ 2.51 Å), intermediate (1.96 Å ≤ *d*(Mo-O) ≤ 1.99 Å), and short 1.63 Å ≤ *d*(Mo-O) ≤ 1.73 Å). Among the eight crystallographically independent [MoO_6] octahedra four (Mo1-Mo4) are containing *d*(Mo-O) in the range 2.23 Å ≤ *d*(Mo-O) ≤ 2.26 Å (see Figure 9.6a, indicated by red circles) whereas the remaning (Mo5-Mo8) form very long distances *d*(Mo-O) in the range 2.39 Å ≤ *d*(Mo-O) ≤ 2.51 Å (see Figure 9.6a, indicated by violet circles). These two different types of [MoO_6] octahedra are alternatingly connected to each other via molybdenyl oxygen atoms according to the scheme $Mo(=O_t)=O_b{-}Mo(=O_t)=O_b{-}Mo\cdots$ (see Figure 9.6a). It is worth to mention even with the short distances *d*(Mo-O) one can distinguish between shorter, *d*(Mo-O) ≈ 1.65 Å and longer, *d*(Mo-O) ≈ 1.72 Å. Oxygen atoms with the shorter distances are connected only to molybdenum where oxygen atoms with longer distances correspond to the molybdenyl oxygen that bridge to other molybdenum via a very long *d*(Mo-O) ranging in 2.23 Å ≤ *d*(Mo-O) ≤ 2.51 Å.

Molybdenyl groups $(MoO_2)^{2+}$ in α-$(MoO_2)_2P_2O_7$ attain *cis* conformation at ∠(O_t,Mo,O_t) ≈ 103°. The repulsion between the *cis* positioned short bonds Mo=O_t is expected to be strong (VSEPR model) and is at least partially mitigated by expansion of the angle ∠(O_t,Mo,O_t) from 90° to about 103°. We also notice this type of bonding feature in γ-$(Mo^{VI}O_2)_2P_2O_7$ [25], $Mo^{VI}O_2SO_4$ [154], $NaMo^{VI}O_2PO_4$ [155]. The preference for the *cis* conformation can be understood in terms of the spatial arrangement required for $p_\pi \rightarrow d_\pi$ bonding between the strongly π-donating oxygen atoms to the t_{2g} orbitals of the metal. COTTON *et al.* [156] have already discussed this phenomena for [$Mo^{VI}O_6$] species.

The [P_2O_7] groups in α-$(MoO_2)_2P_2O_7$ display radial and angular distortion ranging for 1.46 Å ≤ *d*(P-O) ≤ 1.59 Å and 103.9° ≤ ∠(O,P,O) ≤ 115.1° (see Figure 9.6b). The *d*(P-O_b) are the longest which is typical for pyrophosphates [2]. All the *d*(P-O_b) ≈ 1.58 Å, except an unexpectedly short one *d*(P6-$O26_b$) ≈ 1.53 Å. Apart from this each of the [P_2O_7] group can be distinguished into two parts. One part of the [P_2O_7] contains almost equal *d*(P-O_t) ≈ 1.50 while the other part contains two *d*(P-O_t) ≈ 1.50 and one unexpectedly short bond-length as about 1.47 Å.

It is worth mentioning that the difference in standard deviations of some of the *d*(Mo-O) and *d*(P-O) distances between our X-ray single-crystal refinement and the refinement of the X-ray powder pattern obtained by LISTER *et al.* [25] is upto to four order of magnitude (Sec. 16, Table A3.1 indicated in bold letters). Furthermore, in contrast to average ∠(O_t,Mo,O_t) =

100.5(4)° obtained from LISTER *et al.* our refinement revealed an average $\angle(O_t,Mo,O_t)$ = 102.8(2)° (see Sec. 16, Table A3.1).

It is worth to consider the driving forces of the phase transition from the high temperature γ-phase to the low temperature α-phase. The structural complexity of inorganic materials with simple composition frequently occurs in frameworks based on corner sharing polyhedra (such as $(Mo^{V}O)_2P_4O_{13}$ [29]) due to displacive phase transition on cooling. As with related materials, a balance of local bonding requirements with in the coordination polyhedra and achieving optimum intrapolyhedral angles mainly causes it. Considering this fact, P-O-P linkage in the high temperature phase (γ-phase) has a single angle of 150.2(5)° [25] while the low temperature phase (α-phase) shows four unique P_2O_7 groups with average bond angle of 146.03(1)° [159.6(5)°, 142.2(3)°, 142.2(3)°, 140.1(3)°]. This average value is about 4% smaller than that of the high temperature phase. This lowering of the volume has been given by LISTER *et al.* [25] as an explanation for the phase transition.

9.5 UV/Vis Absorption Spectra

The UV/Vis absorption spectra of the single-crystal of $(MoO_2)_2P_2O_7$ show a very weak absorption band at about 14000 cm^{-1} (see Figure 9.7a). Apart from this, electronic absorption spectrum of the blue amorphous lamella which often accompanies the occurance of α-$(MoO_2)_2P_2O_7$ shows a very broad strong absorption band centered at about 14000 cm^{-1} and shoulder at 9500 cm^{-1} (see Figure 9.7b). In constrast to optical density of reduced molybdenyl(V) phosphates (Chap. 8, Sec. 8.6, Figure 8.12) for the absorption bands at about 13000 cm^{-1} ($^2B_2(dxy) \rightarrow {}^2E(dxz, dyz)$), optical density of the band center at about 14000 cm^{-1}

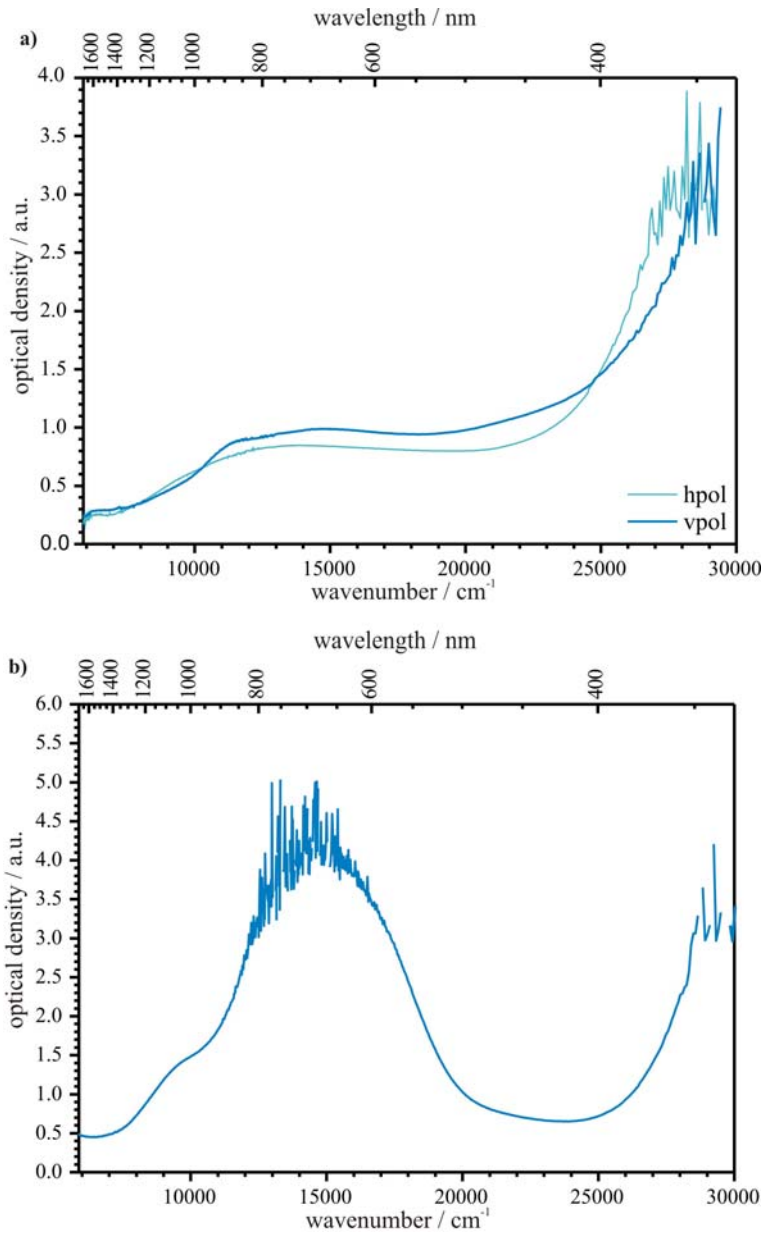

Figure 9.7 UV/Vis absorption spectra of a single-crystal of $(MoO_2)_2P_2O_7$ (a) and amorphous blue lamella (b).

for the blue amorphous lamella is about 3.5 order of magnitude (see Figure 9.7b). This, in addition to an agreement to electronic spectra of the Keggin type anions of molybdenum and tungsten compounds [157, 158], one might assign the shoulder at 9500 cm^{-1} and 14000 cm^{-1} as IVCT where *d* electrons appeared due to the reduction of $Mo^{6+} \rightarrow Mo^{5+}$. The polarized single-crystal UV/Vis absorption spectra (see Figure 9.7) of α-$MoO_2)_2P_2O_7$ show that charge transfer transitions (LMCT) originate at about 28000 cm^{-1} which is expected from $O^{2-} \rightarrow Mo^{6+}$.

Despite the colours of molybdenum phosphates containing pentavalent molybdenum varying (Chap. 8, Sce. 8.6, Figure 8.12) significantly from yellow ($MoOPO_4$), to green ($(MoO)_2P_4O_{13}$), and to dark green ($(MoO)_4(P_2O_7)_3$), the colour of the amourphous lamella is intense blue. This variation in colours is clarly visible from the shift of the absorption minium (Figure 9.7b).

10 The Ternary System Rhenium / Phosphorus / Oxygen

10.1 Introduction

In 1962, KIERKEGAARD, who pioneered the research in systems MO_3-P_2O_5 (M = Mo, W) mentioned that **"*The structural similarity between ReO_3 and WO_3 is well known. Attempts to prepare intermediate compounds in the system ReO_3-P_2O_5 were however unsuccessful*"** [159]. With the discovery of rhenium(IV)-pyrophosphate, $Re^{IV}P_2O_7$, by BANKS [81] in 1982, rhenium entered into the family of metals forming anhydrous transition metal phosphates. Despite the existence of a large number of rather stable and easily accessible oxidation states of rhenium, there was no further report in rhenium phosphates in literature. It is certainly notable that for its neighbour elements molybdenum and tungsten a large number of phosphates has been explored. While molybdenum forms anhydrous phosphates at its oxidation states +III, +IV, +V, and +VI, tungsten adopts in anhydrous phosphates at the oxidation states +IV, +V, and +VI. The similarity of the redox behaviour of these two elements is reflected via the formation of anhydrous phosphates in identical composition ($M^{VI}{}_2P_2O_{11}$, $M^{VI}P_2O_8$, $M^{V}PO_5$, $M^{IV}P_2O_7$; M = Mo, W), however, different crystal structures. In addition to the existence of a large number of stable oxidation states of rhenium for its oxide, oxide halides and rhenates (as mentioned in Chapter 1), its diagonal relationship to Mo as well as its neighbourhood to W, suggested a systematic investigation in to the ternary system Re / P / O to search for new rhenium phosphates and to develop the phase diagram. Such information also should allow understanding of the redox behaviour of rhenium in comparison to its neighbouring elements V, Mo, W and Os.

In the present study, several new anhydrous rhenium phosphates $Re^{VII}O_2(PO_4)$, $Re^{VI}{}_2O_3(PO_4)_2$, $Re^{V}{}_2O_3(P_2O_7)$, and $NaRe^{IV}{}_2(PO_4)_3$ have been synthesized, crystallized and characterized. In addition, two new silicophosphates, $Re^{IV}{}_3[Si_2O(PO_4)_6]$, $(Re^{VII}{}_2O_5)Si_2°[Si^{t}{}_2(PO_4)_6]$ were synthesized and characterized by X-ray and spectroscopic invesitgations.

10.2 Equilibrium Phase Relation in System Re / P / O

In the binary Re/O system exist five crystallographically characterized oxides, $Re^{IV}O_2$ [34], $Re^{\sim V}_{1.16}O_3$ [35], $Re^{VI}O_3$ [36], $Re^{VII}_2Re^{VI}O_{10}$ [37], and $Re^{VII}_2O_7$ [38]. Furthermore, six phosphides Re_2P [160], Re_3P_4 [161], Re_6P_{13} [162], Re_2P_5 [163], ReP_3 [164], and ReP_4 [165] are known in literature. Five condensed phosphorus oxides exist: P_4O_n (n = 6, 7,···10), with three different modifications of P_4O_{10} [166, 167, 168, 169]. Phosphorus(III) oxide is known as P_4O_6 [170]. The other oxides P_4O_n (n = 7, 8, 9) are mixed-valent (III, V) [171, 172, 173]. These phosphorus oxides remain in the gas phase under the experimental conditions of the present work.

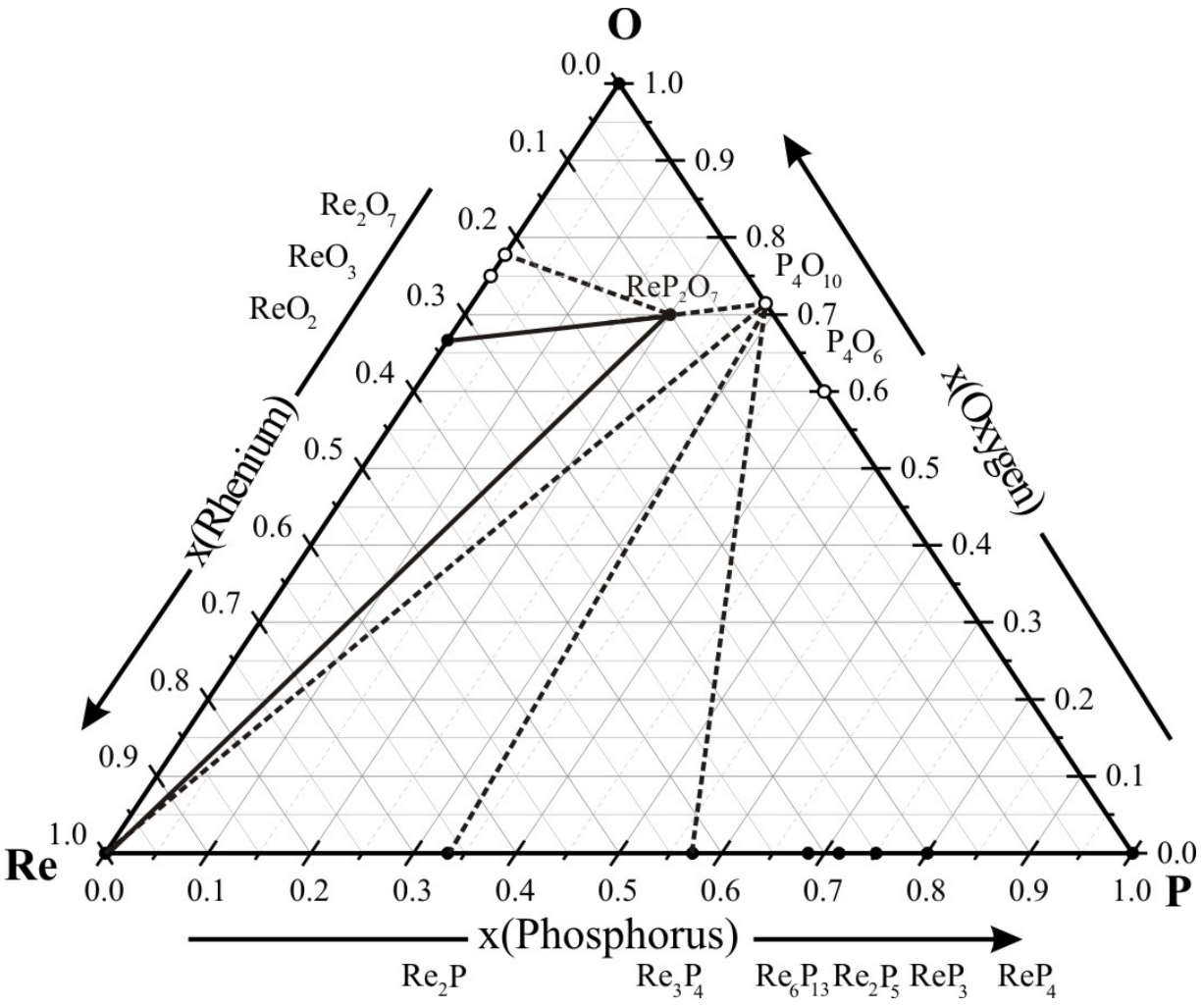

Figure 10.1 Ternary phase diagram developed at 800 °C. Hatched lines represent the solid-gas equilibria. Open circles represent compounds existing at this temperature in the gas phase only.

At 800°C, in ternary system Re / P / O only one phosphate, ReP_2O_7 exists (see Figure 10.1). At this temperature ReP_2O_7, metallic Re and ReO_2 coexist (see Table 10.1). Apart from this, different experimental results confirm the existence of a heterogeneous equilibrium between solid ReP_2O_7 and gaseous Re_2O_7. Heterogeneous equilibrium among metallic rhenium, Re_2P and gaseous P_4O_{10} is suggestted by our experiments (see Table 10.1).

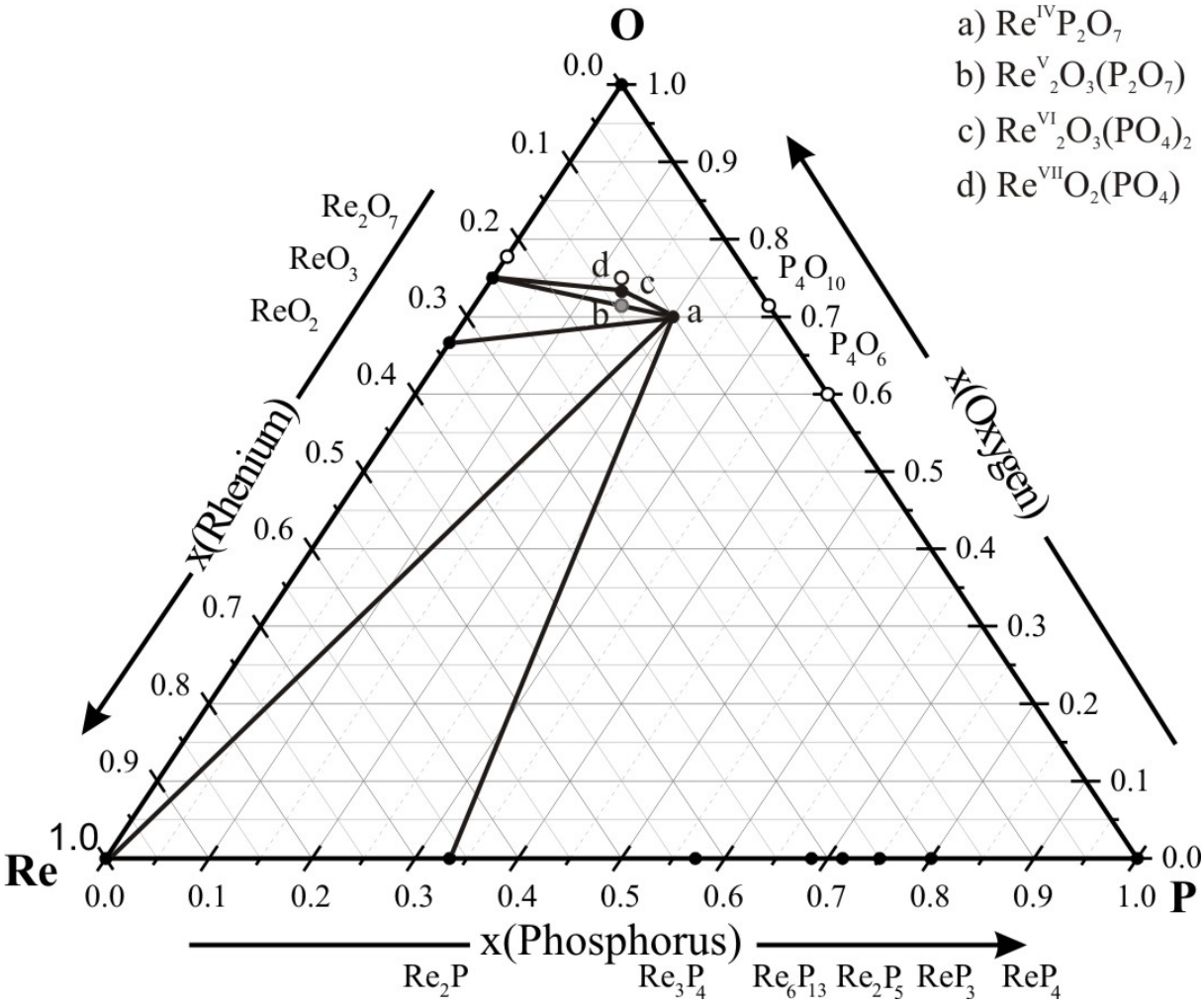

Figure 10.2 Ternary phase diagram developed at 500 °C. Solid lines represent solid-solid equilibria at 500 °C. Open circles represent the gaseous existence of the compounds at this temperature. Grey circle indicates that this phase does not exist at this particular temperature.

In contrast to the simplicity of the phase diagram at 800°C (Figure 10.1), the presence of an additional rhenium phosphate, $Re^{VI}{}_2O_3(PO_4)_2$, shows its complexity at 500°C (Figure 10.2). ReP_2O_7, metallic Re and ReO_2 coexist at 800°C and 500°C. Apart from this, a coexistence of ReP_2O_7, $Re^{VI}{}_2O_3(PO_4)_2$, and ReO_3 is observed only at 500°C (see Table 10.1). Our experimental results at 500°C also suggest an equilibrium between the phosphide Re_2P and ReP_2O_7.

Table 10.1 Experiments determining the equilibria in system Re / P / O at 800° and 500°C, 25-40 mg I_2 was used as mineralizer.

starting solids / mg		temperatures[a] / °C	time / d	products (source) (according to *IP* Guinier photographs)	products (sink)
ReO2	26.9	800	7	ReP_2O_7, Re, ReO_2	----
Re	24.6				
ReP_2O_7	48.1				
ReP_2O_7	62.3	800	7	ReP_2O_7, ReO_2, reddish substances	----
ReO_3	41.9				
ReO_2	37.3				
Re_2O_7	361.4	B.B.[b]	1/12		
P	8.6	700	3		
P_4O_{10}	84.7	800	4	ReP_2O_7, ReO_2, •[c]	----
Re_2O_7	366.4	800	7	ReP_2O_7, ReO_2, •[d]	----
P	8.1				
P_4O_{10}	94.0				
ReO_3	183.9	550 → 650	3		
P_4O_{10}	74.1	600 → 500	7	$Re_2O_3(PO_4)_2$, ReO_3, ReP_2O_7	$Re_2O_3(PO_4)_2$, ReO_3, ReP_2O_7
ReP_2O_7	60.5	500	7	ReO_3, ReO_2, ReP_2O_7	----
ReO_3	40.1				
ReO_2	36.4				
ReP_2O_7	72.0	500	7	ReP_2O_7, Re, Re_2P, $Si_3[Si_2O(PO_4)_6$	----
Re_2P	40.1				
Re_3P_4	68.2				

[a] Starting solids were kept at the temperature at left side of the arrow.
[b] B.B.: Reactants containing end of the closed silica tube were heated in Bunsen burner flame.
[c] • a few week unknown reflections at 4-theta (intensity in %): 26.6 (5), 64.9 (5), 65.7 (3), and 77.2(3).
[d] • a few week unknown reflections at 4-theta (intensity in %): 33.0 (4), 43.9(10), 47(2), 57.9(2) and 67.6(3).

During our systematic investigations, we also found two more phosphates, $Re^{V}_2O_3(P_2O_7)$ (see Chapter 12) and $Re^{VII}O_2PO_4$ (see Chapter 14), at 550 and 300°C, respectively. This observation pronounces that the redox behaviour of rhenium phosphates is considerably different from higher to lower temperatures. The coexistence of ReP_2O_7, $Re^{VI}_2O_3(PO_4)_2$, and ReO_3 as well as the solid-solid equilibrium of ReP_2O_7 and ReO_3 at 500°C show that $Re^{V}_2O_3(P_2O_7)$ does not exist at this temperature. Very likely, it has a narrow stability range with respect to temperature. The thermal decomposition of various rhenium phosphates and thereby the redox behaviour at $350 \leq \vartheta \leq 600$°C can be described according to equations 10.1-10.5.

$$2Re^{VII}O_2PO_4(s) = Re^{VII}_2O_7(g) + \tfrac{1}{2}\, P_4O_{10}(g) \quad (10.1)$$

$$2Re^{VII}O_2PO_4(s) = Re^{VI}_2O_3(PO_4)_2(s) + \tfrac{1}{2}\, O_2(g) \quad (10.2)$$

$$2Re^{VI}_2O_3(PO_4)_2(s) = 2Re^{V}_2O_3P_2O_7(s) + O_2(g) \quad (10.3)$$

$$2Re^{VI}_2O_3(PO_4)_2(s) = 4Re^{VI}O_3(s) + P_4O_{10}(g) \quad (10.4)$$

$$2Re^{V}_2O_3P_2O_7(s) = 2Re^{IV}P_2O_7(s) + 2ReO_2(s) + O_2(g) \quad (10.5)$$

11 Rhenium(IV) phosphates

11.1 Introduction

Up to now, a large number of tetravalent metal cations either transition or main group elements adopt the structure type of cubic SiP_2O_7 [174]. Several modifications are identified for this chemical composition. The largest family of $M^{IV}P_2O_7$ crystallizes in the cubic crystal structure with the space group $Pa\bar{3}$ (subcell with $Z = 4$ and $a \sim 8$ Å; Si [174], Zr [127, 175], Mo [31], W [79], Ce [176], U [177], Sn [178], Th [179]; and the respective superstructure with $Z = 108$ and $a \sim 24$ Å; Ti [180], Si [174], Zr [139, 140,175], Hf [139]). It is perceptible that all the compounds in this structure type encompass a 3 × 3 × 3 superstructure. In addition to the cubic modification, SiP_2O_7 crystallizes in two other crystal structures with a hexagonal [181] and monoclinic [182] phase. OsP_2O_7 [3] exhibits a cubic and a triclinic modification as well. The latter is isotypic to triclinic GeP_2O_7 [183]. Interestingly, triclinic GeP_2O_7 bears a close relationship to the crystal structure of monoclinic PtP_2O_7 [184]. BANKS observed that rhenium(IV) pyrophosphate, $Re^{IV}P_2O_7$ [81], is isotypic to the cubic modification of $M^{IV}P_2O_7$, but until now its structure was not fully characterized.

Electronic absorption spectra of the Re^{4+} ion have already been extensively studied for K_2ReX_6, (X = F, Cl, Br, I) [185, 186], as well as for Re^{4+} doped in halides A_2BX_6 (A = K, Cs; B = Zr, Pt, Hf; X = Cl, Br) [187, 188, 189, 190]. Despite this wealth of investigations of the d^3 electronic state of Re^{4+} ion in the chromophore [ReX_6], up to now no research was undertaken for the oxidorhenium complex. Our investigation in the electronic absorption spectrum of $Re^{IV}P_2O_7$ attains an intense attention due to its rather complicated features. Detailed explanation of this spectrum demands further investigation of other rhenium(IV)-phosphates. Apart from this, the existence of the very prominent family of tetravalent *NASICON* type transition metal phosphates $A^{I}M^{IV}_2(PO_4)_3$ (see Table 11.1) nourished our interest to search for polynary rhenium(IV) phosphates. Furthermore, vanadates like $M^{IV}V_2O_7$ (M^{IV} = Zr [191], Hf [192], W [193] etc.) attracted us to search for "$Re^{IV}V_2O_7$".

In the present work, two new polynary rhenium(IV) phosphates, $NaRe^{IV}_2(PO_4)_3$ and $Re^{IV}_3[Si_2O(PO_4)_6]$ and a rhenium-vanadium oxide, $(Re_{0.17}V_{0.83})O_2$, have been synthesized and structurally characterized. The electronic absorption spectra of tetravalent rhenium phosphates will be discussed.

Table 11.1 Crystallographic information on different members of *NASICON* structure of type $A^{I}M^{IV}_{2}(PO_4)_3$, (A^{I} = Li, Na, K, Rb, Cs, Cu; M^{IV} = Ti, Ge, Zr, Nb, Mo, Sn, Re, U).

compounds	symmetry	*a* / Å	*c* / Å	*c* / *a*	refinement[a)]	references
$LiTi_2(PO_4)_3$	$R\bar{3}c$	8.5110(1)	20.843(4)	2.45	NPD	[194]
$NaTi_2(PO_4)_3$	$R\bar{3}c$	8.502(5)	21.833(9)	2.57	XRSC	[195]
$KTi_2(PO_4)_3$	$R\bar{3}c$	8.367(1)	23.074(3)	2.75	XRSC	[196]
$RbTi_2(PO_4)_3$	$R\bar{3}c$	8.2896(8)	23.530(4)	2.84	XRSC	[197]
$RbTi_2(PO_4)_3$[b)]	$R3$	7.9200(8)	23.373(1)	2.95	XRSC	[198]
$CuTi_2(PO_4)_3$	$R\bar{3}c$	8.523(2)	21.303(4)	2.50	XRSC	[199]
$LiGe_2(PO_4)_3$	$R\bar{3}c$	8.275(5)	20.47(3)	2.47	XRSC	[200]
$KGe_2(PO_4)_3$	$R\bar{3}$	8.0066(7)	22.566(4)	2.82	XRPD	[201]
$NaGeTi(PO_4)_3$	$R\bar{3}$	8.3058(5)	21.696(1)	2.61	XRPD	[202]
$LiZr_2(PO_4)_3$	$R\bar{3}c$	8.847(1)	22.24(3)	2.52	XRSC	[203]
$NaZr_2(PO_4)_3$	$R\bar{3}c$	8.813(3)	22.800(10)	2.59	XRSC	[204]
$KZr_2(PO_4)_3$	$R\bar{3}c$	8.367(1)	23.074(3)	2.75	XRSC	[196]
$CsZr_2(PO_4)_3$	$R\bar{3}c$	8.5758(2)	24.9061(4)	2.90	XRPD	[205]
$CuZr_2(PO_4)_3$	$R\bar{3}c$	8.9018(2)	22.2021(6)	2.49	XRPD	[206]
$\square Nb_2(PO_4)_3$[c)]	$R\bar{3}c$	8.6974(7)	22.123(2)	2.54	XRSC	[207]
$NaMo_2(PO_4)_3$	$R\bar{3}c$	8.6160(7)	22.075(3)	2.56	XRSC	[208]
$NaSn_2(PO_4)_3$	$R\bar{3}$	8.51324(8)	22.5106(3)	2.64	NPD	[209]
$CuSn_2(PO_4)_3$	$R\bar{3}c$	8.588(5)	21.960(30)	2.55	XRPD	[210]
$NaRe_2(PO_4)_3$	$R\bar{3}$	8.4631(9)	22.347(5)	2.64	XRSC	[this work]
$KU_2(PO_4)_3$	$R\bar{3}c$	9.113(1)	24.997(1)	2.73	XRPD	[211]

[a)] NPD: Neutron powder diffraction
XRPD: X-ray powder diffraction
XRSC: X-ray single-crystal
[b)] synthesized at high pressure
[c)] $\square$ indicates a void instead of a A^{I} cation.

11.2 Syntheses and Crystallization of Rhenium(IV) phosphates

ReP_2O_7. Greenish yellow microcrystalline powders of ReP_2O_7 were synthesized isothermally from stoichiometric mixtures of Re_2O_7 (ABCR, 99.99%), red phosphorus (Knapsack Electronic), and P_4O_{10} (KMF Laborchemie, 97%) according to equation 11.1. The reactants were placed in evacuated sealed silica tubes ($l \approx 11$ cm, $d \approx 1.5$ cm, $V \approx 20$ cm^3) and heated stepwise at 400 and 700°C for 2 and 4 days, respectively. A mixture of Re_2O_7 and elemental phosphorus according to equation 11.2, leads under aforementioned experimental conditions to a mixture of ReP_2O_7 and metallic rhenium.

$$10\ Re_2O_7 + 12\ P + 7\ P_4O_{10} \rightarrow 20\ ReP_2O_7 \qquad (11.1)$$

$$Re_2O_7 + 2\ P \rightarrow ReP_2O_7 + Re \qquad (11.2)$$

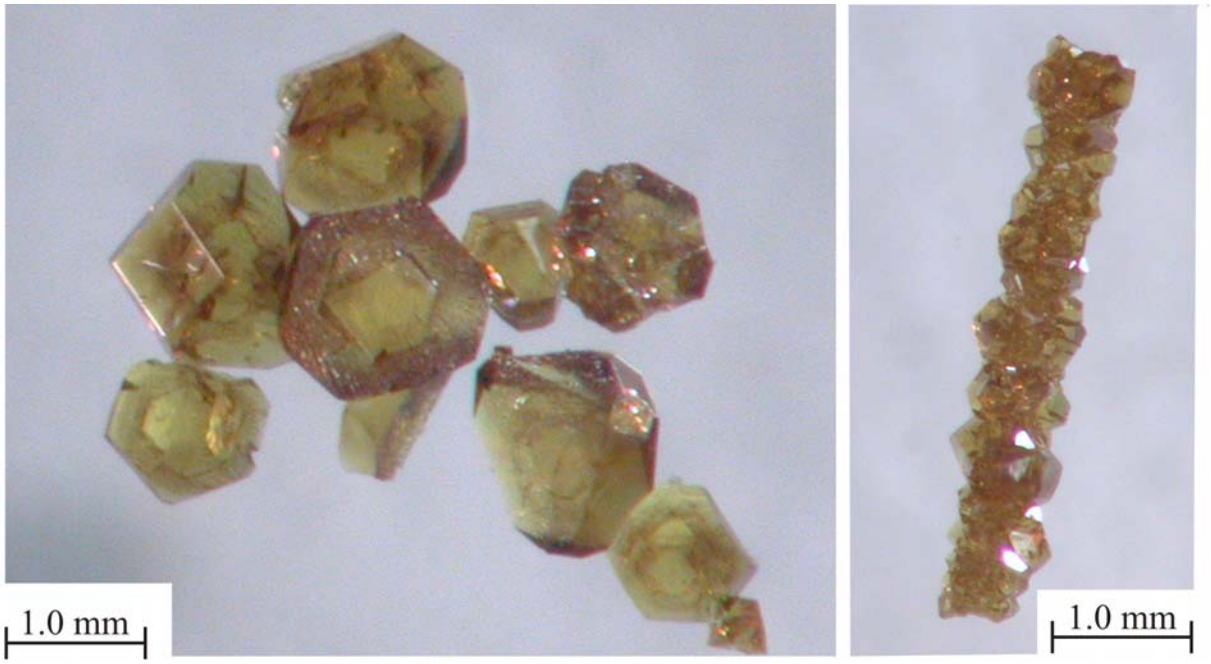

Figure 11.1 Crystals of ReP_2O_7 obtained by CVT.

Yellow-orange crystals of ReP_2O_7 were obtained by chemical vapour transport using iodine or platinum chloride as transport agent. Microcrystalline ReP_2O_7 was heated in a temperature gradient 900 → 800°C for about seven days in an evacuated sealed silica tube ($l \approx 11$ cm, $d \approx 1.5$ cm, $V \approx 20$ cm^3). This procedure led to the formation of icosahedrally shaped crystals of ReP_2O_7 up to 2.0 mm in diameter (Figure 11.1) at the sink end of the ampoule. Details on thermal behaviour and chemical vapour transport of ReP_2O_7 are described in section 11.3.

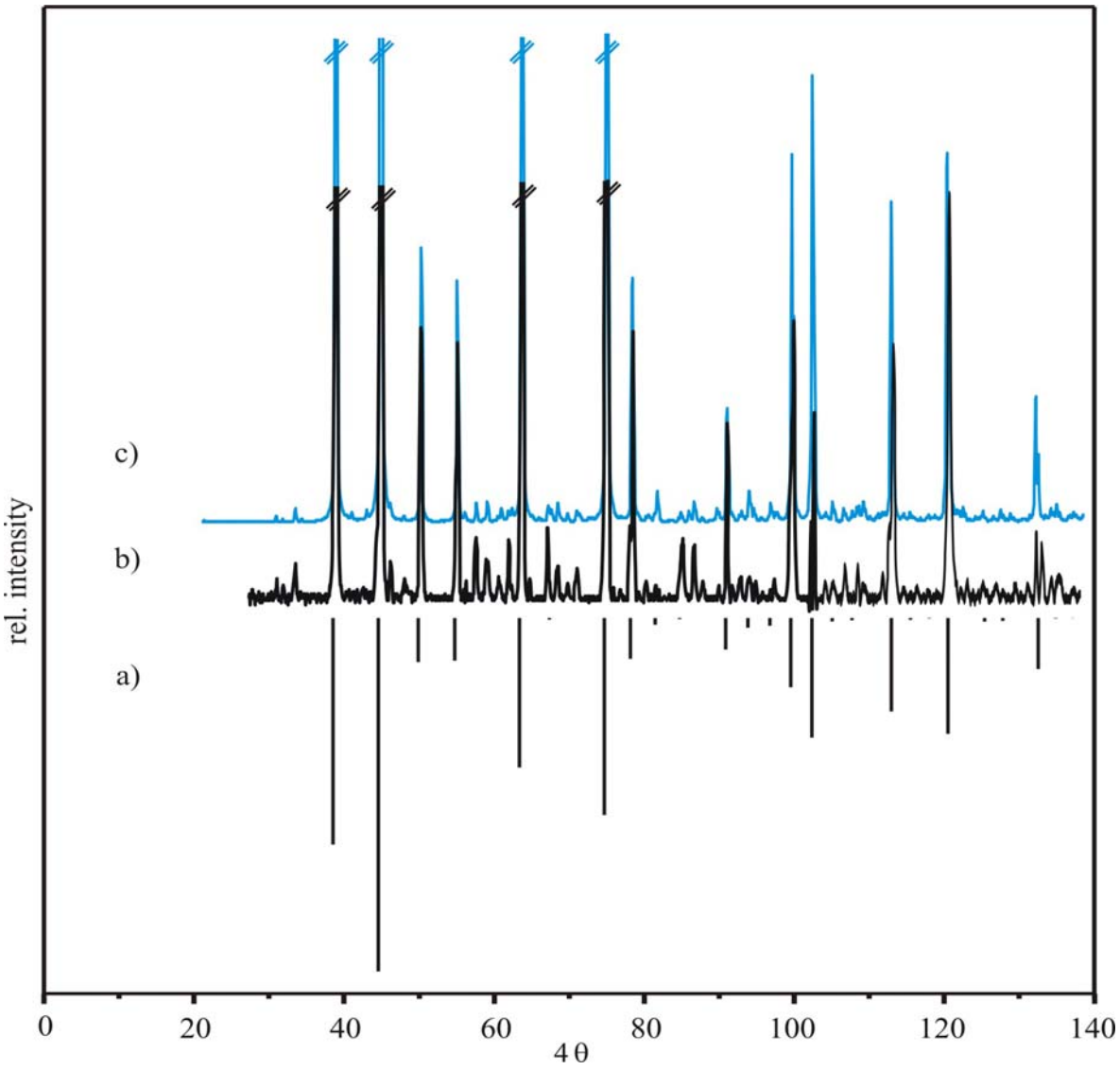

Figure 11.2 Comparison of the simulation (a) and Guinier photograph (b, magnified) of the selected crystals of ReP_2O_7, parameters used from the subcell of ReP_2O_7 [83]. Magnification of a section of the simulation of the superstructure of HfP_2O_7 (c) [140]. Unassigned lines in the Guinier photograph of ReP_2O_7 (b) are assumed as superstructure reflections.

$NaRe^{IV}_2(PO_4)_3$. Syntheses and crystallization of $NaRe^{IV}_2(PO_4)_3$ were achieved by isothermal heating as well as by chemical vapour transport. $NaRe^{IV}_2(PO_4)_3$ was synthesized isothermally from a mixture of ReO_3, P_4O_{10} (KMF Laborchemie, 97%) and NaI (Applichem, 99%) either by using red phosphorus or by metallic rhenium as reducing agent according to equations 11.3 and 11.4.

$$10\ ReO_3 + 3\ P + 3\ P_4O_{10} + 5\ NaI \rightarrow 5\ NaRe_2(PO_4)_3 + 5/2\ I_2 \qquad (11.3)$$

$$6\ ReO_3 + 2\ Re + 3\ P_4O_{10} + 4\ NaI \rightarrow 4\ NaRe_2(PO_4)_3 + 2\ I_2 \qquad (11.4)$$

The mixtures of the reactants were transferred into evacuated sealed silica tubes ($l \approx 11$ cm, $d \approx 1.5$ cm, $V \approx 20$ cm^3) with subsequent stepwise isothermal heating at 200, 400, and 800°C for 2, 2, and 6 days, respectively. Iodine was used as a mineralizer, obtained from the oxidation of NaI. Nicely grown cube shaped red crystals of $NaRe^{IV}_2(PO_4)_3$ upto 1 mm edge lengths were obtained together with a large amount of ReO_2. In order to get a single phase product a surplus of P_4O_{10} (20% to 35%) from the stoichiometric mixture of ReO_3, red phosphorus, and NaI was heated according to aforementioned conditions. This surplus of P_4O_{10} did not lead single phase of $NaRe^{IV}_2(PO_4)_3$. However, only a tiny amount of ReO_2 was observed under this condition.

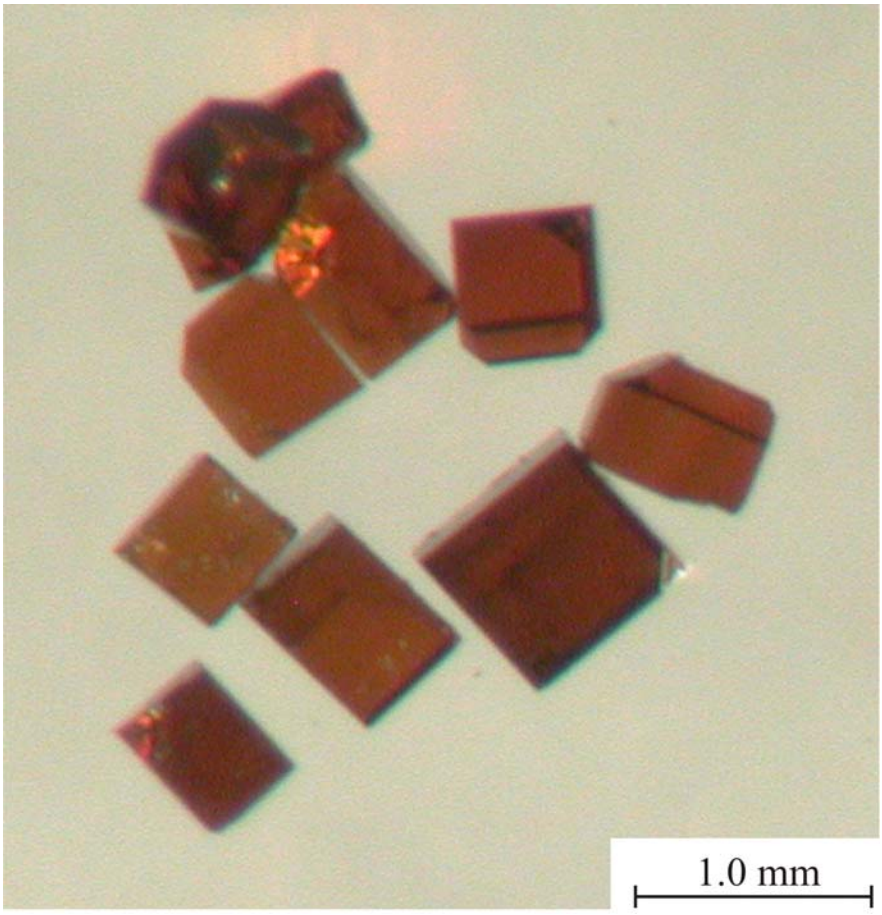

Figure 11.3 Crystals of $NaRe_2(PO_4)_3$ obtained by CVT.

$NaRe^{IV}_2(PO_4)_3$ was also synthesized from a stoichiometric mixture of Re_2O_7 (ABCR, 99.99%), red phosphorus, P_4O_{10} (KMF Laborchemie, 97%), and $NaPO_3$ (see Equation 11.5). The reactants were heated isothermally in sealed evacuated silica tubes at 200, 400, and 800°C for 2, 2, and 4 days, respectively. Red crystals identified as $NaRe^{IV}_2(PO_4)_3$,

intermingled with large amounts of a dark powder of ReO_2. Re_2O_7 and P_4O_{10} were handled in a glove bag in argon atmosphere since both compounds are hygroscopic.

$$8\ Re_2O_7 + 12\ Re + 7\ P_4O_{10} + 14\ NaPO_3 \rightarrow 14\ NaRe_2(PO_4)_3 \qquad (11.5)$$

Rectangular or cubic shaped reddish crystals of $NaRe_2(PO_4)_3$ (see Figures 11.3, 11.4) were obtained by chemical vapour transport when a previously obtained mixture of $NaRe_2(PO_4)_3$ and ReO_2 was heated in a temperature gradient of 850 →700°C for 7 days in sealed evacuated silica tubes ($l \approx 11$ cm, $d \approx 1.5$ cm, $V \approx 20$ cm^3). Iodine was used as a transport agent. Further details on syntheses and crystallization are summarized in table 11.2.

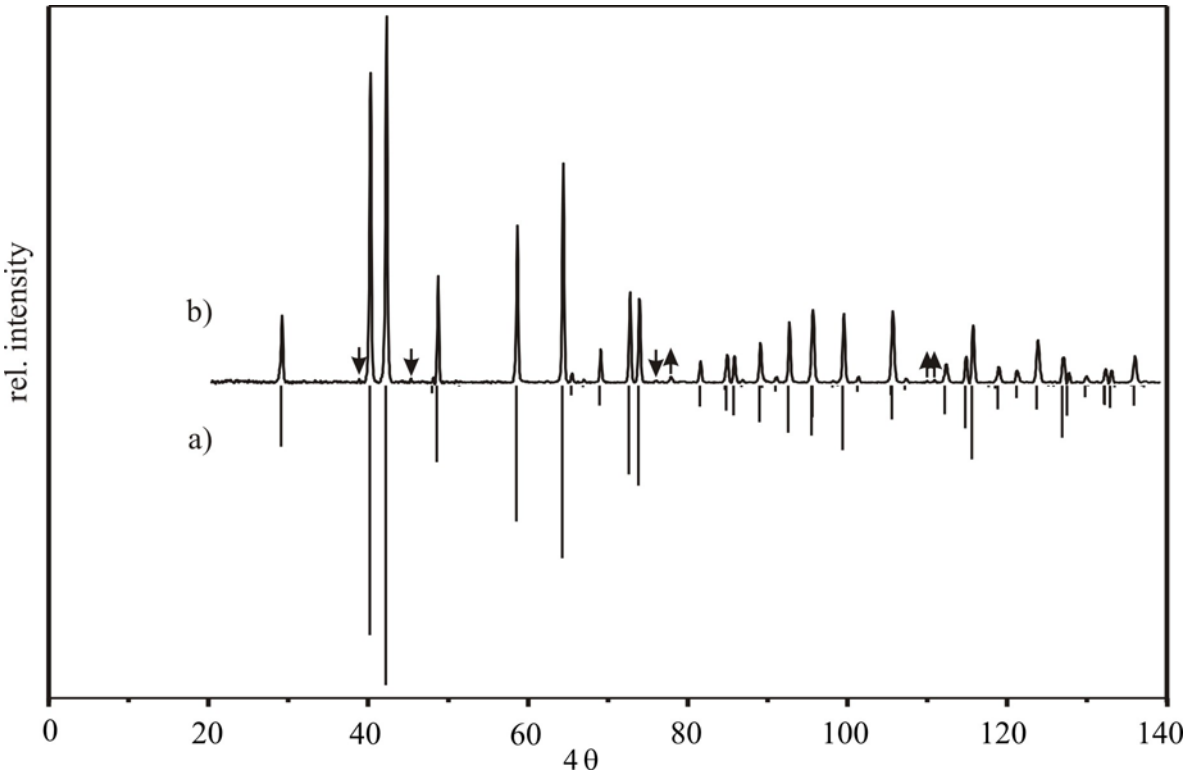

Figure 11.4 Comparison of the simulation (a) and Guinier photograph (b) of $NaRe_2(PO_4)_3$. Parameters for the simulation were obtained from XRSC refinement from this work (see Section 11.4). Downward arrows point to reflections of ReP_2O_7. Reflections indicated by upward arrows are not assigned.

Table 11.2 Experiments for synthesis and crystallization of $NaRe^{IV}_2(PO_4)_3$.

starting solids / mg		I_2 / mg	temperatures[a] / °C	time / d	products (source) (according to *IP* Guinier photographs)	products (sink)
ReO_3	96.8	25[b]	400	2		
P	3.8		850	6	$NaRe_2(PO_4)_3$,	---
P_4O_{10}	35.0				ReP_2O_7 (-), ReO_2(-)[c]	
NaI	30.1					
ReO_3	135.2	36[b]	200	2		
P	5.5		400	2		
P_4O_{10}	75.6		800	6	$NaRe_2(PO_4)_3$, ReO_2 (--)[d]	----
NaI	43.3					
ReO_3	138.2	37[b]	200	2		
P	5.4		400	2		
P_4O_{10}	62.2		800	6	$NaRe_2(PO_4)_3$, ReO_2 (--)	----
NaI	43.8					
ReO_3	94.2	34[b]	250	2		
Re	74.9		400	2		
P_4O_{10}	57.0		800	6	ReO_2, Re (-),	----
NaI	40.2				$NaRe_2(PO_4)_3$ (-)	
Re_2O_7	82.8	---	250	2		
Re	47.8		400	2		
P_4O_{10}	42.5		800	6	$NaRe_2(PO_4)_3$, ReO_2 (--)	----
$NaPO_3$	30.5				ReP_2O_7 (--)	
{$NaRe_2(PO_4)_3$ +		72	400	4		
ReO_2(--)}	117.0		850→700	4	ReO_2	$NaRe_2(PO_4)_3$, ReP_2O_7 (-)
{$NaRe_2(PO_4)_3$ +		50	850→700	7	ReO_2	$NaRe_2(PO_4)_3$[e], ReP_2O_7(-)
ReO_2(--)}	112.0					

a) given are the various heating periods for an ampoule at different temperature. Starting solid always resided at the temperature at the left side of the arrow. Solid reaction products were characterized by their XRPD pattern after the final heating period, only.
b) calculated amounts of iodine by complete oxidation of NaI to I_2.
c) (-) minor compound.
d) (--) a trace of compound.
e) crystals selected for X-ray single-crystal investigation.

$Re^{IV}_3[Si_2O(PO_4)_6]$. Rhenium(IV) silicophosphate, $Re^{IV}_3[Si_2O(PO_4)_6]$, was synthesized by vapour phase mediated solid state reaction using iodine as mineralizer. Orange-yellow crystals of $Re^{IV}_3[Si_2O(PO_4)_6]$ (see Figure 11.5) were obtained when a mixture of Re_2O_7 (289.3 mg, 0.597 mmol), elemental phosphorus (14.6 mg, 0.477 mmol) and P_4O_{10} (49.0 mg, 0.173 mmol) was heated in a temperature gradient aiming for the synthesis of $RePO_5$ (700 → 600 °C and 700 → 550 °C, for 11 and 5 days respectively; evacuated sealed silica tube, $l \approx 11$ cm, $d \approx 1.5$ cm, $V \approx 20$ cm^3). SiO_2 entered into the system from the wall of the silica tube. Triangular and rectangular plate like crystals of $Re^{IV}_3[Si_2O(PO_4)_6]$ up to 1.0 mm in length were obtained in the sink region along with ReP_2O_7 and an unknown phase (see Figure 11.6). About 17 mg of iodine were used as a mineralizer.

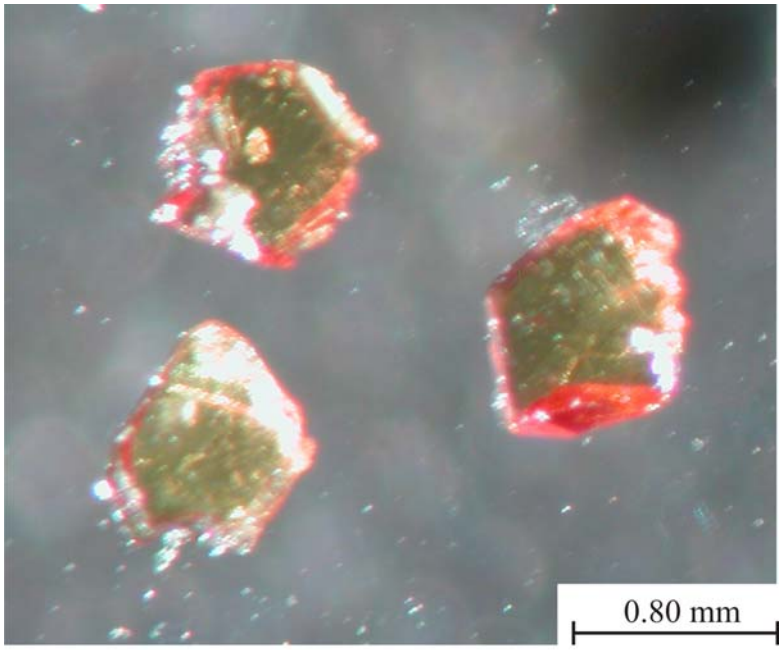

Figure 11.5 Photograph of the crystals of $Re_3[Si_2O(PO_4)_6]$.

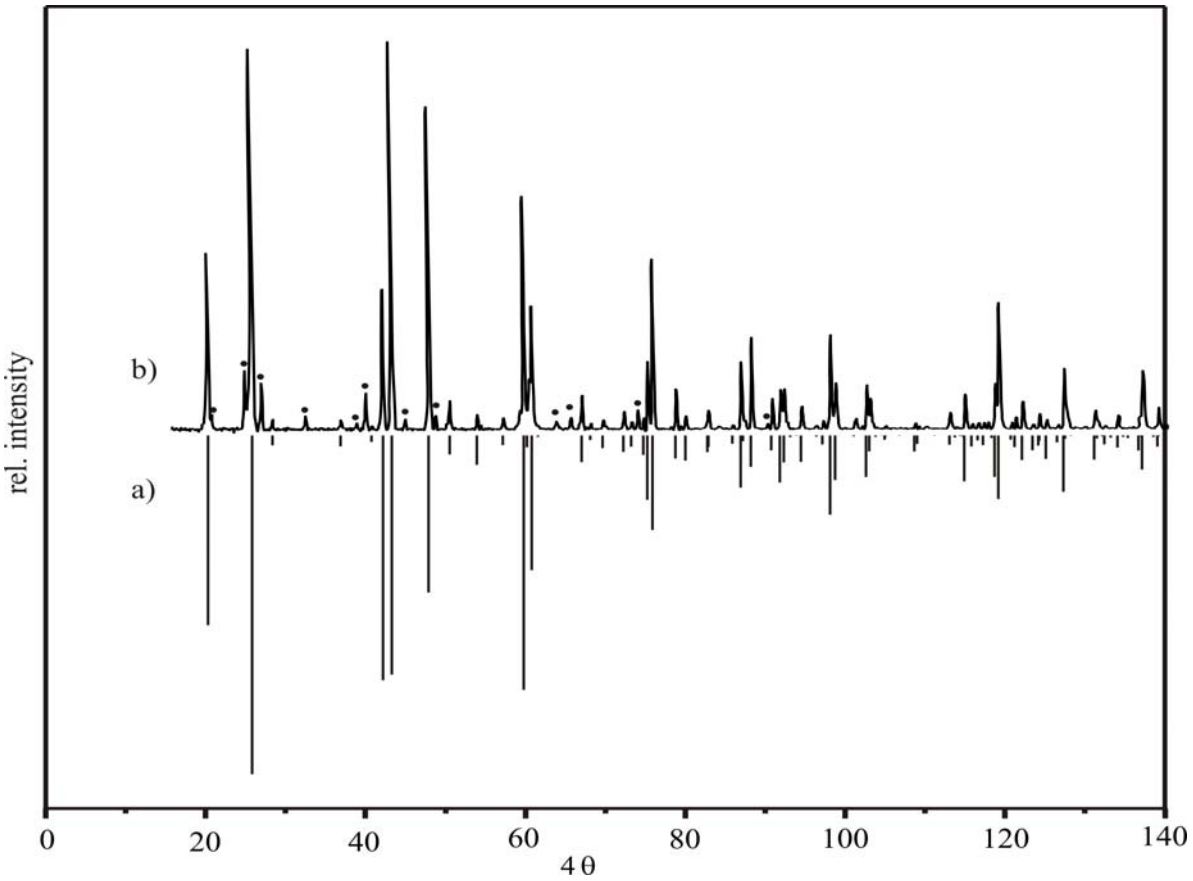

Figure 11.6 Comparison of the simulation (a) and Guinier photograph (b) of $Re_3[Si_2O(PO_4)_6]$; data from single-crystal study (this work). Unassigned reflections are marked by black circles.

Attempts to synthesize $Re^{IV}_3[Si_2O(PO_4)_6]$ by heating stoichiometric mixtures of ReO_3, SiO_2 (reactive silica), P and P_4O_{10} at 600 → 500°C and 700 → 550°C for 7 and 11 days, respectively, failed. They led to formation of ReO_3 and ReP_2O_7 at the source region, wheareas the sink contained only ReP_2O_7. According to various observations [2] prolonged heating of transition metal phosphate in presence of NH_4Cl in a closed silica tube frequently leads to the formation of silicophosphates. Despite the attack of silica tube, inseatd of $Re^{IV}_3[Si_2O(PO_4)_6]$, our experiment formed ReO_2 and ReP_2O_7 under similar condition.

Re_2O_7 and P_4O_{10} were handled in a glove bag in argon atmosphere since both compounds are hygroscopic. The starting materials were at least of p.a. grade.

$(Re_{0.17}{}^{IV}V_{0.83})O_2$. Black crystals of $(Re_{0.17}{}^{IV}V_{0.83})O_2$ upto 1.0 mm in length were synthesized and crystallized by chemical vapour transport. Well shaped black rectangular crystals of $(Re_{0.17}{}^{IV}V_{0.83})O_2$ were obtained when a pellet ($12\times2\times2$ mm^3) of a stoichiometric mixture of ReO_2 and V_2O_5 aiming for "ReV_2O_7" was heated in a sealed silica tube ($l \approx 11$ cm, $d \approx 1.5$ cm, $V \approx 20$ cm^3) in a temperature gradient 700 → 600°C for four days. About 40 mg iodine were used as transport agent. The pellet was prepared with the help of a hydraulic press by applying a pressure of ~25 kN for about 20 minutes.

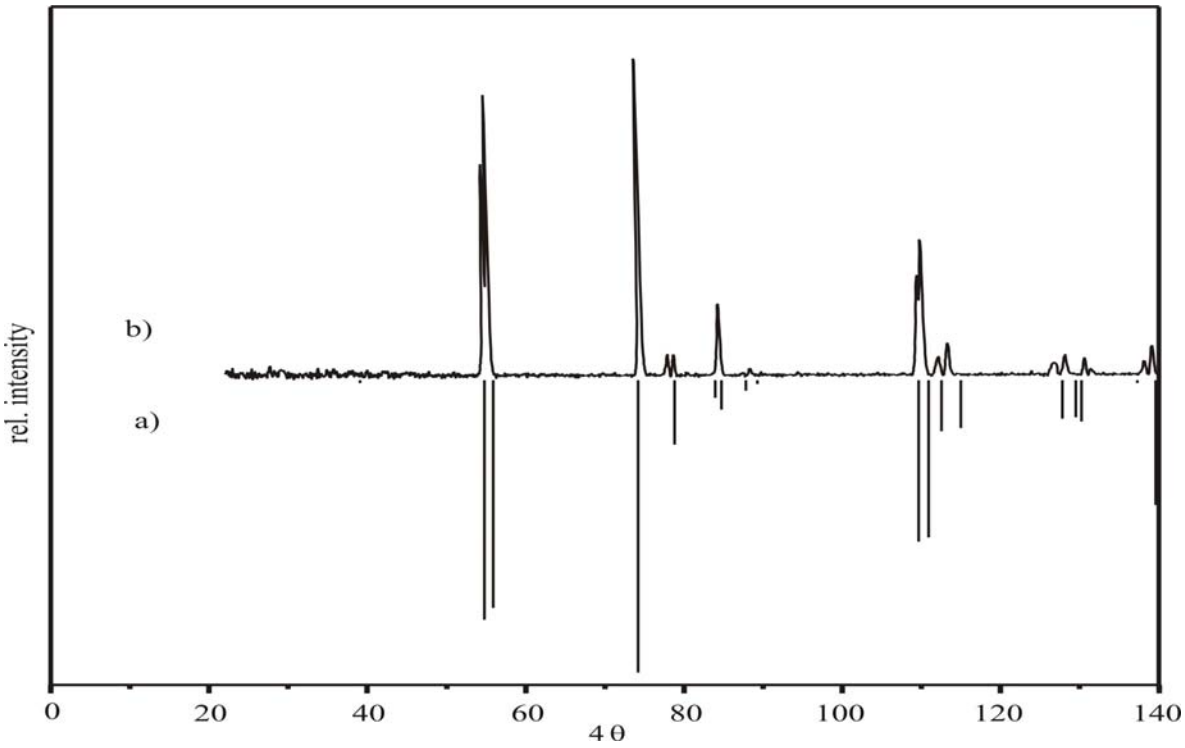

Figure 11.7 Comparison of Guinier photograph (b) and simulation (a) of $(Re_{0.17}{}^{IV}V_{0.83})O_2$ (data according to X-ray single crystal study; this work; isotypic to monoclinic VO_2 [212])

11.3 Thermal Behaviour and Chemical Vapour Transport of Rhenium(IV) phosphates

Various experimental results show that ReP_2O_7 exists up to T = 850°C in sealed ampoule. This observation points to the large stability of Re^{4+} in the diphosphate. Prolonged heating of ReP_2O_7 above 850°C in sealed evacuated silica tube leads to decomposition into ReO_2 and gaseous P_4O_{10} (Equation 11.6), while the ultimate decomposition products are metallic rhenium and gaseous P_4O_{10} (Equation 11.7) at about 1000°C. Thus both the thermal decomposition and thermal reduction of ReP_2O_7 occur within 850 to 1000°C. In contrast to rhenium pyrophosphate, thermal decomposition of $Zr^{IV}P_2O_7$ [213] leads to the formation of $Zr^{IV}{}_2O(PO_4)_2$ and gaseous P_4O_{10} (Equation 11.8) at about 1250°C.

$$ReP_2O_7(s) \rightarrow ReO_2(s) + ½\ P_4O_{10}(g) \qquad \vartheta \geq 850°C \qquad (11.6)$$

$$ReP_2O_7(s) \rightarrow Re(s) + ½\ P_4O_{10}(g) + O_2(g) \qquad \vartheta \geq 1000°C \qquad (11.7)$$

$$4\ ZrP_2O_7(s) \rightarrow 2\ Zr_2O(PO_4)_2(s) + P_4O_{10}(g) \qquad \vartheta \geq 1250°C \qquad (11.8)$$

Sodium rhenium(IV) phosphate, $NaRe_2(PO_4)_3$, was synthesized and crystallized within the temperature range 700 to 850°C. The synthesis of this phosphate can be achieved from different starting solids (see Reactions 11.3 to 11.5). The easy access to this compound points to its large stability. In addition, the coexistence and the thermal stability of $NaRe_2(PO_4)_3$ and ReP_2O_7 at 850°C express the comparable thermal behaviour of these two phosphates.

Due to the high volatility of $ReO_3X(g)$ (X = I, Cl) and $P_4O_{10}(g)$, the method chemical vapour transport (CVT) [85] works nicely for the crystallization of the pyrophosphate (see Equation 11.9). Migration of the phosphate proceeds from higher to lower temperature ($T_2 \rightarrow T_1$, $T_2 > T_1$, $\Delta T \approx 100$ K) due to endothermic reactions. The formation of $NaRe_2(PO_4)_3$ along with ReP_2O_7 in the sink of the silica tube was also achieved by chemical vapour transport at 850 → 700°C for about 7 days. Iodine was used as transport agent. Phosphorus forms various volatile oxides P_4O_n, $6 \leq n \leq 10$, $PO_2(g)$ and $PO(g)$. Among them $P_4O_{10}(g)$ seems to be the most important species for the transport of phosphorus due to its distinct thermodynamic stability [134] under the given conditions. In addition to this, the stability of $ReO_3X(g)$ ($X = I^-, Cl^-, OH^-$) has already been mentioned by SCHÄFER [84]. Therefore, CVT of ReP_2O_7 proceeds according to equation 11.9. On the other hand, migration of sodium may occur via the formation of NaI(g) along with $ReO_3I(g)$, $P_4O_{10}(g)$, and $O_2(g)$. This leads to the formation of $NaRe_2(PO_4)_3$ (see Equation11.10) in the sink side of the ampoule.

$$ReP_2O_7(s) + X_2(g) + ½\ O_2(g) = ReO_3X(g) + ½\ P_4O_{10}(g),\ (X = I^-, Cl^-, OH^-) \quad (11.9)$$

$$4\ NaRe_2(PO_4)_3(s) + 6\ I_2(g) + 3\ O_2(g) =$$
$$4\ NaI(g) + 8\ ReO_3I(g) + 3\ P_4O_{10}(g) \quad (11.10)$$

Synthesis of anhydrous transition metal phosphates in sealed silica tubes is frequently accompanied by formation of silicophosphates [2, 214, 215]. $SiO_2(s)$ is mobilized from the wall of the silica ampoule. The formation of $Re_3[Si_2O(PO_4)_6]$ is an another example for this general observation. While synthesis and crystallization of other rhenium(IV) phosphates like ReP_2O_7 and $NaRe_2(PO_4)_3$ can be easily achieved, synthesis of single-phase $Re_3[Si_2O(PO_4)_6]$ turned out to be rather difficult.

11.4 X-ray Investigations

Energy-dispersive X-ray fluorescence analyses [116, 117, 118] (EDX system, scanning microscope DMS 940, Zeiss) of $NaRe^{IV}_2(PO_4)_3$, $Re^{IV}_3[Si_2O(PO_4)_6]$, and $(Re_{0.17}{}^{IV}V_{0.83})O_2$ showed the presence of the respective elements. Experimentally obtained compositional details of the aforementioned compounds are given in table 11.3-11.6.

Table 11.3 EDX analyses of the different crystals of ReP_2O_7.

ReP_2O_7	**Re [%]**	**P [%]**	**O [%]**
crystal 1	11.10	29.88	59.02
crystal 2	16.85	41.38	41.77
crystal 3	8.97	25.16	65.87
average	**12.31**	**32.14**	**55.55**
theoretical	**10**	**20**	**70**

Table 11.4 Results of the EDX analyses from different crystals of $NaRe_2(PO_4)_3$.

$NaRe^{VI}_2(PO_4)_3$	**Na [%]**	**Re [%]**	**P [%]**	**O [%]**
crystal 1	5.76	12.96	22.97	58.0
crystal 2	5.74	13.90	23.91	56.45
crystal 3	6.14	12.88	23.51	57.47
average	**5.94**	**13.25**	**23.46**	**56.96**
theoretical	**5.56**	**11.12**	**16.67**	**66.67**

Table 11.5 Results of the EDX analyses in (%) from different crystals of $Re^{IV}_3[Si_2O(PO_4)_6]$.

$Re^{IV}_3[Si_2O(PO_4)_6]$	**Re [%]**	**Si [%]**	**P [%]**	**O [%]**
crystal 1	6.72	4.79	13.64	74.85
crystal 2	7.87	5.54	13.05	73.54
crystal 3	8.25	5.69	14.0	72.06
crystal 4	6.51	4.64	11.55	77.30
crystal 5	7.48	5.20	12.35	77.98
crystal 6	7.03	4.82	12.43	75.75
average	**7.3**	**5.1**	**12.84**	**75.24**
theoretical	**8.33**	**5.56**	**16.66**	**69.44**

Table 11.6 Results of the EDX analyses from different crystals of $(Re_{0.17}{}^{IV}V_{0.83})O_2$[a)].

$(Re_{0.17}{}^{IV}V_{0.83})O_2$	**Re [%]**	**V [%]**	**O [%]**
crystal 1	4.49	31.90	63.64
crystal 2	3.70	22.19	74.17

crystal 3	5.22	39.0	55.78
average	**4.47**	**31.03**	**64.53**
theoretical	**5.66**	**27.67**	**66.67**

[a)] composition based on X-ray single-crystal structure refinement.

For the identification and examination of the purity of the obtained solids image-plate (*IP*) Guinier-photographs were taken (Chap. 9, Sec. 9.3). The assignement of the cell parameters of **ReP_2O_7** was made from 13 reflections in the angular range of $9.7 \leq \theta \leq 30.49°$ which led *a* = 7.8859(8) Å. For this assignement *hkl* values were obtained from subcell of ReP_2O_7 [83]. Twenty eight reflections in the range of $7.2 \leq \theta \leq 31.8°$ for powder pattern of **$NaRe_2(PO_4)_3$** were assigned. The obtained cell parameters were *a* = 8.4631(9) Å and *c* = 22.347(5) Å. This result is in agreement with the X-ray single crystal analysis. The assignment of the cell parameters of **$Re^{IV}_3[Si_2O(PO_4)_6]$** was carried out by using 34 reflections in the range $5.02 \leq \theta \leq 31.91°$ and led to *a* = 8.191(2) and *c* = 26.065(9) Å. A reasonable fit of the position of the reflections in the simulation and the Guinier powder diffraction pattern was not obtained for **$(Re_{0.17}{}^{IV}V_{0.83})O_2$** at higher diffraction angles (see Figure 11.7). Therefore, the assignment of the cell parameters exhibits large standard deviations. Consequently, for the final refinement the cell parameters obtained from X-ray single-crystal investigation were used.

X-ray single-crystal intensity data for $NaRe_2(PO_4)_3$, $Re_3[Si_2O(PO_4)_6]$ and $(Re_{0.17}V_{0.83})O_2$ have been measured on a κ-CCD diffractometer at ambient temperature. Structure determination and refinement were performed using the SHELX-97 [105] suite in the WinGx [135] framework.

In order to collect X-ray single-crystal intensity data, a very small crystal of **$NaRe_2(PO_4)_3$** ($0.09 \times 0.07 \times 0.05$ mm^3) was mounted on a glass fibre under a polarized microscope. A full sphere in the range of $2.92 \leq \theta \leq 35.04°$ was measured (1368 independent reflections from 19661). On the basis of systematic absences and intensity distributions the space group $R\bar{3}$ was derived. *E* statistics E^2-1 = 0.644, however, did not support this result and suggested a non-centrosymmetric crystal structure. Direct Methods in SHELXS [137] failed to produce a refinable starting model (even for the rhenium atoms). Therefore, starting positional parameters were taken from the isotypic $KGe_2(PO_4)_3$, ($R\bar{3}$, *a* = 8.0066(7)Å, *c* = 22.566(4)Å) [201] which led to a refinement with R_1 = 0.067, wR_2 = 0.1667, residual electron density of 5.61 (close to O2) and -7.34 Å^{-3} (close to Re2). Allowing for a two-fold axis along [1 1 0] as twin element 0 1 0 1 0 0 0 0 $\bar{1}$ gave an immediate improvement in the refinement of the crystal structure. It led to R_1 = 0.019, wR_2 = 0.049, and maximum / minimum residual electron densities of 2.12 (close to Na2) and -2.82 Å^{-3} (close to Re1). Due to the high absorption

coeffient, μ = 26.809 mm^{-1}, an empirical absorption correction with multi-scans [115] was applied and eventually the structure refinement converged at R_1 = 0.015, wR_2 = 0.033, and thus the residual electron density dropped to 1.55 (close to Re2) and -1.27 Å^{-3} (close to Re1).

For data collection, a yellow prismatic crystal of **$Re_3[Si_2O(PO_4)_6]$** with dimensions 0.05 × 0.04 × 0.01 mm^3 was used. A full sphere in the range 2.98 ≤ θ ≤ 35.06° was measured (from 11479 reflections 1482 were independent). On the basis of systematic absences and intensity distributions the space group $R\bar{3}$ was derived. Starting parameters for the single crystal structure refinement were obtained by Direct Methods in SHELXS [137]. Thus rhenium, silicon and phosphorus positions were revealed. Subsequent Δ-Fourier syntheses allowed the localization of the oxygen atoms. An empirical absoprtion correction with multi-scan [115] was applied. The anisotropic displacement parameters of O1 (the bridging oxygen of two silicon atoms) showed a very large displacement only along the Si-O-Si axis. Therefore, final refinement was carried out leaving O1 isotropically. Despite the reasonable bond-lengths and angles, the structure refinement converged rather high residuals R_1 = 0.059, wR_2 = 0.157 and residual electron densities of 19.25 Å^{-3} (close to O1) and -3.37 Å^{-3} (close to Re2). These higher residuals might related either to the poor quality of the X-ray single crystal data set or to the twining problem. A combination of the two can not be completey ruled out. Attempts to refine the crystal structure by using the lower symmetry space group $R3$, $P3_1$ and $P3$ failed.

For the data collection, a rectangular black crystal of **$(Re_{0.17}{}^{IV}V_{0.83})O_2$** with dimensions 0.05 × 0.04 × 0.01 mm^3 was used. The full sphere in the range 0.998 ≤ θ ≤ 40.25° was measured (from 2240 reflections 371 were independent). On the basis of systematic absences and intensity statistics the space group $P2/m$ was derived. Starting parameters for the single crystal structure refinement were obtained by Direct Methods in SHELXS [137]. Thus the metals positions were revealed. Subsequent Δ-Fourier syntheses allowed the localization of the oxygen atoms. The restraints EXYZ and EADP were used for mixed occupancy of vanadium and rhenium. The introduction of the twin law $\bar{1}\ 0\ 0\quad 0\ \bar{1}\ 0\quad 0\ 0\ 1$ avoided non positive definitive displacement parameters for O1 as well as reduced the residuals from R_1 = 0.09 (wR_2 = 0.30) to R_1 = 0.065 (wR_2 = 0.17). An empirical absorption correction with multiscan [115] led to the final residual values R_1 = 0.044 (wR_2 = 0.122).

Details on crystal data, data collections as well as on the structure refinements are given in table 11.7. Atomic positions and isotropic displacement parameters are given in tables 11.8 to 11.10. Selected interatomic distances and angles are summarized in tables 11.12 and 11.13. Indexing of the Guinier photograph and anisotropic displacement parameters are given in Appendix B1 (Table B1.1.1-Table B1.1.3 and Table B1.2.1-Table B1.2.3).

Table 11.7 Details concerning data collection and structure refinement of $NaRe_2(PO_4)_3$, $Re_3[Si_2O(PO_4)_6]$ and $(Re_{0.17}V_{0.83})O_2$.

	$NaRe_2(PO_4)_3$	$Re_3[Si_2O(PO_4)_6]$	$(Re_{0.17}V_{0.83})O_2$
crystal data			
crystal system	trigonal	trigonal	monoclinic
space group	$R\bar{3}$ (No. 148)	$R\bar{3}$ (No. 148)	$P2/m$ (10)
a / Å	8.4631(9)	8.191(2)	4.5387(4)
b / Å			2.8385(4)
c / Å	22.347(5)	26.065(9)	4.5387(4)
β / °			91.13(1)
V / Å^3	1386.2(4)	1514.5(3)	58.46(1)
Z	6	3	2
μ / mm^{-1}	26.809	18.658	7.75
$D_{X\text{-ray}}$ / g·cm^{-3}	4.89	3.949	4.71
colour	reddish yellow	reddish yellow	black
crystal shape	rectangular	triangular	rectangular
size /mm^3	0.09×0.07×0.05	0.05×0.04×0.01	0.5×0.2× 0.1
MW / g·mol^{-1}	680.3	1200.60	165.8
F(000)	1812	1629	78
data collection			
Nonius κ-CCD diffractometer, Mo-Kα radiation, λ = 0.71073Å, graphite-monochromator			
temperature / K	293	293	293
scan range θ / °	$2.92 \le \theta \le 35.04$	$2.98 \le \theta \le 35.06$	$0.998 \le \theta \le 40.25$
	$-13 \le h \le 13$	$-13 \le h \le 12$	$-8 \le h \le 8$
	$-13 \le k \le 13$	$-13 \le k \le 13$	$-4 \le k \le 4$
	$-36 \le l \le 36$	$-42 \le l \le 42$	$-7 \le l \le 8$
absorption correction	multi-scans [115]	multi-scans [115]	multi-scans [115]
structure refinement			
software	SHELX97 [105]	SHELX97 [105]	SHELX97 [105]
measured reflections	19661	11479	2240
independent reflections	1368; 1355 with $\lvert F_o \rvert > 4\sigma(F_o)$	1482; 1134 with $\lvert F_o \rvert > 2\sigma(F_o)$	371, 334 with $\lvert Fo \rvert > 4\sigma(Fo)$
parameters; Goof	58; 1.24	58; 1.057	25, 1.06
residuals			
R_{int}	0.036	0.085	0.111
R_1[a)]	0.015	0.059	0.044
wR_2[b)]	0.032	0.168	0.122
BASF	0.534	---	0.619
extinction coefficient	0.00122(4)	0.000125	0.306
weighting scheme	A = 0.0057; B = 15.09	A = 0.1102; B = 0.0	A = 0.0853; B = 0
res. electron density			
$\Delta\rho_{max}$ / Å^{-3}	1.55 (close to Re2)	19.25 (close to O1)	2.6 (close to Re1)
$\Delta\rho_{min}$ / Å^{-3}	-1.27 (close to Re1)	-3.37 (close to Re2)	-2.7 (close to Re2)

a) $R_1 = \Sigma||F_o| - |F_c|| / |F_o|$, $F_o^2 \ge 2\sigma(F_o^2)$

b) $wR_2 = 1 / [\sigma^2(F_o^2) + (A \cdot P)^2 + B \cdot P]$; $P = (F_o^2 + 2F_c^2) / 3$

Table 11.8 Atomic co-ordinates and isotropic displacement parameters of $NaRe_2(PO_4)_3$.

atom	site	*x*	*y*	*z*	U_{eq} /Å$^{2\ a)}$
Na1	3*a*	0	0	0	0.0303(9)
Na2	3*b*	0	0	1/2	0.037(1)
Re1	6*c*	0	0	0.14392(1)	0.0058(0)
Re2	6*c*	0	0	0.64653(1)	0.0061(0)
P1	18*f*	0.2889(1)	0.0018(1)	0.25041(4)	0.0067(1)
O1	18*f*	0.0566(4)	-0.1597(4)	0.6956(1)	0.0162(5)
O2	18*f*	0.1749(3)	0.1874(3)	0.0868(1)	0.0099(4)
O3	18*f*	-0.1465(3)	-0.2088(4)	0.5907(1)	0.0128(4)
O4	18*f*	0.1926(4)	-0.0039(4)	0.1926(1)	0.0144(5)

a) $U_{eq} = (⅓)\Sigma_i\Sigma_j U_{ij} a_i^* a_j^* \mathbf{a}_i \cdot \mathbf{a}_j$

Table 11.9 Atomic co-ordinates and isotropic displacement parameters of $Re^{IV}_3[Si_2O(PO_4)_6]$.

atom	site	*x*	*y*	*z*	U_{eq} /Å$^{2\ a)}$
Re1	3*a*	0	0	0	0.0104(2)
Re2	6*c*	0	0	0.17932	0.0107(2)
Si1	6*c*	0	0	0.43900	0.0130(8)
P1	18*f*	0.28772	0.28617	0.09323	0.0114(4)
O1	3*b*	0	0	1/2	0.027(4)
O2	18*f*	0.14033	0.22961	0.13592	0.019(1)
O3	18*f*	0.20721	0.19129	0.04237	0.018(1)
O4	18*f*	0.36724	0.50053	0.08424	0.018(1)
O5	18*f*	0.44432	0.25201	0.10854	0.018(1)

a) $U_{eq} = (⅓)\Sigma_i\Sigma_j U_{ij} a_i^* a_j^* \mathbf{a_i} \cdot \mathbf{a_j}$

Table 11.10. Atomic co-ordinates and isotropic displacement parameters of $(V_{0.83}Re_{0.17})O_2$.

atom	site	*x*	*y*	*z*	sof	U_{eq} /Å$^{2\ a)}$
V1	1*a*	0	0	0	0.864(2)	0.0125(4)
Re1	1*a*	0	0	0	0.136(2)	0.0125(4)
V2	1*h*	½	½	½	0.800(2)	0.0126(3)
Re2	1*h*	½	½	½	0.200(2)	0.0126(3)
O1	2*n*	0.7967(5)	½	0.2028(5)	1	0.0098(6)
O2	2*m*	0.7022(5)	0	0.7026(5)	1	0.0102(6)

a) $U_{eq} = (⅓)\Sigma_i\Sigma_j U_{ij} a_i^* a_j^* \mathbf{a}_i \cdot \mathbf{a}_j$

11.5 Descriptions and Discussions of the Crystal structures

11.5.1 Rhenium(IV) pyrophosphate ReP_2O_7

In agreement to previous reports we found that ReP_2O_7 is isotypic to the cubic $M^{IV}P_2O_7$ (M^{IV} = Si [174], Ti [180], Zr [127], Mo [31], W [79], Hf [139], U [177], Ce [176]). Figure 11.8 represents the typical crystal structure of $M^{IV}P_2O_7$. The cubic structure of $M^{IV}P_2O_7$ can be derived from NaCl structure type. M^{4+} is the cation, and the anion is $P_2O_7^{4-}$ (discussed in detailed in Chap. 8, Sec 8.5). The ordered orientation of the $P_2O_7^{4-}$ group necessarily lowers the symmetry; the highest symmetry possible for the framework is $Pa\bar{3}$. In this ideal structure with $Z = 4$, the $[P_2O_7]$ group lies on a 3-fold axis where the bridging oxygen atom is on the

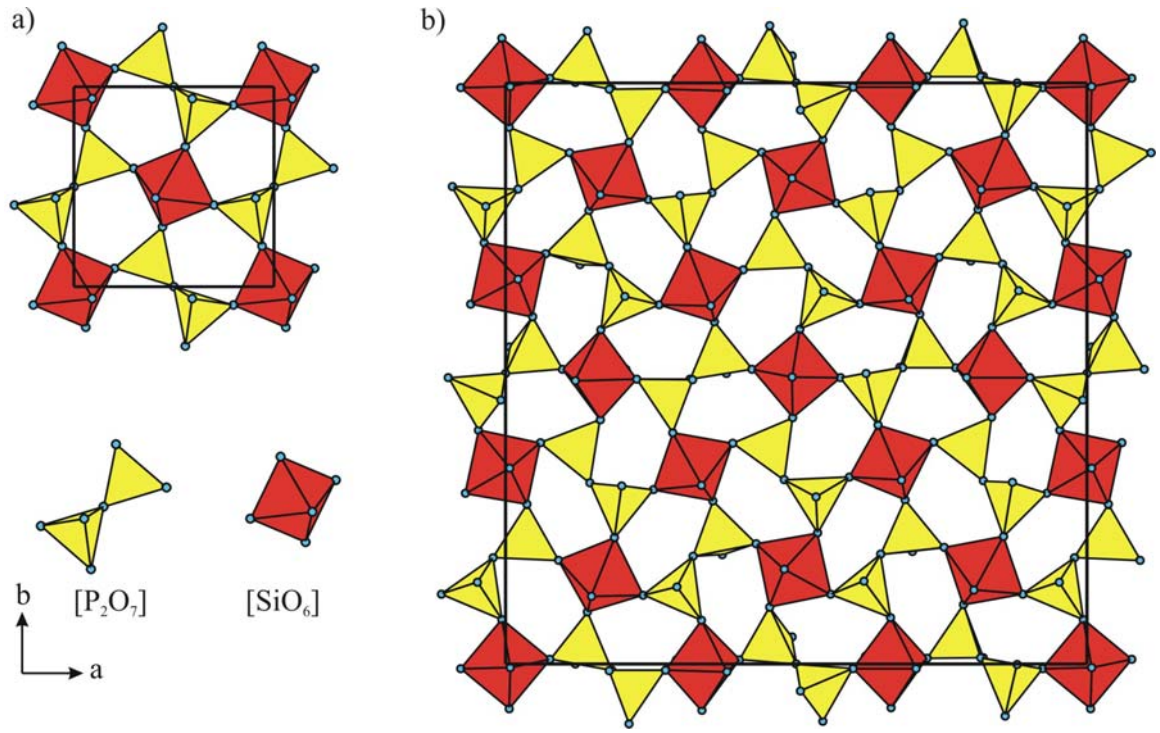

Figure 11.8 Polyhedral representations of cubic SiP_2O_7. For better understanding only polyhedra at $z \approx 0$ of the subcell with $Z = 4$ (a) and the superstructure with $Z = 108$ (b) are displayed [174] (Diamond version 3.2c [138]).

inversion center that leads to an unrealistic P-O-P bond angle of 180°. Up to now the superstructure of this type of diphosphate was refined for Ti [180], Si [174], Zr [139,140,175], Hf [139]. Among them only the superstructure of TiP_2O_7 was refined from X-ray single-crystal data [216]. Attempts to refine the supersuructure of MoP_2O_7 from X-ray single-crystal data by HAUSHALTER *et al*. [128] failed. The authors observed the appearance of an orthorhombic cell with Laue symmetry *mmm*. However, the crystal structure of the subcell of

MoP_2O_7 was published [31] from X-ray single crystal investigations, in which unfortunately its superstructure problem was not mentioned.

A comparison of the Guinier photograph to the simulation of the subcell of ReP_2O_7 reported by LISNYAK *et al.* [83] led to a large number of missing weak reflections (Figure 11.2). We assume that these missing reflections are attributed to superstructure. An X-ray single crystal study of $Re^{IV}P_2O_7$ shows a 3×3×3 fold superstructure ($Z' = Z \times 27 = 108$, $a' = 3a$ = 23.658(2)Å) isostructural to the known $M^{IV}P_2O_7$.

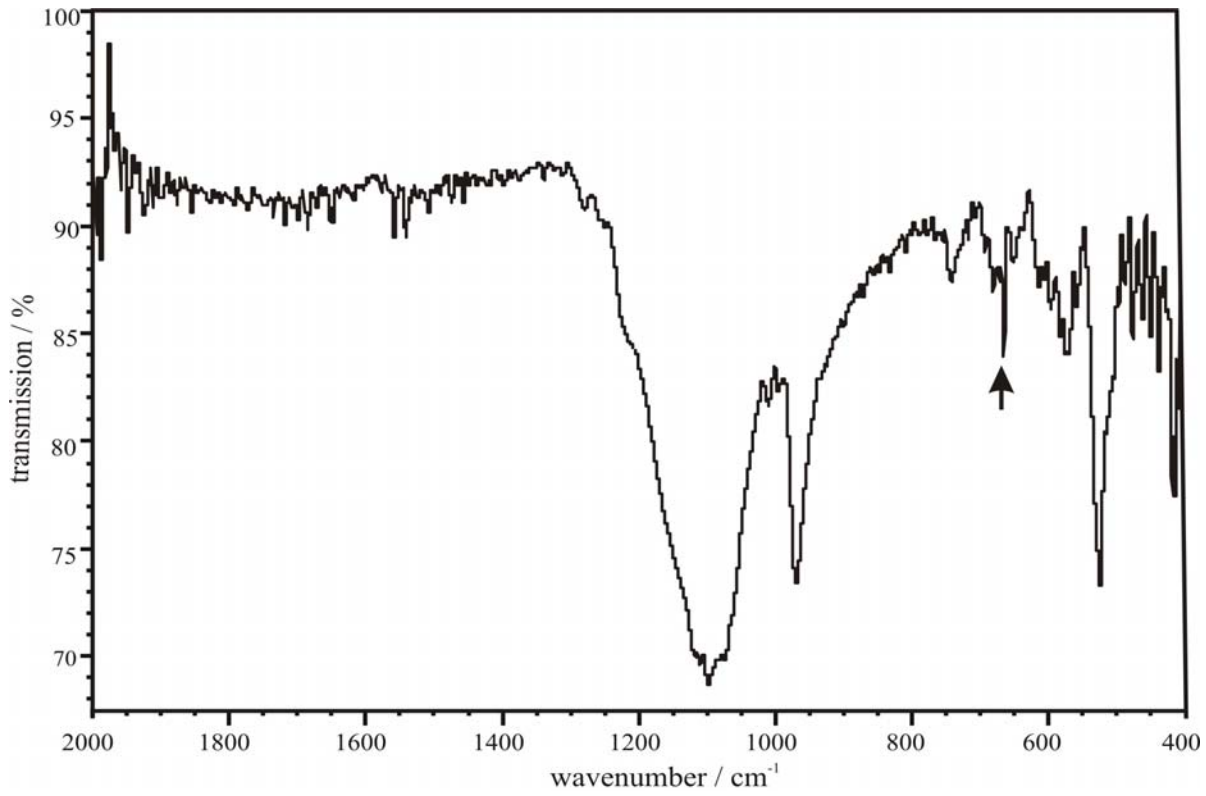

Figure 11.9 IR spectrum of ReP_2O_7; upward arrow indicates the band from unknown impurity in comparision to POPA *et al.* [83].

The presence of a weak band at about 746 cm^{-1} in the i. r. spectrum of ReP_2O_7 (see Figure 11.9, Table 11.11) is in agreement with POPA *et al.* [83] corresponding to the symmetric stretching of P-O-P in the $[P_2O_7]$ group. According to factor group analyses for the $M^{IV}P_2O_7$ [217, 218], this vibration should be i. r. inactive if the anion is being of the symmetry D_{3d} or D_{3h}. Thus, this observation precludes the P-O-P bridge from being linear as implied by space group $Pa\bar{3}$ for the subcell of this family. From X-ray single crystal investigation, we assume that an *mmm* Laue symmetry exists for the crystal structure of ReP_2O_7. However, on the basis of systematic absences and intensity distributions no space group determination was possible. Therefore, we failed to refine the superstructure of ReP_2O_7.

Table 11.11 IR spectrum of ReP_2O_7. Vibrational transitions and their tentative assignment.

wavenumber (cm^{-1})	**intensity**	**vibrational modes**
1279	w, sharp	ν_{asy}(P-O_{ext}) and ν_{sym}(P-O_{ext})
1252	w, shoulder	
1202	m, shoulder	
1125	s, sharp	
1099	vs, sharp	
1076	m, sharp	
1026	m, sharp	
971	vs, sharp	ν_{asy}(P-O_{int}) and ν_{sym}(P-O_{int})
746	m, sharp	
598	w, sharp	ν_{asy}(Re-O)
576	m, sharp	δ(O-P-O)
575	m, sharp	
527	s, sharp	
413	m, sharp	

w: weak intensity
m: medium intensity
s: strong intensity
vs: very strong intensity

11.5.2 Sodium Rhenium(IV) phosphate $NaRe_2(PO_4)_3$

$NaRe_2(PO_4)_3$ crystallizes in the rhombohedral crystal system ($R\bar{3}$, $Z = 6$, $a = 8.4631(9)$ Å, $c = 22.347(5)$ Å). It is isotypic to the aristotype of the *NASICON* structure family $NaZr_2(PO_4)_3$ [219], ($R\bar{3}c$, $Z = 3$, $a = 8.043(2)$ Å, $c = 22.7585(9)$ Å). The crystal structure of $NaRe_2(PO_4)_3$ is formed by a framework of $[Re^{IV}O_6]$ octahedra and $[PO_4]$ tetrahedra (see Figure 11.10). Between two $[Re^{IV}O_6]$ octahedra there is an additional octahedral void which is occupied by Na^+ cations. The trimeric units $[NaRe_2O_{12}]$ of face-sharing octahedra are stacked along the *c*-axis. Each $[MO_6]$ group shares its six vertices with phosphate tetrahedra, consequently all $[NaRe_2O_{12}]$ units are linked to 8 further trimers via 12 $[PO_4]$ groups.

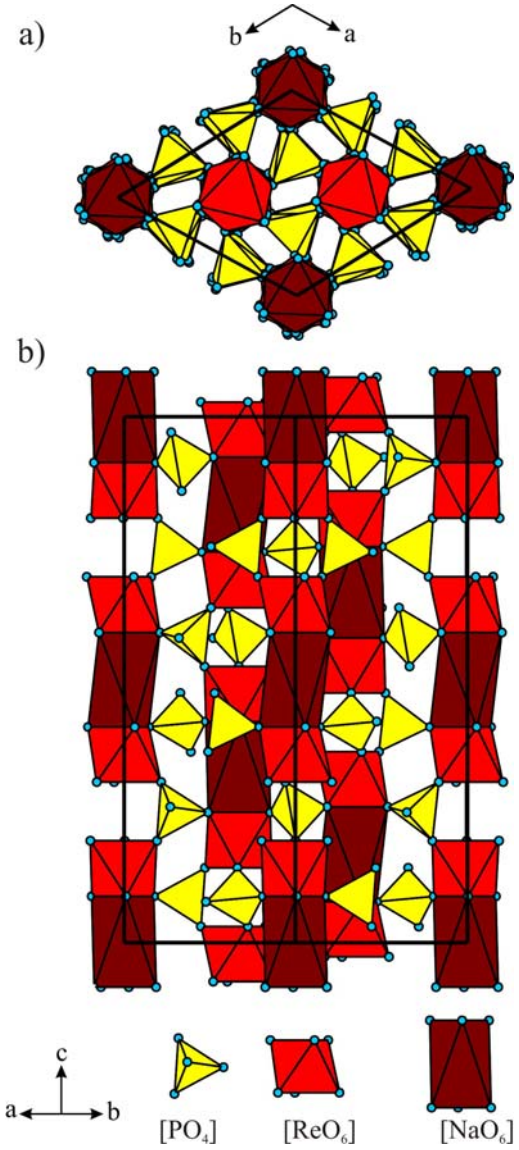

Figure 11.10 Polyhedral representation of the crystal structure of $NaRe_2(PO_4)_3$ (Diamond version 3.2c [138]).

The single-crystal structure refinement for sodium rhenium(IV) phosphate converged at rather low residuals and led to crystal chemical plausible interatomic distances, 2.474(2) Å ≤ *d*(Na-O) ≤ 2.564(3) Å and 1.973(3) Å ≤ *d*(Re-O) ≤ 2.007(2) Å (see Figure 11.11, Table 11.12). The distances *d*(Re-O) are also in good agreement with those obtained for other rhenium(IV) phosphates.

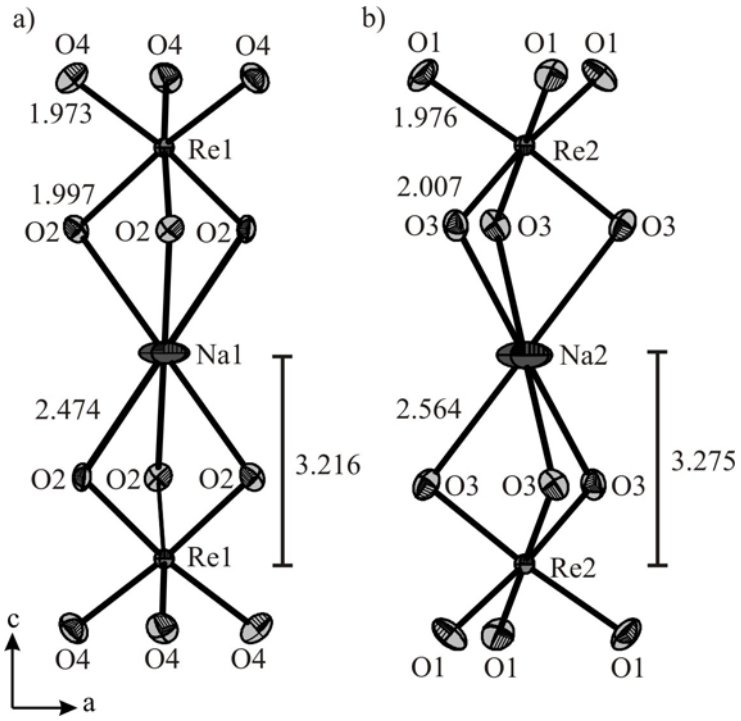

11.11 ORTEP representation of $[NaRe_2O_{12}]$ in $NaRe_2(PO_4)_3$. Ellipsoids at 70% probability level (Diamond version 3.2c [138]).

Table 11.12 Selected interatomic distances (Å) and angles (°) for $NaRe_2(PO_4)_3$. Standard deviations are given in parentheses.

d(Na1-O2)×6	2.474(2)	*d*(P1-O4)	1.517(3)	∠(O1,Re2,O1)	92.21(12)
d(Na2-O3)×6	2.564(3)	*d*(P1-O1)	1.528(3)	∠(O3,Re2,O3)	85.40(11)
d(Na1-Re1)×2	3.2162(7)	*d*(P1-O2)	1.532(3)	∠(O4,P1,O1)	113.06(15)
d(Na2-Re2)×2	3.2745(7)	*d*(P1-O3)	1.534(3)	∠(O4,P1,O2)	110.33(15)
d(Re1-O4)×3	1.973(3)	∠(O4,Re1,O4)	92.58(12)	∠(O1,P1,O3)	112.99(16)
d(Re1-O2)×3	1.997(2)	∠(O2,Re1,O2)	83.53(11)	∠(O1,P1,O2)	105.29(16)
d(Re2-O1)×3	1.976(3)	∠(P1,O3,Re2)	141.81(16)	∠(P1,O2,Re1)	139.40(15)
d(Re2-O3)×3	2.007(2)	∠(P1,O4,Re1)	154.77(19)	∠(P1,O1,Re2)	146.00(19)

On the basis of symmetry considerations in terms of group-subgroup relations, SCHÖNEBORN *et al*. [214, 220] showed, that the *NASICON* structure type can be derived from the NiAs crystal structure ($P6_3/mmc$, $Z = 2$, $a = 3.57$ Å, $c = 5.1$ Å [221]). In this crystal structure the arsenide ions form a hexagonal close packing (site *2c*) and all of the octahedral voids are occupied by nickel atoms on position *2a*. In the *NASICON* structure type phosphate tetrahedra form the hexagonal close packing with metal cations in 2/3 of the octahedral voids. The sequence of layers along the *c*-axis is $[a_1\, b_1\, a_2\, b_2\, a_3\, b_3\, a_1\, b_1]$. Figure 11.12 derived by SCHÖNEBORN *et al*. [220] illustrates the arrangement of As ions, that results from the transformation of the unit cell of NiAs from space group $P6_3/mmc$ to $R\bar{3}c$ according to group-subgroup relations. Actually, the symmetry reduction observed from $R\bar{3}c$ to $R\bar{3}$ is caused by the loss of a 2-fold axis parallel to the *a*-axis. This transition causes a splitting of Wyckoff position 6*b* to 3*a* and 3*b*, 12*c* to 2×6*c*. Our structure refinement revealed that both the splitted positions 3*a* and 3*b* are occupied by sodium ions only. The two 6*c* sites are occupied by two Re^{4+} cations.

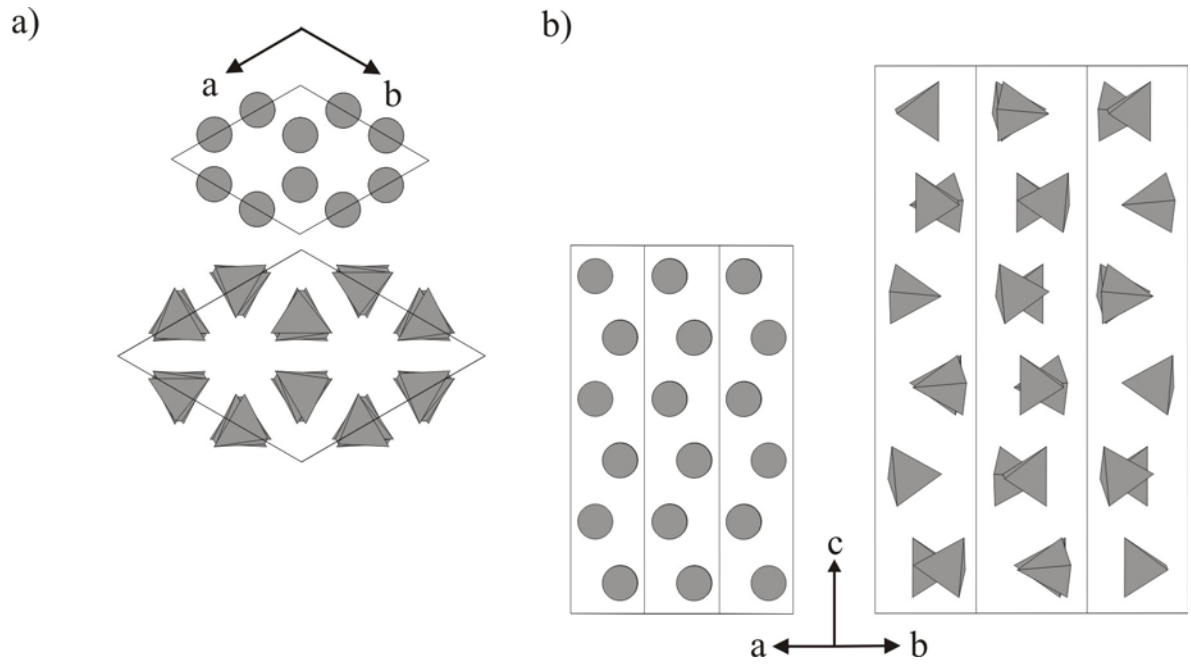

Figure 11.12 Arrangement of phosphate groups within the crystal structure of $NaZr_2(PO_4)_3$ in comparison to the arrangement of As in NiAs structure after transformation. Projections along [0 0 1] (a) and along [1 1 0] (b) [214].

11.5.3 Rhenium(IV) silicophosphate $Re_3[Si_2O(PO_4)_6]$

Structural investigations based on X-ray single crystal data illustrate that the structure of $Re_3[Si_2O(PO_4)_6]$ (see Figure 11.13) is isotypic to $Si°_3[Si^t_2O(PO_4)_6]$ [222], $Ge°_3[Ge^t_2O(PO_4)_6]$ [223], and $(Ir_{(1-x)}Si_x)°_3[Si^t_2O(PO_4)_6]$ (x = 0,54) [215]. $Re_3[Si_2O(PO_4)_6]$ is obtained from these structures through the substitution of octahedrally coordinated Si^{+4}, Ge^{+4} or Ir^{+4} by Re^{+4} ions. The elementary cell of $Re_3[Si_2O(PO_4)_6]$ contains three formula units with two crystallographically independent Re (Re1 and Re2), one Si, one P, and five O (O1, O2, O3, O4, O5).

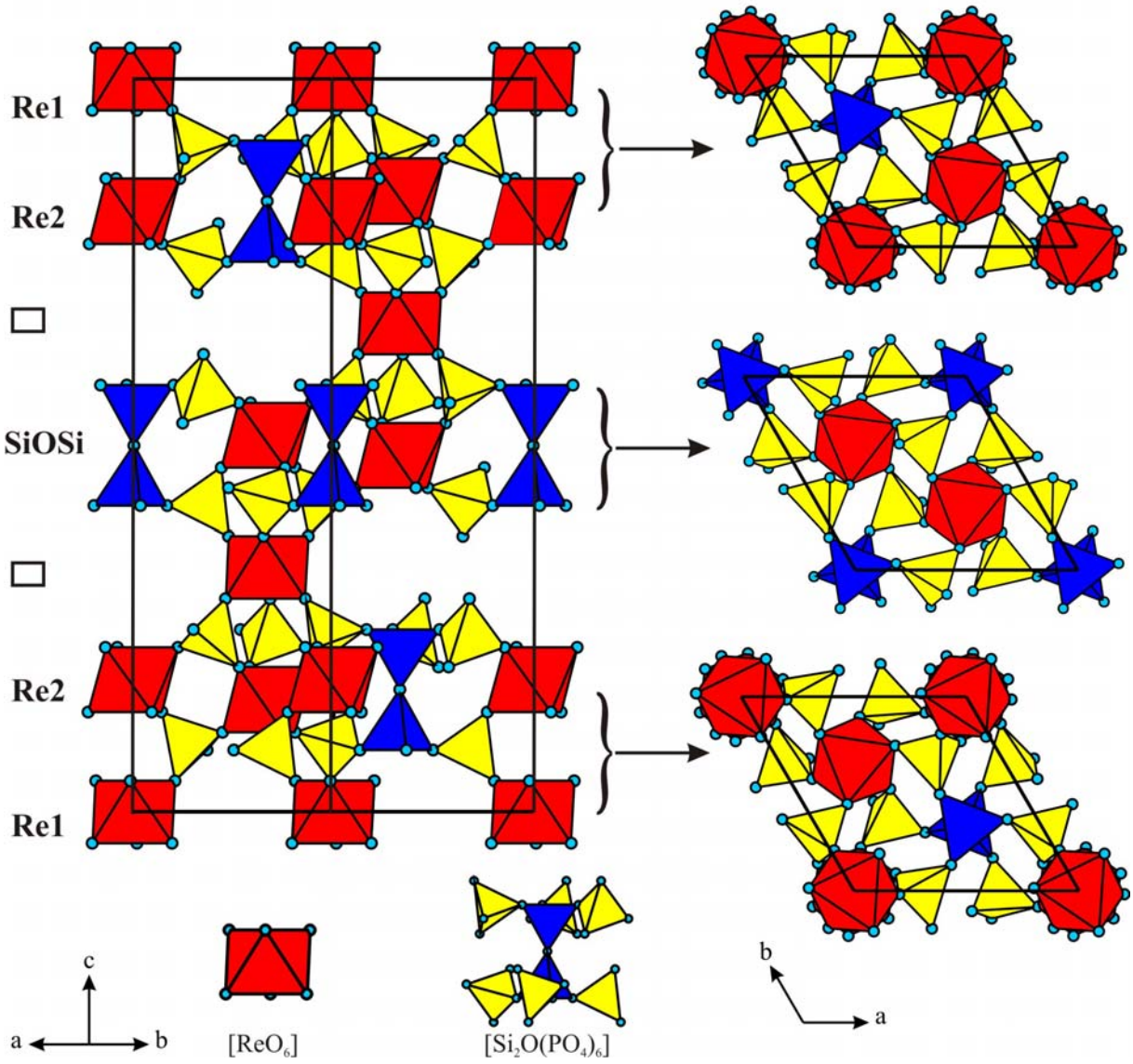

Figure 11.13 Crystal structure of $Re_3[Si_2O(PO_4)_6]$ with $[ReO_6]$ octahedra (red), $[Si_2O_7]$ groups (blue), and $[PO_4]$ tetrahedra (yellow) (Diamond version 3.2c [138]).

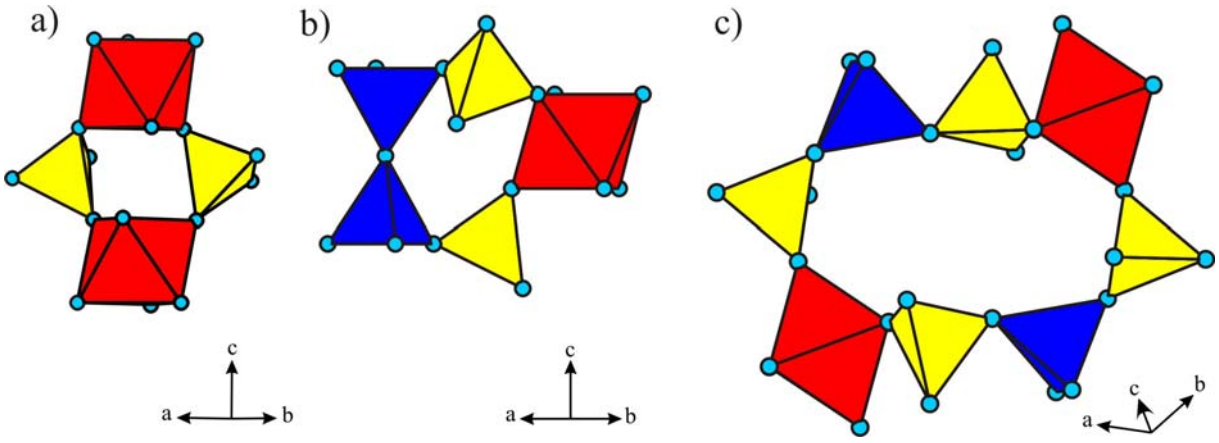

Figure 11.14 Linkage of polyhedra in the crystal structure of $Re_3[Si_2O(PO_4)_6]$. [ReO_6] octahedra (red), [SiO_4], and [PO_4] tetrahedra are blue and yellow, respectively (Diamond version 3.2c [138]).

The three-dimensional structure shows that the framework of $Re_3[Si_2O(PO_4)_6]$ consists of only corner sharing of [ReO_6] octahedra, disilicate groups [Si_2O_7], and [PO_4] tetrahedra where the former two are linked only by [PO_4] tetrahedra (see Figures 11.13, 11.14). Phosphate groups exhibit interatomic distances in the range of 1.49(2) Å ≤ *d*(P-O) ≤ 1.56(3) Å which is very close to its isotypic compounds, $M^{IV}{}_5O(PO_4)_6$ (*M* = Si, Ir, Ge) (see Figue 11.15, Table 11.13). The *d*(P-O) distances and ∠(O,P,O) angles show that the phosphorus atom is slightly off-center in its tetrahedron. The longest distance *d*(P-O4) = 1.56 Å in the [PO_4] tetrahedra is found for the oxygen bridging phosphorus and silicon. Apart from this, the other *d*(P-O) are smaller, and range from 1.49(2) Å ≤ *d*(P-O) ≤ 1.53(3) Å. The [ReO_6] groups exhibit a rather regular octahedral coordination with distances, 1.972(3) ≤ *d*(Re-O) ≤ 1.998(2) Å (Figure 11.15, Table 11.13).

The disilicate group [Si_2O_7] is formed through the combination of two tetrahedrally coordinated silicon atoms by a common oxygen atom O1 which is located at a special position, 3*b* (at $\bar{3}$). Therefore, the [Si_2O_7] group shows a Si-O1-Si bond-angle of 180°, whereas, most of the silicates and SiO_2-modifications show Si-O-Si bond angles between 128° and 166° [224]. The distance of the bridging silicon oxygen, *d*(Si-O_b) = 1.59 Å in the [Si_2O_7] group is slightly smaller than that of silicon to the terminal oxygen atoms, *d*(Si-O_t) = 1.62 Å. This observation clearly indicates that the silicon atom is slightly displaced towards the bridging oxygen of the disilicate group. In addition to isotytic $M^{IV}{}_3[Si_2O(PO_4)_6]$ (*M* = Si, Ir), this observation is adequately in agreement with the thortveitit structure, $Sc_2Si_2O_7$ [225, 226].

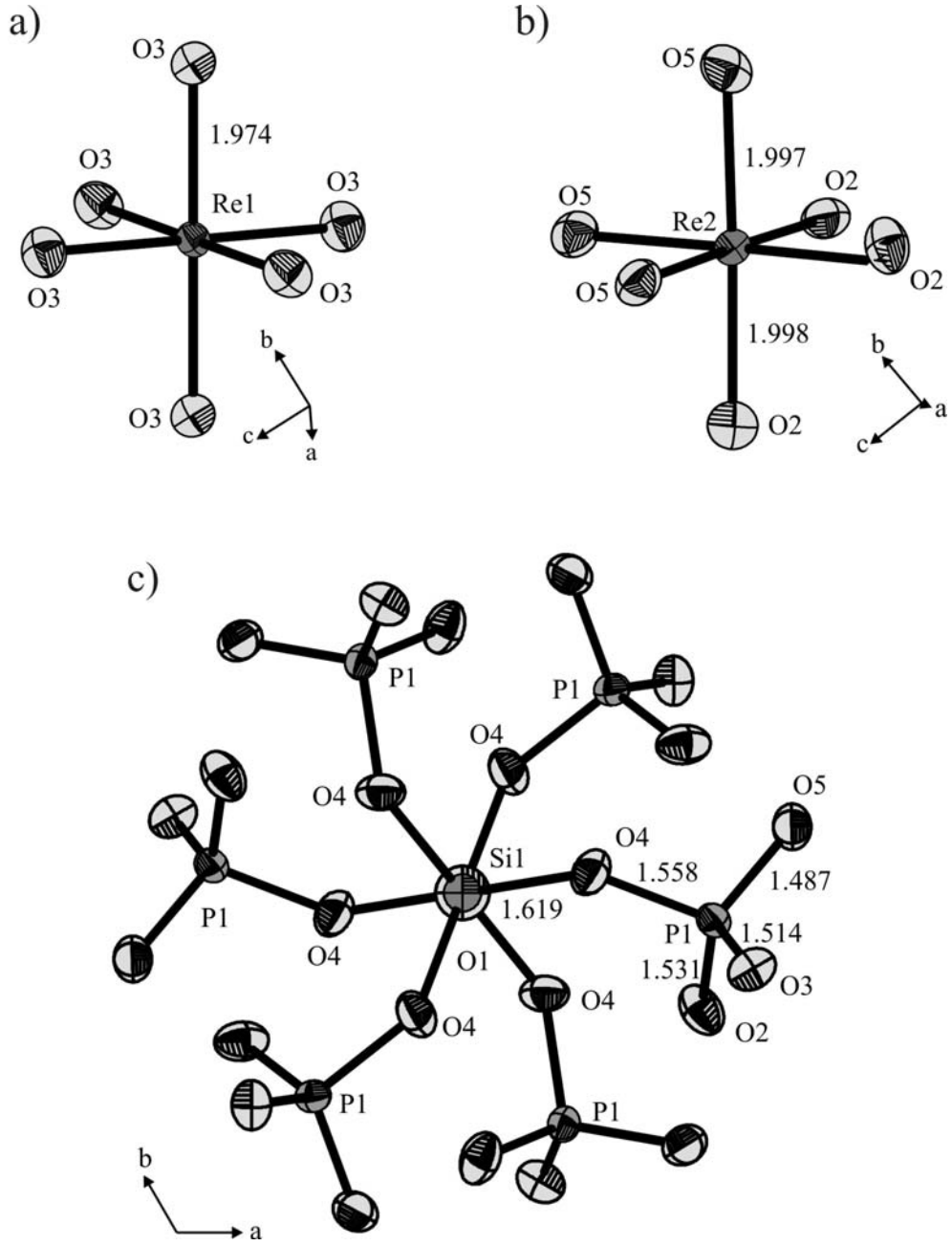

Figure 11.15 ORTEP representation of $[ReO_6]$ (a, b) and $[Si_2O(PO_4)_6]^{12-}$ (c) in $Re_3[Si_2O(PO_4)_6]$. Ellipsoids at 70% probability level (Diamond version 3.2c [138]).

The crystal structure of $Re_3[Si_2O(PO_4)_6]$ can also be explained in a different way, which refers to it as a hexagonal close packing of phosphate groups, where half of the octahedral voids are occupied by Re^{4+} ions, and 1/3 by Si_2O units [214, 227]. The latter leads to the formation of the heteropolyanion $[Si_2O(PO_4)_6]^{12-}$. The hexagonal close packing of phosphate groups can be

found also in *NASICON* type phosphates. Thus a structural correlation between *NASICON* type phosphates and silicophosphates is obtained.

Table 11.13 Selected interatomic distances (Å) and angles (°) for $Re_3[Si_2O(PO_4)_6]$. Standard deviations are given in parentheses.

d(Re1-O3)×6	1.973(7)	*d*(P1-O5)	1.486(7)
d(Re2-O2)×3	1.996(7)	*d*(P1-O3)	1.513(7)
d(Re2-O5)×3	1.997(7)	*d*(P1-O2)	1.530(7)
d(Si1-O1)	1.589(4)	*d*(P1-O4)	1.557(7)
d(Si1-O4)	1.618(7)	∠(O5,P1,O2)	105.8(4)
∠(Si1,O,Si1)	180	∠(O3,P1,O2)	111.4(4)
∠(O1,Si1,O4)	110.2(3)		
∠(O4,Si1,O4)	108.7(3)		

11.5.4 Rutile-related $(Re_{0.17}V_{0.83})O_2$

X-ray single-crystal investigation of $(Re_{0.17}V_{0.83})O_2$ revealed a rutile related monoclinic structure (see Figure 11.14a). Details on bond lengths are given in figure 11.14b. The assymetric unit contains two differenet metal (V1, V2 and Re1, Re2) sites. V1 and Re1 are randomly distributed on 1*a* crystallographic site whereas V2 and Re2 occupy the 1*h* site. The crystal structure consists of hexagonal close packed oxygen atoms where 83% of the octahedral interstices are occupied by V^{4+} and only 17% by Re^{4+} cations. EDX analysis of crystals of $(Re_{0.17}V_{0.83})O_2$ ensures the presence of rhenium and vanadium atoms. This analysis gave a Re : V = 0.14 which is close to the value obtained from the X-ray single crystal structure refinement.

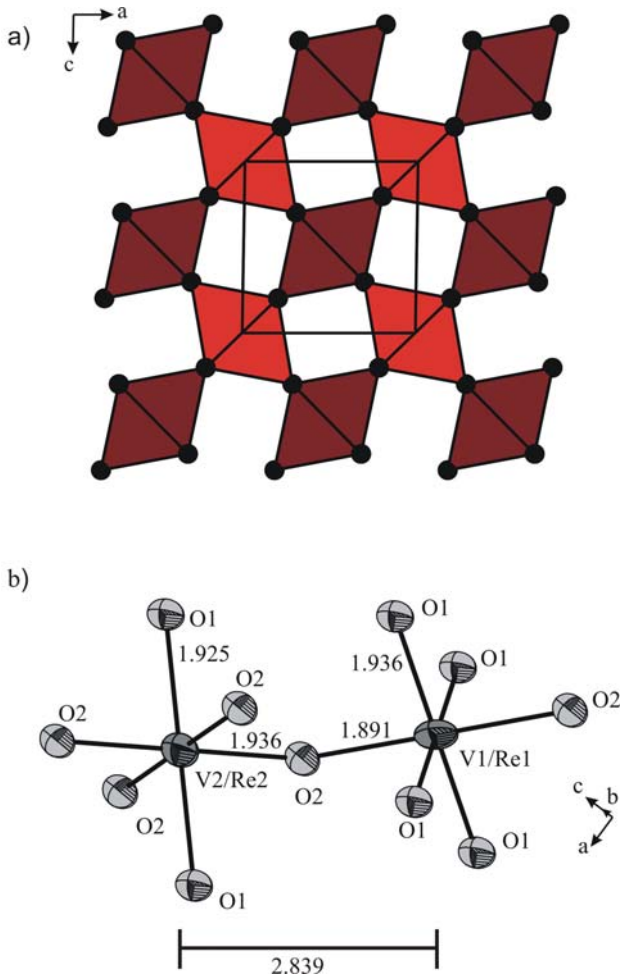

Figure 11.14 Crystal structure of $(Re_{0.17}V_{0.83})O_2$ (a). Red and dark red octahedra represent Re1/V1 and Re2/V2 sites, respectively. ORTEP representation of $(Re_{0.17}V_{0.83})O_2$ (b). Ellipsoids are at 90% probability level (Diamond version 3.2c [138]).

The cell parameters obtained as a = 4.5387(4) Å, b = 2.8385(4) Å, c = 4.5387(4) Å, and β = 91.13(1)° are very close to a = 4.6357(4) Å, c = 2.8292(3) Å found for the only other mixed rhenium vanadium oxide, $(Re_{0.50}V_{0.50})O_2$ [228]. The slight increase of the cell volume of $(Re_{0.50}V_{0.50})O_2$ is due to the introduction of more larger Re^{4+} cations. Apart from this, $(Re_{0.50}V_{0.50})O_2$ crystallizes in space group $P42/mnm$ whereas $(Re_{0.17}V_{0.83})O_2$ crystallizes in space group $P2/m$. $(Re_{0.50}V_{0.50})O_2$ was synthesized under high pressure of 60 Kbar at 1000°C. As it was mentioned previously $(Re_{0.17}V_{0.83})O_2$ was synthesized by CVT at 700 → 600°C. Therefore, the space group $P4_2/mnm$ is likely due to high pressure and high temperature. It is worth mentioning that the symmetry $P2/m$ was also obtained for isotypic VO_2 (a = 4.506 Å, b = 2.899 Å, c = 4.614(4) Å, and β = 91.79) [212].

11.6 Electronic Spectra of Rhenium(IV) phosphates

Ligand field splitting. Rhenium(IV) has a $5d^3$ electronic configuration. When this ion is placed in an octahedral field, the following terms result within the half filled t_{2g}^3 electronic configuration in order of increasing energy: $^4A_{2g}$, ^2E_g, $^2T_{1g}$, and $^2T_{2g}$. The spin-orbit coupling of the 5*d* elements is considerably stronger than that of 3*d* and 4*d*. It can be related according to $\zeta_{5d} \approx 2\zeta_{4d} \approx 5\zeta_{3d}$ [229]. The energy terms will split further under the influence of strong spin-orbit interaction into states which can be denoted in Bethes notation as Γ_i (i = 6, 7, 8) where Γ_i is the appropriate irreducible representation of the cubic group. Thus $^2T_{1g}$ splits into Γ_6 and Γ_8, $^2T_{2g}$ into Γ_7 and Γ_8. The irreducible notations Γ_6, Γ_7, and Γ_8 are two-, two- and four-fold degenerate, respectively. Doublet ^2E_g and quartet $^4A_{2g}$ remain four-fold degenerate and are transformed as Γ_8 in double group O'_h. Thus the absorption spectrum of Re^{4+} ions exhibits in the NIR/Vis five spin forbidden transitions. A schematic representation of the splitting of the t_{2g}^3 configuration is given in figure 11.15.

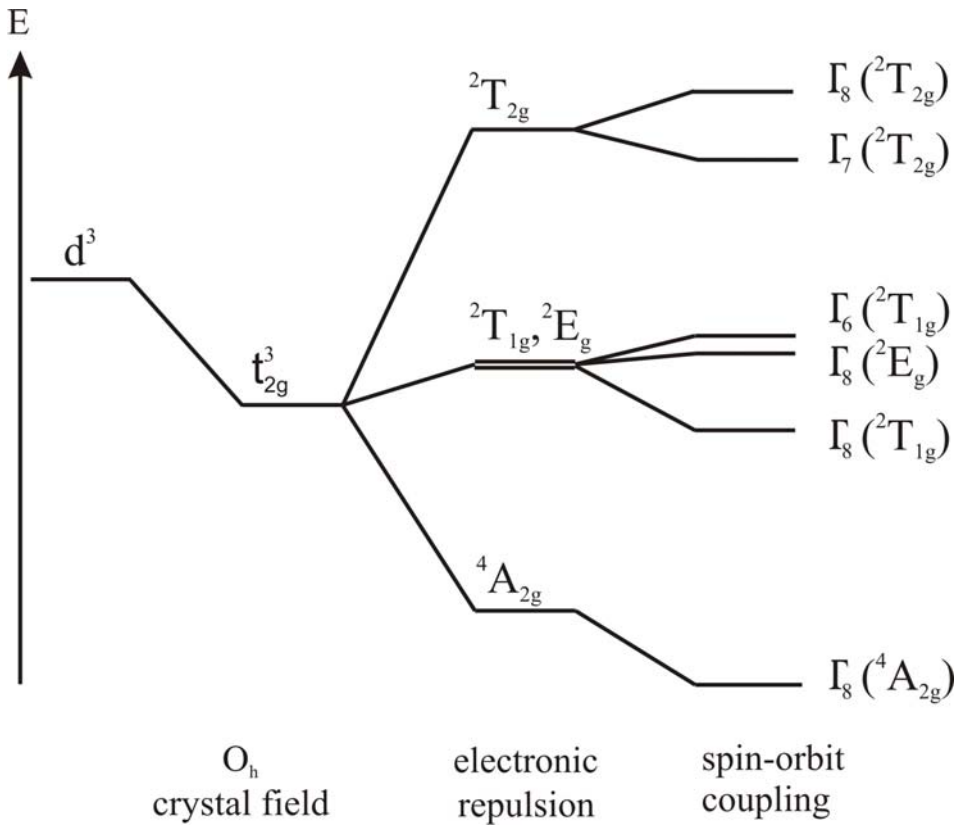

Figure 11.15 Schematic representation of the energy levels showing the effect of interelectronic repulsion and spin-orbit coupling on a t_{2g}^3 strong field configuration of Re^{4+} (d^3) ions in an octahedral field [230].

Angular overlap modelling parameters. To get an intricate knowledge for the correlation between radial and angular distortion of the chromophores and their *d*-electron energies, calculations within the framework of the angular overlap model (AOM) [231, 232, 233] were performed. A big advantage of this model is its ability to use the chromophores with their actual geometric structures derived from the crystal structure analysis. Instead of using global parameters, like 10*Dq* or Δ, one σ- and two π-interactions (a total of 18 bonding parameters for an octahedral complex) of each ligand with the five *d*-orbitals of the central ion are used for the fitting between calculated and observed transition energies. The decomposition of the global ligand-field parameter (10*Dq* or Δ) allows, in particular, for symmetry effects due to the second-sphere ligand-field, e.g. the competition between the central ion and neighboring cations for the *p*-electrons of bridging oxygen atoms, to be taken into account. In order to reduce the number of independent bonding parameters, relations between some of the parameters were introduced. Thus, for the energy e_σ(Re-O), proportionality to the distance $d(\text{Re-O})^{-5.0}$ was assumed [234]. The energy e_π was set to one-quarter of the corresponding energy e_σ in the case of an "undisturbed" π-interaction, [233]. Thus, for oxygen atoms with a coordination number (CN) of 2, $e_{\pi,x}$ and $e_{\pi,y}$ are equal. In the simplest case, these relations reduce the 18 interaction energies to only one independent parameter, which is recommended to be $e_{\sigma,\max}$(Re-O) for the shortest *d*(Re-O).
Interelectronic repulsion is introduced into the AOM calculations via the Racah parameters *B* and *C* (cm^{-1}), and spin-orbit coupling is introduced by ζ (cm^{-1}).

Chromophore geometry. While the crystal structures of ReP_2O_7 and $Re_3[Si_2O(PO_4)_6]$ contain isolated $[ReO_6]$ octahedra, $NaRe^{IV}_2(PO_4)_3$ contains a trimetric unit $[NaRe_2O_{12}]$ (see Figure 11.10) of three face sharing octahedra.
In $Re_3[Si_2O(PO_4)_6]$ two crystallographically independent isolated $[Re^{IV}O_6]$ (Figure 11.13) octahedra are found. As described previously, Re1 occupies the point symmetry $\bar{3}$, while the other at 3. The angular distortion of each of these units is less than 2° with respect to the ideal octahedra. The radial distortion, Δd(Re2-O) = 0.001 Å (difference between the longest and shortest Re2-O distances) is also fairly small. All oxygen ligands have a coordination number of 2 (one Re^{4+} and one P^{5+}).
In the crystal structure of $NaRe^{IV}_2(PO_4)_3$, two crystallographically independent $[ReO_6]$ octahedra are found. The angular distortion of the $[Re1O_6]$ unit is less than 7° with respect to the ideal octahedron while the radial distortion is Δd(Re1-O) = 0.024 Å. Whereas, the angular and radial distortions of $[Re2O_6]$ octahedra is Δd(Re2-O) of about 5° and 0.031 Å, respectively. For the both cases the distortions are rather small. One half of the oxygen

ligands (O2, O3) have a coordination number of 3 (one Re^{4+}, one Na^{+} and one P^{5+}) whereas the remaining O1 and O4 contain two-fold coordinations (one Re^{4+} and one P^{5+}).
As described in section 11.5.1, the crystal structure of ReP_2O_7 shows a 3×3×3 superstructure and is not refined yet. The superstructure of $M^{IV}P_2O_7$ (M^{IV} = Si [174], Ti [180], Zr [175]) with a $Pa\bar{3}$ symmetry reveal six crystallographically independent M^{IV} sites. In contrast to these, fourteen independent M^{IV} sites are observed in the superstructure of $M^{IV}P_2O_7$ (M^{IV} = Zr, Hf) [139] for the *Pbca* symmetry. As mentioned in section 11.5.1, Laue symmetry *mmm* was assumed for the crystal structure of ReP_2O_7. Such observations clearly indicate the presence of a large number of rhenium sites in the superstructure of ReP_2O_7; however, all the $[ReO_6]$ octahedra are very similar.

Fitting procedure. AOM calculations were carried out for $Re^{IV}P_2O_7$ and $Re_3[Si_2O(PO_4)_6]$ by the PC program CAMMAG [235]. In the calculations the transition energies are matched to the observed bands by the variation of the AOM parameters $e_{\sigma,max}$, B and the ratio of the $e_{\pi,x}$ / $e_{\pi,y}$ for bridging oxygen atoms. AOM calculations for ReP_2O_7 and $Re_3[Si_2O(PO_4)_6]$ using the distorted coordination geometry and isotropic e_π ($e_{\pi,x}$ = $e_{\pi,y}$ = 1/4 e_σ) interections between oxygen and Re^{4+} did not reproduce the spectra. In particular, splitting of the absorption bands was not matched. An introduction of strongly anisotropic π-overlap for oxygen immediately allows a reasonable fit to the observed transition bands. However, for a more accurate fit anisotropic π-interactions for the bridging oxygen atoms according to $e_{\pi,x} = 0.8e_{\pi,y}$ had to be introduced. The best fit was found for ReP_2O_7 with $e_{\sigma,max}$ = 12500 cm^{-1}, β = 0.80 and $e_{\pi,x}$ = $0.8e_{\pi,y}$. The Racah parameters B, C and spin-orbit coupling ξ as 525, 1700 and 2450 cm^{-1} allowed this fitting. The fitting parameters for $Re_3[Si_2O(PO_4)_6]$ was obtained as $e_{\sigma,max}$ = 11400 cm^{-1}, β = 0.80 and $e_{\pi,x} = 0.8e_{\pi,y}$, B = 550, C = 1680 cm^{-1} and spin-orbit coupling ξ = 2500 cm^{-1}. Due to very similar results for the two aformentioned phosphates, AOM calculations were not performed for $NaRe_2(PO_4)_3$.

Analyses of the spectra. The electronic absorption spectra of single-crystals of the rhenium(IV) phosphates, ReP_2O_7, $Re_3[Si_2O(PO_4)_6]$, and $NaRe_2(PO_4)_3$ were measured at ambient temperature and at about 100 K in the UV/Vis/NIR region (see Figure 11.16, Table 11.14) using a strongly modified CARY 17 microcrystal spectrophotometer [121, 122].
As expected, polarized single-crystal absorption spectra of rhenium(IV) phosphates are quite similar. For d^3 electronic configuration of oxo-rhenium complexes first spin-allowed transition $^4A_{2g} \rightarrow {}^4T_{2g}$ is found at $\Delta_o \sim 25000$ cm^{-1}. Other *d-d* transitions at higher

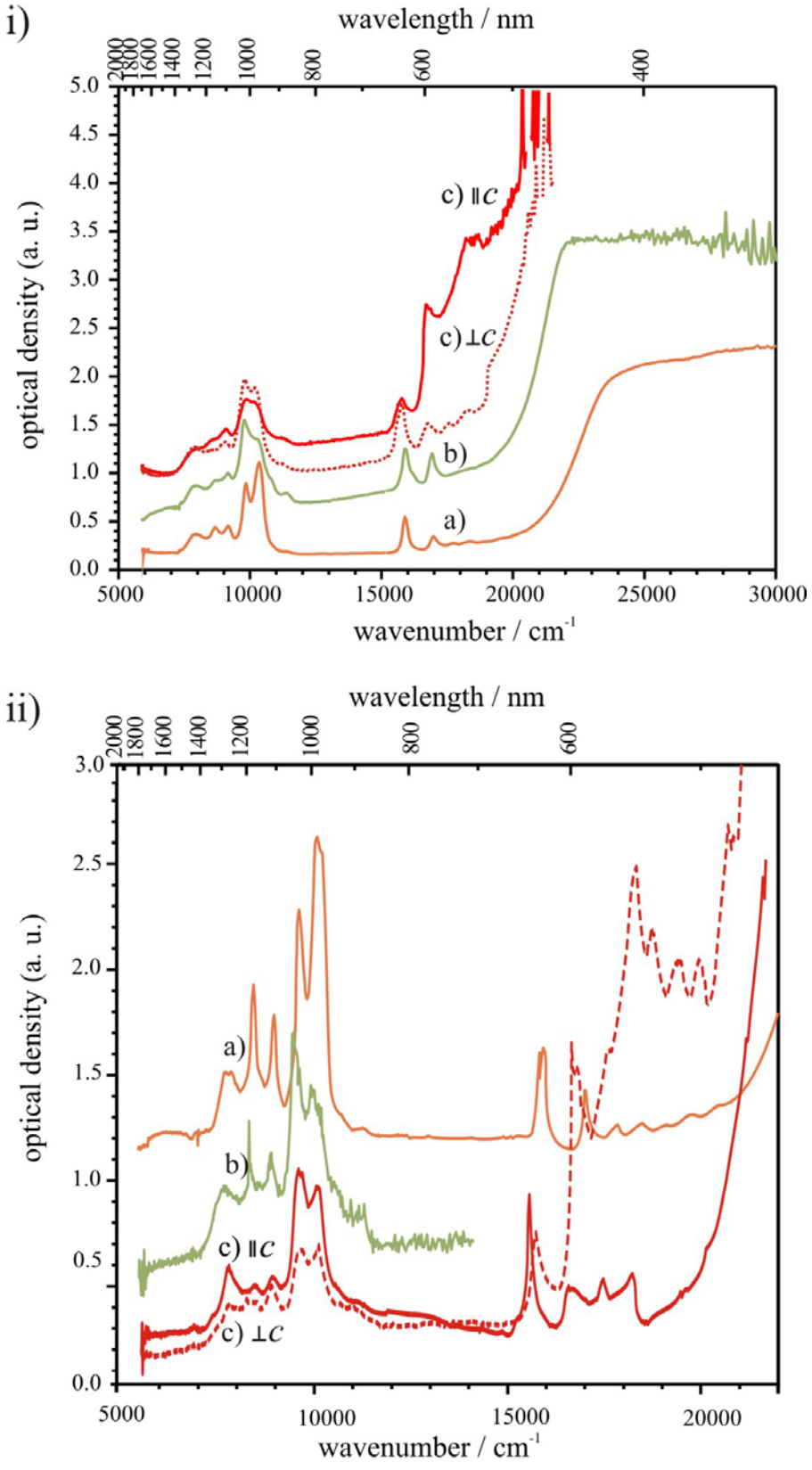

Figure 11.16 UV/Vis/NIR absorption spectra of rhenium(IV) phosphates, $Re_3[Si_2O(PO_4)_6]$ (a), ReP_2O_7 (b), and $NaRe_2(PO_4)_3$ (c) at ambient temperature (i) and at about 100 K (ii).

wavenumber are obscured by strong charge transfer transitions. The presence of several groups of weak signals at lower wavenumbers is the result of interelectronic repulsion and strong spin-orbit coupling. Our observations are in agreement with the results obtained for Re^{4+} ions in [ReX_6] ($X = F^{-1}$, Cl^{-1}, Br^{-1}) complexes [185, 186, 187, 188, 189, 190]. The weak signals are assigned as $^4A_{2g} \rightarrow {}^2T_{1g}$, $^4A_{2g} \rightarrow {}^2E_g$, and $^4A_{2g} \rightarrow {}^2T_{2g}$. The splitting of the energy levels results under the influence of spin-orbit interaction: $^2T_{1g}$ splits into Γ_6 and Γ_8; $^2T_{2g}$ into Γ_7 and Γ_8 (two-fold degenarate for each) whereas ^2E_g and $^4A_{2g}$ remains four-fold degenerate and transformed as Γ_8 in double group O'_h. Thus, low energy absorption spectra of Re^{4+} ions exhibit five spin forbidden transitions what we can see from the spectra. Further splitting of the energy states of the Re^{4+} ions might result from the deviations of symmetry from O_h. Apart from this, weak bands are attributed to vibronic coupling.

AOM best fit parameters ($B \sim 550$, $C \sim 1700$, $\xi \sim 2500$ cm^{-1}) for rhenium(IV) phosphates give some evidence for the presence of the *d-p* π-interactions between the Re^{4+} ions and oxygen atoms. This behaviour was already observed for the 3*d* transition metal complexes [236, 237, 234]. The effective magnetic moment for ReP_2O_7 at room temperature is 3.22 μ_B which is close to the values calculated by AOM ($\mu_{cal} = 3.87$ μ_B, for spin only system).

Table 11.14 Assignment of the band positions of the UV/Vis/NIR absorption spectra of Re^{4+} (d^3 electronic configuration) ion rhenium phosphates.

ReP_2O_7, ν / cm^{-1}		$Re^{IV}{}_3[Si_2O(PO_4)_6]$, ν / cm^{-1}		$NaRe^{IV}{}_2(PO_4)_3$, ν / cm^{-1}
observed	calculated	observed	calculated	observed
7917	7659	7918	7866	7885
8639	8865	8660	9051	8547
9166	9414	9177	9572	9070
9785	9607	9839	9813	9791
10275	10234	10356	10435	10173
10813	---	--	--	--
11400	--	11465	--	11174
15906	15984	15901	16030	15766
16929	16633	16972	16863	16768
17758	17924	17448	17635	17600
18116	---	18114	--	18296
21700	25396	23416	23724	21295

11.7 Magnetic Behaviour of ReP_2O_7 and $NaRe_2(PO_4)_3$

The temperature dependence of the reciprocal susceptibily of ReP_2O_7 is presented in figure 11.17a. A maximum observed at about 12 K, clearly indicates the presence of antiferromagnetic interactions in this pyrophosphate. The effective magnetic moment and paramagnetic Curie temperature were calculated to be 3.27 μ_B per formula unit and -47 K respectively. This reduction of effective magnetic moment from the spin only system (for d^3 system μ_{eff} = 3.87 μ_B) can be easily explained by the effect of spin-orbit coupling for Re^{4+} cation. Taking into account the structural features exhibited by this compound, antiferromagnetic interaction propagates a superexchange mechanism via $[P_2O_7]$ groups.

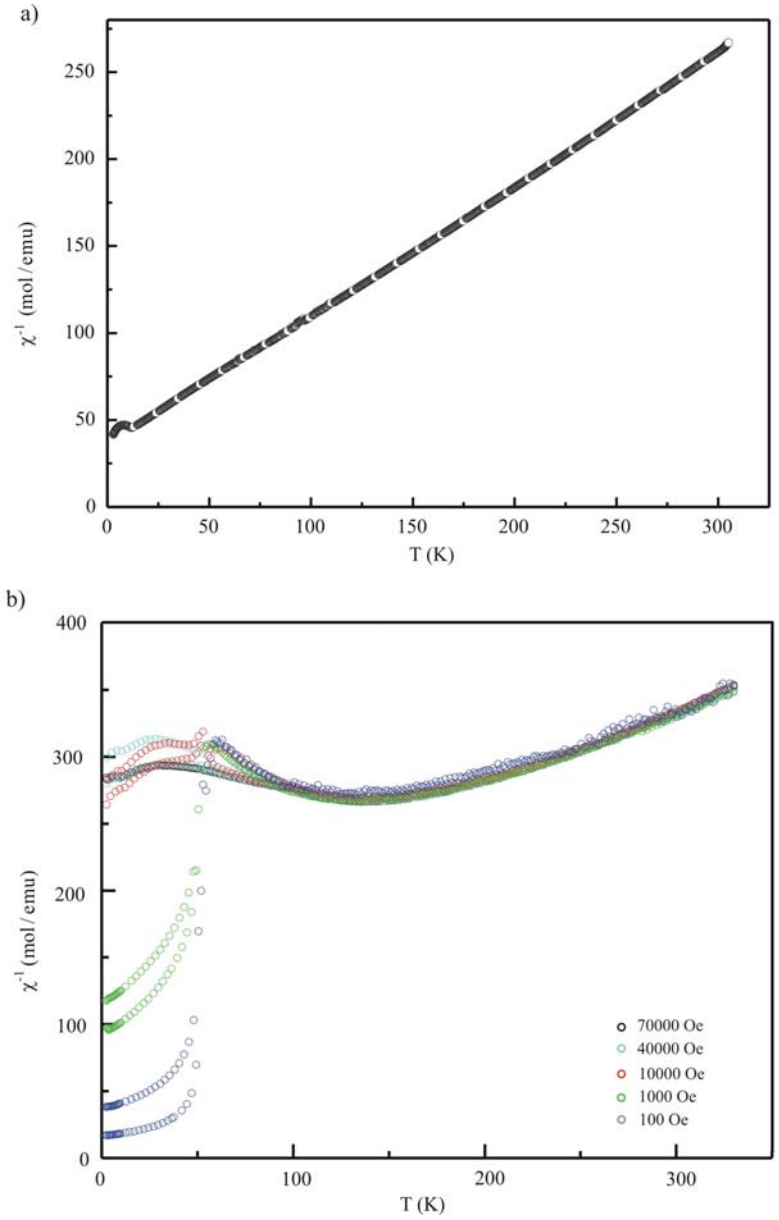

Figure 11.17 Temperature dependent reciprocal susceptibily for ReP_2O_7 (a) and $NaRe_2(PO_4)_3$ (b).

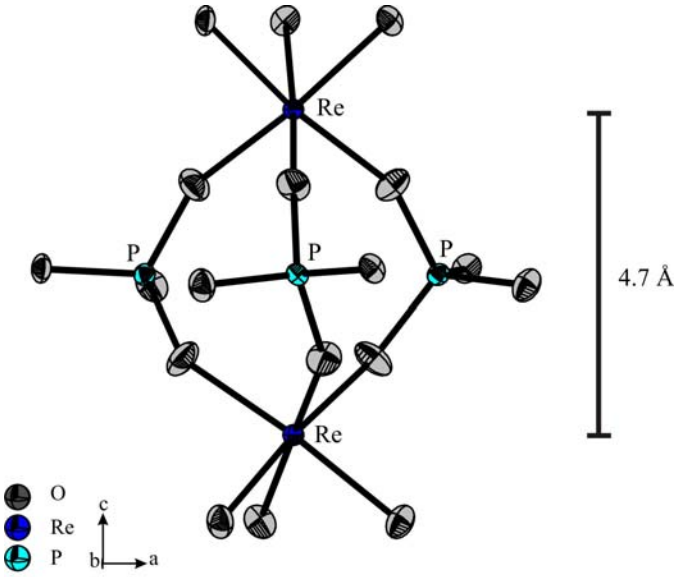

Figure 11.18 Structure of $[Re_2(PO_4)_3]^-$ dimer.

Reciprocal susceptibiliy vs temperature for $NaRe_2(PO_4)_3$ differs significantly from ReP_2O_7 (see Figure 11.17). The crystal structure of $NaRe_2(PO_4)_3$ consists of $[Re_2(PO_4)_3]^-$ dimers with the minimum *d*(Re-Re) ≈ 4.7 Å along the crystallographic *c*-axis (see Figure 11.18). An antiferromagnetic zero dimensional coupling within the nearest magnetic centers (Re^{4+} cations) in $NaRe_2(PO_4)_3$ is observed in the range of about $75 \geq \vartheta \geq 250$K. Due to very strong coupling of the two nearest neighbour free ion paramagnetic behaviour becomes absent even at higher temperature. Based on the structual feature of this compound an antiferromagnetic interaction propagates superexchange mechanism via $[PO_4]$ groups. The χ^{-1} vs T plot shows that a phase transition at 50 K where the main interaction is ferromagnetic. Magnetic behaviour below 50 K is not clear to us.

Magnetic measurements were carried out of the selected crystals of ReP_2O_7 and $NaRe_2(PO_4)_3$ with a "SQUID magnetometer (MPMS, Quantum design)" at Max-Planck-Institute for Solid-state Research (MPIFKT Stuttgart; Dr. Kremer).

12 Rhenium(V)-oxidepyrophosphate $Re_2O_3(P_2O_7)$

12.1 Introduction

In ternary systems *M* / P / O (*M* = V, Nb, Mo, Ta, W), up to now a plethora of anhydrous transition metal(V)-phosphates have been synthesized and characterized [2, 4].

Interestingly, niobium forms the largest number anhydrous phosphates at its pentavalent oxidation state, such as $NbOPO_4$ (shows three modifications: tetragonal [238, 239], orthorhombic [240, 241] and monoclinic [242]), $(NbO)_2(P_4O_{13})$ [243], $Nb_3(NbO)_2(PO_4)_7$ [244], $NbP_{1.8}O_7$ [143], $Nb_{1.91}P_{2.82}O_{12}$ [245], $Nb^{V/IV}{}_2(PO_4)_3$ [207], and a metal rich niobium phosphorus oxide, PNb_9O_{25} [246]. Molybdenum, too, shows several phosphates at its pentavalent oxidation state, $Mo^{V}OPO_4$ [24], β-$Mo^{V}OPO_4$ [129], β_I-$Mo^{V}OPO_4$ [this thesis] (see Chap. 8], $(Mo^{V}O)_2P_4O_{13}$ [29], $(Mo^{V}O)_4(P_2O_7)_3$ [19, this thesis, see Chap. 8] and $Mo^{\sim V}{}_{1.3}O(P_2O_7)$ [30]. Vanadium and tantalum form only one phosphate at a composition $M^{V}OPO_4$ (*M* = V, Ta). It is rather surprising that $VOPO_4$ exists in six modifications, α_I [247], α_{II} [247, 248], β [130], γ [249], δ [249], ε [250, 251] and ω [252]. $TaOPO_4$ also shows two modifications, tetragonal [253] and monoclinic [254]. Tungsten, on the other hand, exhibits two phosphates at its 5+ oxidation state, $W^{V}OPO_4$ [77] and $W^{V}{}_2O_3(P_2O_7)$ [78]. Apart from this, a very prominent series of mixed valent tungsten(IV/V) phosphates, so called monophosphate tungsten bronzes, with a general formula of $(PO_2)_4(WO_3)_{2m}$ ($2 \leq m \leq 14$) [80] has been characterized.

An important feature of rhenium is its ability to be stabilized in several oxidation states in oxo- and halogeno-componds. Its capability to be stabilized as rhenates at its pentavalent oxidation state has already been mentioned in the Introduction (see Chapter 1, Table 1). In rhenates rhenium forms the anionic part of the structure, while in phosphates metal cations form the cationic part of the structure. For rhenium identical behaviour has already been found for ReP_2O_7 [81]. Therefore, the existence of a large number of pentavalent transition metal phosphates pays a considerable inquisitive for the systematic investigation in the ternary system Re / P / O in order to search for new rhenium(V)-phosphates.

In the present work, a new rhenium(V)-pyrophosphate, $Re^{V}{}_2O_3(P_2O_7)$ has been synthesized and characterized. The following sections contain synthesis, crystal structure and infrared spectrum of this pyrophosphate. Characteristic similarities and differences to the already known chemistry and crystal chemistry of rhenium in its various oxo-compounds will be discussed.

12.2 Experimental

12.2.1 Syntheses and Crystallization

Crystals of $Re_2^{V}O_3(P_2O_7)$ were obtained in chemical vapour transport experiments in a temperature gradient (700 → 600 °C for 11 days and 700 → 550 °C for 5 days; evacuated sealed silica tubes, $l \approx 11$ cm, $d \approx 1.5$ cm, $V \approx 20$ cm^3) from a mixture of Re_2O_7 (331.1 mg, 0.6814 mmol), elemental phosphorus (17.2 mg, 0.555 mmol) and P_4O_{10} (58.1 mg, 0.2046 mmol). About 23 mg of iodine was used as transport agent. Needle shaped bronze coloured crystals (see Figure 12.1) of $Re_2O_3(P_2O_7)$ were obtained in the sink region along with ReP_2O_7, ReO_2, ReO_3, and $Re^{IV}_3Si_2O(PO_4)_6$ ($Si_3[Si_2O(PO_4)_6]$ structure type [222], a = 8.1953(2) Å, c = 26.0901 Å). The phases were identified from *IP* Guinier photographs (see Figure 12.2) of crushed crystals which had been selected under a microscope.

Figure 12.1 Crystals of $Re_2O_3(P_2O_7)$ from CVT experiment.

A similar experiment, aiming for the reduction of $Re^{VI}_2O_3(PO_4)_2$ (220.1 mg, 0.3606 mmol) by elemental phosphorus (5.3 mg, 0.1711 mmol) (660 → 500 °C, 30 mg iodine as transport agent, evacuated silica ampoule) led to no chemical vapour transport. However, a mixture of $Re^{V}_2O_3(P_2O_7)$ and ReO_3 was obtained at the source temperature. Several attempts for the synthesis of single phase $Re_2O_3(P_2O_7)$ failed. Experimental details for the synthesis of

rhenium(V) phosphates are given in table 12.1. Generally, mixtures of $Re^{IV}P_2O_7$ and ReO_3 were obtained instead. Re_2O_7 and P_4O_{10} were handled in a glove bag in argon atmosphere since both compounds are hygroscopic. The starting materials were at least of p.a. grade.

Table 12.1 Experiments aiming for the synthesis of $Re^{V}{}_2O_3(P_2O_7)$. Experiments led to $Re^{V}{}_2O_3(P_2O_7)$ are given in bold letters.

starting solids	amount / mg	I_2 / mg	temp.[a] / °C	time /d	products (source) (according to *IP* Guinier	products (sink) photographs)
ReO_3	420.20	165	400→300	4		
P_4O_{10}	113.12		500→400	4		
P	10.85		650→500	5	ReP_2O_7 / ReO_3 / ReO_2	thin lamella of ReO_3
Re_2O_7	316.61	174	700→600	11		
P_4O_{10}	55.85		700→500	7	ReP_2O_7 / ReO_3	thin lamella of ReO_3
P	16.33					
Re_2O_7	402.70	50	400→500	6		
P_4O_{10}	70.94		700→550	5	ReP_2O_7 / ReO_3 / ReO_2	ReP_2O_7 / thin lamella of ReO_3
P	20.60					
Re_2O_7	349.30	60	B.B.[b]	3h[c]		
P_4O_{10}	80.02		500→600	5		
P	15.50		500→400	7		
			600→450	4	ReO_3 / ReP_2O_7	thin lamella of ReO_3
ReO_3	204.01	60	B.B.[b]	5h		
P_4O_{10}	56.03		500→600	5		
P	4.50		550→400	7		
			550→450	4	ReO_3 /ReP_2O_7	ReO_3 / ReP_2O_7
$Re_2P_2O_{11}$	**220.12**	**60**	**500→400**	**4**		
P	**5.30**		**600→500**	**6**		
			660→500	**6**	**$Re_2P_2O_{10}$ / ReO_3**	**thin lamella of ReO_3**
Re_2O_7	279.30	20	700→600	11		
P_4O_{10}	49.03		700→550	5	ReO_2	ReP_2O_7 / $Re_3Si_2P_6O_{25}$ / *[d]
P	14.60					
ReO_3	161.50	----	700	5	ReP_2O_7 / ReO_3 / ReO_2	----
P_4O_{10}	39.04					
P	4.30					
Re_2O_7	436.90	115	600	10		
P_4O_{10}	76.60		550→500	9	ReO_3	ReP_2O_7 / $Re_2P_2O_{11}$
P	22.60					
Re_2O_7	**331.10**	**23**	**700→600**	**11**		
P_4O_{10}	**58.10**		**700→550**	**5**	**ReO_3 /ReO_2**	**$Re_3Si_2P_6O_{25}$ / ReP_2O_7 ReO_3 / ReO_2 / $Re_2P_2O_{10}$ / *[d]**
P	**17.20**					
Re_2O_7	333.80	34	B.B.[b]	1h		
P_4O_{10}	58.71		700	5		
P	17.05		800	2	ReO_2 / ReP_2O_7	----
Re_2O_7	242.92	30	410	3		
P_4O_{10}	12.70		800	4	ReP_2O_7 / ReO_2	
P	42.56				/ ReO_3	----
ReO_3	117.40	60	400	13d		
P	3.21		700	7	ReP_2O_7 / ReO_3 / ReO_2	----
P_4O_{10}	35.00					

ReP_2O_7	75.10	140	400	11		
ReO_3	46.92		700	4	ReP_2O_7 / ReO_2	----
(pallet)						
ReP_2O_7	62.42	60	400	1		
ReO_3	39.10		600	5		
(pallet)			800→700	5		
			900→800	4	ReP_2O_7 / ReO_2 /	ReP_2O_7
ReP_2O_7	60.60	115	400	1		
ReO_3	40.30		600	5		
(pallet)			750→650	5	ReP_2O_7 / ReO_2	ReP_2O_7
ReP_2O_7	58.52	----	330	8h		
ReO_3	42.20		390	4h		
(pallet)			400	4h		
			840	3	ReP_2O_7 / ReO_2	----

[a] Given are the various heating periods for an ampoule. Starting solid were always at the left side of the arrow. Solid reaction products were characterized by their XRPD pattern after the final heating period, only.

[b] B. B.: mild heating in the Bunsen burner flame.

[c] h indicates hours.

[d] weak lines of unknown phase (see Chap. 11, Sec. 11.2, Figure 11.6).

12.2.2 Characterization

For identification, examination of the purity, and for determination of the lattice parameters of $Re_2O_3(P_2O_7)$ image-plate (*IP*) **Guinier photographs** (Guiner camera FR-552 Enraf-Nonius, quartz-monochromator, Cu-Kα_1 radiation, λ = 1.54052 Å, α-SiO_2 as internal standard, BAS-TR 2025 image plate film (Fa. Fuji), BAS-1800 scanner (Fa. Fuji), software: BASREADER, [151]), AIDA [91] for digitization) are taken (see Figure 12.2). Details on this method were already reported in literature [90, 152, 153]. Assignment of the powder pattern led to a = 12.246(2) Å, b = 12.681(2) Å, c = 5.2178(7) Å, β = 89.98(2) ° (51 reflections with $20.09^o \leq 4\theta \leq 119.74°$).

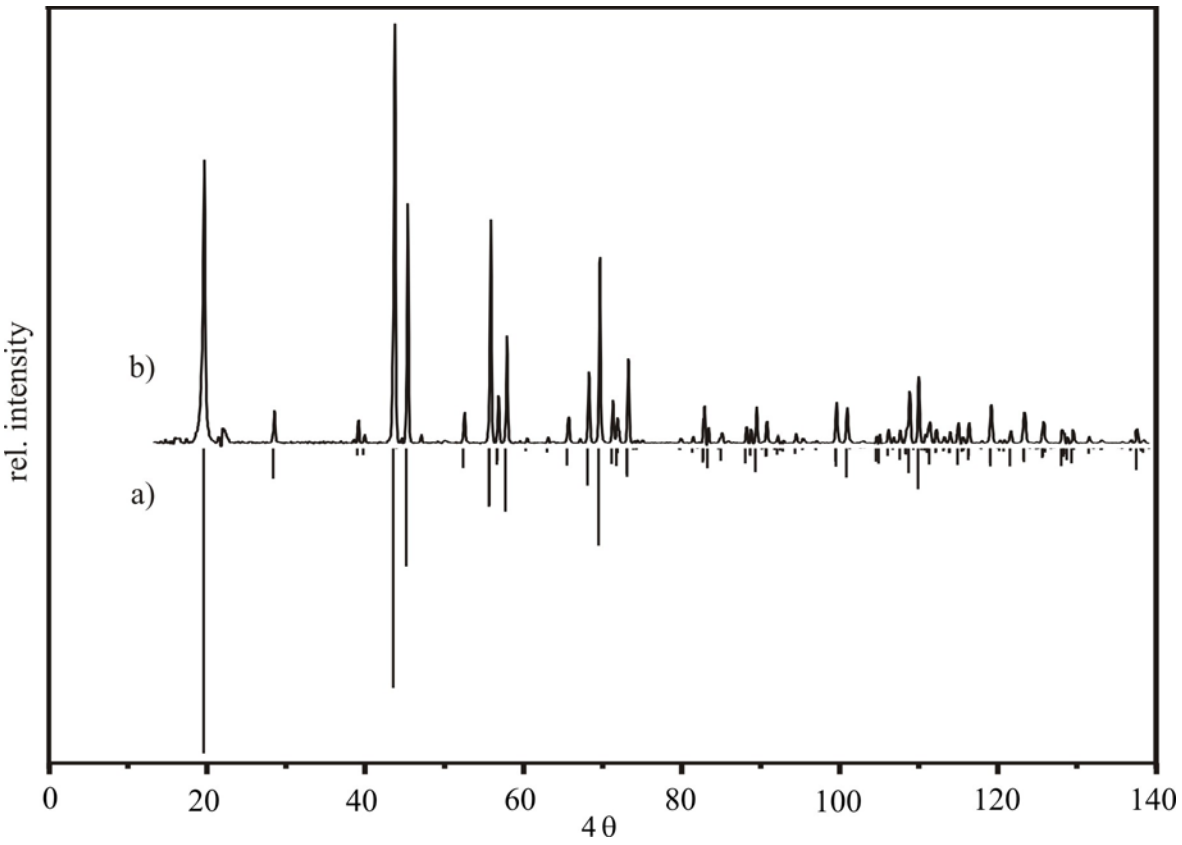

Figure 12.2 Comparison of the simulation (a) and Guinier photograh (b) of $Re_2O_3(P_2O_7)$. A few weak unassigned lines represent unknown impurity.

Single-crystal intensity data were measured on a κ-CCD diffractometer (Enraf-Nonius Inc.) at ambient temperature. Structure determination and refinement were performed using the SHELX-97 [105] suite in the WinGX framework [135]. Despite the pseudo-orthorhombic unit cell dimensions and the very close structural relationship to $W_2O_3(P_2O_7)$ (space group *Pnma*) [78] reasonable refinement of the crystal structure of $Re_2O_3(P_2O_7)$ was only possible in space

group *C2/c*. The space group choice is supported by the intensity statistics, which provides strong evidence for a *C*-centered lattice, by the absence of correlations between refined parameters and significant deviations of site coordinates from special values (e. g. 1/4). In addition, the merging residual R_{int} for point group *mmm* was almost twice as high as that for 2/*m*. Nevertheless, refinement in space group *Pnma* was attempted according to the structure model of $W_2O_3(P_2O_7)$ [78]. Thus, site parameters obtained for the rhenium pyrophosphate were very similar to those of the tungsten compound. However, the conventional residual was twice that of the refinement in *C*2/*c*, *wR*2 = 0.60, and all atoms had physically meaningless displacement parameters.

Details concerning data collection, structure solution and refinement of $Re_2O_3(P_2O_7)$ are summarized in table 12.2. The final atomic coordinates and displacements parameters are reported in table 12.3. Selected interatomic distances and angles are listed in table 12.4. Indexing of the Guinier simulation and anisotrpic displacement parameters are placed in Appendix B2 (Table B2.1 and Table B2.2).

Energy-dispersive X-ray fluorescence analyses [116, 117, 118] (EDAX system, scanning microscope DMS 940, Zeiss) showed no additional elements besides rhenium, phosphorus and oxygen. The infrared spectrum of Guinier-pure $Re_2O_3(P_2O_7)$ was measured using a NICOLET 380 FT-IR spectrometer (SMART ORBIT). An attempt to measure the Raman spectrum of the oxidepyrophosphate failed due to strong absorption of the powdered sample.

Table 12.2 Details concerning data collection, crystal structure solution and refinement of $Re_2O_3(P_2O_7)$.

crystal data	
formula	$Re^{V}{}_2O_3(P_2O_7)$
crystal system	monoclinic
space group	*C*2/*c* (Nr. 15)
a / Å	12.2503(5)
b / Å	12.6731(5)
c / Å	5.2188(2)
β / °	89.968(2)
V / Å^3	810.21(6)
Z	4
μ / mm^{-1}	30.29
$D_{X\text{-}ray}$ / g·cm^{-3}	4.872
colour	bronze
crystal shape	needle
size /mm^3	0.1×0.01×0.01
molecular weight / g·mol^{-1}	594.35
F(000)	1040
data collection	
Nonius κ-CCD diffractometer	
temperature / K	293(2)
scan range θ / °	$0.998 \le \theta \le 30.034$
	$-16 \le h \le 17$
	$-17 \le k \le 17$
	$-7 \le l \le 7$
absorption correction	multi-scans [115]
structure refinement	
program	SHELX97 [105]
extinction coefficient	0.00167(9)
measured reflections	25012
independent reflections	1198; 983 with $\lvert F_o \rvert > 4\sigma(F_o)$
parameters; Goof	66; 1.042
residuals	
R_{int}	0.078
R_1[a)]	0.023
wR_2[b)]	0.049
weighting scheme	A = 0.0183; B = 0.36
residual electron density	
$\Delta\rho_{max}$ / Å^{-3}	2.642 (close to O2)
$\Delta\rho_{min}$ / Å^{-3}	-2.092 (close to Re)

[a)] $R_1 = \Sigma||F_o| - |F_c|| / |F_o|, F_o^2 \ge 2\sigma(F_o^2)$

[b)] $w = 1 / [\sigma^2(F_o^2) + (A \cdot P)^2 + B \cdot P]; P = (F_o^2 + 2F_c^2) / 3$

Table 12.3 Atomic coordinates and isotropic displacement parameters of $Re_2O_3(P_2O_7)$.

atoms	**site**	***x***	***y***	***z***	U_{eq} /Å$^{2a)}$
Re1	8*f*	0.64901(2)	0.40206(2)	0.24609(4)	0.0067(1)
P1	8*f*	0.8812(1)	0.2731(1)	0.2721(2)	0.0081(3)
O1	8*f*	0.669(3)	0.5159(3)	0.0286(7)	0.0099(8)
O2	4*e*	1/2	0.4195(4)	1/4	0.0083(12)
O3	8*f*	0.6297(3)	0.2689(3)	0.4558(7)	0.0119(9)
O4	8*f*	0.1926(3)	0.3671(3)	0.2743(8)	0.0112(9)
O5	8*f*	0.6280(3)	0.3117(3)	-0.0717(8)	0.0170(10)
O6	4*e*	0	0.3242(4)	1/4	0.0114(13)

a) $U_{eq} = (⅓)\Sigma_i\Sigma_j U_{ij} a_i^* a_j^* \mathbf{a}_i \cdot \mathbf{a}_j$

Table 12.4 Selected interatomic distances (Å) and angles (°) in $Re_2O_3(P_2O_7)$; estimated standard deviations in parentheses.

d(Re1-O1$_b$)	1.822(4)	*d*(P1-O5)	1.505(4)
d(Re1-O2$_b$)	1.8390(7)	*d*(P1-O4)	1.515(5)
d(Re1-O1$_b$)	1.853(4)	*d*(P1-O3)	1.522(4)
d(Re1-O4)	1.993(4)	*d*(P1-O6$_b$)	1.597(3)
d(Re1-O3)	2.025(4)	∠(P1,O6,P1)	132.1(4)
d(Re1-O5)	2.031(4)	∠(Re1,O3,P1)	143.7(3)
∠(Re1,O1,Re1)	157.1(3)	∠(Re1,O4,P1)	138.4(3)
∠(Re1,O2,Re1)	166.1(3)	∠(Re1,O5,P1)	168.5(3)

12.3 Results and Discussions

Reaction of Re_2O_7, P_4O_{10}, and phosphorus in the presence of iodine as mineralizer led in a temperature range 550 to 700°C to the formation of $Re^V{}_2O_3(P_2O_7)$. Despite this undisputable result further experiments showed problems with its reproducibility. Mixtures of ReP_2O_7 and ReO_3, occasionally containing some ReO_2, were obtained instead of $Re_2O_3(P_2O_7)$. Heterogeneous equilibria determining stability and chemical vapour transport of rhenium phosphates have already been discussed in literature [281]. Though we believe that a very narrow thermal stability range and, possibly a rather narrow range for the equilibrium decomposition pressures $p(O_2)$ and $p(P_4O_{10})$ are responsible for our failure in finding reproducible synthesis conditions, kinetic effects like seed formation from the gas phase can not be ruled out completely.

The crystal structure of $Re_2O_3(P_2O_7)$ consists of octahedra $[ReO_{3/1}O_{3/2}]$ which are linked via three oxygen atoms to form chain-ladder type ribbons undulating along the crystallographic *c*-axis (see Figure 12.3). In another approach to the crystal structure these ribbons might be considered as sections from a ReO_3-type lattice which are linked via pyrophosphate groups to give rather wide octagonal tunnels. In the isostructural quaternary phosphate $CsW_8(P_2O_7)_4O_{12}$ [255] these tunnels are occupied by Cs^+. Distances *d*(Re-O) for oxygen atoms bridging two rhenium atoms are rather short (*d*(Re-O) ≈ 1.83 Å), while *d*(Re-O) for oxygen atoms bridging rhenium and phosphorus are significantly longer (*d*(Re-O) ≈ 2.02 Å; Figure 12.4, Table 12.4). Distances found for $Re_2O_3(P_2O_7)$ are in agreement with those of other rhenium(V) oxo-compounds (e. g.: Sm_3ReO_7 [49], $Cd_2Re_2O_7$ [51], $BiReO_4$ [48], $La_5CoRe_3O_{16}$ [256]). In contrast to oxo-compounds containing rhenium with oxidation state +VI or +VII no extraordinarily short ("double-bonded" or "terminal") contacts *d*(Re-O) are found for rhenium(V). Typically, distances *d*(Re-O) for rhenium in oxidation states +IV to +VII range from 1.80 to 2.05 Å. A distinction of the various oxidation states of rhenium in oxo-compounds just on the basis of interatomic distances is therefore rather ambiguous. Our structural investigation shows that rhenium(V) ions belong to a small group of highly charged cations which are able to compete with phosphorus(V) for basic oxide ions in terms of an Lewis acid-base reaction. In this respect $V^{IV}{}_2P_2O_9$ is no oxide-orthophosphate but a vanadyl-pyrophosphate $(VO)_2P_2O_7$ [6], and the thermodynamically stable form of $V^{IV}P_2O_7$ is a vanadyl(IV)-metaphosphate $(VO)(PO_3)_2$ [257, 258]. The same applies to $Mo^{VI}{}_2P_2O_{11}$ (≡ $(MoO_2)_2P_2O_7$ [24, 25]), $Mo^{VI}P_2O_8$ (≡ $(MoO_2)(PO_3)_2$ [26]), $Mo^V{}_4P_6O_{25}$ (≡ $(MoO)_4(P_2O_7)_3$ [19]), $Mo^V{}_2P_4O_{15} \equiv (MoO)_2P_4O_{13}$ [28, 29]), and $W^V{}_2P_2O_{10}$ (≡ $W_2O_3(P_2O_7)$ [78]). Obviously,

equilibria (12.1) and (12.2), which describe the competition between rhenium(V) and phosphorus(V) for oxide ions, are shifted to the left.

$$Re_2O_3^{4+} + P_2O_7^{4-} = 2\,(ReO)^{3+} + 2\,PO_4^{3-} \quad (12.1)$$

$$(ReO)^{3+} + P_2O_7^{4-} = Re^{5+} + 2\,PO_4^{3-} \quad (12.2)$$

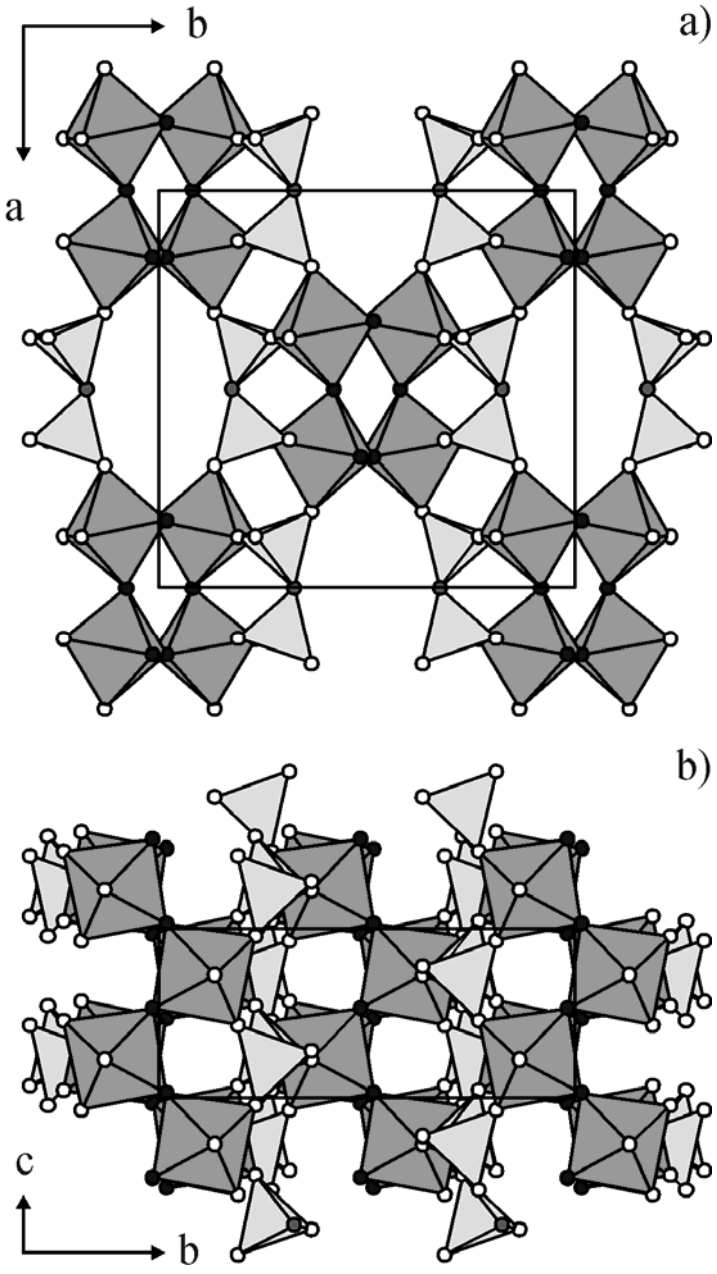

Figure 12.3 Crystal structure of $Re_2O_3(P_2O_7)$ with $[ReO_6]$ octahedra (grey) and $[P_2O_7]$ groups (light grey). Oxygen atoms bridging two rhenium atoms in black, bridging two phosphorus atoms in grey, bridging rhenium and phosphorus in white (ATOMS v. 6.3 [259).

The P_2O_7 groups in $Re_2O_3(P_2O_7)$ display the typical interatomic distances, i.e. one long bond, d(P1-O6$_b$) = 1.596(2) Å, corresponding to the oxygen atom bridging the two phosphorus atoms and three short bonds 1.505(4) ≤ d(P-O$_t$) ≤ 1.522(4) Å between phosphorus and the terminal oxygen atoms. The diphosphate anion displays an eclipsed conformation with a torsion angle of 29.46(1)° along O4, P1, O6, P1 and O4 and a rather small bridging angle ∠(P,O,P) = 132.1(4)°.

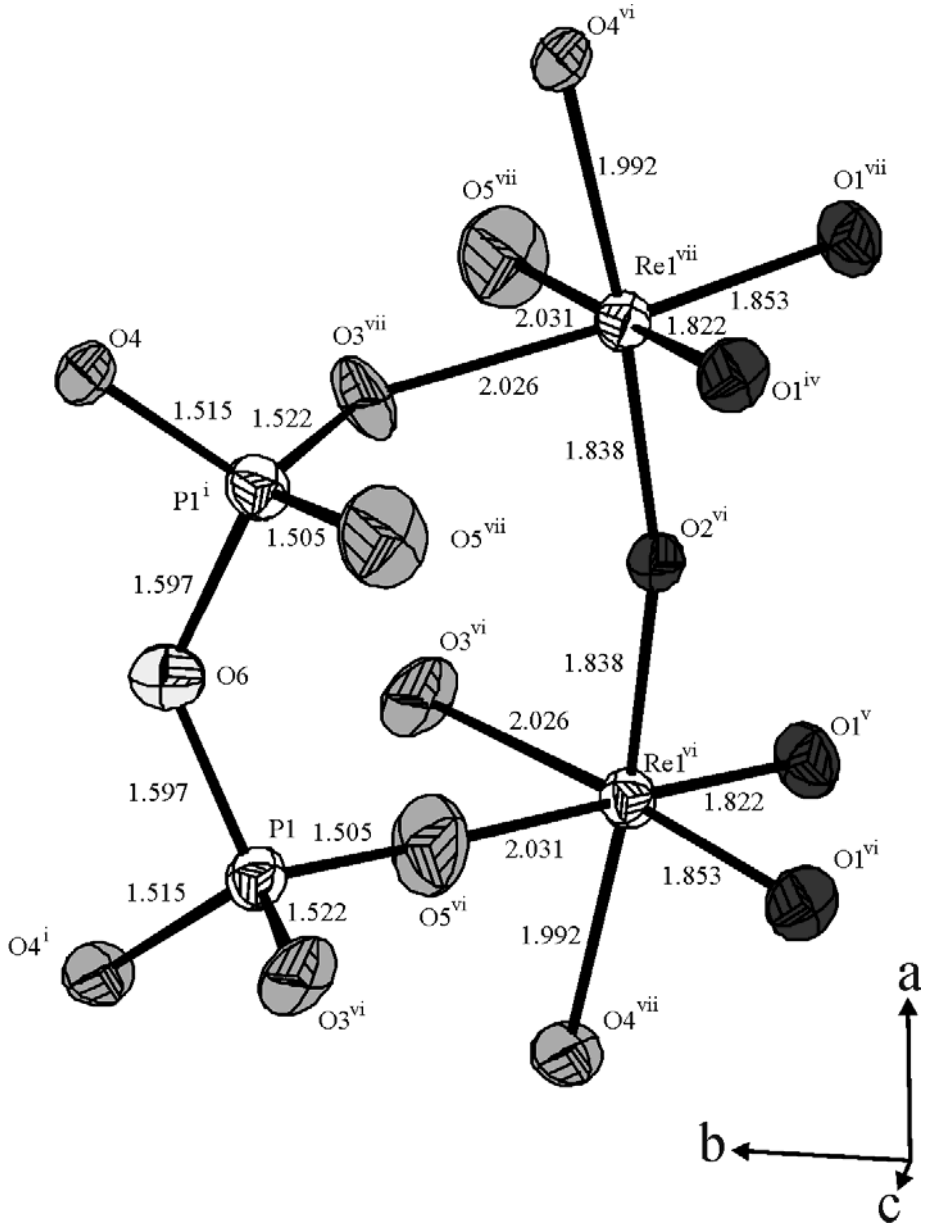

Figure 12.4 ORTEP representation of [ReO_6] octahedra and [P_2O_7] groups in $Re_2O_3(P_2O_7)$. Oxygen atoms bridging two rhenium atoms in dark grey, bridging two phosphorus atoms in light grey, bridging rhenium and phosphorus in grey; ellipsoids at 90% probability level.

In the infrared spectrum of $Re^{V}_2O_3(P_2O_7)$ the bands at about 1061 cm^{-1}, 1089 cm^{-1}, and 1139 cm^{-1} are attributed to the P-O_{ext} stretching vibrations of PO_3 groups (see Figure 12.5). On the other hand, an antisymmetric stretching vibration at 958 cm^{-1} and a weak symmetric stretching vibration at 750 cm^{-1} are corresponding to the P-O-P bridge. These vibrations are typical for many diphosphates [260]. The absorption band at 913 cm^{-1} is likely to be related to the Re-O vibration as this result is consistent with that ReO_3 [261]. The symmetric stretching vibration of Re-O-Re is observed at 453 cm^{-1} which is very close to that of the symmetric stretching vibration of Re-O-Re bridge of Re_2O_7 [262]. However, both the high valency of the cation (Re^{5+}) and the low symmetry of the diphosphate anion make it very difficult to assign the other bands.

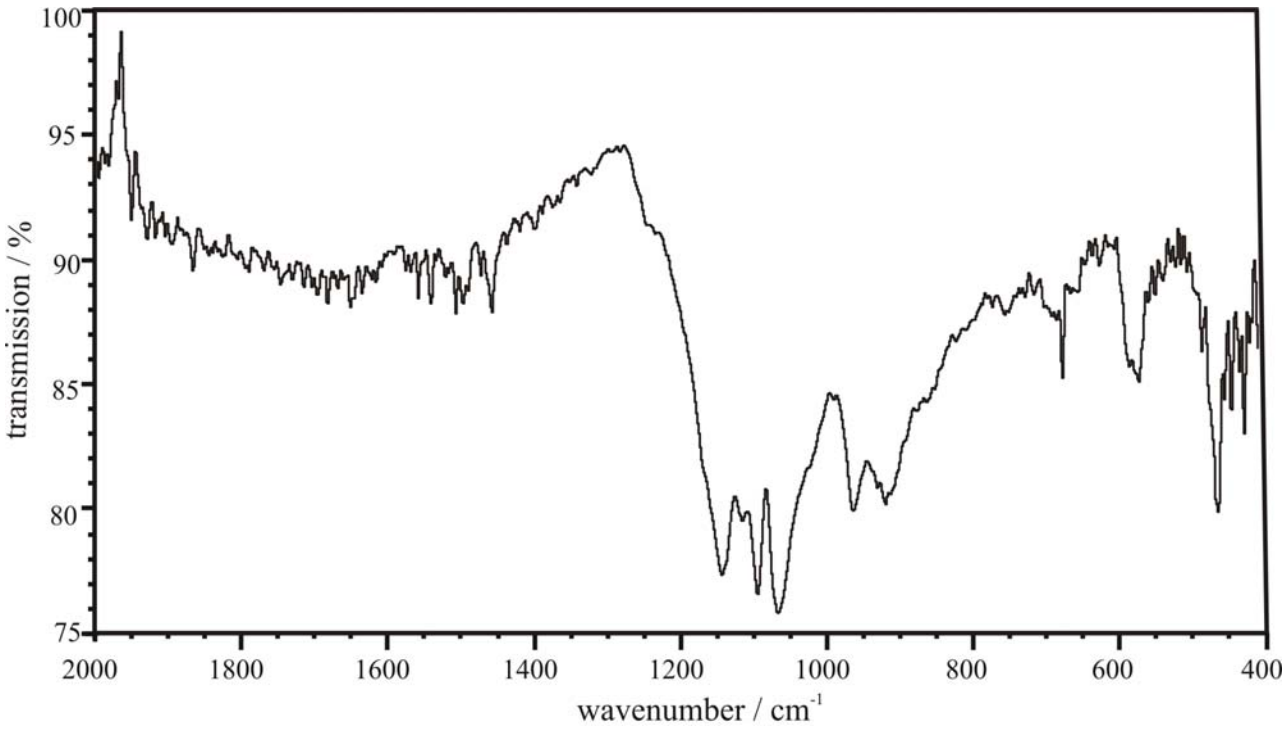

Figure 12.5 IR spectrum of $Re_2O_3(P_2O_7)$.

13 Rhenium(VI)-oxidephosphate $Re_2O_3(PO_4)_2$

13.1 Introduction

In ternary systems *M* / P /O, anhydrous phosphates of the transition metal at its hexavalent oxidation state are observed only for tungsten and moybdenum. Although, these elements form phosphates in a general formula of $M^{VI}{}_2P_2O_{11}$, they are different from their structural point of view. Tungsten forms an orthophosphate, $W^{VI}{}_2O_3(PO_4)_2$, which exhibits an orthorhombic [75] and a monoclinic [72, 73, 74] modification, while molybdenum forms the pyrophosphate $(Mo^{VI}O_2)_2P_2O_7$ with four different modifications. Besides the structurally characterized orthorhombic γ-$(Mo^{VI}O_2)_2P_2O_7$ [24, 25] and monoclinic, α-$(Mo^{VI}O_2)_2P_2O_7$ [25, this thesis] (see Chap. 9), an intermediate β-phase was also reported which was assumed to adopt an incommensurately modulated structure [25]. In addition to this, the fourth modification is known as δ-$(MoO_2)_2(P_2O_7)$ [129]. Apart from this, a mixed-metal phosphate, $Mo^{VI}W^{VI}O_3(PO_4)_2$ [263] was characterized. Another class of phosphates exists also at 6+ oxidation state of tungsten and molybdenum with the general formula $M^{VI}P_2O_8$. Molybdenum forms a metaphosphate, $Mo^{VI}O_2(PO_3)_2$ [26], while tungsten exhibits a pyrophosphate, $W^{VI}O(P_2O_7)$ [76, 75].

The existence and the stability of the oxide, $M^{VI}O_3$ (M^{VI} = Mo [264], W [265], Re [36]); and oxide halides, $M^{VI}OX_4$ (*M* = Mo [266, 267], W [268, 269], Re [39, 40]; *X* = F, Cl), indicate the similar chemical properties of Mo, W and Re. This similarity can be easiliy understood by considering the diagonal relationship between molybdenum and rhenium, as well as its neighborhood to tungsten. Owing to these interesting similarities in the chemical properties of these three elements, in addition to molybdenum(VI)- and tungsten(VI)-phosphates one may clearly expect rhenium(VI)-phosphates. As a consequence, we attributed our effort in order to synthesize and crystallize hexavalent rhenium phosphates.

Consequently, we have synthesized and crystallized a rhenium(VI) phosphate, $Re^{VI}{}_2O_3(PO_4)_2$. According to literature, electronic spectra and magnetic behaviour of the compounds of $5d^1$ element are not well characterized. In the present work, we report on synthesis, crystallization, crystal structure, electronic absorption spectrum and magnetic behaviour of a rhenium(VI)-oxidephosphate, $Re^{VI}{}_2O_3(PO_4)_2$.

13.2 Experimental

13.2.1 Syntheses and Crystallization

Microcrystalline powders of $Re_2O_3(PO_4)_3$ were obtained by isothermal heating of ReO_3 and P_4O_{10} (Equation 13.1) or via reduction of Re_2O_7 by red phosphorus in presence of P_4O_{10} (Equation 13.2) in sealed silica tubes ($l \approx 11$ cm, $d \approx 1.5$ cm, $V \approx 20$ cm ^{3}). ReO_3 was synthesized according to literature [84, 125]. Re_2O_7 and P_4O_{10} were handled in a glove bag in argon atmosphere since both materials are hygroscopic. The starting materials were at least of p.a. grade. The reactions were always conducted in two steps, i.e. prereaction by mild heating with a Bunsen burner and subsequent heating, keeping the starting materials at 450 °C in a two zone furnace, with the other end of the tube at 550 °C. Iodine (≈32 mg) was used as mineralizer. To get a single-phase product approximately 40% more P_4O_{10} and 20% less red phosphorus with respect to the stoichiometry of $Re_2O_3(PO_4)_2$ were used. At about 700 °C, the reaction aiming for $Re_2O_3(PO_4)_2$ led to ReP_2O_7 (Equation 13.3a). Even without phosphorus as reductand ReO_3, $Re_2O_3(PO_4)_2$, and ReP_2O_7 exist in equilibrium besides $O_2(g)$ at all temperatures in the range $450^oC \leq \vartheta \leq 650^oC$ (Equation 13.3b). Reaction of Re_2O_7 and P_4O_{10} at $\vartheta \leq 400°C$ led to the formation of $ReO_2(PO_4)$ (see Equation 13.3c) and $(Re_2O_5)Si^o_2[Si^t_2O(PO_4)_6]$ [this thesis] (see Chapter14).

$$4\ ReO_3 + P_4O_{10} \rightarrow 2\ Re_2O_3(PO_4)_2 \qquad (13.1)$$

$$5\ Re_2O_7 + 2\ P + 2P_4O_{10} \rightarrow 5\ Re_2O_3(PO_4)_2 \qquad (13.2)$$

$$2\ Re_2O_7 + P_4O_{10} \rightarrow 2\ ReO_3 + 2\ ReP_2O_7 + 2\ O_2(g) \quad (\vartheta \geq 700°C) \qquad (13.3a)$$

$$2\ Re_2O_7 + P_4O_{10} \rightarrow 2\ Re_2O_3(PO_4)_2 + O_2(g) \quad (450^oC \leq \vartheta \leq 650^oC) \qquad (13.3b)$$

$$Re_2O_7 + ½\ P_4O_{10} \rightarrow 2\ ReO_2(PO_4) \quad (\vartheta \leq 400°C) \qquad (13.3c)$$

The crystallization of $Re_2O_3(PO_4)_2$ was achieved by chemical vapour transport (CVT) in sealed silica tubes ($l \approx 11$ cm, $d \approx 1.5$ cm, $V \approx 20$ cm ^{3}), which were placed in a temperature gradient of electrically heated two zone furnaces. Figure 13.1 shows crystals of $Re_2O_3(PO_4)_2$ obtained by CVT. A summary of representative experiments on synthesis, thermal behaviour and CVT of $Re_2O_3(PO_4)_2$ is given in Table 13.1.

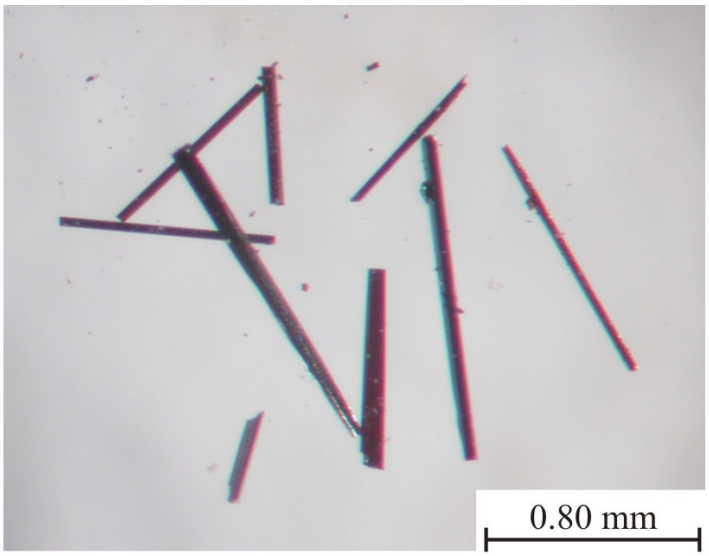

Figure 13.1 Crystals of $Re_2O_3(PO_4)_2$ obtained by CVT.

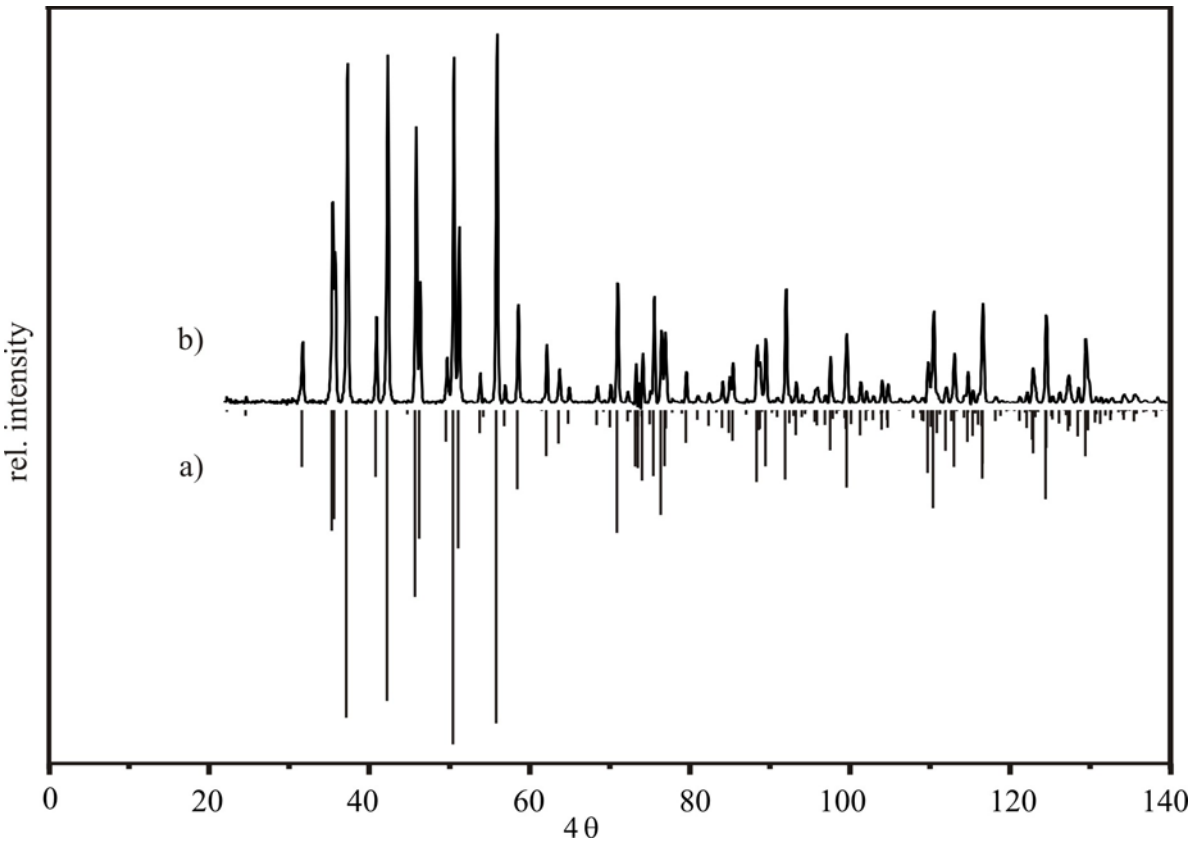

Figure 13.2 Comparison of the simulation (a) and Guinier photograph of $Re_2O_3(PO_4)_2$ (b).

Table 13.1 Experiments for synthesis and chemical vapour transport of $Re^{VI}_2O_3(PO_4)_2$.

starting solids / mg		I_2 / mg	temp.[a] / °C	time / h	products(source) (according to Guinier photographs)	products(sink)
ReO_3	112.2	30	400 → 500	96		
P_4O_{10}	67.1		500 → 400	240		no transport
			600 → 500	240	ReP_2O_7 / $Re_2O_3(PO_4)_2$	$Re_2O_3(PO_4)_2$ / ReP_2O_7
ReO_3	183.9	48	B. B.[b]	4		
P_4O_{10}	74.1		550 → 650	120		no transport
			600 → 500	216	ReO_3 / $Re_2O_3(PO_4)_2$ / ReP_2O_7	$Re_2O_3(PO_4)_2$ / ReO_3 / ReP_2O_7
ReO_3	197.9	57	B. B.	1		
P_4O_{10}	59.9		550 → 650	120		no transport
			600 → 500	216	ReO_3 / ReP_2O_7 / $Re_2O_3(PO_4)_2$	ReO_3 / ReP_2O_7 / $Re_2O_3(PO_4)_2$
ReO_3	253.1	50	B. B.	3.5		
P_4O_{10}	97.2		500 → 550	170		no transport
			600 → 500	240	ReP_2O_7 / $Re_2O_3(PO_4)_2$	$Re_2O_3(PO_4)_2$ / ReP_2O_7
$Re_2P_2O_{11}$	120.0	24	500 → 400	120		no transport
			600 → 500	168	$Re_2O_3(PO_4)_2$ / ReP_2O_7	no transport
Re_2O_7	131.5	----	400 → 300	120	----	$ReO_2(PO_4)$
P_4O_{10}	55.8					
Re_2O_7	350.2	----	300 → 400	168		
P_4O_{10}	104.6		400 → 300	192	$(Re_2O_5)Si^o_2[Si^t_2O(PO_4)_6]$	$(Re_2O_5)Si^o_2[Si^t_2O(PO_4)_6]$
Re_2O_7	353.8	----	300 → 400	96		
P_4O_{10}	101.6		400 → 300	192		
			450 → 350	144	$Si^o_3[Si^t_2O(PO_4)_6]$	$(Re_2O_5)Si^o_2[Si^t_2O(PO_4)_6]$
Re_2O_7	571.5	32	600 → 700	96		no transport
P_4O_{10}	133.9		700 → 600	144	ReP_2O_7	ReP_2O_7 / $Re_2O_3(PO_4)_2$
P	12.4					
Re_2O_7	378.0	40	B. B.	~1/3		
P_4O_{10}	89.73		450	72		----
P	9.71		450 → 500	120	$Re_2O_3(PO_4)_2$ / ReO_3	
Re_2O_7	255.7	47	B. B.	3		
P_4O_{10}	85.1		450 → 550	144	$Re_2O_3(PO_4)_2$	----
P	5.1					

[a] Given are the various heating periods for an ampoule. Starting solid were always at the left side of the arrow. Solid reaction products were characterized by their XRPD pattern after the final heating period, only.

[b] B. B.: mild heating in the Bunsen burner flame.

13.2.2 Characterization

Energy-dispersive X-ray fluorescence analyses [116, 117, 118] (EDX system, scanning microscope DMS 940, Zeiss) showed no additional elements besides rhenium, phosphorus and oxygen.

For identification, examination of the purity, and for determination of the lattice parameters of $Re_2O_3(PO_4)_2$ image-plate **(*IP*) Guinier photographs** (Guiner camera FR-552 Enraf-Nonius, quartz-monochromator, Cu-Kα_1 radiation, λ = 1.54052 Å, α-SiO_2 as internal standard, BAS-TR 2025 image plate film (Fa. Fuji), BAS-1800 scanner (Fa. Fuji), software: BASREADER [151], AIDA [91] for digitization) were taken. Details on this method were already reported in literature [90, 152, 153]. Assignment of the powder pattern led to a = 6.2986(6)Å, b = 7.7965(6)Å, c = 15.271(1)Å (78 reflections with 32.47° ≤ 4θ ≤ 124.99°).

Single-crystal X-ray study. Intensity data were measured on a κ-CCD diffractometer (Enraf-Nonius Inc.) at ambient temperature. Structure determination and refinement was performed using the SHELX-97 [105] suite in WinGx [135] framework. Sarting parameters for the single-crystal structure refinement were obtained by Direct methods in SHELXS [137]. Thus rhenium and phosphorus positions were revealed. Subsequent Δ-Fourier syntheses allowed the localization of the oxygen atoms. An empirical absortion correction with mutiscan [115] was applied.

Details concerning data collection, structure solution and refinement of $Re_2O_3(PO_4)_2$ are summarized in table 13.2. The final atomic coordinates and displacements parameters are reported in table 13.3. Selected interatomic distances and angles are listed in table 13.4. Indexing of the Guinier simulation and anisotrpopic displacement parameters are given in Appendix B3 as (Table B3.1 and Table B3.2).

Table 13.2 $Re_2O_3(PO_4)_2$ Crystallographic data, structure solution and refinement.

crystal data	
chemical formula	$Re_2O_3(PO_4)_2$
formula weight (g/mol)	610.35
crystal system	orthorhombic
space group	*Pmcn* (no. 62)
a / Å	6.2986 (6)
b / Å	7.7965 (6)
c / Å	15.2714 (12)
V / Å^3	749.93(11)
Z	4
D_{calc} (g/cm³)	5.406
radiation, wavelength, monochromator	Mo-$K\alpha$ (λ = 0.71073 Å), graphite
μ (mm^{-1})	32.74
colour	Dark red crystal, reddish powder
data collection	
diffractometer	κ-CCD (NONIUS)
crystal size	~ 0.2 · 0.2 · 0.1
F(000)	1072.0
temperature	293 K
theta range / °	$0.998 \leq \theta \leq 30.034$
collected reflections	20576
independent reflections	1185
index ranges	$-8 \leq h \leq 8$
(whole sphere)	$-10 \leq k \leq 10$
	$-21 \leq l \leq 21$
refinement	
sofware	SHELX-97 [105]
absorption correction	multi-scans [115]
no. of parameters used	86
R_1/wR_2 (for all data)	0.028 / 0.066
goof on F^2	1.234
weighting scheme	$w = 1/[\sigma^2(F_o^2) + (0.0208P)^2 + 11.98P]$
	where $P = (F_o^2+2F_c^2)/3$

Table 13.3 $Re_2O_3(PO_4)_2$. Atomic coordinates and displacement parameters. Standard deviations are given in parentheses.

atom	*x*	*y*	*z*	U_{eq} [Å^2] [a]
Re1	1/4	0.5522(4)	0.2865(2)	0.0084(1)
Re2	1/4	0.2430(0)	-0.0292(2)	0.0068(1)
P1	1/4	0.3765(2)	-0.2387(1)	0.0076(3)
P2	1/4	0.6406(2)	0.0665(1)	0.0064(3)
O1	1/4	0.7543(8)	-0.1675(4)	0.0206(16)
O2	1/4	0.4343(7)	0.3908(4)	0.0097(11)
O3	1/4	0.3099(8)	0.2311(4)	0.0122(12)
O4	1/4	0.3941(7)	-0.1393(3)	0.0135(13)
O5	1/4	0.1163(8)	0.0587(4	0.0146(13)
O6	1/4	0.6386(8)	0.1657(4)	0.0157(13)
O7	1/4	0.4574(9)	0.0346(5)	0.0400(28)
O8	0.4416(8)	0.4725(6)	-0.2774(3)	0.0142(9)
O9	0.0606(10)	0.7396(8)	0.0324(3)	0.0297(15)

$U_{eq} = (⅓)\Sigma_i\Sigma_j U_{ij} a_i^* a_j^* \mathbf{a}_i \cdot \mathbf{a}_j$

Table 13.4 Selected interatomic distances (Å) and angles (°) for $Re_2O_3(PO_4)_2$. Standard deviations are given in parentheses.

d(Re1-O1$_t$)	1.662(6)	*d*(Re2-O5$_t$)	1.667(6)
d(Re1-O2$_b$)	1.838(6)	*d*(Re2-O2$_b$)	1.844(5)
d(Re1-O8) 2x	1.957(5)	*d*(Re2-O7)	1.935(7)
d(Re1-O6)	1.964(6)	*d*(Re2-O9) 2x	1.961(6)
d(Re1-O3)	2.070(6)	*d*(Re2-O4)	2.053(6)
∠(Re1,O2,Re2)	161.4(4)		
d(P1-O3)	1.524(6)	*d*(P2-O7)	1.508(7)
d(P1-O4)	1.525(6)	*d*(P2-O9) 2x	1.513(5)
d(P1-O8) 2x	1.537(5)	*d*(P2-O6)	1.515(6)
∠(Re1,O6,P2)	160.5(4)	∠(Re2,O4,P1)	139.8(4)
∠(Re1,O8,P1)	139.3(3)	∠(Re2,O7,P2)	168.6(6)
∠(Re1,O3,P1)	138.3(4)	∠(Re2,O9,P2)	146.1(4)

The **electronic absorption spectrum** (see Figure 13.3) of a single-crystal of $Re^{VI}_2O_3(PO_4)_2$ (0.1 0.05 0.02 mm^3) was measured at ambient temperature using a strongly modified CARY 17 microcrystal spectrometer (spectral services, ANU Canberra, Australia [121, 122]. The spectrometer allows measurement of polarized absorption spectra of very small single-crystals with diameters down to 0.1 mm in the UV/Vis/NIR range (36000 $cm^{-1} \geq \tilde{\nu} \geq 5800$ cm^{-1}). The spectrum shows one weak absorption at $\tilde{\nu} = 12000$ cm^{-1}. Above $\tilde{\nu} = 16000$ cm^{-1} all light is absorbed by $Re^{VI}_2O_3(PO_4)_2$.

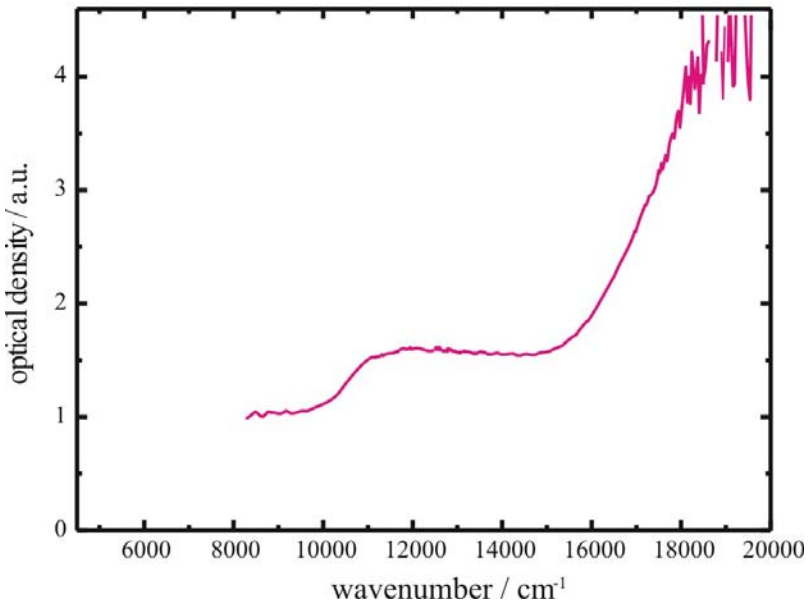

Figure 13.3 Electronic absorption spectrum of $Re_2O_3(PO_4)_2$.

Vibrational spectra of $Re_2O_3(PO_4)_2$ (see Figure 13.4) were measured on a FT-IR (IFS 113v, BRUKER) and on a FT-Raman spectrometer (RFS 100, BRUKER). For IR investigations tablets of the phosphate dispersed in KBr were used. For the Raman spectrum the pure material was used.

Magnetic susceptibility of $Re_2O_3(PO_4)_2$ (see Figure 13.5) as a function of temperature was measured in a Quantum Design Physical-Property-Measurement-System (Institut für Anorganische und Analytische Chemie, Uni Münster) in the temperature range 5 - 300 K with magnetic flux densities up to 80 kOe. The sample was packed in kapton foil and attached to the sample holder rod of the VSM. The susceptibility given in Figure 13.5 is corrected for the diamagnetic contribution of the core electrons. Based on the diamagnetic susceptibilities $\chi_{dia}(Re^{6+}) = -16 \cdot 10^{-6}$ mol/cm^3, $\chi_{dia}(O^{2-}) = -12 \cdot 10^{-6}$ mol/cm^3, and $\chi_{dia}(PO_4^{3-}) = -47 \cdot 10^{-6}$ mol/cm^3 [270, 271, 272] the correction $\chi_{dia}(Re_2O_3(PO_4)_2) = -162 \cdot 10^{-6}$ mol/cm^3 was estimated.

Using $\mu_{exp}/\mu_B = 2.8279 \cdot (T \cdot \chi_{mol})^{1/2}$ the magnetic moment per Re^{6+} ion (Figure 13.5) was calculated.

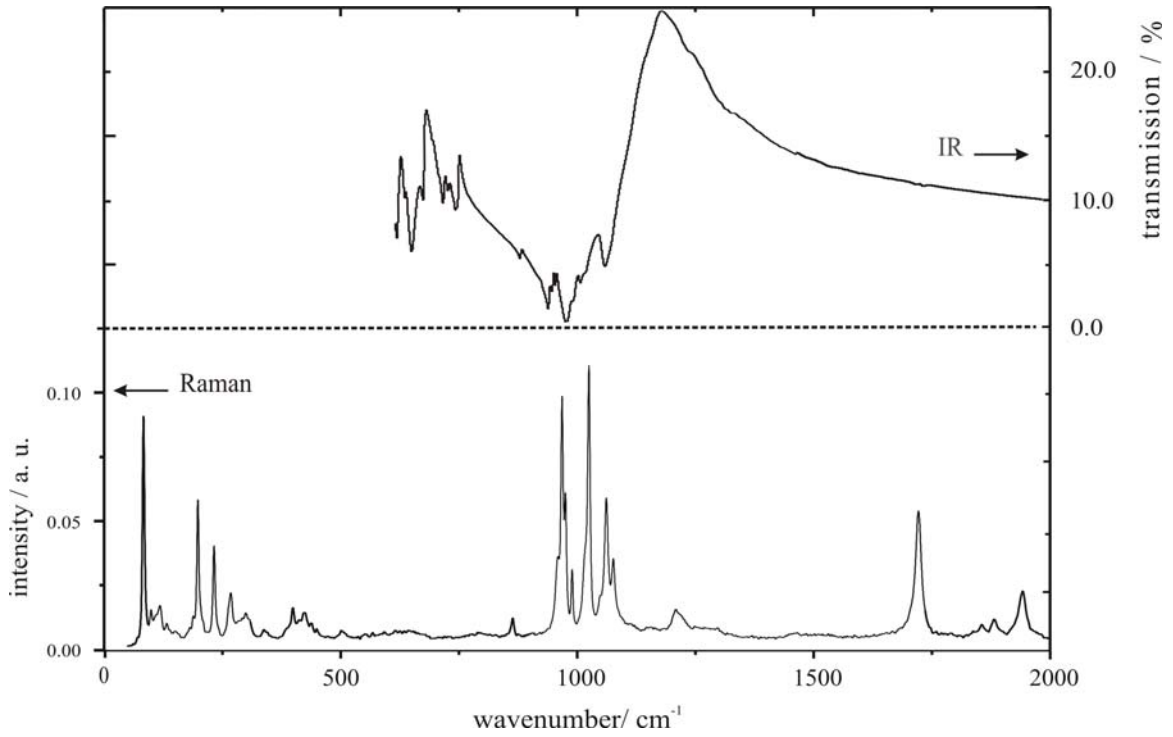

Figure 13.4 Vibrational spectra of $Re_2O_3(PO_4)_2$.

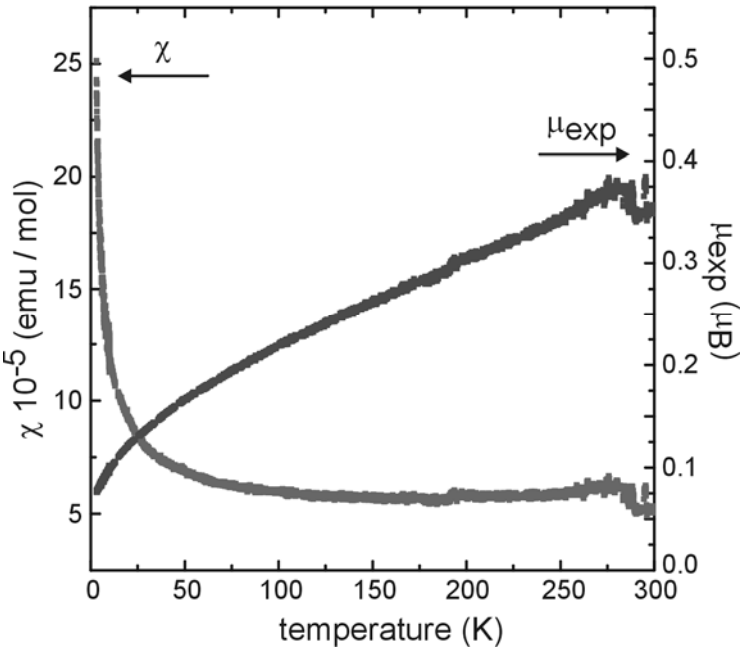

Figure 13.5 Magnetic susceptibility χ vs. T and magnetic moment μ vs. T for $Re_2O_3(PO_4)_2$.

13.3 Results and Discussions

13.3.1 Syntheses and Crystallization

In contrast to most other transition metal phosphates, for $Re_2O_3(PO_4)_2$ and most other rhenium phosphates, both, thermal reduction as well as thermal decomposition into $P_4O_{10}(g)$ is observed already at temperatures as low as 450°C. Thus, synthesis of rhenium phosphates, other than ReP_2O_7, requires precise control of $p(O_2)$, $p(P_4O_{10})$, and temperature. The empirically optimized experimental conditions for the synthesis of $Re_2O_3(PO_4)_2$ indicate that the rhenium(VI)-oxidephosphate is stable at T > 500°C only in equilibrium with considerable pressures $p(O_2)$ and $p(P_4O_{10})$.

Due to the limited thermal stability of $Re_2O_3(PO_4)_2$ and the high volatility of $ReO_3I(g)$ and $P_4O_{10}(g)$ the method of chemical vapour transport (CVT) [85] works nicely for crystallization of the oxide phosphate. Migration proceeds from higher to lower temperature ($T_2 \rightarrow T_1$, $T_2 > T_1$, $\Delta T \approx 100$ °C) due to endothermic reactions (see Table 13.1). Phosphorus forms various volatile oxides P_4O_n, $6 \leq n \leq 10$, PO(g) and $PO_2(g)$. Among them $P_4O_{10}(g)$ seems to be the most important species for the transport of phosphorus due to its already known thermodynamic stability [133, 134] under the given (oxidizing) conditions. The stability and importance of gaseous ReO_3X (X = OH, I) for CVT of rhenium oxides has been discussed by SCHÄFER [84]. Hence, CVT of $Re_2O_3(PO_4)_2$ is expected to proceed according to reaction 13.4. In our experiments P_4O_{10}, which is hygroscopic, was used as a starting material, so we may expect the presence of small amounts of water in the ampoules. Due to hydrolysis of $ReO_3I(g)$ and $P_4O_{10}(g)$ reactions (13.5) and (13.6) are expected to contribute to the composition of the gas phase.

$$Re_2O_3(PO_4)_2(s) + I_2(g) \rightarrow 2\ ReO_3I(g) + {}^1/_2P_4O_{10}(g) \qquad (13.4)$$

$$n/4\ P_4O_{10}(g) + n/2\ H_2O(g) \rightarrow (HPO_3)_n(g) \qquad (n = 1, 3, 4) \qquad (13.5)$$

$$2\ ReO_3I(g) + H_2O(g) \rightarrow 2ReO_3OH(g) + 2\ HI(g) \qquad (13.6)$$

13.3.2 Crystal structure

While $[Re_2O_{10}]$ groups and $[ReO_6]$ octahedra in various degrees of condensation are frequently encountered in the crystal chemistry of oxo-rhenates [273], isolated $[Re_2O_{11}]$ units were hitherto unknown. In the crystal structure of rhenium(VI)-oxidephosphate, $Re_2O_3(PO_4)_2$, double-octahedra $[Re_2O_{11}]$ and $[PO_4]$ tetrahedra form chains running parallel to the crystallographic *c*-axis (see Figure 13.6). These are linked to four adjacent chains via the phosphate groups only. There are no direct links via oxygen atoms from one $[Re_2O_{11}]$ group to another. Despite the same space group and very similar lattice parameters the orthorhombic modification of $W_2O_3(PO_4)_2$ [74] is not immediately structurally related to rhenium(VI)-oxidephosphate.

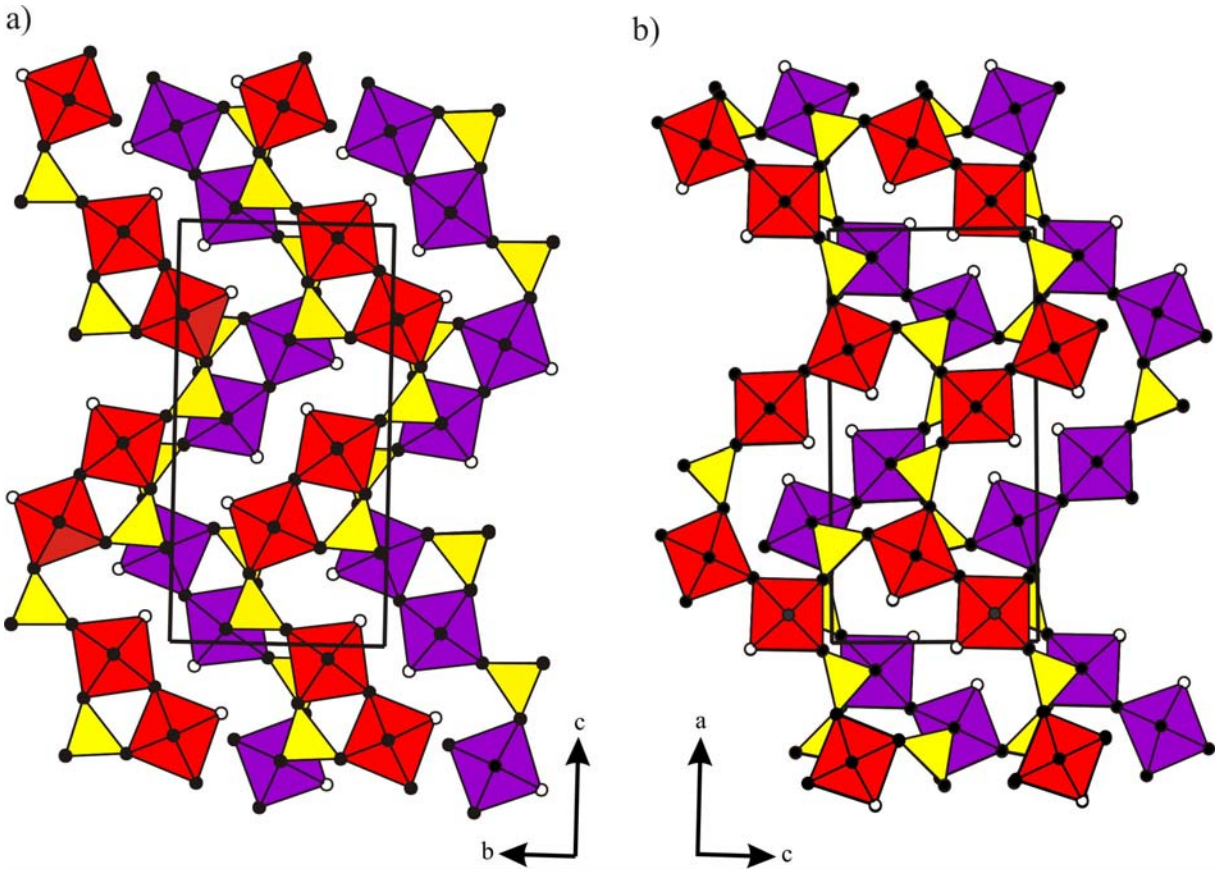

Figure 13.6 Crystal structure of $M_2O_3(PO_4)_2$ [*M* = Re (a), W(b)] with ribbons of tetrahedra $[PO_4]$ (yellow) and $[M_2O_{11}]$ double-octahedra (red and lila). Lila and red $[Re_2O_{11}]$ are at x = 3/4 and x = 1/4, respectively. Lila and red $[W_2O_{11}]$ are at y = 3/4 and y = 1/4, respectively Open circles represent oxygen atoms connected to rhenium only (Diamond version 3.2c [138]).

The Re^{6+} ions in $Re_2O_3(PO_4)_2$ show a distorted octahedral coordination by oxygen atoms with 1.66Å ≤ *d*(Re-O) ≤ 2.07 Å (see Figure 13.7, Table 13.4). Four oxygen ligands are provided by

phosphate groups. The coordination sphere of Re1 and Re2 is completed by one oxygen atom bridging two rhenium atoms (d(Re-O_b) ≈ 1.84 Å) and by one terminal oxygen atom per rhenium (d(Re-O_t) ≈ 1.66 Å). The latter distance might be interpreted as $(Re{=}O)^{4+}$ group, a structural feature so far unobserved for oxo-compounds of hexavalent rhenium. In agreement with literature data for dinuclear rhenium(V) coordination compounds of the type $Re_2O_3L_8$ [274] signals in the Raman spectrum (see Fig. 13.4) observed around 970 cm^{-1} are assigned to ν(Re=O).

The phosphate groups have a geometric structure close to an ideal tetrahedron, with all oxygen atoms coordinated to just rhenium (see Figure 13.7, Table 13.4).

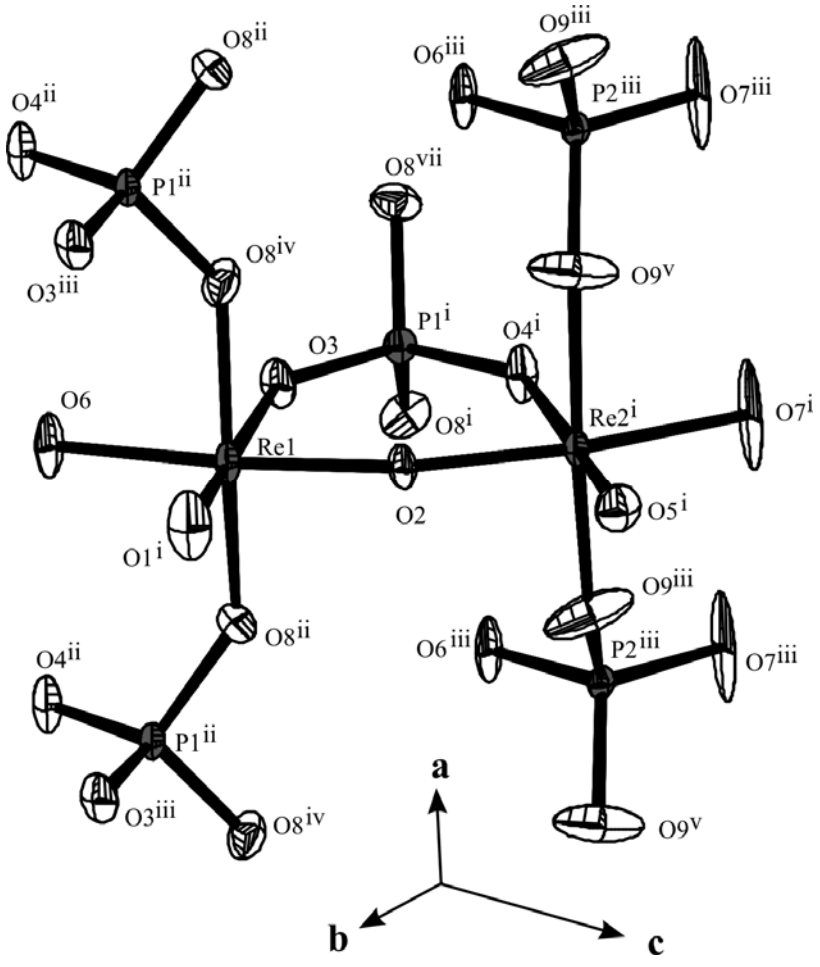

Figure 13.7 ORTEP representation of the $[PO_4]$ and $[Re_2O_{11}]$ groups in $Re_2O_3(PO_4)_2$. Ellipsoids with 70% probability.

13.3.3 Electronic structure

Due to the low symmetry of the ligand-field around the Re^{6+} ions and the strong interaction between rhenium and the double-bonded oxygen a quantitative treatment of the Re^{6+} *d*-electron states was not attempted. The rather low magnetic moment observed for Re^{6+} in $Re_2O_3(PO_4)_2$ ($0.07 \leq \mu_{exp}/\mu_B \leq 0.38$; $1.4\ K \leq T \leq 300\ K$; Figure 13.5) and its strong temperature dependence is indicative for strong spin-orbit coupling, as expected for a $5d^1$ system [229]. In addition, the temperature dependence might be a consequence of the low-symmetry ligand field. We relate the absorption band observed around $\tilde{\nu} = 12000\ cm^{-1}$ (see Figure 13.3) to a *d-d* electronic transition, due to its rather low absorbance. The strong absorption at $\tilde{\nu} > 16000\ cm^{-1}$ is likely to originate from a charge transfer transition $O^{2-} \rightarrow Re^{6+}$. Whether additional *d-d* transitions at higher wavenumbers are thus obscured remains unclear.

14 Rhenium(VII)-oxidephosphates $Re^{VII}O_2(PO_4)$ and $(Re^{VII}{}_2O_5)Si_2°[Si_2{}^tO(PO_4)_6]$

14.1 Introduction

In anhydrous phosphates, transition metals tend to prefer lower oxidation states. This preference is exemplified by $Ti^{III}PO_4$ [275], $V^{II,III}{}_2O(PO_4)$ [276], $Cr^{II}{}_3(PO_4)_2$ [277, 278], $Cr^{II}{}_2P_2O_7$ [279, 280] or $Mo^{III}(PO_3)_3$ [32]. Obviously, even phosphates of the non-existing binary oxides "CrO" and "Mo_2O_3" can be obtained. With the recent characterization of $Re^{VI}{}_2O_3(PO_4)_2$ [281] and $Re^{V}{}_2O_3(P_2O_7)$ [282] in addition to the long known pyrophosphate $Re^{IV}P_2O_7$ [81, 82, 83] our attention was attracted by the thermodynamic stability of phosphates containing rhenium in its various oxidation states. Eventually, the question arose whether a phosphate of Re_2O_7 or even OsO_4 might exist.

The acid-base concept by LUX and FLOOD treats the formation of a solid or liquid ternary oxide from its binary components as oxide ion exchange reaction [283, 284]. Based on the strength of acid (oxide ion acceptor) and base (oxide ion donor) generally a good estimate for the enthalpy of reaction is possible [285]. Following this concept, the above mentioned preference for lower oxidation states of transition metals in phosphates can readily be rationalized. On the other hand, backed by the same concept, one would not expect two acidic oxides like Re_2O_7 and P_4O_{10} to form a thermodynamically stable ternary oxide. Actually, not even a clear distinction between acid and base in this particular reaction appears to be possible.

In this present work, we report on synthesis and crystal structure of $Re^{VII}O_2(PO_4)$ and $(Re^{VII}{}_2O_5)Si_2°[Si^t{}_2(PO_4)_6]$, the first phosphates of a heptavalent metal. Chemical bonding in these compounds is further characterized by ^{31}P- and ^{29}Si-MAS-NMR, UV/Vis and IR spectroscopy.

14.2 Experimental

14.2.1 Syntheses and Crystallization

Synthesis and crystallization of $Re^{VII}O_2(PO_4)$ was achieved from Re_2O_7 (ABCR, 99.99%) and P_4O_{10} (KMF Laborchemie, 97%). Mixtures of the starting materials ($\Sigma m \approx 400$ mg) were heated in sealed evacuated silica tubes ($l \approx 11$ cm, $d \approx 1.5$ cm, $V \approx 20$ cm^3) in a temperature gradient 400 → 300 °C for two days. After the experiment, the high temperature end of the ampoule was removed first from the furnace and cooled in liquid nitrogen so that condensation of the equilibrium gas phase occurs rapidly in the source region. Thus, contamination of the crystals grown in the deposition region at the lower temperature was avoided.

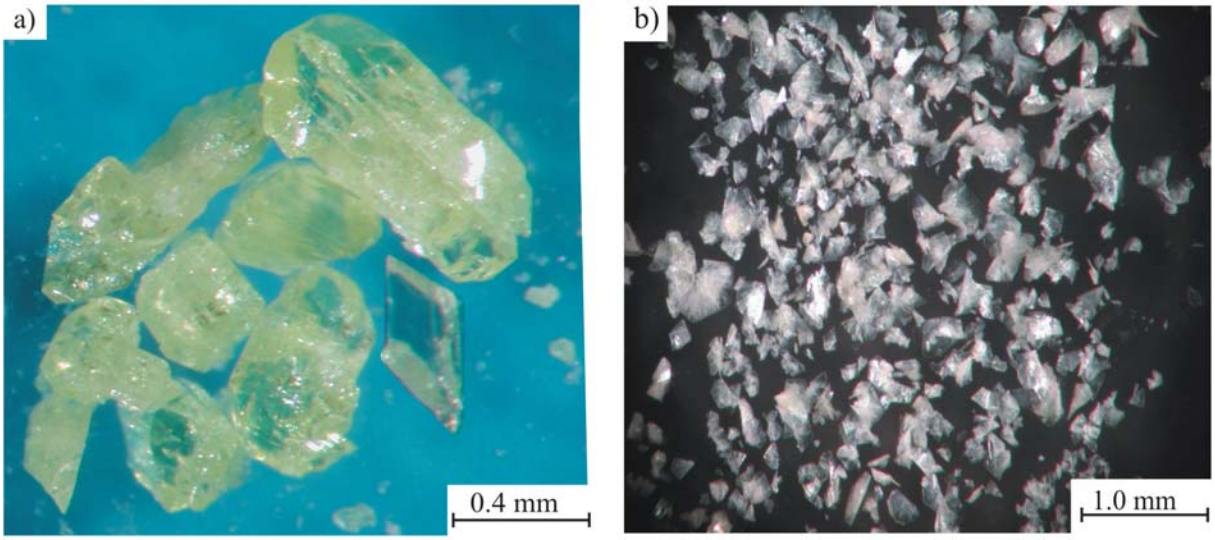

Figure 14.1 Photograph of the crystals of $Re^{VII}O_2(PO_4)$ (a) and $(Re^{VII}_2O_5)Si^o_2[Si^t_2O(PO_4)_6]$ (b).

Occasionally, formation of $Re^{VII}O_2(PO_4)$ was accompanied by the occurrence of the silicophosphate $(Re^{VII}_2O_5)Si^o_2[Si^t_2O(PO_4)_6]$ (see Figure 14.1). The amount of the latter could be reduced to a minimum by using prereacted (ϑ = 300°C, 5 days) oxide mixtures as starting material, avoiding reaction temperatures higher than 400°C, and by heating periods not longer than 2 days. Longer reaction times and higher temperatures led to increasing amounts of $(Re^{VII}_2O_5)Si^o_2[Si^t_2O(PO_4)_6]$ and eventually the formation of silicon silicophosphate $Si^o_3[Si^t_2O(PO_4)_6]$ [222] besides ReO_3 as reaction products. In one experiment a not yet structurally characterized polymorph of $Re^{VII}O_2(PO_4)$ (see Figure 14.2) was obtained along with $(Re^{VII}_2O_5)Si^o_2[Si^t_2O(PO_4)_6]$ when a mixture of Re_2O_7 (449.3 mg, 0.93 mmol) and P_4O_{10}

(198.5 mg, 0.70 mmol) with a molar ratio $n(Re_2O_7)/n(P_4O_{10})$ = 1.33 was heated at 400 → 300°C for about seven days. Re_2O_7 and P_4O_{10} were handled in a glove bag in argon atmosphere since both compounds are hygroscopic. Further details on syntheses and crystallization experiments are summarized in Table 14.1.

In experiments aiming at "$VReO_6$" a mixture of Re_2O_7 (259.1 mg) and V_2O_5 (97.4 mg) was heated in a teprerature gradient 450 → 350°C for 4 days. Ice blue crystal were deposited in the middle of the ampoule whereas the sink contains only green crystals of $VO(ReO_4)_2$ [71]. However, unsatisfactory results, the structuaral refinement of the ice blue crystal is likely to a second polymorph of $VO(ReO_4)_2$ [71] so called α-$VO(ReO_4)_2$. Details on the crystal structure of α-$VO(ReO_4)_2$ are given in Appendix C1.

Table 14.1 Experiments for synthesis and crystallization of $ReO_2(PO_4)$.

starting solids / mg		**$n[Re_2O_7]$ / $n[P_4O_{10}]$**	**I_2 / mg**	**temperature[a] / °C**	**time / d**	**products (source) (according to *IP* Guinier photographs)**	**products (sink)**
Re_2O_7	190.7	1.20	---	400→300	7	---	$ReO_2(PO_4)$
P_4O_{10}	93.8						
Re_2O_7	449.3	1.33	---	400→300	7	---	"$RePO_6$"[b] /
P_4O_{10}	198.5						$Re_2O_5Si_2[Si_2O(PO_4)_6]$
Re_2O_7	177.9	1.34	26.0	B.B.[c]	1/24	---	
P_4O_{10}	77.6			300	5		$ReO_2(PO_4)$
				400→300	2		
Re_2O_7	144.5	1.36	---	400→255	6	---	$ReO_2(PO_4)$ /
P_4O_{10}	62.3						$Re_2O_5Si_2[Si_2O(PO_4)_6]$
Re_2O_7	118.68	1.36	---	380→300	5	---	$ReO_2(PO_4)$
P_4O_{10}	50.81						
Re_2O_7	290.8	1.37	---	350→250	7	---	$ReO_2(PO_4)$
P_4O_{10}	124.3						
Re_2O_7	131.5	1.38	---	400→300	7	---	$ReO_2(PO_4)$
P_4O_{10}	55.8						
Re_2O_7	289.6	1.38	---	250→150	7	ReO_2PO_4	---
P_4O_{10}	122.9						
Re_2O_7	273.6	1.67	---	300→400	5		
P_4O_{10}	95.9			400→500	1		
				400→300	5	deliquescence in air	$ReO_2(PO_4)$
Re_2O_7	479.6	1.77	---	120	3	deliquescence in air	---
P_4O_{10}	158.8						
Re_2O_7	250.3	1.78	---	400→300	4		
P_4O_{10}	82.2			550→600	18	$Si°_3[Si^t{}_2O(PO_4)_6]$	$Si°_3[Si^t{}_2O(PO_4)_6]$
Re_2O_7	159.9	1.82	---	200→300	4		
P_4O_{10}	51.5			300→400	3		
				350→300	5	$Re_2O_3(PO_4)_2$ /	$Re_2O_5Si_2[Si_2OPO_4)_6]$
				400→350	2	$Re_2O_5Si_2[Si_2OPO_4)_6]$	
Re_2O_7	170.7	1.91	---	250→350	4		
P_4O_{10}	52.3			400→350	6	$Re_2O_5Si_2[Si_2OPO_4)_6]$	$Re_2O_5Si_2[Si_2OPO_4)_6]$

Re_2O_7	291.9	1.93	---	300→400	3		
P_4O_{10}	89.0			350→300	5		
				400→350	6	deliquescence in air	$ReO_2(PO_4)$
Re_2O_7	156.7	1.95	---	400→270	6	---	$ReO_2(PO_4)$ //
P_4O_{10}	47.0						$Re_2O_5Si_2[Si_2O(PO_4)_6$
Re_2O_7	280.0	1.99	---	300	2	$ReO_2(PO_4)$ /	$ReO_2(PO_4)$ /
P_4O_{10}	82.3			400→300	5	$Re_2O_5Si_2[Si_2O(PO_4)_6]$	$Re_2O_5Si_2[Si_2O(PO_4)_6]$
Re_2O_7	194.5	2.0	---	400→300	3	$Re_2O_5Si_2[Si_2OPO_4)_6]$	$Re_2O_5Si_2[Si_2O(PO_4)_6]$
P_4O_{10}	56.9						
Re_2O_7	353.8	2.05	---	300→400	5		
P_4O_{10}	101.0			400→300	8		
				450→350	5	$Re_2O_5Si_2[Si_2OPO_4)_6]$	$Re_2O_5Si_2[Si_2OPO_4)_6]$
Re_2O_7	255.13	2.30	---	300→400	2	amorphous purple	$Re_2O_5Si_2[Si_2OPO_4)_6]$
P_4O_{10}	65.10			420→300	5	powder	
Re_2O_7	365.6	2.30	---	300→400	3	$Si°_3[Si^t{}_2O(PO_4)_6]$	$Si°_3[Si^t{}_2O(PO_4)_6]$
P_4O_{10}	92.9			420→300	10		
Re_2O_7	359.2	2.42	---	300→400	3	$Si°_3[Si^t{}_2O(PO_4)_6]$	$Si°_3[Si^t{}_2O(PO_4)_6]$
P_4O_{10}	86.8			420→300	8		
Re_2O_7	240.4	2.42	---	300→320	3	amorphous purple	$Re_2O_5Si_2[Si_2OPO_4)_6]$
P_4O_{10}	58.2			380→280	7	powder	
Re_2O_7	249.9	2.59	---	300→400	3	$Re_2O_5Si_2[Si_2OPO_4)_6]$	$Re_2O_5Si_2[Si_2OPO_4)_6]$
P_4O_{10}	56.4			400→300	5		
Re_2O_7	234.8	3.01	---	300→400	3	amorphous purple	$Re_2O_5Si_2[Si_2OPO_4)_6]$
P_4O_{10}	45.6			400→300	7	powder	
Re_2O_7	111.0	0.41	---	350→400	7	unknown /	---
P_4O_{10}	158.5					$Re_2O_5Si_2[Si_2OPO_4)_6]$	
SiO_2	56.1						
$ReO_2(PO_4)$	159	---	---	400→330	4	---	$ReO_2(PO_4)$

[a] Given are the various heating periods for an ampoule. Starting solids were always at the temperature at the left side of the arrow. Solid reaction products were characterized by their XRPD pattern after the final heating period, only.

[b] New polymorph of $ReO_2(PO_4)$.

[c] B. B.: mild heating in the Bunsen burner flame.

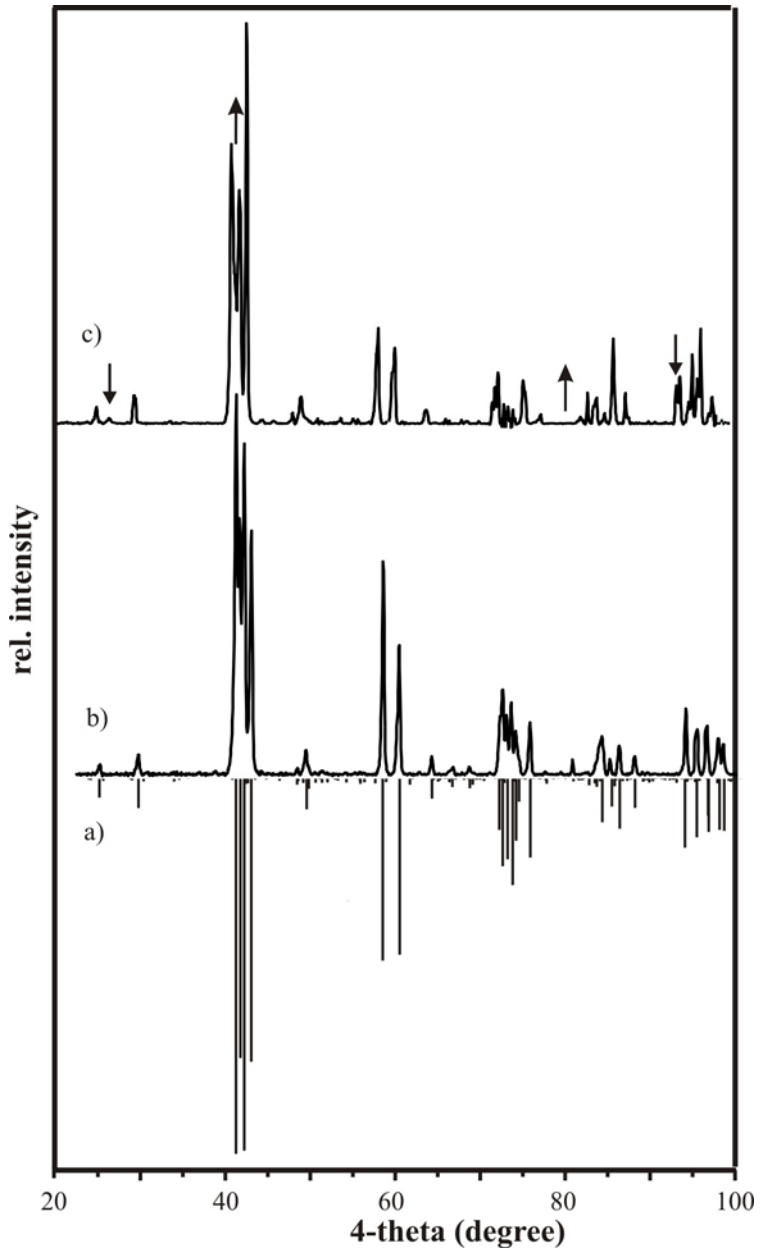

Figure 14.2 Comparison of the simulation and Guinier photograph of $ReO_2(PO_4)$ (diagram a and b respectively). Comparison of the Guinier photograph of $ReO_2(PO_4)$ to that of the new polymorph of "$RePO_6$" (diagram b and c, respectively). Downward arrows indicate the presence of additional lines and the upward arrows indicate the absence of the lines with respect to $ReO_2(PO_4)$.

14.2.2 Characterizations

For identification and examination of the purity of the obtained solids image-plate (*IP*) **Guinier-photographs** (Guinier camera FR-552 Enraf-Nonius, quartz-monochromator, Cu-Kα_1 radiation, λ = 1.54052 Å, BAS-TR 2025 image plate film (Fuji), BAS-1800 scanner (Fuji), software: BASREADER, [151], AIDA [91] for digitization) were taken. Details on this method were already reported in literature [90, 152, 153]. During X-ray exposure the samples were protected from air by scotch tape. Assignment of the powder pattern of $(Re^{VII}{}_2O_5)Si^{o}{}_2[Si^{t}{}_2O(PO_4)_6]$ led to a = 7.862(9) Å, b = 7.868(8) Å, c = 10.813(11) Å, α = 85.22(10)°, β = 73.071(10)°, and γ = 60.06(9)° (83 reflections with 27.05° ≥ 4θ ≥ 99.92°) which is close to the values from the X-ray single-crystal measurement. Rather high standard deviations of the derived cell parameters for this triclinic unit cell might be a consequence of the overlapping of many reflections in the powder pattern. Therefore, the final refinement was restricted to the cell parameters obtained from the X-ray single-crystal study.

In a first attempt **single-crystal** intensity data of $Re^{VII}O_2(PO_4)$ were measured on a κ-CCD diffractometer (Enraf-Nonius Inc.) up to 2θ = 70° at ambient temperature. Solution of the crystal structure with Direct Methods (SHELX-97 [105] suite in the WinGX [137] framework) led to a monoclinic structure model with space group *C*2/*c*. Though crystal chemically reasonable, refinement of the model converged only at high residuals R_1 = 0.16, wR_2 = 0.47. An attempt to obtain better starting parameters for the structure refinement with SUPERPFLIP [114] failed.

In a second attempt another single-crystal data set was measured up to 2θ = 90° at 123 K. These data were initially indexed on the basis of a triclinic cell (*P*1, a = 8.323(1) Å, b = 8.356(6) Å, c = 20.6474(2) Å, α = 87.32(0)°, β = 87.21(1)°, γ = 60.58(0)°). A triclinic structure model was obtained by SUPERFLIP [114] and refined using SHELX-97 [105] in the WinGX [137] framework. Refinement of this model led to R_1 = 0.075, wR_2 = 0.23 and residual electron density maxima at 21.2 $Å^{-3}$ (close to one Re) and -18.9$Å^{-3}$ (close to another Re). Program KPLOT [137] was used, in order to search for higher symmetry. Thus, on the basis of the Re and P positions of the triclinic model, a monoclinic unit cell and space group *C*2/*c* was suggested. The monoclinic unit cell (a = 14.403(1) Å, b = 8.412(1) Å, c = 20.647(3) Å, β = 93.16(8)°) is related to the triclinic cell by the transformation matrix [1 1 0 1 $\bar{1}$ 0 0 0 $\bar{1}$]. Eventually, the starting parameters for the refinement of the monoclinic model were obtained by SUPERFLIP [114]. The refinement with SHELX-97 [105] converged at R_1 = 0.04 and wR_2 = 0.10 leaving a residual electron density of 6.42 $Å^{-3}$ (close to Re3) and -10.02

$Å^{-3}$ (close to Re1). The finally obtained structure model differs from the very first model just by a coordinate shift along (-1/3, 0, 1/6). Obviously, the very first structure solution led to the wrong origin due to several hypercentrosymmetric positions, which are observed in the crystal structure. This, in addition to the rather poor quality of the initial data set measured at room temperature explains the initially obtained high residuals.

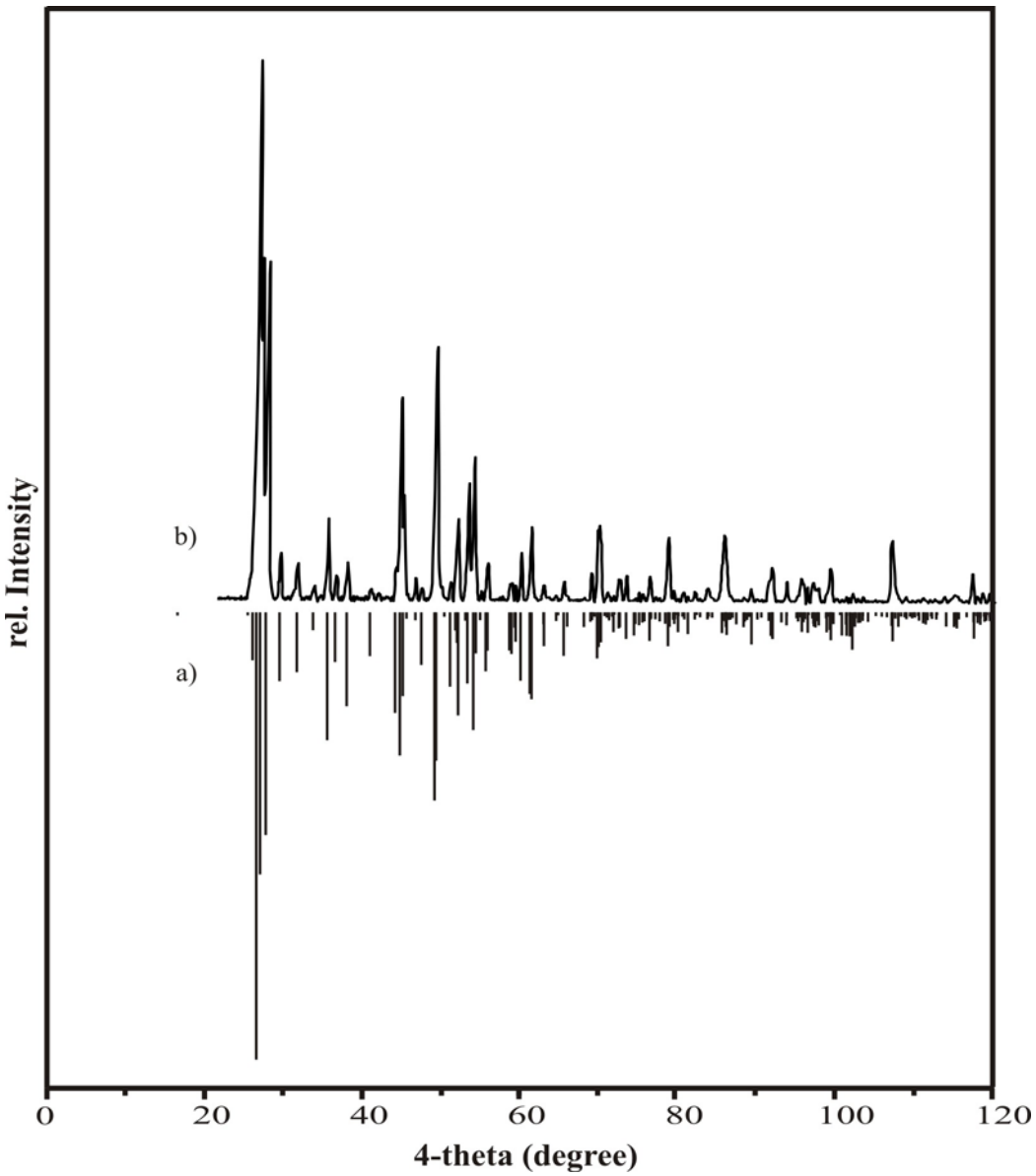

Figure 14.3 Comparison of the simulation (a) and Guinier photograph of $(Re^{VII}{}_2O_5)Si°_2[Si^t{}_2O(PO_4)_6]$ (b).

Single-crystal intensity data of $(Re^{VII}{}_2O_5)Si^o{}_2[Si^t{}_2O(PO_4)_6]$ were measured on a κ-CCD diffractometer (Enraf-Nonius Inc.) at ambient temperature. In order to search for a suitable single-crystals three different crystals were measured. In each case multiply twinned crystals were found, showing two strongly dominant domains. Intensity data of the dominant domain

were indexed and integrated. For structure determination and refinement SHELX-97 [105] and WinGX [137] were used. Despite the relatively small residuals and reasonable interatomic distances, two oxygen atoms (O1 and O12) showed "*non positive definitive*" displacement parameters. We relate this problem to the limited quality of the data set obtained from a multiply twinned crystal. Therefore, the structure was refined allowing for O1 and O12 isotropic displacement parameters only.

Details concerning data collection, structure solution and refinement of $Re^{VII}O_2(PO_4)$ and $(Re^{VII}{}_2O_5)Si^o{}_2[Si^t{}_2O(PO_4)_6]$ are summarized in Table 14.2. The final atomic coordinates, selected interatomic distances and angles for both compounds are given in table 14.3 - 14.6. Indexing of the Guinier simulation and anisotropic displacement parameters are given in Appendix B4 (Table B4.1, B4.3 and Table B4.2-B4.4).

Single-crystal X-ray study of *α*-vanadyl(V) rhenate. Intensity data were measured on a κ-CCD diffractometer (Enraf-Nonius Inc.) at 123 K. Structure determination and refinement was performed using the SHELX-97 [105] suite in WinGx [135] framework. Sarting parameters for the single crystal structure refinement of *α*-$(VO)(ReO_4)_2$ were obtained by direct methods in SHELXS [137]. Thus rhenium and vanadium positions were revealed. Subsequent Δ-Fourier syntheses allowed the localization of the oxygen atoms. An empirical absorption correction with mutiscan [115] was applied.

Details concerning the structure solution and the refinement, starting positional parameters, interatomic distances and angles as well as anisotropic displacement parameters of *α*-$(VO)(ReO_4)_2$ are given in Appendix as C1.

Energy-dispersive X-ray fluorescence analyses [116, 117, 118] (EDXS system, Thermo NIS7 with a germanium detector) for $Re^{VII}O_2(PO_4)$ and $(Re^{VII}{}_2O_5)Si^o{}_2[Si^t{}_2O(PO_4)_6]$) (EDAX system, scanning microscope DMS 940, Zeiss) were performed. For both compounds the results were in agreement with the composition from the structure determination. No additional elements were detected.

Table 14.2 Details concerning data collection, structure determination and refinement of $Re^{VII}O_2(PO_4)$ and $(Re^{VII}{}_2O_5)Si°_2[Si^t{}_2O(PO_4)_6]$.

crystal data		
formula	$Re^{VII}O_2(PO_4)$	$(Re^{VII}{}_2O_5)Si°_2[Si^t{}_2O(PO_4)_6]$
crystal system	monoclinic	triclinic
space group	C2/c (No. 15)	P-1 (No. 2)
a / Å	14.403(1)	7.8589(3)
b / Å	8.414(1)	7.8609(3)
c / Å	20.647(3)	10.8311(4)
α / °		85.312(2)
β / °	93.165(8)	73.078(2)
γ / °		60.075(2)
V / Å^3	2498.3(5)	553.18(4)
Z	24	1
$\tilde{\mu}$, mm^{-1}	29.497	11.728
$D_{X\text{-}ray}$ / g·cm^{-3}	4.996	3.454
colour	light yellow	light rose colored
crystal shape	rectangular	hexagonal plate
size /mm^3	0.17×0.11×0.07	0.08×0.07×0.008
molecular weight / g·mol^{-1}	313.17	1150.58
F(000)	3312	536
data collection		
Nonius κ-CCD diffractometer, graphite-monochromator		
temperature / K	123	293
scan range θ /°	$1.97 \le \theta \le 44.96$	$2.9 \le \theta \le 27.5$
	$-28 \le h \le 28$	$-10 \le h \le 10$
	$-16 \le k \le 16$	$-10 \le k \le 10$
	$-41 \le l \le 41$	$-14 \le l \le 14$
absorption correction	multi-scans [115]	multi-scans [115]
structure refinement		
software	SHELX97 [105]	SHELX97 [105]
measured reflections	134507	17093
ind. reflections	10318; 8721 with $\lvert F_o \rvert > 4\sigma(F_o)$	2551; 2360 with $\lvert F_o \rvert > 2\sigma(F_o)$
parameter; Goof	218; 1.1.03	174; 1.21
residuals		
R_{int}	0.143	0.084
R_1[a)]	0.041	0.078
wR_2[b)]	0.106	0.208
weighting scheme	A = 0.0500; B = 76.78	A = 0.0838; B = 62.29
residual electron density		
$\Delta\rho_{max}$ / Å^{-3}	6.412 (close to Re3)	12.90 (1.86 Å from O10)
$\Delta\rho_{min}$ / Å^{-3}	-10.017 (close to Re1)	-2.86 (1.77 Å from P2)

[a)] $R_1 = \Sigma||F_o| - |F_c|| / |F_o|$, $F_o^2 \ge 2\sigma(F_o^2)$

[b)] $w = 1 / [\sigma^2(F_o^2) + (A \cdot P)^2 + B \cdot P]$; $P = (F_o^2 + 2F_c^2) / 3$

Table 14.3 Atomic coordinates and isotropic displacement parameters of $ReO_2(PO_4)$.

atom	site	*x*	*y*	*z*	U_{eq} /Å$^{2\,a)}$
Re1	8*f*	0.15653(1)	0.52007(2)	0.27954(1)	0.00666(3)
Re2	8*f*	0.33167(1)	0.99796(2)	0.96092(1)	0.00652(3)
Re3	8*f*	0.99657(1)	0.00036(2)	0.63099(1)	0.00656(3)
P1	8*f*	0.21064(7)	0.1464(1)	0.32989(5)	0.0066(1)
P2	8*f*	0.46974(7)	0.1103(1)	0.85173(5)	0.0072(1)
P3	8*f*	0.36961(7)	0.6046(1)	0.98707(5)	0.0070(1)
O1	8*f*	0.0771(2)	0.5149(4)	0.1054(2)	0.0089(4)
O2	8*f*	0.4183(2)	0.5201(4)	0.0434(2)	0.0094(4)
O3	8*f*	0.5978(2)	0.4625(4)	0.0777(2)	0.0104(5)
O4	8*f*	0.2433(2)	0.5175(4)	0.2107(2)	0.0094(4)
O5	8*f*	0.3923(2)	0.5976(4)	0.1693(2)	0.0102(4)
O6	8*f*	0.0695(2)	0.4544(4)	0.3425(2)	0.0099(4)
O7	8*f*	0.2647(2)	0.5612(4)	-.0184(2)	0.0092(4)
O8	8*f*	0.1148(2)	0.7179(4)	0.0111(2)	0.0097(4)
O9	8*f*	0.2180(2)	0.3055(4)	0.2971(2)	0.0100(5)
O10	8*f*	0.0247(2)	0.2363(4)	0.1104(2)	0.0096(4)
O11	8*f*	0.0822(2)	0.3734(4)	0.2139(2)	0.0105(5)
O12	8*f*	0.5663(2)	0.5091(4)	0.1993(2)	0.0113(5)
O13	8*f*	0.2553(2)	0.1523(4)	0.3979(2)	0.0094(4)
O14	8*f*	-0.0439(3)	0.8122(4)	0.1342(2)	0.0140(5)
O15	8*f*	-0.0982(2)	0.5867(4)	0.0183(2)	0.0124(5)
O16	8*f*	0.0950(3)	0.6768(5)	0.2489(2)	0.0144(6)
O17	8*f*	0.2270(3)	0.3446(5)	0.0717(2)	0.0140(5)
O18	8*f*	0.2307(3)	0.6093(5)	0.3344(2)	0.0139(5)

a) $U_{eq} = (⅓)\Sigma_i\Sigma_j U_{ij} a_i^* a_j^* \mathbf{a}_i \cdot \mathbf{a}_j$

Table 14.4 $ReO_2(PO_4)$. Selected interatomic distances (Å) and angles (°); estimated standard deviation in parentheses.

d(Re1-O18$_t$)	1.690(3)	*d*(Re2-O15$_t$)	1.687(3)	*d*(Re3-O14$_t$)	1.684(4)
d(Re1-O16$_t$)	1.692(4)	*d*(Re2-O17$_t$)	1.692(4)	*d*(Re3-O12$_t$)	1.689(3)
d(Re1-O6)	1.936(3)	*d*(Re2-O7)	1.940(3)	*d*(Re3-O3)	1.900(3)
d(Re1-O4)	1.944(3)	*d*(Re2-O1)	1.953(3)	*d*(Re3-O5)	1.922(3)
d(Re1-O9)	2.034(3)	*d*(Re2-O8)	2.043(3)	*d*(Re3-O10)	2.081(3)
d(Re1-O11)	2.085(3)	*d*(Re2-O13)	2.085(3)	*d*(Re3-O2)	2.086(3)
∠(O18,Re1,O16)	101.73(19)	∠(O15,Re2,O17)	101.50(19)	∠(O14,Re3,O12)	101.70(1)
∠(O9,Re1,O11)	78.08(14)	∠(O8,Re2,O13)	79.35(13)	∠(O10,Re3,O2)	81.11(13)
∠(O6,Re1,O4)	162.60(14)	∠(O7,Re2,O1)	161.19(14)	∠(O3,Re3,O5)	162.00(15)
d(P1-O9)	1.507(3)	*d*(P2-O10)	1.509(3)	*d*(P3-O2)	1.502(3)
d(P1-O13)	1.512(3)	*d*(P2-O11)	1.517(3)	*d*(P2-O8)	1.510(3)
d(P1-O5)	1.539(3)	*d*(P2-O1)	1.554(3)	*d*(P3-O3)	1.549(3)
d(P1-O4)	1.542(3)	*d*(P2-O6)	1.558(3)	*d*(P3-O7)	1.552(3)

Table 14.5 Atomic co-ordinates and isotropic displacement parameters of $(Re^{VII}{}_2O_5)Si°{}_2[Si^t{}_2O(PO_4)_6]$.

atom	site	*x*	*y*	*z*	U_{eq} /Å$^{2a)}$
Re1	2*i*	0.46889(1)	0.2304(1)	0.42641(7)	0.0081(9)
Si1	2*i*	0.3217(7)	-0.1621(7)	0.0259(5)	0.0063(9)
Si2	2*i*	0.9303(7)	-0.4825(7)	0.1534(5)	0.0093(3)
P1	2*i*	0.3174(7)	0.1654(6)	0.1743(4)	0.0082(9)
P2	2*i*	0.5654(7)	-0.5211(7)	0.1739(4)	0.0079(9)
P3	2*i*	0.8780(7)	-0.0829(7)	0.1739(4)	0.0073(9)
O1	1*f*	1/2	0	1/2	0.010(2)
O2	1*c*	0	-1/2	0	0.008(2)
O3	2*i*	0.373(2)	0.138(2)	0.299(1)	0.010(3)
O4	2*i*	0.934(2)	-0.299(2)	0.208(1)	0.009(2)
O5	2*i*	0.751(2)	0.048(2)	0.297(1)	0.012(3)
O6	2*i*	0.715(2)	-0.697(2)	0.076(1)	0.010(2)
O7	2*i*	0.762(2)	-0.039(2)	0.072(1)	0.011(2)
O8	2*i*	0.358(2)	-0.026(2)	0.125(1)	0.014(4)
O9	2*i*	0.698(2)	-0.446(2)	0.209(1)	0.010(2)
O10	2*i*	0.595(2)	0.284(2)	0.506(1)	0.012(3)
O11	2*i*	0.461(2)	-0.572(2)	0.300(1)	0.010(2)
O12	2*i*	0.418(2)	0.259(2)	0.073(1)	0.007(2)
O13	2*i*	0.400(2)	-0.359 (2)	0.124(1)	0.010(2)
O14	2*i*	0.071(2)	-0.073(2)	0.124(1)	0.012(3)
O15	2*i*	0.223(2)	0.380(2)	0.512(1)	0.014(3)
O16	2*i*	0.081(2)	0.318(2)	0.207(1)	0.013(4)

a) $U_{eq} = (⅓)\Sigma_i\Sigma_j U_{ij} a_i^* a_j^* \mathbf{a}_i \cdot \mathbf{a}_j$

Table 14.6 $(Re^{VII}{}_2O_5)Si°{}_2[Si^t{}_2O(PO_4)_6]$. Selected interatomic distances (Å) and angles (°); estimated standard deviations in parentheses.

d(Re1-O15$_t$)	1.686(13)	*d*(Si1-O14)	1.738(14)	*d*(Si2-O2$_b$)	1.584(5)
d(Re1-O10$_t$)	1.696(13)	*d*(Si1-O8)	1.749(13)	*d*(Si2-O16)	1.610(14)
d(Re1-O1$_b$)	1.8466(7)	*d*(Si1-O13)	1.749(13)	*d*(Si2-O4)	1.621(14)
d(Re1-O11)	1.975(14)	*d*(Si1-O7)	1.776(14)	*d*(Si2-O9)	1.625(13)
d(Re1-O5)	2.073(13)	*d*(Si1-O12)	1.794(13)		
d(Re1-O3)	2.078(13)	*d*(Si1-O6)	1.796(13)		
d(P1-O8)	1.482(13)	*d*(P2-O13)	1.499(13)	*d*(P3-O14)	1.494(13)
d(P1-O3)	1.505(13)	*d*(P2-O11)	1.511(14)	*d*(P3-O5)	1.498(13)
d(P1-O12)	1.521(13)	*d*(P2-O6)	1.521(13)	*d*(P3-O7)	1.541(14)
d(P1-O16)	1.572(13)	*d*(P2-O9)	1.568(13)	*d*(P3-O4)	1.569(14)
∠(O10$_t$,Re1,O15$_t$)	101.1(7)	∠(Re1,O1$_b$,Re1)	179.999(1)	∠(Si2,O2$_b$,Si2)	180.0(4)
∠(O15$_t$,Re1,O5)	170.4(6)	∠(O10$_t$,Re1,O3)	168.0(6)	∠(O1$_b$,Re1,O12)	162.5(3)
∠(Re1,O3,P1)	147.5(9)	∠(Re1,O11,P2)	148.4(8)	∠(Re1,O5,P3)	150.9(9)
∠(Si1,O12,P1)	130.9(8)	∠(Si1,O8,P1)	150.5(9)	∠(Si1,O7,P3)	131.2(8)
∠(Si1,O6,P2)	132.5(8)	∠(Si1,O12,P1)	130.9(8)	∠(Si1,O13,P2)	150.1(9)
∠(Si2,O9,P2)	137.4(9)	∠(Si2,O4,P3)	137.9(9)	∠(Si2,O16,P1)	138.4(8)

MAS-NMR experiments (^{31}P, ^{29}Si) were carried out on a Varian Infinity+ spectrometer equipped with a commercial 2.5 mm MAS double-resonance probe (Chemagnetics) operating at 162.534 and 79,769 MHz, respectively. The ^{31}P-MAS spectra are the average of up to 64 transients acquired with a repetition delay up to 120 s (ca. 5 times T_1), a 90° pulse duration of 1.8 μs, and 10 Hz line broadening during data processing. The spin lattice relaxation times T_1 were determined. For the measurement the magnetization was extinguished by a train of pulses followed by a rectangular pulse with different delay. ^{29}Si-MAS spectrum was obtained with a repetition rate of 600 s and 800 transients, a 90° pulse duration of 3.5 μs, and no line broadening during data processing. Magic angle adjustment was carefully performed by the maximum numbers of "spikes" in FID of a KBr sample. The chemical shifts are reported in parts per million (ppm) from an external standard of 85% H_3PO_4 and tetramethylsilane for the ^{31}P- and ^{29}Si-MAS-NMR spectra, respectively.

The electronic absorption spectra of single-crystals of $Re^{VII}O_2(PO_4)$ and $(Re^{VII}{}_2O_5)Si^o{}_2[Si^t{}_2O(PO_4)_6]$ were measured at ambient temperature using a strongly modified CARY 17 microcrystal spectrophotometer (Spectra Services, ANU Canberra, Australia) [121, 122]. Two different crystals were chosen for the absorption spectra. A single-crystal of $Re^{VII}O_2(PO_4)$ (≈ 0.2, 0.15, 0.08 mm^3) was measured just after recovering the crystal from the ampoule. The spectrum shows a very strong absorption above $\tilde{\nu}$ = 22000 cm^{-1}. The first crystal was collected directly from the ampoule, whereas the second crystal (≈ 0.15, 0.10, 0.07 mm^3) crystal was soaked in acetone for about 20 minutes in order to remove it from the wall of the quartz tube. It was measured twice; three and six days after opening of the crystal growth ampoule. The former shows a very broad absorption band centered at about $\tilde{\nu}$ = 13000 cm^{-1} in addition to the transition at $\tilde{\nu}$ = 22000 cm^{-1}. A hexagonal plate like crystal (≈ 0.4, 0.3, 0.05 mm^3) of $(Re^{VII}{}_2O_5)Si^o{}_2[Si^t{}_2O(PO_4)_6]$ was measured after one day since opening the tube had passed. The spectrum shows a very strong absorption band at about $\tilde{\nu}$ = 26500 cm^{-1}.

The infrared spectrum of Guinier-pure $Re^{VII}O_2(PO_4)$ was measured using a NICOLET 380 FT-IR spectrometer (SMART ORBIT).

14.3 Results and Discussions

14.3.1 Syntheses and Crystallization

Rhenium(VII)-oxidephosphate $ReO_2(PO_4)$ can be obtained by reaction of Re_2O_7 and P_4O_{10} in sealed silica tubes in the temperature range $250 \leq \vartheta \leq 400°C$. The phosphate migrates in a temperature gradient $400 \rightarrow 300°C$ from the higher to the lower temperature. Thus, pale yellow rectangular shaped crystals were obtained. According to mass spectrometric studies [149] the gas phase over solid $ReO_2(PO_4)$ contains under perfectly dry conditions only $Re_2O_7(g)$ and $P_4O_{10}(g)$. The migration in the temperature gradient has to be regarded as dissociative sublimation (see Equation. 14.1).

$$2Re^{VII}O_2(PO_4)(s) = Re_2O_7(g) + ½\ P_4O_{10}(g) \qquad (14.1)$$

Small amounts of moisture, however, give rise to the occurrence of gaseous $ReO_3(OH)$ and in the presence of even more water to gaseous H_3PO_4 [149]. Therefore, traces of water present in the reaction tubes might lead to chemical vapour transport of $ReO_2(PO_4)$ according to eq. 14.2 and 14.3, respectively. It is known [286, 287] that Re_2O_7 shows increased volatility in the presence of even tiny amounts of water. The stability and importance of gaseous $ReO_3(OH)$, for chemical vapor transport of rhenium oxides has been discussed in detail [84].

$$2\ Re^{VII}O_2(PO_4)(s) + H_2O(g) = 2\ ReO_3(OH)(g) + ½\ P_4O_{10}(g) \qquad (14.2)$$

$$Re^{VII}O_2(PO_4)(s) + 2\ H_2O(g) = ReO_3(OH)(g) + H_3PO_4(g) \qquad (14.3)$$

From its thermal stability and the observed sublimation rates of up to 10 $mg \cdot h^{-1}$ a stabilization of $Re^{VII}O_2(PO_4)$ by –10 to –40 $kJ \cdot mol^{-1}$ with respect to decomposition into 1/2 $Re_2O_7(s)$ and 1/4 $P_4O_{10}(s)$ is estimated. This rather small stabilization extends nicely the series of heats of neutralization observed for Na_3PO_4 (–544 $kJ \cdot mol^{-1}$) [288], $LaPO_4$ (–360 $kJ \cdot mol^{-1}$) [289], and $AlPO_4$ (–145 $kJ \cdot mol^{-1}$) [290] and reflects the rather low basicity (oxide donor strength) of Re_2O_7.

The experiments (see Table 14.1) indicate that reaction of gaseous Re_2O_7 and P_4O_{10} with the wall of the silica tube becomes dominant at temperatures slightly above 400°C and extended reactions times. Thus, $(Re_2O_5)Si^o{}_2[Si^t{}_2O(PO_4)_6]$ is formed. Well above 400°C, neither $ReO_2(PO_4)$ nor $(Re_2O_5)Si^o{}_2[Si^t{}_2O(PO_4)_6]$ were observed as reaction products. Instead, silicon-silicophosphate, $Si^o{}_3[Si^t{}_2O(PO_4)_6]$ [222] did occur, with the release of Re_2O_7 into the gas phase and occasional formation of ReO_3 and/or ReP_2O_7.

In one experiment, alongside $(Re_2O_5)Si^{o}{}_2[Si^{t}{}_2O(PO_4)_6]$, light yellow rectangular crystals were obtained which gave an XRPD pattern similar, however distinctly different to that of $ReO_2(PO_4)$ from the other experiments (see Figure 14.2). The crystal quality did so far not allow a single crystal study. We assume that a second polymorph of $ReO_2(PO_4)$ had been formed. Experiments to reproduce this result failed so far.

The chemical stability of rhenium(VII)-phosphate and -silicophosphate at room temperature depends on the particle size, homogeneity of the surface of the crystals as well as the surrounding atmosphere. While finely powdered material is hydrolyzed in a couple of minutes, well developed crystals can persist up to several days. Light-yellow crystals of $ReO_2(PO_4)$ start to turn greenish once they are removed from the ampoule, indicating reduction of Re^{7+}.

14.3.2 Crystal structure

$Re^{VII}O_2(PO_4)$. The crystal structure of $ReO_2(PO_4)$ can be regarded as a superstructure of the ReO_3 structure type [36]. The crystal chemical transition from the cubic ReO_3 structure type to the monoclinic structure of $ReO_2(PO_4)$ is visualized in figure 14.4. In a first step there is heterovalent substitution of two Re^{6+} by Re^{7+} and P^{5+}. Due to the different coordination requirements of Re^{7+} and P^{5+} in comparison to Re^{6+} the ideal octahedral coordination around the cations in the cubic ReO_3 structure type is relaxed by small shifts of some oxygen atoms and P^{5+}. Thus, the coordination number of phosphorus is reduced to four (as is typical for phosphates), leaving two oxygen atoms exclusively bound to rhenium. In this way two short $Re{=}O_t$ bonds per $[ReO_6]$ octahedron are generated with $d(Re\text{-}O_t) \approx 1.69$ Å and $\angle(O_t,Re,O_t) \approx 101.6°$ (see Figure 14.5). The relationship between the structures of $ReO_2(PO_4)$ and ReO_3 is also described by figure 14.4 and the transformation matrix eq. (14.4).

$$\begin{pmatrix} a_{RePO_6} \\ b_{RePO_6} \\ c_{RePO_6} \end{pmatrix} = \begin{pmatrix} 2 & 4 & 0 \\ 0 & 0 & 2 \\ 4 & -4 & 0 \end{pmatrix} \begin{pmatrix} a_{ReO_3} \\ b_{ReO_3} \\ c_{ReO_3} \end{pmatrix} \qquad (14.4)$$

The structure of $ReO_2(PO_4)$ is closely related to that of the monoclinic modification of $MoO_2(SO_4)$ [154] (see Figure 14.6) where a three dimensional framework is formed by corner sharing $[MoO_6]$ octahedra and $[SO_4]$ tetrahedra. For $MoO_2(SO_4)$ hints on at least two further polymorphs, yet not structurally characterized in detail, are reported [154]. We believe, that the XRPD for $ReO_2(PO_4)$ in figure 14.2c points in this direction, too.

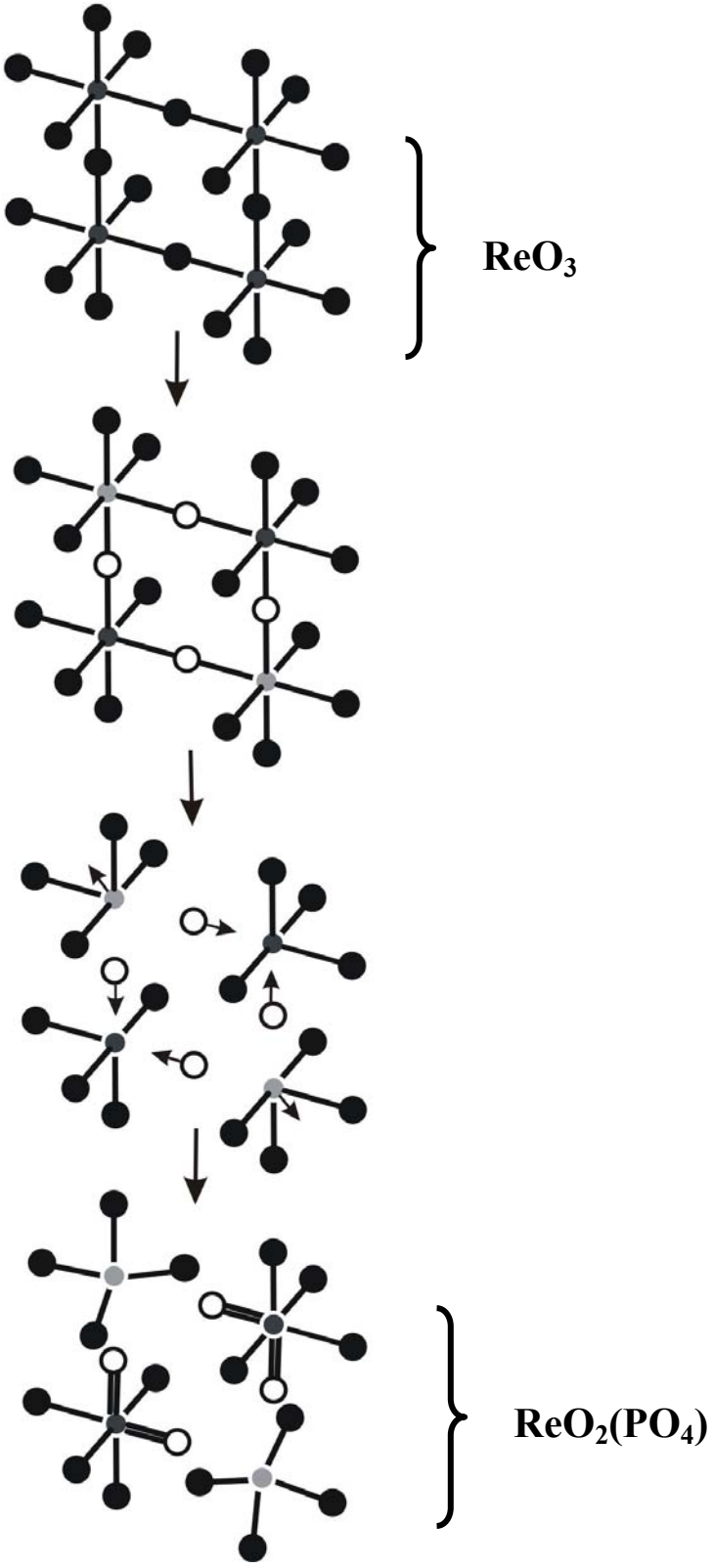

Figure 14.4 Schematic representation of $[ReO_6]$ octahedra and $[PO_4]$ tetrahedral derived from the ReO_3 structure. Black and open circles point to oxygen atoms, dark grey and light grey designate rhenium and phosphorus atoms, respectively.

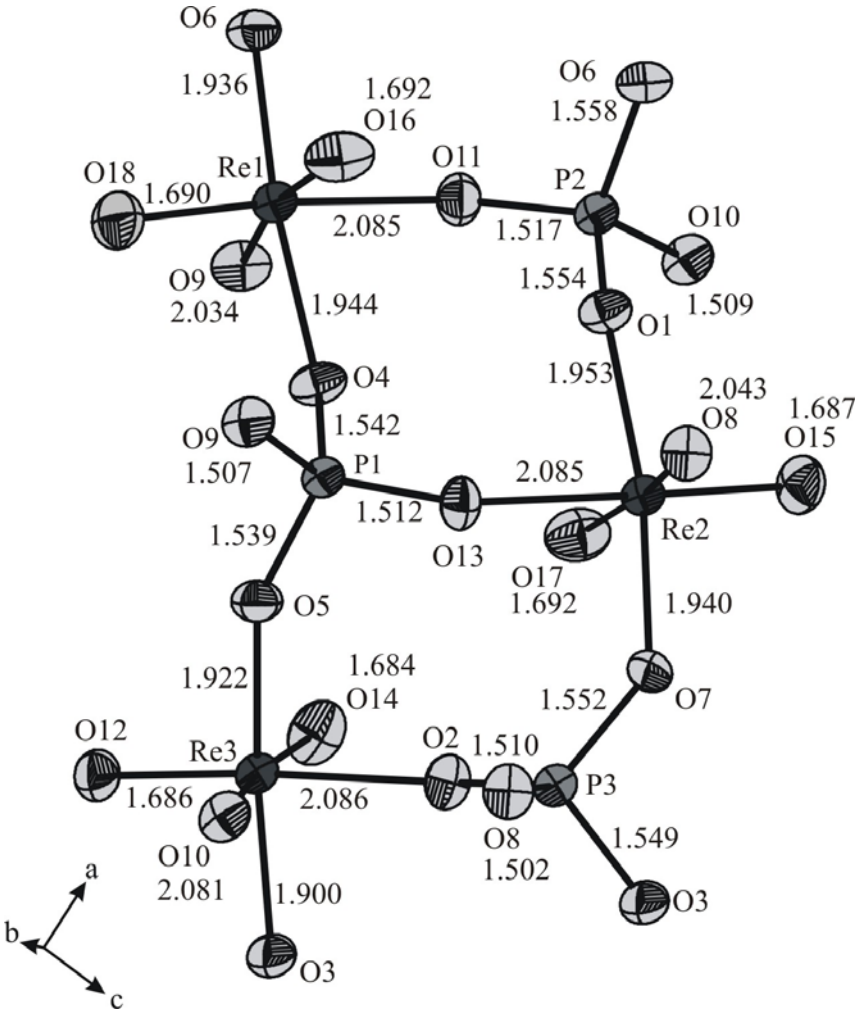

Figure 14.5 ORTEP representation of $[ReO_6]$ octahedra and $[PO_4]$ tetrahedra in $ReO_2(PO_4)$, ellipsoids at 90% probability level (Diamond version 3.2c [138]).

The structure of $ReO_2(PO_4)$ consists of three crystallographically independent sites of rhenium and of phosphorus, each of them coordinated by oxygen atoms forming $[ReO_6]$ octahedra and $[PO_4]$ tetrahedra, respectively (Figures 14.5, 14.7). The coordination polyhedra $[ReO_6]$ (1.69 Å ≤ *d*(Re-O) ≤ 2.09 Å) (Figure 14.5, Table 14.4) deviate strongly from the structure of an ideal octahedron. Three pairs of Re-O bond-lengths can be distinguished, e.g. long (2.03 Å ≤ *d*(Re-O) ≤ 2.09 Å), intermediate (1.90 Å ≤ *d*(Re-O) ≤ 1.95 Å), and short (*d*(Re-O) ≈ 1.69 Å). These large differences in bond lengths can be compared to MoO_2SO_4 [154] where also three pairs *d*(Mo-O) of different bond lengths in the range of 1.64 Å ≤ *d*(Mo-O) ≤ 2.27 Å are found. It is worth to mention that in the $[ReO_6]$ octahedra each long bond Re-O_b is in *trans* position to a short bond Re=O_t ("*trans* effect"). The two intermediate

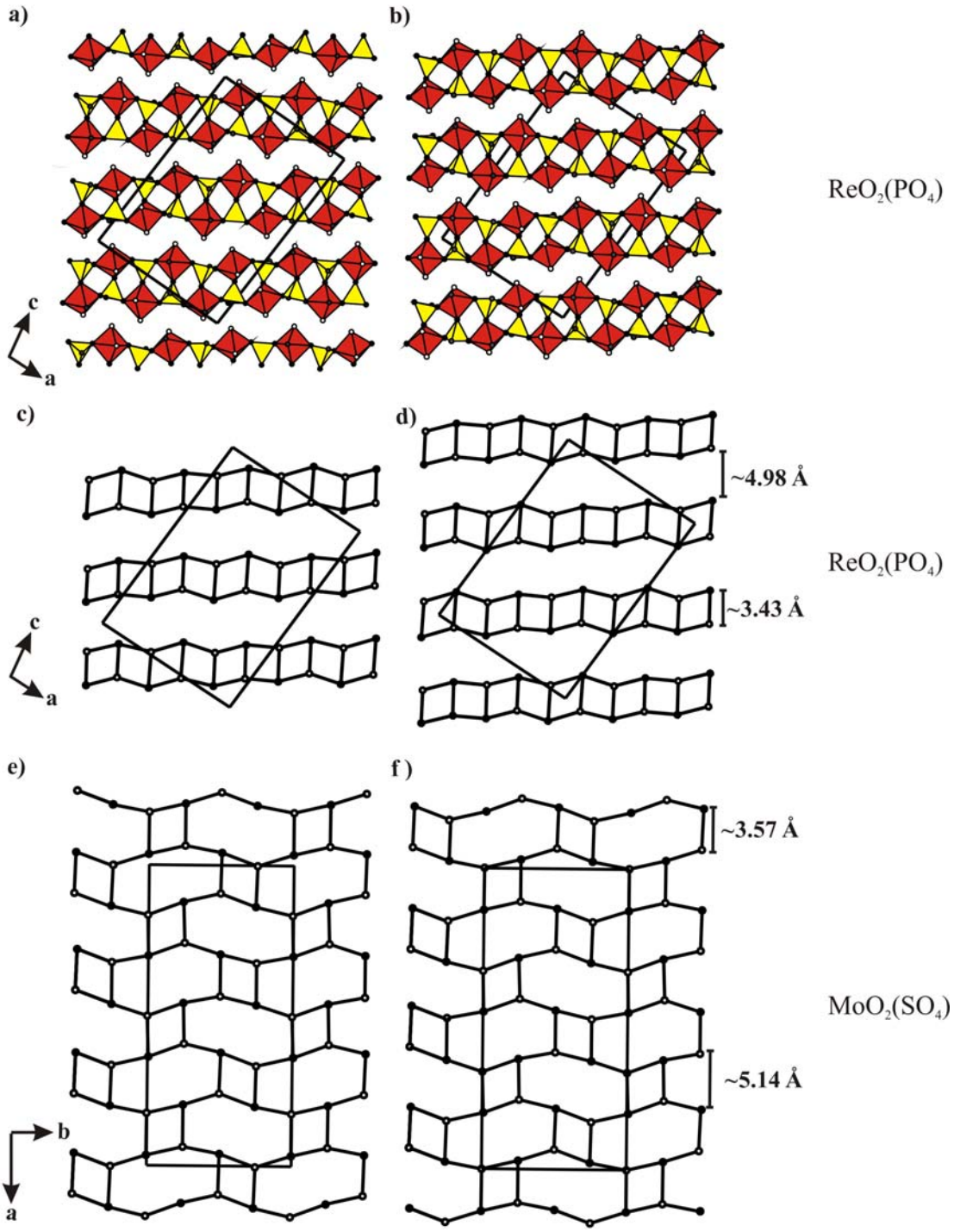

Figure 14.6 Ribbons obtained from the crystal structure of $ReO_2(PO_4)$ with $[ReO_6]$ octahedra (red) and $[PO_4]$ (yellow). Terminal oxygen atoms in white, bridging to rhenium and phosphorus in the same ribbon in dark, and bridging to different ribbons are in grey. The two crystallographically different ribbons at y = ½ and y = 0 are labelled as (a) and (b), respectively**.** $ReO_2(PO_4)$ peeled-off network projected along [0 1 0] with its four-membered rings at y = ½ and y = 0 are labelled as (c) and (d), respectively. $MoO_2(SO_4)$ [154] peeled-off network projected along [0 0 1] with its four- and eight-membered rings at y = ½, and y = 0 are labelled as (e) and (f) (Diamond version 3.2c [138]). For clarity in case of peeled-network all the oxygen atoms were omitted.

Re-O_b bonds per [ReO_6] octahedron are in *trans* position to each other. They link rhenium to two [PO_4]. The existence of two short bonds in the [ReO_6] octahedra reflects the double bond-character of the binding between rhenium and these terminal oxygen atoms, thus forming perrhenyl ions, $(ReO_2)^{3+}$. The repulsion between the *cis* positioned short bonds Re=O_t is expected to be strong (VSEPR model) and is at least partially mitigated by expansion of the angle ∠(O_t,Re,O_t) from 90° to about 101.6°. These bond-lengths and -angles are in good

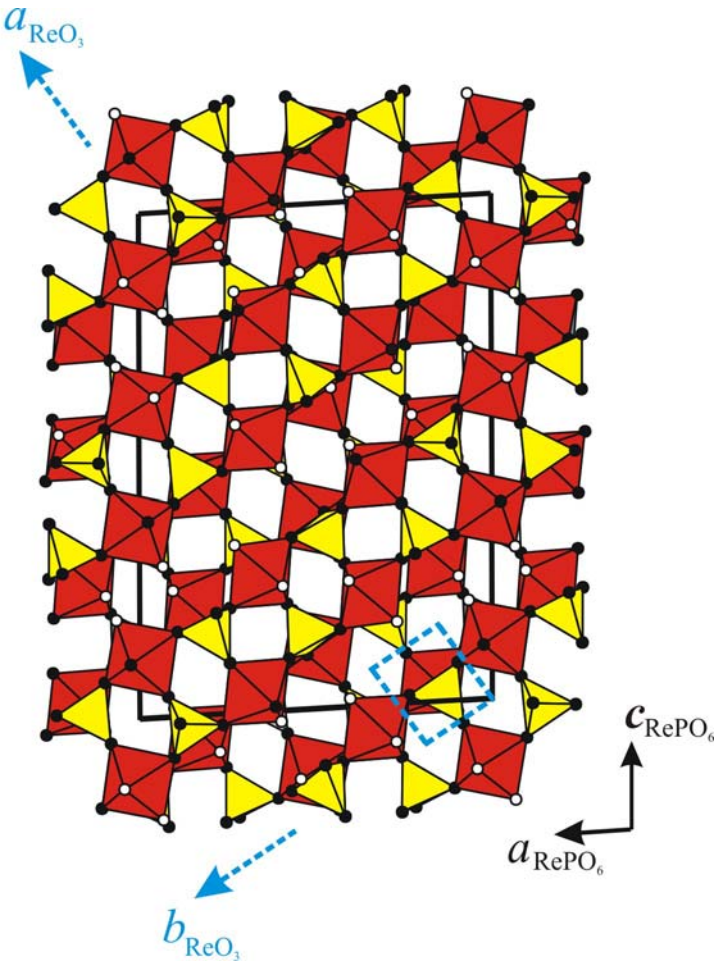

Figure 14.7 Crystal structure of $ReO_2(PO_4)$ with [ReO_6] octahedra (red) and [PO_4] tetrahedra (yellow). Terminal oxygen atoms in white, bridging oxygen atoms in black. (Progr. Diamond version 3.2c [138]).

agreement with those of other MO_2^{3+} ions in Re_2O_7 [38], ReO_2X_3, (*X* = Cl, F) [41, 42], TcO_2F_3 [291, 292], OsO_2F_3 [293] as well as $MoO_2(SO_4)$ [154]. The preference for the *cis* conformation can be understood in terms of the spatial arrangement required for $p_\pi \rightarrow d_\pi$ bonding between the strongly π-donating oxygen atoms to the t_{2g} orbitals of the metal. This has already been discussed by COTTON and co-workers for [$Mo^{VI}O_6$] species [156] and by MERCIER *et al.* [291] for TcO_2F_3.

The $[PO_4]$ tetrahedra in $ReO_2(PO_4)$ display slight radial and angular distortions with 1.50 Å ≤ d(P-O) ≤ 1.56 Å and 101.0° ≤ ∠(O,P,O) ≤ 113.3° (see Figure 14.5, Table 14.4). These bond-lengths and -angles are typical for orthophosphates [2]. A more detailed analysis of bond lengths d(P-O) might distinguish between two short (1.50 Å ≤ d(P-O) ≤ 1.51 Å) and two longer bonds (1.54 Å ≤ d(P-O) ≤ 1.56 Å). Short bonds d(P-O) correspond to the long bonds d(Re-O_b). Conversely, long distances d(P-O) correspond to the intermediate bonds d(Re-O_b).

$(Re_2O_5)Si^o_2[Si^t_2O(PO_4)_6]$. Frequently, synthesis and crystallization of anhydrous transition metal phosphates in silica tubes is accompanied by formation of silicophosphates. A survey on this class of compounds together with a new crystal chemical classification scheme has been given recently [214]. The classification of these crystal structures is based on close-packed arrays of phosphate groups, containing M^{n+} and $[Si_2O]$-units in octahedral voids. The former leads to $[MO_6]$ octahedra, the later to $[Si_2O_7]$ groups. This classification scheme allows also incorporation of crystal structures related to the *NASICON* structure family. Thus, a rather simple description of the complicated crystal structure of phosphate-silicophosphates $M^{III}_2Ti_6(PO_4)_6(Si_2O(PO_4)_6)$ (M^{III} = Ti, V, Cr, Fe, In) as hybrid structure has become possible [227]. The crystal structure of $(Re_2O_5)Si^o_2[Si^t_2O(PO_4)_6]$ (see Figure 14.8) extends the crystal chemistry of transition metal silicophosphates. Its unit cell contains one formula unit with only one crystallographic site for rhenium, two independent sites for silicon in octahedral and tetrahedral coordination (Si^o, Si^t) and three independent sites for phosphorus. Double layers // (0 0 1) of close-packed phosphate groups are containing Si ions in 2/3 and $[Si_2O]$ groups in 1/3 of the octahedral voids, thus forming $[SiO_6]$ octahedra and $[Si_2O_7]$ groups.

These double layers are stacked along the crystallographic c-axis and linked by $(Re_2O_5)^{4+}$ groups, which can be regarded as oxygen-bridged perrhenyl cations (d(Re=O_t) ≈ 1.69 Å, ∠(O_t,Re,O_t) ≈ 101.1°, d(Re-O_b) = 1.85 Å, ∠(Re1,O_b,Re1) = 180°; Figure 14.9b and Table 14.6). By oxygen atoms from the phosphate layers the coordination around rhenium is completed to form double octahedra $[Re_2O_{11}]$. In addition to rhenium(VII)-silicon-silicophosphate, $[Re_2O_{11}]$ groups appear in the crystal structure of $Re^{VI}_2O_3(PO_4)_2$ [281]. The latter containing $(Re^{VI}_2O_3)^{3+}$ cations instead of $(Re^{VII}_2O_5)^{4+}$, however with very similar distances d(Re-O).

Interatomic distances d(P-O) and d(Si-O) in $(Re_2O_5)Si^o_2[Si^t_2O(PO_4)_6]$ (Figure 14.9, Table 14.6) are comparable to those in other silicophosphates, e. g. $Si°_3[Si^t_2O(PO_4)_6]$ [218], $(Ir_{1-x}Si_x)_3[Si_2O(PO_4)_6]$ [294] and $In^{III}_2Ti_6(PO_4)_6(Si_2O(PO_4)_6)$ [227].

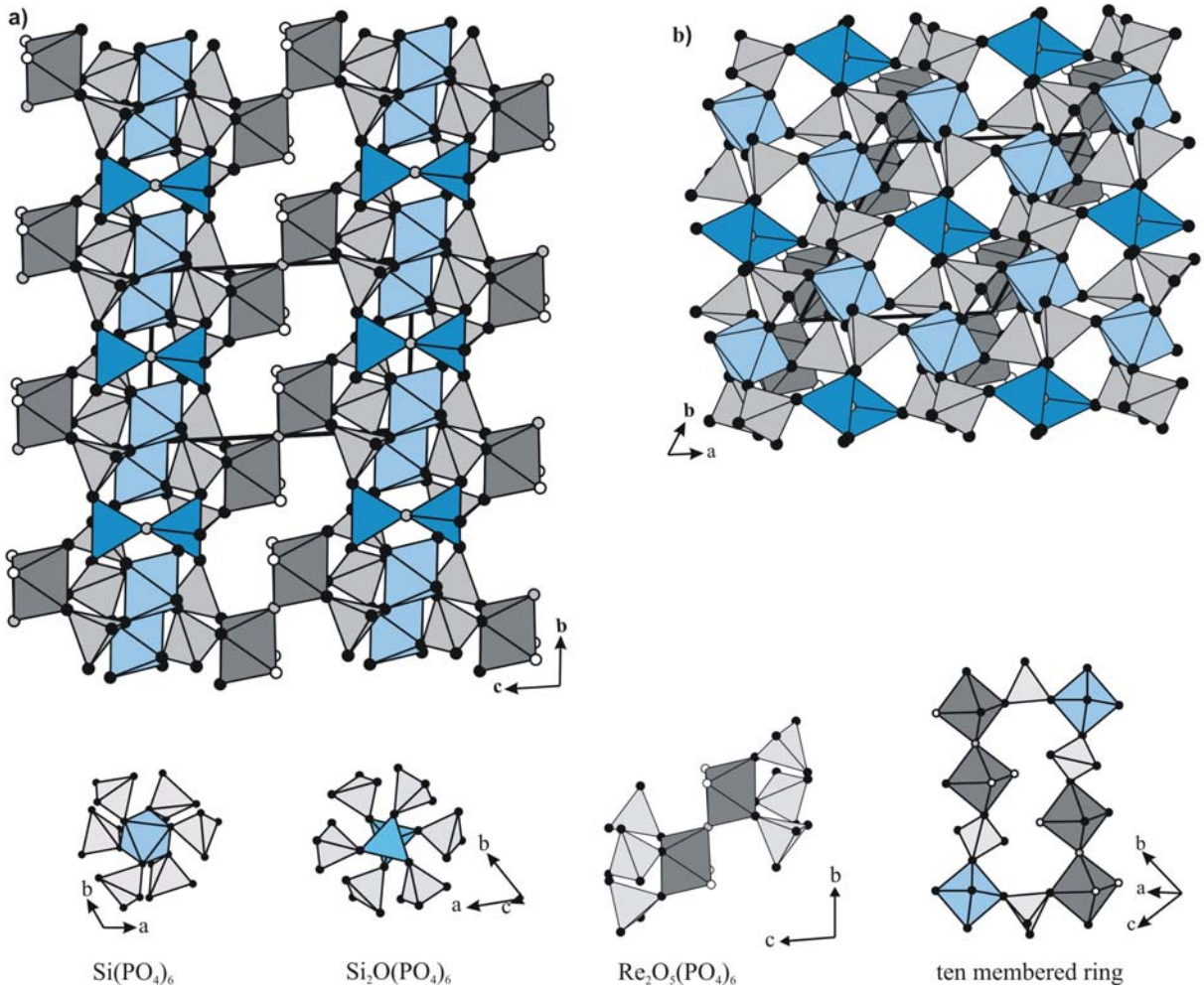

Figure 14.8 Crystal structure of $(Re_2O_5)Si^o{}_2[Si^t{}_2O(PO_4)_6]$ with $[Re_2O_{11}]$ dioctahedra (grey), $[PO_4]$ tetrahedra (light grey), $[SiO_6]$ octahedra (ice blue) and $[Si_2O_7]$ group (deep blue). Terminal oxygen atoms in white, bridging oxygen atoms between two rhenium and silicon atoms are in grey (Diamond Version 3.2c [138].

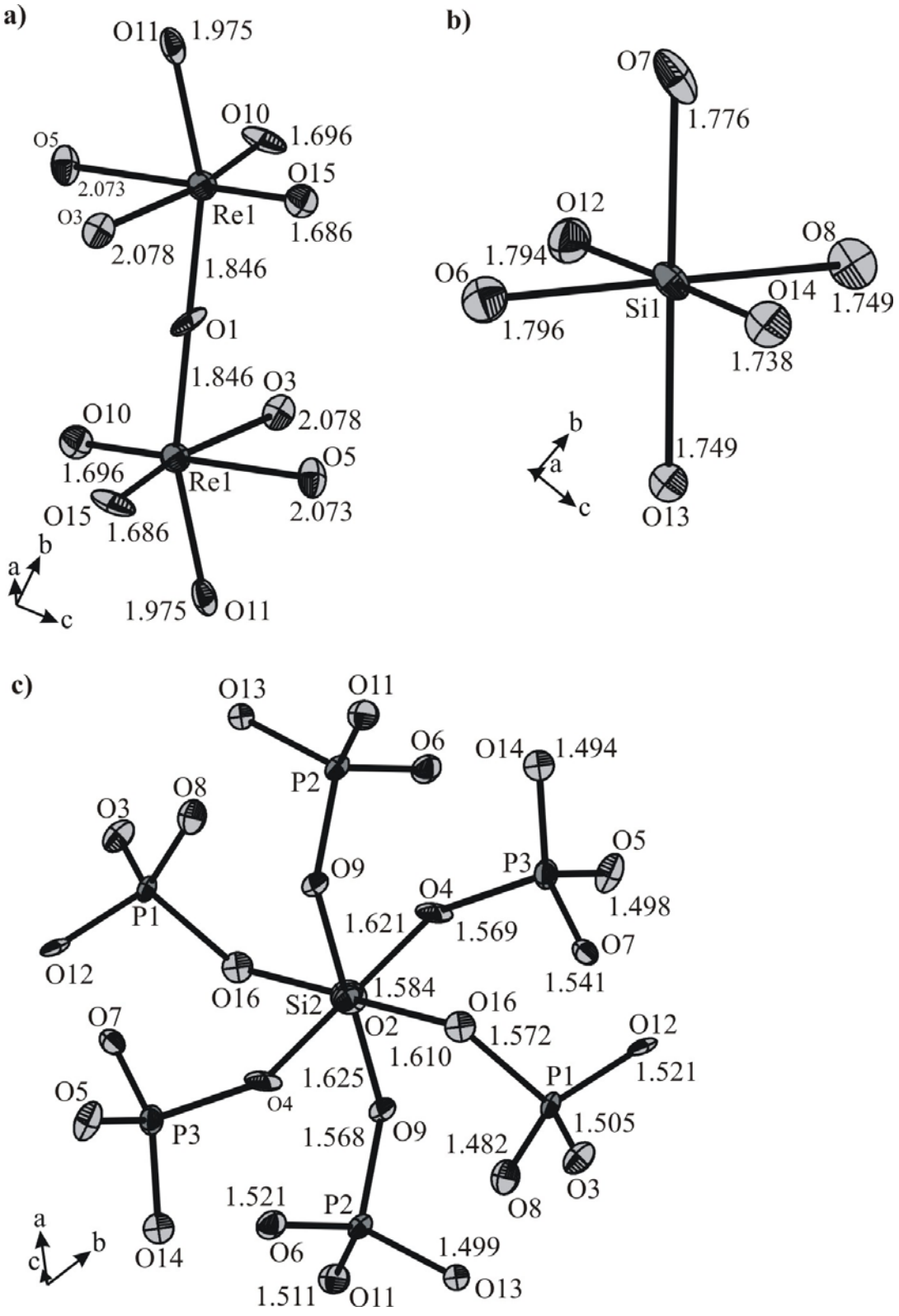

Figure 14.9 ORTEP representation of $[Re_2O_{11}]$, $[SiO_6]$ octahedra, and $[Si_2O(PO_4)_6]$ in $(Re_2O_5)Si^{o}{}_2(Si^{t}{}_2O(PO_4)_6]$ are labelled as in Fig. a, b and c, respectively. Ellipsoids at 70% probability level (Diamond version 3.2c [138]).

14.3.3 Spectroscopic Investigations

^{31}P-and ^{29}Si-MAS-NMR spectroscopy. The isotropic chemical shift parameters of $Re^{VII}O_2(PO_4)$ and $(Re^{VII}{}_2O_5)Si^o{}_2[Si^t{}_2O(PO_4)_6]$ were determined from ^{31}P-MAS-NMR measurements at different rotation frequencies using a deconvolution routine provided by the spectrometer software. Thus, the ^{31}P-MAS-NMR spectrum of $Re^{VII}O_2(PO_4)$ (Figure 14.10a) can be decomposed into three equally intense signals. The isotropic chemical shift parameters were obtained as δ^I_{iso} = -6.8, δ^{II}_{iso} = -11.4 and δ^{III}_{iso} = -13.8 ppm in accordance with the crystal structure of $ReO_2(PO_4)$ containing three independent sites for phosphorus atoms in the ratio 1:1:1. Assignment of the strong signal around -12.6 ppm to two overlapping Gaussians is backed by the very similar chemical environment of all phosphorus atoms as it is found from the structure refinement. Isotropic chemical shifts obtained for $ReO_2(PO_4)$ are close to those of other orthophosphates like $GaPO_4$ (δ_{iso} = -9.8 ppm) [295], $Be_3(PO_4)_2$ (δ_{iso} = -9.2 ppm) [295] and Cs_3PO_4 (δ_{iso} = -3.1, -5.1, -6.4, -7.1 ppm) [296]. It should be noted that spin lattice relaxation times T_1 for the three phosphorus sites amount to 19 s and that they are equal within the error of the estimation.

The ^{31}P-MAS-NMR spectrum of $(Re^{VII}{}_2O_5)Si^o{}_2[Si^t{}_2O(PO_4)_6]$ (see Fig. 14.10b) shows three isotropic chemical shift parameters at δ^I_{iso} = -33.3, δ^{II}_{iso} = -34.8, and δ^{III}_{iso} = -36.7 ppm. Relaxation times T_1 of each phosphorus site are equal to 10.0(5) s. There is no change in line shape by increasing the rotation frequency up to 24 kHz. It is necessary to state that the integrals of the different resonance peaks in the ^{31}P-MAS-NMR spectrum of the silicophosphate show a ratio of about 1:2:2, which does not agree with the ratio 1:1:1 expected from the crystal structure of the silicophosphate (see Table 14.5). We attribute this deviation to a possibly larger unit cell than it was used for the refinement so far. Actaually to accommodate the appropriate amount of phosphorus atoms the unit cell has to have 5.n (n = 1, 2, 3, 4…..) volume of our triclinic ce1l. The isotropic chemical shift parameters are close to those of other silicophosphates like $In_2Ti_6(PO_4)_6[Si_2O(PO_4)_6]$ [227] (δ_{iso} = -27.2 ppm for phosphorus within the $[Si_2O(PO_4)_6]^{12-}$ group) and $Si^o{}_3[Si^t{}_2O(PO_4)_6]$ (δ_{iso} = -44.1 ppm) [297].

The ^{29}Si-MAS-NMR spectrum (see Figure 14.10c) of $(Re^{VII}{}_2O_5)Si^o{}_2[Si^t{}_2O(PO_4)_6]$ (rotation frequency = 10.0 kHz) reveals two isotropic chemical shifts at δ^I_{iso} = -119.0 and δ^I_{iso} = -213.5 ppm. These correspond to the two independent crystallographic sites for silicon. The more shielded resonance corresponds to $[SiO_6]$, the less shielded to $[SiO_4]$.

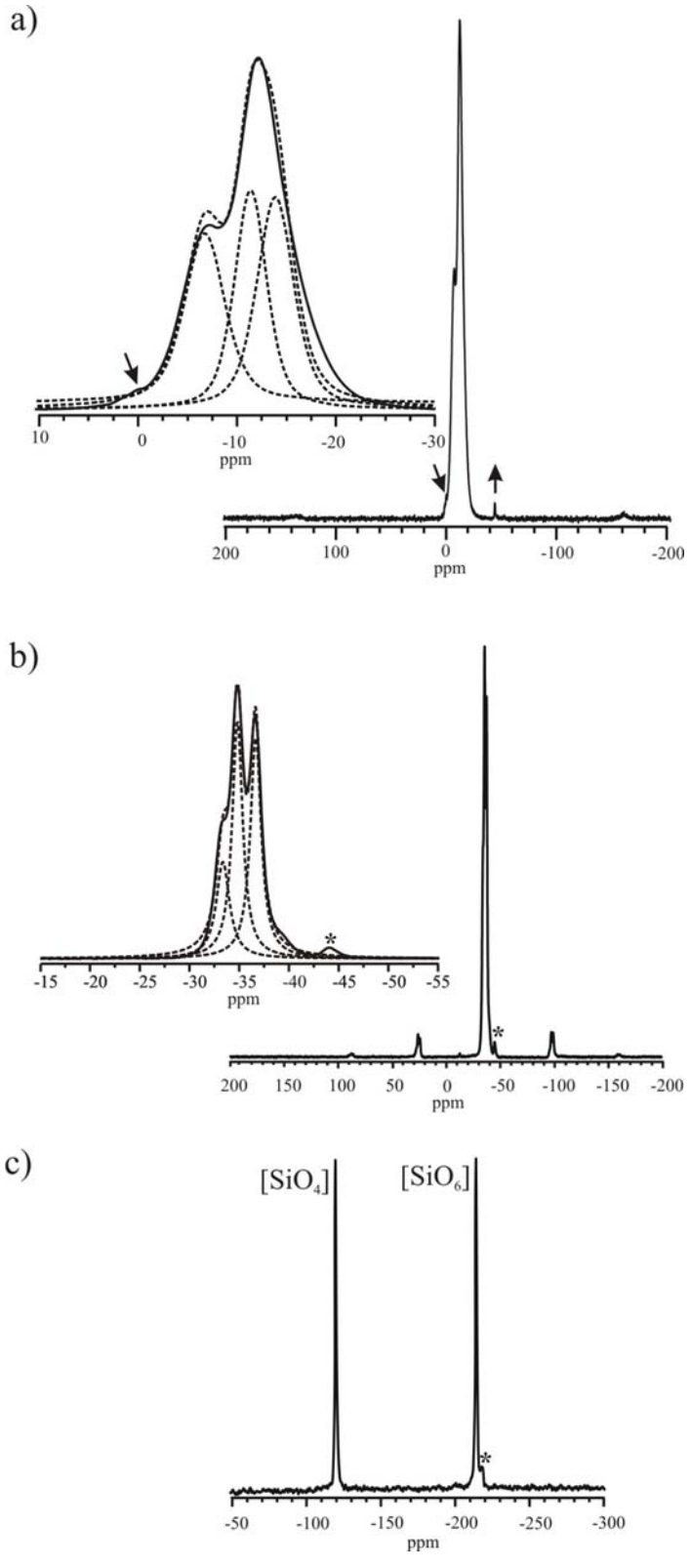

Figure 14.10 Quantitative ^{31}P-MAS-NMR spectra of ReO_2PO_4 (ν_{MAS} = 24 kHz) (a). Signals indicated by downward arrows represent the presence of H_3PO_4. Upward arrow represents an unknown impurity. Quantitative ^{31}P-MAS-NMR (ν_{MAS} = 10 kHz) and ^{31}Si-MAS-NMR (ν_{MAS} = 10 kHz) spectra of $(Re_2O_5)Si^o{}_2(Si^t{}_2O(PO_4)_6]$ (b and c respectively). Signals indicated by asterisks appear from $Si^o{}_3[Si^t{}_2O(PO_4)_6]$ [297, 298]. Solid lines represent the experimental spectra and dashed lines are the results of calculated spectra.

The ^{29}Si-MAS-NMR spectrum of $(Re^{VII}_2O_5)Si^o_2[Si^t_2O(PO_4)_6]$ compares nicely to that of $Si^o_3[Si^t_2O(PO_4)_6]$ ($\delta_{iso} \approx$ -119, $\delta_{iso} \approx$ -213.5, $\delta_{iso} \approx$ -218 ppm) [297, 298] and $In_2Ti_6(PO_4)_6[Si_2O(PO_4)_6]$ (δ_{iso} = -125.7 ppm) [227]. A weak resonance in the ^{29}Si-MAS-NMR spectra of $(Re^{VII}_2O_5)Si^o_2[Si^t_2O(PO_4)_6]$ located at $\delta_{iso} \approx$ -218 ppm is related to $Si°_3[Si^t_2O(PO_4)_6]$ [297, 298] as an impurity. The other peaks of the silicon-silicophosphates are hidden under the much stronger signals of rhenium(VII)-silicon-silicophosphate.

UV/Vis Spectroscopy. Despite the very similar chemical environment for the Re^{7+} ions $Re^{VII}O_2(PO_4)$ (yellow) and $(Re^{VII}_2O_5)Si°_2[Si^t_2O(PO_4)_6]$ (pale rose) show different colors. The difference is reflected by the UV/Vis spectra (Figure 14.11a) with a rather steep rise to the UV around $\tilde{\nu}$ = 22000 cm^{-1} for $ReO_2(PO_4)$ and a moderately rising curve around $\tilde{\nu}$ = 25000 cm^{-1} for $(Re^{VII}_2O_5)Si°_2[Si^t_2O(PO_4)_6]$. In both cases the absorptions might be attributed to charge transfer transitions $O^{2-} \rightarrow Re^{7+}$.

Besides the strong LMCT absorption in $Re^{VII}O_2(PO_4)$, a band centered at about $\tilde{\nu}$ =13000 cm^{-1} (Figure 14.11a-ii) appears when a single crystal of $ReO_2(PO_4)$ was measured three days after opening the tube. This band might be an effect of partial reduction of Re^{7+} to Re^{6+} with an IVCT as consequence. The absorption minimum centered at about $\tilde{\nu}$ = 18500 cm^{-1} is an agreement with the visually observed color change from yellow to greenish for crystals of $ReO_2(PO_4)$.

Infrared Spectroscopy. In the infrared spectrum of $ReO_2(PO_4)$ (Table 14.7) the bands at about 1190 cm^{-1}, 1155 cm^{-1}, 1082 cm^{-1} and 1024 cm^{-1} are attributed to the P-O symmetric and asymmetric stretching vibrations of $[PO_4]$ group [144, 260, 282]. The assignment of two bands at about 968 cm^{-1} and 942 cm^{-1} is straightforward for the stretching mode of ν(O=Re=O) due to their high frequencies and relative intensities. This assignment is in agreement with the i. r. spectrum of Re_2O_7 [262] where the authors mentioned several bands in a broad region between 1006 cm^{-1} and 876 cm^{-1} for the vibration of rhenium along with its two terminal oxygen atoms. SEPPELT, *et al.* [41] noticed in ReO_3F two strong bands at 1009 cm^{-1} and 980 cm^{-1} which, as we believe, should also be assigned to *cis* ν(O=Re=O) stretching modes. It is worth to mention that two vibrational bands at 908 cm^{-1} and 840 cm^{-1} were assigned for stretching vibrational mode of ν(O=Re=O) in *cis*-$[(O_2)Re(bpy)(3\text{-Cl-py})_2](PF_6)$ [299] whereas for the *trans*-$[(O_2)(Re(py)_2(4\text{-Cl-Py})_2](PF_6)$ [299] a band at 817 cm^{-1} was reported. Apart from two bands for Re=O bonds in $ReO_2(PO_4)$, other bands could not be

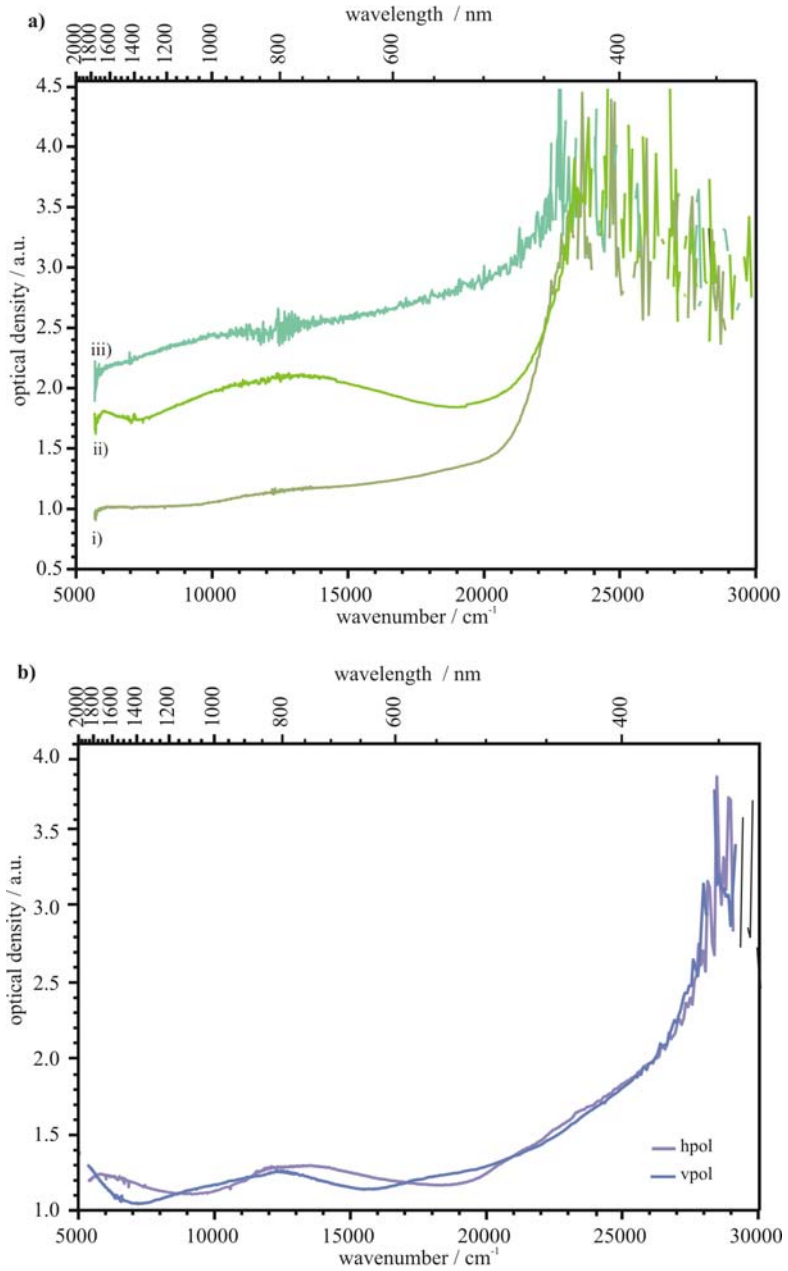

Figure 14.11 (a) UV/Vis/NIR absorption spectra of $Re^{VII}O_2(PO_4)$, (i) spectra just after opening of the ampoule, spectra from (ii) and (iii) belong to the same crystal three days and six days after opening of the ampoule and (**b**) UV/Vis/NIR absorption spectra of $(Re^{VII}{}_2O_5)Si^o{}_2(Si^t{}_2O(PO_4)_6]$.

identified due to the appearance of a very broad band over a region from 930 cm^{-1} to 700 cm^{-1}. In contrast to one broad absorption band for $ReO_2(PO_4)$, two broad bands in the spectrum of Re_2O_7 [262] at about 800 and 930 cm^{-1} were observed. These two bands were explained as a consequence of the presence of perrhenic acid that was formed due to very high sensitivity of Re_2O_7 to water. BEATTIE *et al.* [300] also noticed the presence of $HReO_4$ in the infrared spectrum of Re_2O_7. In the i. r. spectrum of $ReO_2(PO_4)$, the broad band covers basically the

same region to that of Re_2O_7. In spite of moderate water sensitivity of $ReO_2(PO_4)$, this broad band can not be explained in accordance with the authors, [262, 300] as no absorption band observed for –OH group. It is important to mention that a strong broad band for ν_{as}(Re-O-Re) was identified by BEATTIE *et al.* [300] at about 868 cm^{-1} whereas KREBS and MÜLLER [262] reported a broad band for the same vibrational mode between 800 cm^{-1} and 830 cm^{-1}. In the crystal structure of $ReO_2(PO_4)$, only Re-O_b-P bridging bonds are observed, neither Re-O_b-Re nor P-O_b-P are present. We may therefore, correlate the source of the broad band of $ReO_2(PO_4)$ centered at 873 cm^{-1} to the vibration of ν(Re-O-P). In accord with ReO_3 [261] and $Re^V{}_2O_3(P_2O_7)$ [282] a stretching vibrational mode of ν(Re-O), if it is active, is obscured by this broad band. An asymmetric stretching vibrational mode of ν(Mo-O) for the orthophosphate of molybdenum, $MoOPO_4$ [144] was assigned at 625 cm^{-1}. Thus the strong absorption band at about 635 cm^{-1} may be the consequence of ν_{as}(Re-O). Bands in between 581 and 406 cm^{-1} can be assigned as deformation bands δ(O-P-O). However, owing to very high valency of the cation (Re^{7+}), extremely high distortion of [ReO_6] octahedra as well as the complex three dimensional crystal structure of $ReO_2(PO_4)$, it becomes difficult to explain the source of the broad band precisely.

Table 14.7 IR spectrum of $ReO_2(PO_4)$. Vibrational transitions and their tentative assignment.

wavenumber	intensity	vibrational modes
1190	m, sharp	
1155	m, sharp	ν_{asy}(P-O) and
1082	s, sharp	ν_{sym}(P-O)
1024	m, sharp	
968	s, sharp	ν(O=Re=O)
942	vs, sharp	
874	vs, very broad	ν(Re-O-P)
635	s, sharp	ν_{asy}(Re-O)
581	m, sharp	
575	m, sharp	
553	s, broad	
452	m, sharp	δ(O-P-O)
432	m, sharp	
406	m, sharp	

m: medium intensity
s: strong intensity
vs: very strong intensity

15 Conclusion

In the present work, extensive investigations have been carried out for syntheses, crystal chemistry and the bonding phenomena in anhydrous molybdenum and rhenium phosphates. The phosphates were synthesized mainly by chemical vapour transport (CVT) and characterized by X-ray single-crystal, UV/Vis/NIR, IR/Raman, ^{31}P- and ^{29}Si-MAS-NMR, and magnetic measurements.

Molybdenyl(V) phosphates $(MoO)_4(P_2O_7)_3$ and β_I-$MoOPO_4$ were synthesized reducing $Mo^{VI}{}_2P_2O_{11}$ by red phosphorus followed by CVT using I_2 as transport agent.

The formation of molybdenyl(V) pyrophosphate, $(MoO)_4(P_2O_7)_3$, is rather sensitive to the choice of starting solids and other experimental conditions. The best results were obtained at molar ratio 2.5 of the starting materials ($Mo_2P_2O_{11}$ and P); at 400°C, 800 → 650°C, (4 and 6 days, respectively), and crystallization via vapour phase transport. At very similar experimental conditions a second modification of $(MoO)_4(P_2O_7)_3$ named as "Phase X1", (tetragonal, a = 7.8887(5) Å, c = 15.778(19) Å) was frequently obtained. Apart from this, a third polymorph of $MoOPO_4$ isotypic to β-$VOPO_4$ [130] was obtained once.

The crystal structure of $(MoO)_4(P_2O_7)_3$ can be derived from the SiP_2O_7 structure type according to the scheme $(Mo^{V}O)_4(P_2O_7)_3 = 4M^{IV}P_2O_7$ - "P_2O_3". Pyrophosphates MP_2O_7 are structurally related to the rock salt type via the pyrite structure type. Thus, a very complicated structure can be derived from a rather simple one according to the relationship NaCl → FeS_2 → $M^{IV}P_2O_7$ (Z = 4, a ≈ 8 Å) → $(Mo^{V}O)_4(P_2O_7)_3$ (Z = 36, a ≈ 24, b ≈ 24, c ≈ 32 Å). As a consequence, the crystal structure of $(MoO)_4(P_2O_7)_3$ is considered as a hybrid of non-defect like $M^{IV}P_2O_7$ layer (A) and P_2O_3 deficient layer (B), built up by alternating stacking forming ABA´B´AB…. along the crystallographic c-axis (see Figure 15.1). This structure model for $(MoO)_4(P_2O_7)_3$ i.e. "$Mo^{V}P_{1.5}O_{6.25}$" is distinctly different to that of $Nb^{V}P_{1.8}O_7$ [143], another variation of the MP_2O_7 structure type. The crystal structure of $(MoO)_4(P_2O_7)_3$ has been regarded as 3×3×4 superstructure of the MP_2O_7 structure type. The compositional difference is related by the loss of "P_2O_3" from every second pyrophosphate group at layers z = 1/8, 3/8, 5/8, and 7/8 (see Figure 15.1).

Despite our detailed knowledge on the structural model of the pyrophosphate, $(MoO)_4(P_2O_7)_3$, structural refinement in many cases gave physically meaningless distances d(P-O) and d(Mo-O). In addition to this, splitting of half of the molybdenum atoms (18 atoms) appeared in the defect layer. These observations might indicate that the true cell is even larger which we were unable to identify from X-ray single-crystal investigations or the symmetry is even lower.

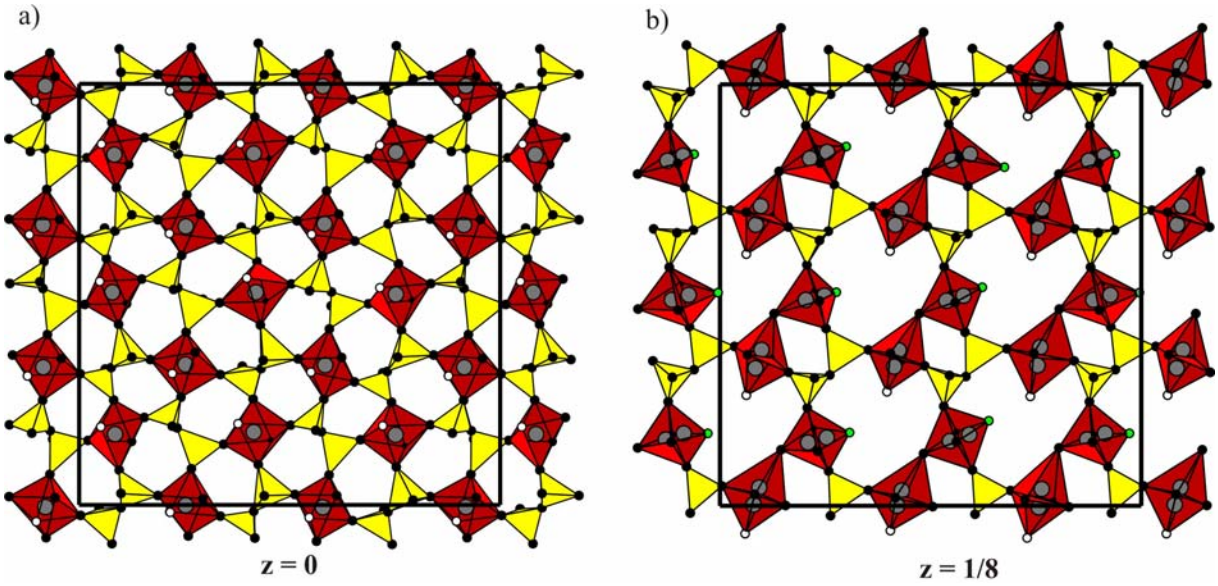

Figure 15.1 Crystal structure of various layers of $(MoO)_4(P_2O_7)_3$. $[MoO_6]$ octahedra (red), $[P_2O_7]$ groups (yellow). Open and green circles indicate terminal oxygen atoms with site occupancy factor 1 and 0.5, respectively (Diamond version 3.2c [138]).

α-$(MoO_2)_2P_2O_7$, one of the four polymorphs, was crystallized by CVT. In contrast to reduced molybdenum phosphates [19], H_2O plays a vital role for its crystallization. X-ray single-crystal diffractions of α-$(MoO_2)_2P_2O_7$ reveal the presence of twinning. Assumption of the loss of a mirror plane perpendicular to the *b*-axis of α-$(MoO_2)_2P_2O_7$ as twin element 0 0 1 0 1 0 1 0 0 gave an immediate improvement in the refinement of the crystal structure. Our refinement from X-ray single-crystal showed improved precision in bond-lengths and -angles (see Figure 15.2) in comparision to that of LISTER *et al.* [25] obtained by X-ray powder diffraction.

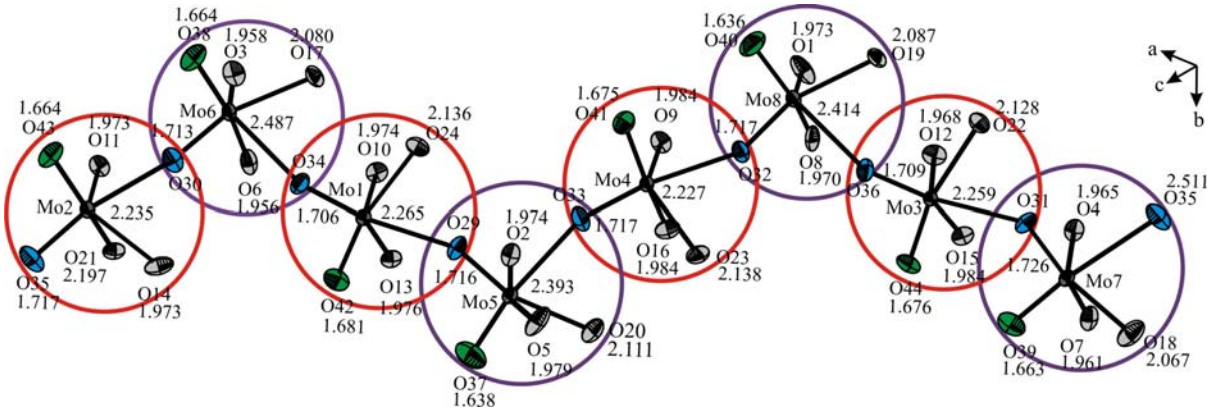

Figure 15.2 ORTEP of $[MoO_6]$ octahedra in α-$(MoO_2)_2P_2O_7$. Green and blue ellipsoids represent molybdenyl(VI) oxygen atoms where the former is bound only to molybdenum; the latter connect two molybdenum atoms. Ellipsoids with 50% probability (Diamond version 3.2c [138]).

In the present work several new **anhydrous phosphates of rhenium** at oxidations states +IV, +V, +VI and +VII have been synthesized and characterized. Apart from the new ternary rhenium phosphates, $Re^{V}_2O_3(P_2O_7)$, $Re^{VI}_2O_3(PO_4)_2$ and $Re^{VII}O_2PO_4$, three quaternary rhenium phosphates, $Re^{IV}_3[Si^{t}_2O(PO_4)_6]$, $NaRe^{IV}_2(PO_4)_3$ and $(Re^{VII}_2O_5)Si^{o}_2[Si^{t}_2O(PO_4)_6]$ have been obtained for the first time.

The ternary phase diagram of Re / P / O has been developed at 800 and 500°C. It shows that the redox behaviour of rhenium phosphates is considerably different from higher to lower temperatures. At 800°C, only ReP_2O_7 coexists with ReO_2 and metallic Re. While ReP_2O_7, ReO_2 and metallic Re coexist at 500 and 800°C, the coexistence of $Re^{VI}_2O_3(PO_4)_2$, ReO_3 as well as ReO_2 observed only at 500°C (see Figure 15.3). Formations of $Re^{V}_2O_3(P_2O_7)$ and $Re^{VII}O_2(PO_4)$ at 500 and 300°C, respectively point to the pronounced complexity of the Re / P / O phase diagram with the lowering of temperature.

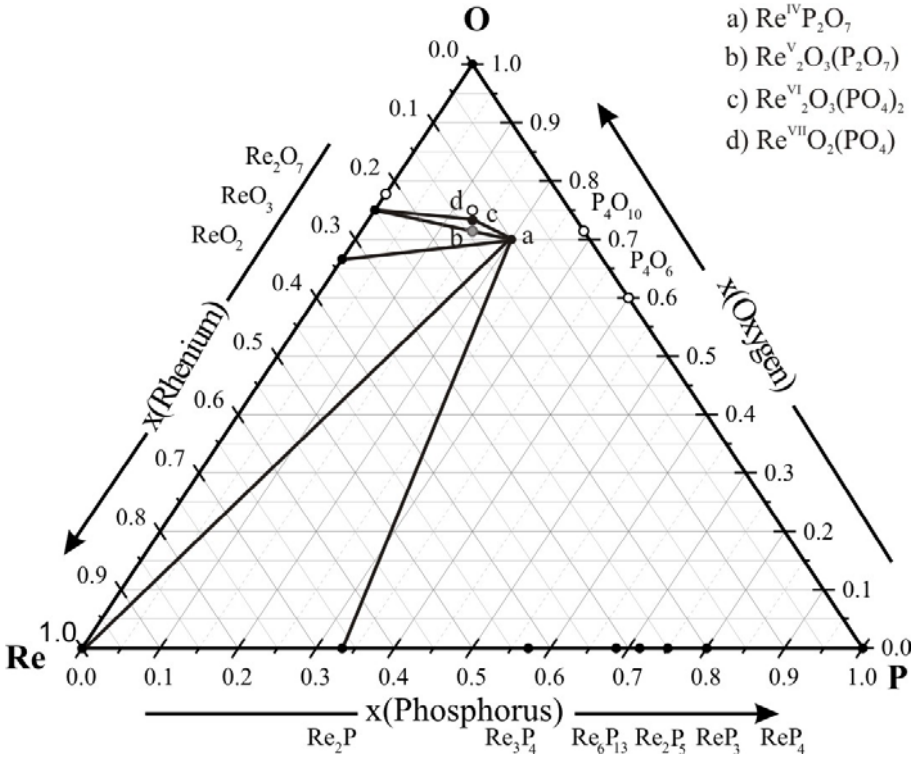

Figure 15.3 Ternary phase diagram developed at 500 °C. Solid lines represent solid-solid equilibria at 500°C. Open circles represent gaseous compounds at this temperature. Grey circle indicates that this phase does not exist at this particular temperature.

Our study shows that CVT experiments are particularly suitable for the crystallization of rhenium phosphates. High volatility of Re_2O_7(g) and ReO_3X(g) (X = Cl, I, OH) allows crystallization of rhenium phosphates by chemical vapour transport. Under perfectly dry conditions, dissociative sublimation of $Re^{VII}O_2(PO_4)$ in a temperature gradient 400 → 300°C is possible.

In addition to the long known $Re^{IV}P_2O_7$, formation of the further tetravalent rhenium phosphates $NaRe^{IV}_2(PO_4)_3$ and $Re^{IV}_3[Si^t_2O(PO_4)_6]$ evidently show the significant thermal stability of this oxidation state of rhenium. $NaRe^{IV}_2(PO_4)_3$ is isotypic to *NASICON* $NaZr_2^{IV}(PO_4)_3$ [204], the crystal structure of $Re^{IV}_3[Si^t_2O(PO_4)_6]$ is isotypic to $Si^{oIV}_3[Si^t_2O(PO_4)_6]$ [222]. Single-crystal electronic absorption spectra of $Re^{IV}P_2O_7$, $NaRe^{IV}_2(PO_4)_3$ and $Re^{IV}_3Si_2O(PO_4)_6$ were measured in the UV/Vis/NIR region (see Figure 15.4). As expected, the observed spectra for all the rhenium(IV)-phosphates are quite similar. The first spin allowed transition $^4A_{2g} \rightarrow {}^4T_{2g}$ is observed for the rhenium(IV)-phosphates at $\Delta_o \sim 25000$ cm^{-1}. Other spin allowed *d-d* transitions are obscured by strong charge transfer transitions at higher wavenumber. At 8000-11000 cm^{-1} and around 16500 cm^{-1} spin-forbidden transitions are observed. These signals are attributed to the spin forbidden transitions $^4A_{2g} \rightarrow {}^2T_{1g}$, $^4A_{2g} \rightarrow {}^2E_g$, and $^4A_{2g} \rightarrow {}^2T_{2g}$. According to AOM, $B \sim 550$ cm^{-1} and $\xi \sim 2500$ cm^{-1} are found. AOM calculations show that for rhenium(IV)-phosphates a *d-p* π-interactions between the Re^{4+} and O^{2-} ions are present. The effective magnetic moment for $Re^{IV}P_2O_7$ is 3.22 μ_B. This value is close to the value 3.28 μ_B calculated within the AOM.

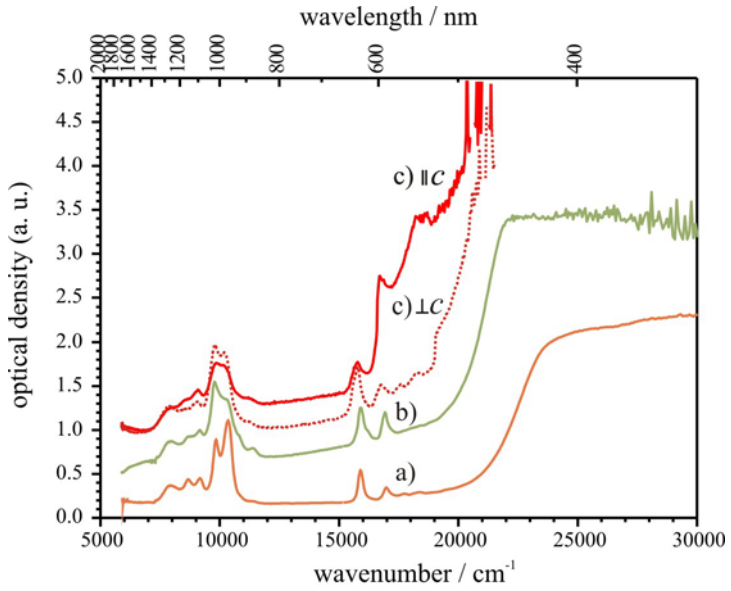

Figure 15.4 UV/Vis/NIR absorption spectra of rhenium(IV) phosphates, $Re_3[Si_2O(PO_4)_6]$ (a), ReP_2O_7 (b), and $NaRe_2(PO_4)_3$ (c) at ambient temperature.

$Re^V_2O_3(P_2O_7)$ is isostructural to $W_2O_3(P_2O_7)$ [78]. It consists of octahedra $[ReO_{3/1}O_{3/2}]$ which are linked via three oxygen atoms to form chain-ladder type ribbons undulating along the crystallographic *c*-axis. In another approach to describe the crystal structure these ribbons might be considered as sections from a ReO_3-type lattice which are linked via pyrophosphate groups to give rather wide octagonal tunnels. In the isostructural $CsW_8(P_2O_7)_4O_{12}$ [255] these tunnels are occupied by a large Cs^+ ion.

The crystal structure analysis of rhenium(VI)-oxidephosphate, $Re_2O_3(PO_4)_2$ revealed isolated di-octahedral $[Re^{VI}_2O_{11}]$ groups with two terminal (Re=O) bonds as building units besides phosphate tetrahedra. Despite the same space group and very similar lattice parameters the orthorhombic modification of $W_2O_3(PO_4)_2$ [74] is not immediately structurally related to rhenium(VI)-oxidephosphate. In contrast to molybdenyl(V) phosphates, rather low magnetic moment for Re^{6+} in $Re_2O_3(PO_4)_2$ ($0.07 \leq \mu_{exp} / \mu_B \leq 0.38$; $1.4\ K \leq T \leq 300\ K$) and its strong temperature dependence are indicative for a very strong spin-orbit interaction. The electronic absorption spectra of d^1 systems in molybdenyl(V)- and rhenyl(VI)- phosphates are similar.
$Re^{VII}O_2(PO_4)$ and $(Re^{VII}_2O_5)Si^o_2[Si^t_2O(PO_4)_6]$ are the first anhydrous phosphates containing a heptavalent metal. These phosphates are stable upto 400°C. The crystal structure of $Re^{VII}O_2(PO_4)$ (see Figure 15.5) might be regarded as superstructure of the ReO_3 structure type, however, with phosphorus in tetragonal environment. The crystal structure of the silicophosphate, $(Re^{VII}_2O_5)Si^o_2[Si^t_2O(PO_4)_6]$ consists of distorted $[Re_2O_{11}]$ dioctahedra, $[Si^{IV}O_6]$ octahedra and $[Si^t_2O(PO_4)_6]^{12-}$ heteropolyanions. ^{31}P-MAS-NMR spectrum of the silicophosphate shows a ratio of about 1:2:2, which is in contrast to the ratio 1:1:1 expected from its crystal structure. We attribute this deviation to a possibly larger unit cell than it was used for the refinement so far.

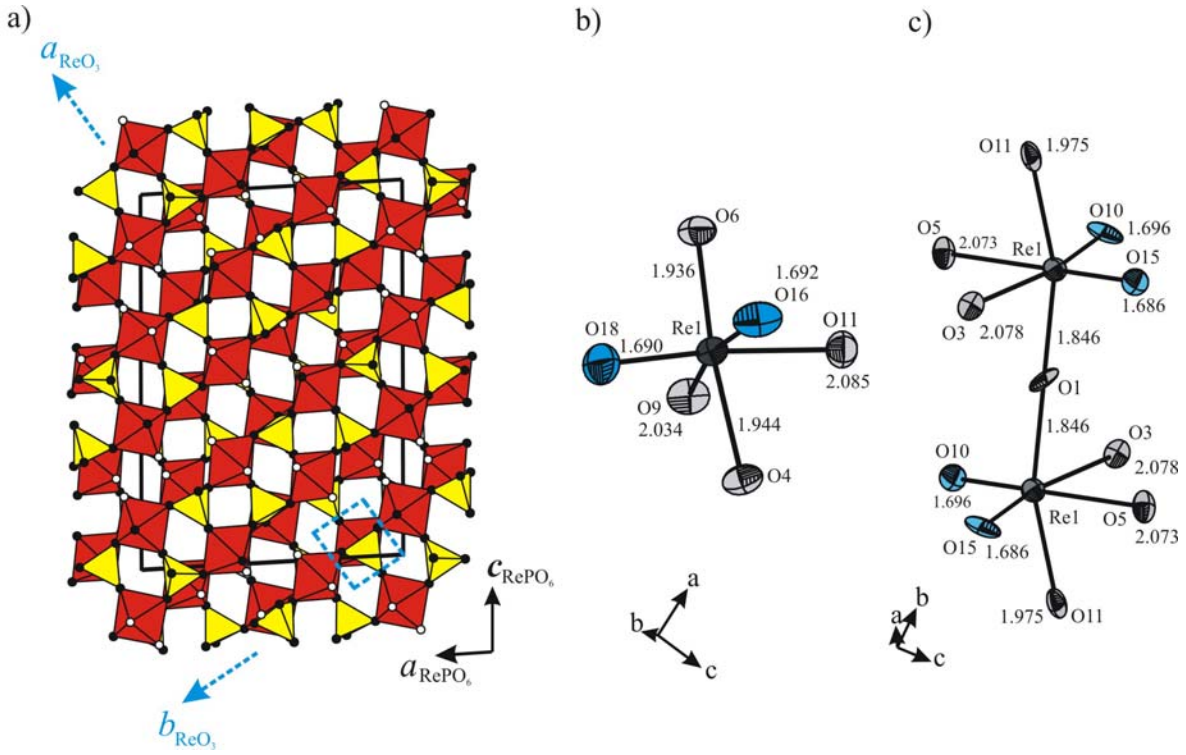

Figure 15.5 Crystal Structure of $Re^{VII}O_2(PO_4)$ with $[ReO_6]$ octahedra (red) and $[PO_4]$ tetrahedra (yellow). Terminal oxygen atoms in white, bridging oxygen atoms in black (a). Representive $[ReO_6]$ octahedra in $Re^{VII}O_2(PO_4)$ (b) and $[Re_2O_{11}]$ group $(Re^{VII}_2O_5)Si^o_2[Si^t_2O(PO_4)_6]$ (c), respectively. Terminal oxygen atoms are in blue (b, c).

It is quite remarkable that the observed range of distances $1.66 \leq d(Re^{VII}\text{-}O) \leq 2.10$ Å in the phosphates is very similar to that found in many other oxide compounds containing rhenium in oxidation states 4+, 5+, 6+ and 7+. Therefore, assignment of oxidation states for rhenium on the basis of distances *d*(Re-O) has to be treated with great care.

As in several coordination compounds of Re^{7+} the formation of the perrhenyl cations $(ReO_2)^{3+}$ and $(Re_2O_5)^{4+}$ are observed in the phosphate and the silico-phosphate, respectively. The presence of two distinctly different types of oxygen atoms (terminal in the perrhenyl-groups and bridging between Re and P) is comparable to oxides and in particular phosphates of V^{4+}, V^{5+}, and Mo^{6+}, which are all active catalysts for selective oxidation of hydrocarbons [301]. These observations might emphasize the catalytic activity of rhenium phosphates.

Chemically and crystal chemically $Re^{VII}O_2(PO_4)$ is very similar to oxide compounds of V^{4+}, V^{5+} and Mo^{6+}, thus providing support for the diagonal relation among V^{5+}, Mo^{6+}, and Re^{7+}. This relation is further expressed by the closely related crystal structures of $Re^{VII}O_2(PO_4)$ and $Mo^{VI}O_2(SO_4)$ [154]. There is even evidence for polymorphism in $Re^{VII}O_2(PO_4)$ as it was observed for $Mo^{VI}O_2(SO_4)$. Phosphates of rhenium in the lower oxidation states +IV, +V, and +VI ($Re^{IV}P_2O_7$ [81], $Re^{V}{}_2O_3(P_2O_7)$ [282], $Re^{VI}{}_2O_3(PO_4)_2$ [281]) are closely related to the corresponding tungsten compounds $W^{IV}P_2O_7$, $W^{V}{}_2O_3(P_2O_7)$, and $W^{VI}{}_2O_3(PO_4)_2$.

Finally, it might be concluded that with the syntheses of anhydrous rhenium phosphates at +IV, +V, +VI, and +VII oxidation states of rhenium, the crystal chemistry of anhydrous transition metal phosphates have been considerably extended. Our study shows that the redox behaviour of rhenium is comparable to that of its neighbour elements; i. e. molybdenum, vanadium. In addition to formation of a large number of ternary phosphates of these elements, up to now a plethora of quaternary phosphates have been synthesized and characterized. The main reason for the formation of such a large number of phosphates is the existence of various oxidation states and their stability in a phosphate matrix. Therefore, it is evident that an enormous research field for polynary rhenium phosphates have been opened by the present work.

16 Appendix

16.A1 Molybdenyl(V) oxidepyrophosphates

Table A1.1 Atomic coordinates and isotropic displacement parameters of subcell of $(MoO)_4(P_2O_7)_3$.

atom	s.o.f	*x*	*y*	*z*	U_{eq} /Å$^{2a)}$
Mo1	1	0.25065(10)	0.50769(12)	0.00378(3)	0.0338(3)
Mo2A	0.449(51)	0.211(5)	0.504(3)	0.2433(7)	0.025(2)
Mo2B	0.540(51)	0.249(2)	0.4979(8)	0.2469(3)	0.0287(15)
Mo3A	0.671(7)	0.7555(2)	0.5002(2)	0.12539(5)	0.0422(6)
Mo3B	0.34(5)	-0.3702(4)	0.4625(3)	0.12443(8)	0.0338(9)
Mo4A	0.678(7)	0.2504(2)	0.0054(2)	0.62464(5)	0.0416(6)
Mo4B	0.34(7)	-0.7122(3)	0.1205(4)	0.12560(8)	0.0346(9)
P1	1	0.3591(4)	0.3872(4)	0.34873(9)	0.0346(8)
P2	1	0.1372(4)	0.6087(4)	0.40130(9)	0.0428(6)
P3	1	0.3471(3)	0.1049(3)	0.47249(8)	0.0417(6)
P4	1	0.1360(3)	-0.1071(3)	0.52739(8)	0.0318(5)
P5	1	-0.1457(3)	0.5971(3)	0.27751(8)	0.03218(5)
P6	1	0.6426(3)	0.3858(3)	0.22253(8)	0.03216(5)
O1	0.5	0.335(3)	0.428(3)	0.5471(4)	0.03217(5)
O2	0.5	0.182(3)	0.588(2)	0.2028(4)	0.0640(6)
O3	1	0.2047(18)	0.4558(18)	0.3755(3)	0.0650(5)
O4	1	0.240(3)	0.016(3)	0.5012(7)	0.0848(3)
O5	1	0.762(4)	0.494(3)	0.2488(8)	0.849(4)
O6	1	0.3756(19)	0.2039(16)	0.3612(6)	0.1976(13)
O7	1	0.309(4)	0.209(2)	0.6217(6)	0.201(14)
O8	1	0.3201(19)	0.402(2)	0.3059(3)	0.117(5)
O9	1	0.0191(17)	0.0195(18)	0.6397(5)	0.166(8)
O10	1	0.2333(19)	0.7669(17)	0.3908(6)	0.107(8)
O11	1	0.4530(16)	-0.1271(19)	0.6106(6)	0.104(5)
O12	1	0.1491(19)	0.5679(18)	0.4448(3)	0.115(6)
O13	1	0.329(3)	0.033(3)	0.4325(4)	0.114(5)
O14	1	0.5125(19)	0.082(3)	0.4891(9)	0.103(5)
O15	1	0.296(3)	0.2768(16)	0.4734(5)	0.148(7)
O16	1	-0.0357(19)	-0.096(4)	0.5133(8)	0.193(13)
O17	1	0.194(3)	0.7170(16)	0.5240(5)	0.131(7)
O18	1	0.167(3)	-0.058(2)	0.5681(4)	0.196(11)
O19	1	0.0315(15)	0.542(3)	0.2777(5)	0.153(9)
O20	1	0.285(3)	-0.083(3)	0.6822(4)	0.1412(7)
O21	1	-0.158(3)	0.7582(18)	0.2574(8)	0.135(9)
O22	1	0.693(2)	0.420(3)	0.1815(4)	0.145(7)
O23	1	0.4695(16)	0.435(3)	0.2276(5)	0.172(10)
O24	1	0.659(3)	0.2086(16)	0.2304(7)	0.1566(8)
O25	1	-0.598(4)	0.358(4)	0.1242(7)	0.141(9)
O26	1	0.046(2)	0.549(3)	0.1287(6	0.169(9

$U_{eq} = (⅓)\Sigma_i\Sigma_j U_{ij} a_i^* a_j^* \mathbf{a}_i \cdot \mathbf{a}_j$

Table A1.2 Atomic coordinates and isotropic displacement parameters of the supercell of $(MoO)_4(P_2O_7)_3$.

atom	s.o.f	*x*	*y*	*z*	U_{eq} /Å$^{2a)}$
Mo1	1	0.4476(4)	0.8130(5)	0.5411(3)	0.0294(4)
Mo2	1	0.4525(3)	0.4656(3)	0.5471(2)	0.0199(5)
Mo3	1	0.4462(4)	0.1422(5)	0.5467(3)	0.0356(5)
Mo4	1	0.1236(3)	0.8057(4)	0.5468(2)	0.0277(4)
Mo5	1	0.1025(3)	0.4595(4)	0.5478(2)	0.0247(4)
Mo6	1	0.1137(4)	0.1389(5)	0.5458(3)	0.0269(4)
Mo7	1	0.7746(4)	0.8074(5)	0.5476(4)	0.0319(4)
Mo8	1	0.7841(3)	0.4843(4)	0.5442(2)	0.0399(5)
Mo9	1	0.7797(4)	0.1437(5)	0.5409(4)	0.0278(4)
Mo10	1	0.0697(4)	0.1855(5)	0.2014(3)	0.0319(4)
Mo11	1	0.0801(3)	0.5253(4)	0.2018(3)	0.0281(4)
Mo12	1	0.9365(5)	0.3543(6)	0.2953(4)	0.0218(4)
Mo13	1	0.3996(4)	0.1846(5)	0.2077(3)	0.0328(5)
Mo14	1	0.4075(3)	0.5243(4)	0.2038(3)	0.0204(4)
Mo15	1	0.3918(4)	0.8398(4)	0.2027(3)	0.0383(5)
Mo16	1	0.7308(4)	0.1882(5)	0.2054(3)	0.0339(4)
Mo17	1	0.7247(3)	0.5118(4)	0.1988(3)	0.0226(4)
Mo18	1	0.7284(5)	0.8581(6)	0.2048(4)	0.0329(5)
M19A	0.5286(14)	0.25325(6)	0.16242(8)	0.12639(5)	0.0202(3)
M19B	0.4714(14)	0.20785(9)	0.15213(11)	0.12360(8)	0.0393(6)
M20A	0.5238(15)	0.20381(11)	0.49019(13)	0.12384(9)	0.0617(8)
M20B	0.4762(15)	0.24759(5)	0.49752(7)	0.12364(5)	0.0079(3)
M21A	0.5701(15)	0.21236(10)	0.82552(13)	0.12249(9)	0.0706(8)
M21B	0.4299(15)	0.25229(7)	0.83995(9)	0.12404(6)	0.0200(4)
M22A	0.5148(16)	0.53969(9)	0.48725(12)	0.12370(8)	0.0492(6)
M22B	0.4852(16)	0.58058(7)	0.49914(8)	0.12410(6)	0.0237(4)
M23A	0.559(15)	0.54874(9)	0.81983(12)	0.12354(8)	0.0590(7)
M23B	0.441(15)	0.59349(6)	0.83427(8)	0.12322(6)	0.0105(4)
M24A	0.526(15)	0.87147(8)	0.15708(11)	0.12628(8)	0.0405(6)
M24B	0.474(15)	0.91364(6)	0.17061(8)	0.12872(5)	0.0208(4)
M25A	0.5436(15)	0.88389(9)	0.48870(11)	0.12466(8)	0.0481(6)
M25B	0.4564(15)	0.92636(6)	0.50092(7)	0.12861(5)	0.0148(4)
M26A	0.5413(18)	0.91094(8)	0.83128(10)	0.12494(7)	0.0456(5)
M26B	0.4587(18)	0.87457(10)	0.81803(13)	0.12446(9)	0.0480(7)
M27A	0.541(15)	0.54618(9)	0.15255(11)	0.12476(8)	0.0491(6)
M27B	0.459(15)	0.59243(7)	0.17094(9)	0.12627(6)	0.0253(4)
M28A	0.6421(16)	0.07967(5)	-0.00112(6)	0.62578(5)	0.0249(3)
M28B	0.3579(16)	0.06853(10)	-0.03655(12)	0.62737(8)	0.0195(6)
M29A	0.6566(15)	0.08460(5)	0.33164(6)	0.62807(4)	0.0221(3)
M29B	0.3434(15)	0.07171(9)	0.29375(11)	0.62640(8)	0.0143(5)
M30A	0.6556(17)	0.08803(6)	0.67028(7)	0.62428(5)	0.0334(4)
M30B	0.3444(15)	0.07616(10)	0.63159(13)	0.62485(9)	0.0211(6)
M31A	0.6828(16)	0.42128(5)	-0.00261(6)	0.62309(4)	0.0280(3)
M31B	0.3172(16)	0.40732(10)	-0.04193(13)	0.62482(9)	0.0130(6)
M32A	0.7211(15)	0.41615(5)	0.33031(7)	0.62628(5)	0.0331(3)
M32B	0.2789(15)	0.40255(10)	0.28791(12)	0.62611(9)	0.0065(6)
M33A	0.621(16)	0.41644(6)	0.67355(8)	0.62192(5)	0.0331(4)

M33B	0.378(16)	0.40164(10)	0.63219(12)	0.62472(9)	0.0283(6)
M34A	0.6692(16)	0.74345(6)	0.00308(7)	0.62296(5)	0.0339(4)
M34B	0.3308(16)	0.73653(10)	-0.03941(12)	0.62612(8)	0.0192(6)
M35A	0.6776(16)	0.74663(6)	0.33962(7)	0.62653(5)	0.0333(3)
M35B	0.3224(16)	0.73579(12)	0.29521(14)	0.62627(10)	0.0281(7)
M36A	0.675(18)	0.74810(7)	0.66757(8)	0.62395(6)	0.0461(5)
M36B	0.325(18)	0.74077(12)	0.62319(14)	0.62363(10)	0.0338(7)
P1	1	0.11501(12)	0.12529(15)	0.34515(10)	0.0338(8)
P2	1	0.04607(13)	0.19935(16)	0.40376(11)	0.0426(9)
P3	1	0.11680(11)	0.45632(14)	0.34671(9)	0.0280(7)
P4	1	0.05327(11)	0.53930(13)	0.40184(9)	0.0254(7)
P5	1	0.11716(12)	0.79744(14)	0.35083(10)	0.0309(7)
P6	1	0.04147(13)	0.87270(15)	0.40398(11)	0.0385(8)
P7	1	0.45374(13)	0.12922(16)	0.34743(11)	0.0396(8)
P8	1	0.37825(10)	0.19830(13)	0.39885(9)	0.0210(6)
P9	1	0.44893(10)	0.46454(13)	0.35304(9)	0.0220(6)
P10	1	0.37395(10)	0.53682(13)	0.40372(9)	0.0240(7)
P11	1	0.45352(14)	0.79426(18)	0.35123(12)	0.0488(10)
P12	1	0.37826(12)	0.87020(14)	0.39884(10)	0.0310(7)
P13	1	0.78838(16)	0.13070(18)	0.34773(13)	0.0574(11)
P14	1	0.71335(11)	0.20823(13)	0.40115(9)	0.0244(6)
P15	1	0.79281(12)	0.46578(14)	0.34832(10)	0.0314(7)
P16	1	0.71175(11)	0.53265(14)	0.39909(10)	0.0287(7)
P17	1	0.78637(13)	0.79172(16)	0.34570(11)	0.0413(9)
P18	1	0.71679(12)	0.87204(15)	0.39852(10)	0.0352(8)
P19	1	0.11386(10)	0.03584(13)	0.46922(9)	0.0224(6)
P20	1	0.0497(1)	0.96046(12)	0.52645(8)	0.0178(6)
P21	1	0.11600(11)	0.37079(13)	0.47249(9)	0.0226(6)
P22	1	0.04428(11)	0.30022(13)	0.52851(9)	0.0247(7)
P23	1	0.11503(10)	0.69604(12)	0.47176(8)	0.0178(6)
P24	1	0.04386(12)	0.62873(14)	0.52884(10)	0.0311(7)
P25	1	0.44692(11)	0.03738(14)	0.47441(10)	0.0301(7)
P26	1	0.37596(12)	0.96347(15)	0.5263(1)	0.0351(8)
P27	1	0.45145(12)	0.36685(15)	0.47258(10)	0.0351(8)
P28	1	0.37932(10)	0.29931(12)	0.52723(8)	0.0199(6)
P29	1	0.45003(11)	0.69944(13)	0.47187(9)	0.0236(7)
P30	1	0.38016(11)	0.62694(14)	0.52714(10)	0.0282(7)
P31	1	0.78263(10)	0.03278(13)	0.47390(9)	0.0207(6)
P32	1	0.70897(12)	0.96416(14)	0.5278(1)	0.0302(7)
P33	1	0.78167(12)	0.36930(14)	0.47573(10)	0.0318(7)
P34	1	0.71278(11)	0.29838(13)	0.52978(9)	0.0216(6)
P35	1	0.77965(11)	0.70483(13)	0.47025(9)	0.0252(7)
P36	1	0.71241(11)	0.63267(14)	0.52774(9)	0.0282(7)
P37	1	0.28408(11)	0.20425(13)	0.27683(9)	0.0257(7)
P38	1	0.21577(10)	0.12602(12)	0.22438(9)	0.0196(6)
P39	1	0.28784(10)	0.53349(12)	0.27877(8)	0.0182(6)
P40	1	0.21347(11)	0.46731(13)	0.22325(9)	0.0221(6)
P41	1	0.28349(11)	0.86169(14)	0.27908(9)	0.0280(7)
P42	1	0.21523(12)	0.79221(14)	0.22034(10)	0.0316(7)
P43	1	0.61840(11)	0.19874(14)	0.27414(9)	0.0273(7)
P44	1	0.54534(11)	0.12661(13)	0.22368(9)	0.0224(6)

P45	1	0.61754(12)	0.53636(14)	0.27681(10)	0.0308(7)
P46	1	0.55121(11)	0.46227(14)	0.22234(9)	0.0247(7)
P47	1	0.61767(12)	0.86289(14)	0.27786(10)	0.0306(7)
P48	1	0.54566(14)	0.79573(17)	0.21951(12)	0.0446(9)
P49	1	0.95283(11)	0.20118(14)	0.27477(9)	0.0253(7)
P50	1	0.88024(11)	0.12570(14)	0.22511(9)	0.0261(7)
P51	1	0.94940(12)	0.53613(15)	0.27786(10)	0.0313(7)
P52	1	0.87810(11)	0.46350(14)	0.22309(10)	0.0290(7)
P53	1	0.95459(10)	0.86390(13)	0.28142(9)	0.0215(6)
P54	1	0.88358(12)	0.79927(15)	0.22414(10)	0.0345(8)
O1	1	0.4476(4)	0.8130(5)	0.5411(3)	0.086(3)
O2	1	0.4525(3)	0.4656(3)	0.5471(2)	0.039(2)
O3	1	0.4462(4)	0.1422(5)	0.5467(3)	0.080(3)
O4	1	0.1236(3)	0.8057(4)	0.5468(2)	0.047(2)
O5	1	0.1025(3)	0.4595(4)	0.5478(2)	0.043(2)
O6	1	0.1137(4)	0.1389(5)	0.5458(3)	0.075(3)
O7	1	0.7746(4)	0.8074(5)	0.5476(4)	0.107(4)
O8	1	0.7841(3)	0.4843(4)	0.5442(2)	0.044(2)
O9	1	0.7797(4)	0.1437(5)	0.5409(4)	0.108(4)
O10	1	0.0697(4)	0.1855(5)	0.2014(3)	0.086(3)
O11	1	0.0801(3)	0.5253(4)	0.2018(3)	0.051(2)
O12	1	0.9365(5)	0.3543(6)	0.2953(4)	0.144(5)
O13	1	0.3996(4)	0.1846(5)	0.2077(3)	0.089(4)
O14	1	0.4075(3)	0.5243(4)	0.2038(3)	0.051(2)
O15	1	0.3918(4)	0.8398(4)	0.2027(3)	0.067(3)
O16	1	0.7308(4)	0.1882(5)	0.2054(3)	0.084(3)
O17	1	0.7247(3)	0.5118(4)	0.1988(3)	0.047(2)
O18	1	0.7284(5)	0.8581(6)	0.2048(4)	0.134(5)
O19X	0.5	0.3062(4)	0.1737(5)	0.1321(3)	0.002(2)
O19Y	0.5	0.1439(5)	0.1324(6)	0.1197(4)	0.019(3)
O20X	0.5	0.2760(4)	0.5118(5)	0.1265(3)	0.000(2)
O20Y	0.5	0.1292(6)	0.4573(7)	0.1148(5)	0.041(4)
O21X	0.5	0.1424(5)	0.7986(6)	0.1193(4)	0.020(3)
O21Y	0.5	0.2886(6)	0.8514(7)	0.1196(5)	0.047(4)
O22X	0.5	0.4714(6)	0.4522(8)	0.1333(5)	0.054(5)
O22Y	0.5	0.6186(6)	0.5166(8)	0.1157(5)	0.054(5)
O23X	0.5	0.4893(4)	0.7900(6)	0.1175(4)	0.015(3)
O23Y	0.5	0.644(2)	0.812(3)	0.0953(18)	0.37(3)
O24X	0.5	0.8034(5)	0.1315(6)	0.1268(4)	0.019(3)
O24Y	0.5	0.9708(5)	0.1720(7)	0.1337(4)	0.031(4)
O25X	0.5	0.8071(7)	0.4716(9)	0.1159(6)	0.073(6)
O25Y	0.5	0.9992(6)	0.5066(7)	0.1353(5)	0.044(4)
O26X	0.5	0.8051(5)	0.7884(6)	0.1240(4)	0.018(3)
O26Y	0.5	0.9391(4)	0.8334(5)	0.1254(3)	0.000(2)
O27X	0.5	0.4823(4)	0.1228(5)	0.1271(4)	0.012(3)
O27Y	0.5	0.6368(5)	0.2010(6)	0.1394(4)	0.016(3)
028	1	0.0967(3)	1.0600(4)	0.6273(3)	0.066(3)
029	1	0.0982(4)	0.3959(6)	0.6323(4)	0.106(4)
O30	1	0.1025(4)	0.7279(5)	0.6252(4)	0.107(4)
O31	1	0.4399(3)	1.0662(4)	0.6229(3)	0.056(3)

O32	1	0.4337(4)	0.4022(5)	0.6196(3)	0.090(4)
O33	1	0.4391(4)	0.7347(5)	0.6192(3)	0.074(3)
O34	1	0.7685(5)	0.0736(6)	0.6213(4)	0.108(4)
O35	1	0.7619(5)	0.4076(6)	0.6265(4)	0.123(5)
O36	1	0.7618(3)	0.7358(4)	0.6207(3)	0.065(3)
O011	1	0.1204(3)	0.0678(4)	0.3530(3)	0.053(2)
O012	1	0.6578(4)	0.3402(5)	0.6467(3)	0.083(3)
O013	1	0.1043(5)	0.1481(5)	0.2974(4)	0.109(4)
O021	1	0.0832(4)	0.2546(4)	0.3883(3)	0.073(3)
O022	1	0.0482(5)	0.1843(7)	0.4504(5)	0.144(5)
O023	1	0.4763(4)	0.2966(5)	0.6022(4)	0.099(4)
OB01	1	0.0627(3)	0.1528(4)	0.3748(3)	0.052(2)
O031	1	0.1212(4)	0.4014(4)	0.3641(3)	0.071(3)
O032	1	0.6729(5)	-0.0011(5)	0.6500(4)	0.106(4)
O033	1	0.1008(3)	0.4764(4)	0.3051(3)	0.048(2)
O041	1	0.9194(4)	0.0958(5)	0.1189(3)	0.089(4)
O042	1	0.0596(6)	0.5187(7)	0.4460(5)	0.172(7)
O043	1	0.4934(3)	0.9477(4)	0.6179(3)	0.063(3)
OB02	1	0.0712(3)	0.4778(4)	0.3769(3)	0.048(2)
O051	1	0.1212(5)	0.7479(5)	0.3572(4)	0.110(4)
O052	1	0.6659(7)	0.6563(10)	0.6393(6)	0.243(9)
O053	1	0.1109(3)	0.8067(4)	0.3060(3)	0.053(2)
O061	1	0.0742(3)	0.9246(4)	0.3957(3)	0.055(3)
O062	1	0.4623(5)	0.6203(7)	0.6140(4)	0.147(6)
O063	1	0.0410(3)	0.8496(3)	0.4457(2)	0.0301(18)
OB03	1	0.0628(2)	0.8214(3)	0.3744(2)	0.0286(18)
O071	1	0.0103(3)	0.3365(4)	0.6465(2)	0.047(2)
O072	1	0.4657(3)	0.0683(4)	0.3558(3)	0.056(3)
O073	1	0.4402(3)	0.1399(4)	0.3049(3)	0.057(3)
O081	1	0.4115(4)	0.2554(4)	0.3831(3)	0.077(3)
O082	1	0.3818(4)	0.1901(4)	0.4445(3)	0.068(3)
O083	1	0.8152(4)	0.3000(5)	0.6150(3)	0.084(3)
OB04	1	0.5893(3)	0.6443(4)	0.1262(3)	0.052(2)
O091	1	0.4409(3)	0.4637(4)	0.3084(3)	0.051(2)
O092	1	-0.0048(3)	-0.0004(3)	0.6388(2)	0.0318(19)
O093	1	0.4571(4)	0.4052(5)	0.3675(3)	0.075(3)
O101	1	0.4011(3)	0.5859(4)	0.3833(3)	0.066(3)
O102	1	0.3868(4)	0.5276(5)	0.4476(3)	0.099(4)
O103	1	0.8111(3)	0.9585(3)	0.6051(2)	0.038(2)
OB05	1	0.3965(3)	0.4812(4)	0.3753(2)	0.041(2)
O111	1	0.0162(4)	0.6711(5)	0.6361(4)	0.099(4)
O112	1	0.4553(3)	0.8103(4)	0.3060(3)	0.055(3)
O113	1	0.4708(4)	0.7333(5)	0.3529(4)	0.090(4)
O121	1	0.3746(3)	0.8507(4)	0.4457(3)	0.060(3)
O122	1	0.8212(7)	0.6255(8)	0.6179(5)	0.192(7)
O123	1	0.4190(4)	0.9152(5)	0.3929(3)	0.077(3)
OB06	1	0.4169(3)	0.8068(4)	0.3750(3)	0.059(3)
O131	1	0.7625(5)	0.1287(6)	0.3118(4)	0.117(4)
O132	1	0.7938(4)	0.0716(4)	0.3689(3)	0.066(3)
O133	1	0.3376(3)	0.3386(4)	0.6485(3)	0.051(2)
O141	1	0.2716(6)	0.7610(8)	0.1060(5)	0.188(7)

O142	1	0.7134(3)	0.1883(4)	0.4455(3)	0.065(3)
O143	1	0.1385(5)	0.2830(6)	0.6024(4)	0.138(5)
OB07	1	0.7405(4)	0.1540(4)	0.3747(3)	0.073(3)
O151	1	0.7822(3)	0.4846(4)	0.3029(2)	0.043(2)
O152	1	0.7952(5)	0.4072(5)	0.3580(4)	0.106(4)
O153	1	0.3452(5)	-0.0017(5)	0.6324(4)	0.104(4)
O161	1	0.7431(3)	0.5877(4)	0.3992(3)	0.063(3)
O162	1	0.7058(3)	0.5146(3)	0.4456(2)	0.0291(18)
O163	1	0.1503(3)	0.9600(4)	0.6197(3)	0.044(2)
OB08	1	0.7398(3)	0.4747(4)	0.3751(3)	0.055(2)
O171	1	0.7747(5)	0.8043(6)	0.2987(4)	0.134(5)
O172	1	0.7951(5)	0.7304(6)	0.3559(4)	0.133(5)
O173	1	0.3391(5)	0.6806(6)	0.6497(4)	0.130(5)
O181	1	0.7489(3)	0.9201(4)	0.3782(2)	0.044(2)
O182	1	0.7222(3)	0.8621(4)	0.4430(2)	0.042(2)
O183	1	0.1467(5)	0.6265(6)	0.6129(4)	0.119(5)
OB09	1	0.7430(4)	0.8115(5)	0.3783(3)	0.089(3)
O191	1	0.0952(5)	0.0274(6)	0.4212(4)	0.136(5)
O192	1	0.0827(5)	0.0799(5)	0.4899(4)	0.101(4)
O193	1	0.1650(4)	0.0224(4)	0.4763(3)	0.068(3)
O201	1	0.0774(5)	0.9049(5)	0.5182(4)	0.103(4)
O202	1	0.0644(3)	0.9835(4)	0.5675(3)	0.056(3)
O203	1	0.9866(5)	0.9759(7)	0.5307(4)	0.138(5)
OB10	1	0.0824(4)	0.0160(5)	0.5052(3)	0.095(4)
O211	1	0.1203(3)	0.3415(4)	0.4378(3)	0.065(3)
O212	1	0.1687(5)	0.3686(6)	0.4987(4)	0.114(5)
O213	1	0.0788(5)	0.4188(6)	0.4761(4)	0.126(5)
O221	1	0.9892(4)	0.3263(5)	0.5328(3)	0.078(3)
O222	1	0.0764(3)	0.2514(4)	0.5181(3)	0.060(3)
O223	1	0.0493(3)	0.3165(4)	0.5712(3)	0.052(2)
OB11	1	0.0807(3)	0.3453(4)	0.5095(3)	0.053(2)
O231	1	0.1140(5)	0.6716(7)	0.4312(4)	0.129(5)
O232	1	0.1675(4)	0.6936(5)	0.5014(3)	0.080(3)
O233	1	0.0878(4)	0.7478(5)	0.4882(3)	0.095(4)
O241	1	0.9829(3)	0.6519(4)	0.5353(3)	0.065(3)
O242	1	0.0711(3)	0.5737(4)	0.5278(3)	0.055(3)
O243	1	0.0665(3)	0.6585(4)	0.5644(2)	0.041(2)
OB12	1	0.0683(5)	0.6683(6)	0.4965(4)	0.112(4)
O251	1	0.4542(4)	0.0106(5)	0.4357(3)	0.086(4)
O252	1	0.4974(3)	0.0236(3)	0.4973(2)	0.0260(17)
O253	1	0.4225(13)	0.0840(15)	0.4752(10)	0.423(18)
O261	1	0.4028(4)	0.9162(4)	0.5084(3)	0.066(3)
O262	1	0.4029(4)	0.9725(5)	0.5653(3)	0.072(3)
O263	1	0.3134(4)	0.9808(5)	0.5367(3)	0.086(3)
OB13	1	0.4019(5)	0.0064(7)	0.5053(4)	0.136(5)
O271	1	0.4416(4)	0.3391(6)	0.4330(4)	0.108(4)
O272	1	0.4970(5)	0.3628(6)	0.4904(4)	0.134(5)
O273	1	0.4355(7)	0.4129(8)	0.4740(5)	0.194(7)
O281	1	0.3169(6)	0.3302(7)	0.5176(5)	0.161(6)
O282	1	0.4150(6)	0.2524(7)	0.5122(5)	0.158(6)
O283	1	0.3758(4)	0.3148(4)	0.5702(3)	0.065(3)

OB14	1	0.4161(4)	0.3498(4)	0.5116(3)	0.066(3)
O291	1	0.5000(4)	0.6888(5)	0.4889(4)	0.094(4)
O292	1	0.4200(4)	0.7499(5)	0.4849(3)	0.097(4)
O293	1	0.5605(5)	0.1788(6)	0.0755(4)	0.114(5)
O301	1	0.4136(7)	0.5688(8)	0.5195(5)	0.186(7)
O302	1	0.3750(4)	0.6520(5)	0.5651(3)	0.071(3)
O303	1	0.3336(6)	0.6604(7)	0.5125(5)	0.164(6)
OB15	1	0.4216(4)	0.6735(5)	0.5084(3)	0.080(3)
O311	1	0.7755(4)	0.0064(5)	0.4400(3)	0.082(3)
O312	1	0.8502(5)	0.0337(7)	0.4925(4)	0.147(6)
O313	1	0.7596(4)	0.0939(5)	0.4654(3)	0.080(3)
O321	1	0.6644(4)	0.9794(5)	0.5054(3)	0.071(3)
O322	1	0.7468(3)	0.9151(4)	0.5220(3)	0.059(3)
O323	1	0.7070(3)	0.9894(3)	0.5736(2)	0.0346(19)
OB16	1	0.7652(4)	1.0158(5)	0.5064(3)	0.087(4)
O331	1	0.7771(3)	0.3522(4)	0.4322(3)	0.061(3)
O332	1	0.8514(6)	0.3655(8)	0.4854(5)	0.176(7)
O333	1	0.7423(5)	0.4266(6)	0.4790(4)	0.134(5)
O341	1	0.6686(3)	0.3239(4)	0.5260(3)	0.049(2)
O342	1	0.7449(4)	0.2397(4)	0.5276(3)	0.063(3)
O343	1	0.7266(5)	0.3175(6)	0.5731(4)	0.129(5)
OB17	1	0.7666(4)	0.3323(5)	0.5025(3)	0.079(3)
O351	1	0.7823(4)	0.6748(5)	0.4279(3)	0.096(4)
O352	1	0.8425(4)	0.7066(5)	0.4845(3)	0.071(3)
O353	1	0.7567(6)	0.7684(7)	0.4668(5)	0.176(7)
O361	1	0.6594(3)	0.6482(4)	0.5308(3)	0.047(2)
O362	1	0.7398(6)	0.5844(8)	0.5173(5)	0.179(7)
O363	1	0.7423(3)	0.6475(4)	0.5677(2)	0.045(2)
OB18	1	0.7709(5)	0.6857(6)	0.5011(4)	0.107(4)
O371	1	0.3452(3)	0.1887(4)	0.2800(2)	0.041(2)
O372	1	0.7340(5)	0.6795(6)	0.1859(4)	0.110(4)
O373	1	0.2621(4)	0.2632(4)	0.2712(3)	0.073(3)
O381	1	0.2287(4)	0.1273(5)	0.1745(3)	0.093(4)
O382	1	0.1549(3)	0.1398(3)	0.2267(2)	0.0315(19)
O383	1	0.2251(4)	0.0692(5)	0.2450(4)	0.107(4)
OB19	1	0.2389(6)	0.1655(7)	0.2493(5)	0.178(6)
O391	1	0.2688(5)	0.5903(6)	0.2752(4)	0.127(5)
O392	1	0.3495(3)	0.5180(4)	0.2772(3)	0.059(3)
O393	1	0.2744(4)	0.5168(5)	0.3251(3)	0.070(3)
O401	1	0.2245(7)	0.4020(9)	0.2292(6)	0.235(9)
O402	1	0.2276(4)	0.4857(5)	0.1838(3)	0.091(4)
O403	1	0.1531(3)	0.4647(4)	0.2318(3)	0.053(2)
OB20	1	0.2329(3)	0.4900(4)	0.2639(3)	0.056(3)
O411	1	0.2744(4)	0.9161(5)	0.2617(3)	0.077(3)
O412	1	0.7549(4)	0.6430(5)	0.6787(3)	0.094(4)
O413	1	0.3459(3)	0.8497(3)	0.2850(2)	0.0258(17)
O421	1	0.1556(3)	0.8021(3)	0.2214(2)	0.036(2)
O422	1	0.2375(6)	0.8072(7)	0.1803(5)	0.150(6)
O423	1	0.2145(4)	0.7319(5)	0.2275(3)	0.089(4)
OB21	1	0.2429(4)	0.8196(4)	0.2661(3)	0.067(3)
O431	1	0.6801(4)	0.1931(5)	0.2779(3)	0.077(3)

O432	1	0.1073(4)	0.3097(5)	0.6883(3)	0.093(4)
O433	1	0.5854(4)	0.2620(5)	0.2559(4)	0.100(4)
O441	1	0.5492(5)	0.0660(6)	0.2322(4)	0.125(5)
O442	1	0.4875(3)	0.1338(4)	0.2337(3)	0.062(3)
O443	1	0.5579(4)	0.1536(5)	0.1852(3)	0.086(3)
OB22	1	0.5760(3)	0.1519(4)	0.2597(3)	0.045(2)
O451	1	0.0849(3)	0.9844(3)	0.6841(2)	0.0323(18)
O452	1	0.6764(3)	0.5215(4)	0.2818(2)	0.042(2)
O453	1	0.6087(6)	0.6028(7)	0.2708(5)	0.175(7)
O461	1	0.9451(5)	0.5183(6)	0.6793(4)	0.107(4)
O462	1	0.4880(4)	0.4681(5)	0.2332(3)	0.082(3)
O463	1	0.5623(5)	0.4096(6)	0.2473(4)	0.108(4)
OB23	1	0.5719(4)	0.5176(5)	0.2441(3)	0.074(3)
O471	1	0.6105(7)	0.9164(9)	0.2641(6)	0.223(9)
O472	1	0.6781(4)	0.8503(4)	0.2829(3)	0.069(3)
O473	1	0.5979(4)	0.8553(5)	0.3144(3)	0.091(4)
O481	1	0.4869(3)	0.8027(4)	0.2226(2)	0.043(2)
O482	1	0.5429(5)	0.7405(6)	0.2310(4)	0.109(4)
O483	1	0.5668(4)	0.8246(5)	0.1800(4)	0.099(4)
OB24	1	0.5723(4)	0.8201(5)	0.2609(3)	0.088(4)
O491	1	0.9269(5)	0.2517(6)	0.2561(4)	0.139(5)
O492	1	0.5172(3)	0.3082(3)	0.7224(2)	0.0307(19)
O493	1	0.9416(4)	0.1938(5)	0.3162(4)	0.089(4)
O501	1	0.8803(5)	0.1498(7)	0.1899(5)	0.142(5)
O502	1	0.8916(5)	0.0694(6)	0.2287(4)	0.106(4)
O503	1	0.8194(3)	0.1308(4)	0.2399(3)	0.049(2)
OB25	1	0.9170(5)	0.1504(5)	0.2538(4)	0.106(4)
O511	1	0.0559(5)	0.0883(6)	0.2297(4)	0.135(5)
O512	1	0.4144(4)	0.9736(5)	0.6814(3)	0.088(3)
O513	1	0.9914(4)	0.0263(5)	0.2212(3)	0.071(3)
O521	1	0.9001(4)	0.4642(4)	0.1837(3)	0.069(3)
O522	1	0.8790(4)	0.4019(4)	0.2408(3)	0.075(3)
O523	1	0.8171(4)	0.4722(4)	0.2230(3)	0.063(3)
OB26	1	0.9051(3)	0.5018(4)	0.2535(3)	0.062(3)
O531	1	0.9494(5)	0.9293(6)	0.2685(4)	0.115(4)
O532	1	0.4326(4)	0.6521(5)	0.6782(4)	0.100(4)
O533	1	0.0145(3)	0.8517(4)	0.2817(3)	0.048(2)
O541	1	0.8944(4)	0.8050(5)	0.1873(4)	0.098(4)
O542	1	0.8786(4)	0.7438(5)	0.2406(3)	0.076(3)
O543	1	0.8199(3)	0.8113(4)	0.2222(2)	0.042(2)
OB27	1	0.9133(3)	0.8352(4)	0.2588(3)	0.061(3)

$U_{eq} = (⅓)\Sigma_i\Sigma_j U_{ij} a_i^* a_j^* \mathbf{a}_i \cdot \mathbf{a}_j$

Table A1.3 Interatomic distances (Å) and angles (°) in the subcell of $(MoO)_4(P_2O_7)_3$.

d(Mo1-O1)	1.621(13)	*d*(Mo3B-O22)	1.918(12)	*d*(P3-O15)	1.410(11)
d(Mo1-O17)	1.932(10)	*d*(Mo3B-O13)	1.926(13)	*d*(P3-O13)	1.407(12)
d(Mo1-O16)	1.953(13)	*d*(Mo3B-O10)	1.940(12)	*d*(P3-O14)	1.416(13)
d(Mo1-O14)	1.965(14)	*d*(Mo4A-Mo4B)	1.036(3)	*d*(P3-O4)	1.429(14)
d(Mo1-O15)	1.988(11)	*d*(Mo4A-O7)	1.67(2)	*d*(P4-O18)	1.378(11)
d(Mo1-O12)	2.127(10)	*d*(Mo4A-O9)	1.885(13)	*d*(P4-O16)	1.426(13)
d(Mo2A-O2)	1.47(3)	*d*(Mo4A-O11)	1.955(12)	*d*(P4-O17)	1.460(12)
d(Mo2A-O19)	1.81(3)	*d*(Mo4A-O20)	1.983(12)	*d*(P4-O4)	1.519(16)
d(Mo2A-O21)	1.98(3)	*d*(Mo4A-O18)	1.986(11)	*d*(P5-O20)	1.402(12)
d(Mo2A-O24)	2.08(3)	*d*(Mo4B-Mo4A)	1.036(3)	*d*(P5-O21)	1.424(14)
d(Mo2A-O23)	2.16(4)	*d*(Mo4B-O20)	1.919(13)	*d*(P5-O5)	1.422(14)
d(Mo2A-O8)	2.32(3)	*d*(Mo4B-O9)	1.929(12)	*d*(P5-O19)	1.459(11)
d(Mo2B-O2)	1.66(2)	*d*(Mo4B-O18)	1.933(12)	*d*(P6-O22)	1.397(11)
d(Mo2B-O23)	1.908(19)	*d*(Mo4B-O11)	1.954(11)	*d*(P6-O24)	1.422(12)
d(Mo2B-O24)	1.947(14)	*d*(Mo4B-O25)	2.07(4)	*d*(P6-O23)	1.424(12)
d(Mo2B-O1)	2.001(16)	*d*(Mo4B-Mo4A)	1.036(3)	*d*(P6-O5)	1.520(16)
d(Mo2B-O21)	2.020(15)	*d*(P1-O8)	1.408(10)		
d(Mo2B-O8)	2.103(18)	*d*(P1-O6)	1.501(12)		
d(Mo3A-Mo3B)	1.032(3)	*d*(P1-O9)	1.503(12)		
d(Mo3A-O26)	1.61(2)	*d*(P1-O3)	1.581(13)		
d(Mo3A-O10)	1.908(12)	*d*(P2-O12)	1.429(11)		
d(Mo3A-O6)	1.952(12)	*d*(P2-O10)	1.494(12)		
d(Mo3A-O22)	1.961(11)	*d*(P2-O11)	1.505(12)		
d(Mo3A-O13)	1.980(12)	*d*(P2-O3)	1.550(13)		
d(Mo3B-Mo3A)	1.032(3)				
d(Mo3B-O6)	1.953(12)				
d(Mo3B-O25)	1.97(4)				
d(Mo3A-Mo3B)	1.032(3)				

Table A1.4 Anisotropic displacement parameters (Å^2) of the subcell of $(MoO)_4(P_2O_7)_3$.

Atom	U_{11}	U_{22}	U_{33}	U_{12}	U_{13}	U_{23}
Mo1	0.0308(5)	0.0392(5)	0.0314(6)	-0.0038(4)	-0.0063(3)	0.0060(3)
Mo2A	0.010(6)	0.033(4)	0.031(4)	0.004(3)	-0.013(4)	0.002(3)
Mo2B	0.027(3)	0.0305(10)	0.0291(16)	-0.0022(13)	0.0020(16)	-0.0066(8)
Mo3A	0.0565(13)	0.0415(10)	0.0286(8)	0.0034(6)	0.0065(6)	0.0028(5)
Mo3B	0.0448(19)	0.0319(12)	0.0246(11)	0.0027(11)	0.0038(11)	0.0022(10)
Mo4A	0.0405(10)	0.0561(13)	0.0284(8)	0.0035(6)	-0.0030(5)	-0.0061(6)
Mo4B	0.0315(11)	0.0464(19)	0.0260(11)	0.0018(11)	0.0028(10)	0.0042(11)
P1	0.0459(15)	0.0390(14)	0.0436(15)	-0.0014(14)	-0.0058(12)	0.0063(12)
P2	0.0380(13)	0.0458(15)	0.0416(15)	0.0009(14)	-0.0063(12)	0.0064(12)
P3	0.0267(10)	0.0360(12)	0.0329(12)	-0.0005(10)	0.0022(9)	0.0041(10)
P4	0.0268(10)	0.0388(12)	0.0309(12)	-0.0028(10)	-0.0007(9)	0.0043(10)
P5	0.0358(12)	0.0262(10)	0.0329(12)	-0.0005(10)	-0.004(1)	-0.0026(9)
P6	0.0378(12)	0.0269(11)	0.0318(12)	-0.0031(10)	-0.0032(10)	0.0017(9)
O1	0.085(13)	0.097(14)	0.010(6)	0.015(13)	-0.020(7)	0.005(7)
O2	0.098(14)	0.085(12)	0.013(6)	0.026(13)	-0.002(8)	0.029(7)
O3	0.091(8)	0.094(8)	0.069(7)	-0.026(7)	0.039(7)	-0.039(6)
O4	0.20(2)	0.22(3)	0.171(19)	-0.06(2)	0.096(17)	0.096(17)
O5	0.23(3)	0.19(2)	0.21(2)	-0.03(2)	-0.13(2)	-0.110(18)
O6	0.084(9)	0.057(7)	0.210(16)	-0.010(6)	-0.015(10)	0.052(9)
O7	0.187(19)	0.105(13)	0.21(2)	-0.024(16)	0.023(17)	-0.056(13)
O8	0.115(11)	0.161(13)	0.045(6)	0.074(11)	0.008(6)	0.018(7)
O9	0.063(7)	0.083(9)	0.167(14)	0.028(7)	0.014(8)	-0.025(9)
O10	0.086(9)	0.058(7)	0.203(17)	-0.033(7)	0.017(10)	0.027(9)
O11	0.057(6)	0.091(9)	0.194(15)	0.012(7)	0.053(8)	0.016(10)
O12	0.146(12)	0.113(10)	0.052(6)	0.078(10)	-0.014(7)	-0.001(6)
O13	0.193(18)	0.193(18)	0.060(8)	0.047(17)	-0.035(10)	-0.048(9)
O14	0.066(8)	0.150(17)	0.36(3)	0.006(11)	-0.097(15)	0.06(2)
O15	0.196(18)	0.062(7)	0.133(12)	0.071(10)	-0.068(12)	-0.053(8)
O16	0.066(9)	0.24(3)	0.28(3)	0.079(14)	-0.074(13)	0.01(2)
O17	0.28(3)	0.059(7)	0.125(11)	0.070(13)	-0.007(15)	-0.047(7)
O18	0.27(2)	0.098(10)	0.060(7)	-0.044(15)	-0.070(11)	-0.012(7)
O19	0.060(7)	0.21(2)	0.133(12)	0.067(10)	0.055(8)	0.052(13)
O20	0.180(17)	0.202(17)	0.054(8)	-0.037(18)	-0.042(9)	0.031(10)
O21	0.128(15)	0.057(7)	0.33(3)	0.025(10)	0.024(18)	0.071(13)
O22	0.081(8)	0.32(3)	0.065(8)	-0.041(15)	-0.002(7)	0.099(12)
O23	0.052(6)	0.21(2)	0.159(15)	0.046(11)	0.043(8)	0.031(15)
O24	0.23(2)	0.047(7)	0.23(2)	0.030(12)	-0.089(19)	0.043(10)
O25	0.24(3)	0.24(3)	0.176(17)	0.17(2)	-0.116(19)	-0.101(19)
O26	0.086(11)	0.21(2)	0.191(19)	0.019(14)	0.052(11)	0.039(18)

Table A1.5 Anisotropic displacement parameters ($Å^2$) for Mo1-Mo18 atoms in the supercell of $(MoO)_4(P_2O_7)_3$.

Atom	U_{11}	U_{22}	U_{33}	U_{12}	U_{13}	U_{23}
Mo1	0.0401(5)	0.0247(6)	0.0415(6)	-0.0076(5)	-0.0166(5)	0.0065(6)
Mo2	0.0198(4)	0.0328(6)	0.0221(5)	-0.0072(4)	-0.0008(4)	0.0040(5)
Mo3	0.0287(4)	0.0375(6)	0.0370(6)	-0.0104(5)	-0.0099(4)	0.0198(5)
Mo4	0.0298(4)	0.0087(4)	0.0466(6)	-0.0020(4)	-0.0136(4)	-0.0044(5)
Mo5	0.0211(4)	0.0369(6)	0.0148(4)	-0.0038(4)	-0.0110(3)	0.0170(4)
Mo6	0.0090(3)	0.0184(5)	0.0558(7)	-0.0031(4)	-0.0021(4)	0.0104(5)
Mo7	0.0245(4)	0.0265(6)	0.0514(6)	0.0078(5)	-0.0148(4)	-0.0083(5)
Mo8	0.0238(4)	0.0639(8)	0.0319(6)	-0.0141(5)	-0.0085(4)	0.0096(6)
Mo9	0.0156(4)	0.0459(7)	0.0286(5)	0.0047(5)	0.0036(4)	0.0118(5)
Mo10	0.0422(5)	0.0257(5)	0.0119(4)	0.0107(5)	0.0067(4)	-0.0041(5)
Mo11	0.0406(4)	0.0263(5)	0.0126(4)	-0.0184(4)	0.0031(4)	-0.0087(5)
Mo12	0.0203(3)	0.0172(4)	0.0296(5)	-0.0040(4)	0.0104(4)	0.0022(5)
Mo13	0.0426(5)	0.0462(6)	0.0241(5)	0.0035(5)	0.0030(4)	-0.0295(5)
Mo14	0.0267(4)	0.0185(5)	0.0211(5)	-0.0102(4)	0.0106(4)	-0.0070(5)
Mo15	0.0590(6)	0.0229(5)	0.0410(6)	-0.0016(5)	-0.0125(5)	-0.0125(6)
Mo16	0.0338(5)	0.0218(5)	0.0462(6)	0.0046(4)	0.0097(5)	0.0135(5)
Mo17	0.0177(3)	0.0089(4)	0.0300(5)	-0.0103(3)	0.0059(4)	-0.0020(4)
Mo18	0.0324(5)	0.0241(5)	0.0427(6)	-0.0077(4)	0.0130(5)	0.0003(5)

16.A2 β_I-Molybdenyl(V) oxidephosphate

Table A2.1 Details concerning data collection, structure determination of β_I-$MoOPO_4$.

crystal data	
chemical formula	β_I-$MoOPO_4$
crystal system	orthorhombic
space group	*Pnma* (No. 62)
a / Å	7.704(2
b / Å	6.301(2)
c / Å	7.080(2)
V / Å^3	343.70(2)
Z	4
μ / mm^{-1}	4.158
$D_{X\text{-}ray}$ / g·cm^{-3}	3.999
colour	red
crystal shape	rectangular
size /mm^3	0.04×0.03×0.02
MW / g·mol^{-1}	206.9
F(000)	388
data collection	
Nonius κ-CCD diffractometer, Mo-Kα-radiation, λ = 0.71073Å, graphite-monochromator	
temperature / K	293
scan range θ / °	$2.91 \le \theta \le 27.485$
	$-9 \le h \le 9$
	$-8 \le k \le 8$
	$-9 \le l \le 7$
absorption correction	multi-scans [115]
structure refinement	
software	SHELX97 [105]
measured reflections	4073
ind. reflections	433; 289 with $\lvert F_o \rvert > 4\sigma(F_o)$
parameter; Goof	40; 1.12
residuals	
R_{int}	0.264
R_1[a)]	0.1005
wR_2[b)]	0.2838
weighting scheme	A = 0.1660; B = 3.7751
residual electron density	
$\Delta\rho_{max}$ / Å^{-3}	4.58 (close to Mo1
$\Delta\rho_{min}$ / Å^{-3}	-1.67 (close to Mo1)

[a)] $R_1 = \Sigma||F_o| - |F_c|| / |F_o|$, $F_o^2 \ge 2\sigma(F_o^2)$

[b)] $wR_2 = 1 / [\sigma^2(F_o^2) + (A \cdot P)^2 + B \cdot P]$; $P = (F_o^2 + 2F_c^2) / 3$

Table A2.2 Atomic co-ordinates and isotropic displacement parameters of β_I-$MoOPO_4$.

atoms	**site**	***x***	***y***	***z***	U_{eq} /Å$^{2a)}$
Mo1	4*c*	0.9239(3)	1/4	0.2277(3)	0.029(1)
P1	4*c*	0.3709(11)	3/4	0.1318(10)	0.029(2)
O1	4*c*	0.791(3)	1/4	-0.018(3)	0.03(4)
O2	8*d*	0.8729(18)	0.557(2)	0.2403(17)	0.026(3)
O3	4*c*	0.464(3)	1/4	-0.007(3)	0.041(6)
O4	4*c*	0.133(3)	1/4	0.159(3)	0.034(5)

a) $U_{eq} = (⅓)\Sigma_i\Sigma_j U_{ij} a_i^* a_j^* \mathbf{a}_i \cdot \mathbf{a}_j$

Table A2.3 β_I-$MoOPO_4$. Selected interatomic distances (Å) and angles (°); estimated standard deviations in parentheses.

d(Mo1-O4)	1.68(2)	*d*(P1-O1)	1.49(2)
d(Mo1-O2)	1.976(14)	*d*(P1-O2)	1.52(1)
d(Mo1-O1)	1.976(14)	*d*(P1-O2)	1.52(1)
d(Mo1-O3)	2.01(2)	*d*(P1-O3)	1.54(3)
d(Mo1-O1)	2.02(2)		
d(Mo1-O4)	2.38(3)	∠(Mo1,O4,Mo1)	177.12 (5)

Table A2.4 β_I-$MoOPO_4$. Anisotropic displacement parameters, in Å^2.

atom	***U*11**	***U*22**	***U*33**	***U*12**	***U*13**	***U*23**
Mo1	0.035(2)	0.0321(15)	0.021(1)	0.00000	0.001(1)	0.00000
P1	0.030(4)	0.040(5)	0.017(4)	0.00000	0.001(3)	0.00000
O1	0.04(1)	0.041(12)	0.023(1)	0.00000	-0.005(9)	0.00000
O2	0.030(7)	0.031(8)	0.019(7)	0.001(5)	0.003(5)	-0.004(5)
O3	0.06(2)	0.06(2)	0.007(9)	0.00000	-0.003(9)	0.00000
O4	0.05(1)	0.022(1)	0.03(1)	0.00000	0.01(1)	0.00000

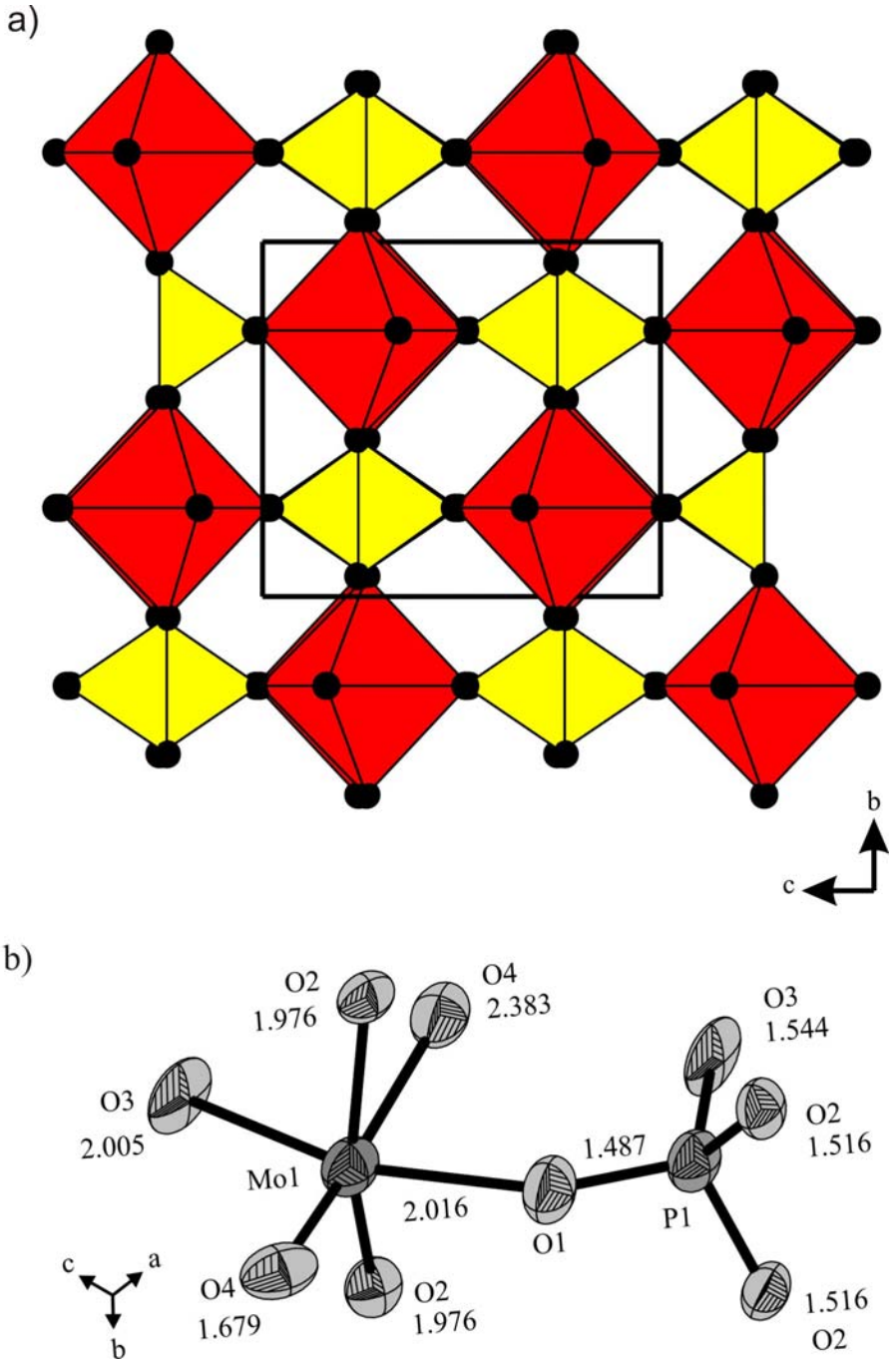

Figure A2.1 Crystal structure of β_I-$MoOPO_4$ (a). ORTEP representation of β_I-$MoOPO_4$ (b). Ellipsoids at 80% probability level (Diamond version 3.2c [138]).

16.A3 α-Molybdenyl(VI) oxidepyrophosphate

Table A3.1 α-$((MoO_2)_2(P_2O_7)$. Selected interatomic distances (Å) and angles (°); estimated standard deviation in parentheses.

X-ray single crystal data at 293 K (this work)		**X-ray powder data at 250 K** (Lister *et al.* [25])	
d(Mo1-O42$_t$)	1.681(4)	d(Mo1-O42$_t$)	1.658(8)
d(Mo1-O34$_t$)	**1.707(4)**	d(Mo1-O34$_t$)	**1.758(9)**
d(Mo1-O10)	1.975(4)	d(Mo1-O10)	1.987(7)
d(Mo1-O13)	1.975(4)	d(Mo1-O13)	2.025(6)
d(Mo1-O24)	2.136(4)	d(Mo1-O24)	2.146(7)
d(Mo1-O2$_b$)	**2.264(4)**	d(Mo1-O2$_b$)	**2.196(9)**
d(Mo2-O43$_t$)	1.664(5)	d(Mo2-O43$_t$)	1.649(8)
d(Mo2-O35$_t$)	**1.717(4)**	d(Mo2-O35$_t$)	**1.787(8)**
d(Mo2-O11)	1.973(5)	d(Mo2-O11)	1.960(7)
d(Mo2-O14)	1.973(4)	d(Mo2-O14)	1.962(8)
d(Mo2-O21)	2.198(4)	d(Mo2-O21)	2.192(7)
d(Mo2-O30$_b$)	**2.234(4)**	d(Mo2-O30$_b$)	**2.200(9)**
d(Mo3-O44$_t$)	1.675(4)	d(Mo3-O44$_t$)	1.699(8)
d(Mo3-O36$_t$)	**1.708(4)**	d(Mo3-O36$_t$)	**1.748(8)**
d(Mo3-O12)	1.968(4)	d(Mo3-O12)	1.975(7)
d(Mo3-O15)	1.985(4)	d(Mo3-O15)	1.997(7)
d(Mo3-O22)	2.128(4)	d(Mo3-O22)	2.146(7)
d(Mo3-O31$_t$)	**2.260(4)**	d(Mo3-O31$_t$)	**2.186(9)**
d(Mo4-O41$_t$)	1.675(4)	d(Mo4-O41$_t$)	1.660(8)
d(Mo4-O33$_t$)	**1.717(4)**	d(Mo4-O33$_t$)	**1.802(8)**
d(Mo4-O16)	1.985(5)	d(Mo4-O16)	1.982(7)
d(Mo4-O9)	1.985(4	d(Mo4-O9)	1.992(7)
d(Mo4-O23)	2.138(4)	d(Mo4-O23)	2.115(7)
d(Mo4-O32$_b$)	2.227(4)	d(Mo4-O32$_b$)	2.201(9)
d(Mo5-O37$_t$)	**1.639(5)**	d(Mo5-O37$_t$)	**1.671(8)**
d(Mo5-O29$_t$)	**1.716(4)**	d(Mo5-O29$_t$)	**1.776(9)**
d(Mo5-O2)	1.974(4)	d(Mo5-O2)	1.969(7)
d(Mo5-O5)	1.979(5)	d(Mo5-O5)	1.994(7)
d(Mo5-O20)	**2.110(4)**	d(Mo5-O20)	**2.065(8)**
d(Mo5-O33$_b$)	2.393(4)	d(Mo5-O33$_b$)	2.360(9)
d(Mo6-O38$_t$)	**1.664(5)**	d(Mo6-O38$_t$)	**1.690(9)**
d(Mo6-O30$_t$)	**1.714(4)**	d(Mo6-O30$_t$)	**1.744(9)**
d(Mo6-O6)	1.956(5)	d(Mo6-O6)	1.963(7)
d(Mo6-O3)	1.958(4)	d(Mo6-O3)	1.980(7)
d(Mo6-O17)	2.079(4)	d(Mo6-O17)	2.064(7)
d(Mo6-O34$_b$)	2.487(4)	d(Mo6-O34$_b$)	2.439(8)
d(Mo7-O39$_t$)	1.663(4)	d(Mo7-O39$_t$)	1.646(8)
d(Mo7-O31$_t$)	**1.726(4)**	d(Mo7-O31$_t$)	**1.800(8)**
d(Mo7-O7)	1.962(4)	d(Mo7-O7)	1.961(7)
d(Mo7-O4)	1.966(4)	d(Mo7-O4)	1.967(7)
d(Mo7-O18)	2.066(4)	d(Mo7-O18)	2.045(7)
d(Mo7-O35$_b$)	**2.511(4)**	d(Mo7-O35$_b$)	**2.468(8)**
d(Mo8-O40$_t$)	1.637(5)	d(Mo8-O40$_t$)	1.662(8)
d(Mo8-O32$_t$)	1.717(4)	d(Mo8-O32$_t$)	1.725(9)
d(Mo8-O8)	1.969(5)	d(Mo8-O8)	1.944(7)

d(Mo8-O1)	1.973(5)	*d*(Mo8-O1)	1.954(7)
d(Mo8-O19)	2.087(3)	*d*(Mo8-O19)	2.077(7)
d(Mo8-O36$_b$)	**2.415(4)**	*d*(Mo8-O36$_b$)	**2.365(8)**
d(P1-O21)	**1.462(4)**	*d*(P1-O21)	**1.502(7)**
d(P1-O1)	1.507(5)	*d*(P1-O1)	1.505(7)
d(P1-O5)	1.507(5)	*d*(P1-O5)	1.508(7)
d(P1-O26$_b$)	1.567(5)	*d*(P1-O26$_b$)	1.565(7)
d(P2-O22)	1.479(4)	*d*(P2-O22)	1.486(7)
d(P2-O8)	1.510(5)	*d*(P2-O8)	1.518(7)
d(P2-O4)	1.510(5)	*d*(P2-O4)	1.534(7)
d(P2-O27$_b$)	1.586(4)	*d*(P2-O27$_b$)	1.570(7)
d(P3O23)	1.476(4)	*d*(P3O23)	1.502(7)
d(P3-O3)	1.513(5)	*d*(P3-O3)	1.505(7)
d(P3-O7)	1.516(5)	*d*(P3-O7)	1.510(7)
d(P3-O28$_b$)	1.570(4)	*d*(P3-O28$_b$)	1.566(7)
d(P4-O24)	**1.479(4)**	*d*(P4-O24)	**1.506(7)**
d(P4-O2)	1.509(5)	*d*(P4-O2)	1.516(7)
d(P4-O6)	1.520(5)	*d*(P4-O6)	1.517(7)
d(P4-O25$_b$)	1.575(4)	*d*(P4-O25$_b$)	1.572(7)
d(P5-O17)	1.496(4)	*d*(P5-O17)	1.497(8)
d(P5-O13)	1.510(5)	*d*(P5-O13)	1.511(7)
d(P5-O9)	1.516(5)	*d*(P5-O9)	1.530(8)
d(P5-O25$_b$)	1.583(4)	*d*(P5-O25$_b$)	1.553(7)
d(P6-O18)	**1.497(5)**	*d*(P6-O18)	**1.522(8)**
d(P6-O16)	1.498(5)	*d*(P6-O16)	1.528(7)
d(P6-O12)	1.517(5)	*d*(P6-O12)	1.542(8)
d(P6-O26$_b$)	1.533(5)	*d*(P6-O26$_b$)	1.556(7)
d(P7-O19)	1.499(4)	*d*(P7-O19)	1.493(8)
d(P7-O15)	1.504(5)	*d*(P7-O15)	1.507(8)
d(P7-O11)	1.516(5)	*d*(P7-O11)	1.525(7)
d(P7-O-27$_b$)	1.581(4)	*d*(P7-O-27$_b$)	1.573(7)
d(P8-O20)	1.492(4)	*d*(P8-O20)	1.496(7)
d(P8-O14)	1.508(5)	*d*(P8-O14)	1.493(8)
d(P8-O10)	1.515(5)	*d*(P8-O10)	1.527(8)
d(P8-O28$_b$)	1.585(4)	*d*(P8-O28$_b$)	1.579(7)
∠(O42$_t$,Mo1,O34$_t$)	102.6(2)	∠(O42$_t$,Mo1,O34$_t$)	102.8(4)
∠(O43$_t$,Mo2,O35$_t$)	**104.1(2)**	∠(O43$_t$,Mo2,O35$_t$)	**99.4(4)**
∠(O44$_t$,Mo3,O36$_t$)	**103.0(2)**	∠(O44$_t$,Mo3,O36$_t$)	**99.6(4)**
∠(O41$_t$,Mo4,O33$_t$)	**102.8(2)**	∠(O41$_t$,Mo4,O33$_t$)	**99.9(4)**
∠(O37$_t$,Mo5,O29$_t$)	**102.9(2)**	∠(O37$_t$,Mo5,O29$_t$)	**101.7(4)**
∠(O30$_t$,Mo6,O38$_t$)	**104.0(2)**	∠(O30$_t$,Mo6,O38$_t$)	**100.8(4)**
∠(O39$_t$,Mo7,O31$_t$)	**100.2(2)**	∠(O39$_t$,Mo7,O31$_t$)	**96.9(4)**
∠(O40$_t$,Mo8,O32$_t$)	102.8(2)	∠(O40$_t$,Mo8,O32$_t$)	102.9(4)
∠(P1,O26$_b$,P6)	159.6(5)	∠(P1,O26$_b$,P6)	157.4(5)
∠(P2,O27$_b$,P7)	140.1(3)	∠(P2,O27$_b$,P7)	139.3(5)
∠(P3,O28$_b$,P8)	142.2(3)	∠(P3,O28$_b$,P8)	140.5(4)
∠(P4,O25$_b$,P5)	142.2(3)	∠(P4,O25$_b$,P5)	142.8(4)

Table A3.2 Indexing of the Guinier photograph of α-$(MoO_2)_2P_2O_7$ with the observed and the calculated 4θ-values. $\Delta = |\sin^2\theta_{calc} - \sin^2\theta_{obs}| \cdot 1000$.

h	***k***	***l***	$4\theta_{calc}$	$4\theta_{obs}$	Δ	$d_{calc.}$ (Å)	I_{calc} [a)]	I_{obs}
1	1	1	22.095	22.047	0.04	8.0020	5	4
2	0	2	28.134	28.229	0.10	6.2904	2	2
2	1	-2	32.884	32.891	0.1	5.3867	15	20
3	1	-1	35.799	35.813	0.02	4.9513	24	32
0	0	4	39.838	39.835	.00	4.4535	2	2
4	1	0	43.411	43.398	.02	4.0909	8	9
2	2	2	44.399	44.459	.10	4.0010	100	100
3	1	3	45.709	45.729	.03	3.8877	4	4
3	2	-1	46.586	46.620	.06	3.8156	11	10
0	2	4	52.716	52.715	.00	3.3784	4	3
1	1	5	53.833	53.816	.03	3.3095	18	20
3	2	3	54.657	54.627	.06	3.2606	2	2
4	0	-4	56.580	56.569	.02	3.1519	38	80
5	2	1	61.703	61.654	.11	2.8958	2	3
2	0	6	63.526	63.566	.09	2.8148	1	1
0	3	4	65.537	65.558	.05	2.7307	3	1
6	1	2	65.907	65.929	.05	2.7158	5	4
0	4	0	69.137	69.162	.06	2.5925	5	5
2	2	-6	72.493	72.506	.03	2.4762	4	3
3	4	-1	76.358	76.361	.01	2.3552	7	8
7	1	3	78.999	78.905	.26	2.2795	20	15
8	0	0	80.979	80.988	.03	2.2260	2	2
3	4	3	81.778	81.789	.03	2.2051	4	4
1	4	5	86.871	86.836	.10	2.0816	3	3
6	1	-6	87.853	87.858	.01	2.0594	2	2
5	3	5	88.997	89.080	.25	2.0343	3	3
4	4	4	90.583	90.562	.07	2.0005	3	2
7	2	-5	94.376	94.338	.12	1.9244	5	4
9	1	-3	98.515	98.535	.07	1.8483	10	7
5	3	-7	102.711	102.732	.07	1.7776	2	2
9	2	-3	103.432	103.454	.07	1.7661	6	5
4	3	8	106.116	106.089	.10	1.7245	1	1
5	1	9	107.426	107.441	.05	1.7050	1	1
0	4	8	108.515	108.503	.04	1.6892	3	3
5	4	-7	113.643	113.633	.04	1.6189	2	2
1	1	-11	115.588	115.587	.00	1.5939	6	4
8	0	-8	117.034	117.030	.02	1.5760	1	2

[a)] Intensity standardizes on 100 for the strongest reflection within the angular range $22.09° \leq 4\theta \leq 117.04°$.

Tabele A3.3 Anisotropic displacement parameters for α-$(MoO_2)_2P_2O_7$ / Å^2.

atom	U_{11}	U_{22}	U_{33}	U_{12}	U_{13}	U_{23}
Mo1	0.0090(3)	0.0130(2)	0.0106(3)	-0.0002(2)	0.00183(18)	0.0005(2)
Mo2	0.0090(3)	0.0152(3)	0.0100(3)	0.0009(2)	0.00143(17)	0.0008(2)
Mo3	0.0089(3)	0.0126(3)	0.0097(3)	-0.0001(2)	0.00063(18)	0.0000(2)
Mo4	0.0083(3)	0.0139(3)	0.0097(3)	0.0001(2)	0.00097(17)	0.0002(2)
Mo5	0.0102(3)	0.0160(3)	0.0099(3)	0.0023(2)	0.00149(18)	0.0009(2)
Mo6	0.0087(3)	0.0190(3)	0.0099(3)	0.0011(2)	0.00083(17)	0.0013(2)
Mo7	0.0095(3)	0.0155(3)	0.0108(3)	0.0019(2)	0.00197(19)	0.0016(2)
Mo8	0.0087(3)	0.0164(3)	0.0115(3)	0.0019(2)	0.00142(18)	0.0023(2)
P1	0.0086(8)	0.0129(8)	0.0111(8)	0.0013(6)	0.0025(5)	0.0007(6)
P2	0.0080(8)	0.0137(7)	0.0103(8)	-0.0001(6)	0.0010(5)	-0.0003(6)
P3	0.0081(8)	0.0118(7)	0.0100(8)	0.0012(6)	0.0008(5)	-0.0003(6)
P4	0.0084(8)	0.0134(7)	0.0094(8)	0.0010(6)	0.0015(5)	0.0007(6)
P5	0.0090(8)	0.0138(8)	0.0109(8)	-0.0016(7)	0.0023(5)	-0.0007(6)
P6	0.0102(8)	0.0136(7)	0.0123(8)	-0.0026(6)	0.0022(5)	-0.0018(6)
P7	0.0095(8)	0.0149(8)	0.0100(8)	-0.0011(7)	0.0007(5)	-0.0010(6)
P8	0.0091(8)	0.0116(7)	0.0124(9)	-0.0005(6)	0.0013(5)	0.0002(6)
O1	0.025(3)	0.052(4)	0.015(2)	0.016(2)	0.010(2)	0.015(2)
O2	0.014(2)	0.033(3)	0.010(2)	0.003(2)	0.0055(17)	0.003(2)
O3	0.019(2)	0.039(3)	0.013(2)	0.004(2)	0.0085(18)	0.002(2)
O4	0.014(2)	0.029(3)	0.012(2)	0.001(2)	0.0057(17)	0.0024(19)
O5	0.017(2)	0.051(4)	0.026(3)	-0.016(2)	0.010(2)	-0.014(2)
O6	0.011(2)	0.043(3)	0.015(2)	-0.002(2)	0.0015(17)	-0.006(2)
O7	0.010(2)	0.038(3)	0.016(2)	-0.002(2)	0.0035(17)	-0.001(2)
O8	0.010(2)	0.037(3)	0.016(2)	-0.001(2)	-0.0024(17)	0.001(2)
O9	0.015(2)	0.028(3)	0.013(2)	0.004(2)	0.0070(18)	0.003(2)
O10	0.018(2)	0.020(3)	0.015(2)	-0.001(2)	0.0065(19)	0.0031(19)
O11	0.017(2)	0.025(3)	0.013(2)	0.004(2)	0.0052(18)	0.0017(19)
O12	0.019(3)	0.023(3)	0.020(2)	-0.003(2)	0.010(2)	-0.001(2)
O13	0.012(2)	0.017(3)	0.018(2)	0.0004(19)	0.0073(18)	0.000(2)
O14	0.015(2)	0.016(3)	0.021(3)	0.0002(19)	0.0078(19)	-.0014(19)
O15	0.015(2)	0.017(3)	0.017(2)	-.0002(19)	0.0085(18)	-.0037(18)
O16	0.022(3)	0.020(3)	0.023(3)	0.003(2)	0.009(2)	0.002(2)
O17	0.016(2)	0.024(2)	0.022(3)	-0.007(2)	-0.0018(16)	-0.007(2)
O18	0.036(3)	0.039(3)	0.027(3)	-0.017(3)	0.0043(19)	-0.013(2)
O19	0.022(3)	0.015(2)	0.022(3)	-0.005(2)	-0.0046(16)	-.0045(19)
O20	0.024(3)	0.027(3)	0.026(3)	-0.007(2)	0.0006(18)	-0.010(2)
O21	0.032(3)	0.015(2)	0.031(3)	0.006(2)	0.011(2)	0.006(2)
O22	0.022(3)	0.017(2)	0.019(2)	0.006(2)	-0.0002(17)	0.0012(19)
O23	0.024(3)	0.013(2)	0.029(3)	0.003(2)	0.0008(18)	0.003(2)
O24	0.026(3)	0.014(2)	0.020(3)	0.006(2)	0.0034(17)	0.0010(19)
O25	0.022(3)	0.019(2)	0.028(3)	0.001(2)	-0.0136(18)	0.003(2)
O26	0.057(4)	0.042(3)	0.056(4)	0.027(3)	-0.008(3)	0.017(3)
O27	0.022(3)	0.011(2)	0.029(3)	-0.004(2)	-0.0117(17)	0.001(2)
O28	0.028(3)	0.017(2)	0.036(3)	0.003(2)	-0.0084(19)	0.002(2)
O29	0.015(2)	0.029(3)	0.015(2)	0.005(2)	0.0032(16)	0.009(2)
O30	0.016(2)	0.034(3)	0.019(3)	0.008(2)	0.0050(16)	0.004(2)
O31	0.017(2)	0.021(2)	0.018(2)	0.006(2)	0.0053(16)	0.008(2)
O32	0.016(2)	0.029(3)	0.015(2)	0.002(2)	-0.0003(16)	0.005(2)

O33	0.023(3)	0.033(3)	0.021(3)	-0.005(2)	-0.0052(18)	-0.006(2)
O34	0.019(3)	0.025(2)	0.022(3)	-0.007(2)	-0.0021(17)	-0.002(2)
O35	0.022(3)	0.044(3)	0.026(3)	-0.012(2)	0.0067(18)	-0.017(2)
O36	0.021(2)	0.025(2)	0.020(2)	-0.001(2)	-0.0064(18)	-0.003(2)
O37	0.060(4)	0.036(3)	0.024(3)	-0.008(3)	0.003(3)	-0.006(2)
O38	0.032(3)	0.034(3)	0.039(3)	-0.011(2)	-0.002(2)	-0.010(3)
O39	0.039(3)	0.026(3)	0.028(3)	-0.009(2)	0.004(2)	-0.005(2)
O40	0.030(3)	0.024(3)	0.060(4)	-0.008(2)	-0.009(3)	-0.005(3)
O41	0.023(3)	0.022(2)	0.026(3)	0.001(2)	-0.0002(18)	0.006(2)
O42	0.024(3)	0.023(2)	0.028(3)	0.009(2)	0.0074(18)	0.004(2)
O43	0.025(3)	0.033(3)	0.030(3)	0.010(2)	0.0021(18)	0.010(2)
O44	0.027(3)	0.019(2)	0.024(3)	0.006(2)	0.0031(18)	0.008(2)

16.B1 Rhenium(IV) phosphates

Table B1.1.1 Indexing of the Guinier photograph of ReP_2O_7 with the observed and calculated 4θ-values. $\Delta = |\sin^2\theta_{calc} - \sin^2\theta_{obs}| \cdot 1000$.

h	*k*	*l*	$4\theta_{calc}$	$4\theta_{obs}$	Δ	*d-calc.* (Å)	I_{calc} [a)]	I_{obs}
1	1	1	38.960	38.941	0.03	4.5530	64	58
2	0	0	45.060	45.042	0.03	3.9430	100	100
2	1	0	50.462	50.471	0.02	3.5267	12	16
2	1	1	55.370	55.386	0.03	3.2194	12	15
2	2	0	64.150	64.153	0.01	2.7881	42	35
3	1	1	75.608	75.633	0.07	2.3777	56	50
2	2	2	79.106	79.192	0.24	2.2765	12	17
2	3	0	91.992	91.959	0.10	1.9715	2	3
4	0	0	94.994	94.954	0.13	1.9126	9	13
4	1	0	100.793	00.834	0.14	1.8092	20	18
3	3	1	103.603	03.618	0.05	1.7634	15	14
4	2	0	114.351	14.351	0.00	1.6097	18	21
5	1	1	121.998	21.946	0.20	1.5177	26	23

a) Intensity standardizes on 100 for the strongest reflection within the angular range 38.960 ° ≤ 4θ ≤ 121.946°.

Table B1.1.2 Indexing of the Guinier photograph of $NaRe_2(PO_4)_3$ with the observed and calculated 4θ-values. $\Delta = |\sin^2\theta_{calc} - \sin^2\theta_{obs}| \cdot 1000$.

h	*k*	*l*	$4\theta_{calc}$	$4\theta_{obs}$	Δ	*d-calc.* (Å)	I_{calc} [a)]	I_{obs}
0	1	2	28.893	28.873	0.02	6.1261	21	20
1	0	4	39.947	39.959	0.02	4.4415	83	91
1	1	0	41.969	41.955	0.02	4.2298	100	100
0	0	6	47.757	47.772	0.03	3.7233	3	2
1	1	3	48.356	48.323	0.06	3.6779	12	20
2	0	2	51.140	51.211	0.13	3.4807	1	1
0	2	4	58.257	58.299	0.09	3.0630	45	50
1	1	6	63.992	63.983	0.02	2.7948	29	60
2	1	1	65.111	65.126	0.03	2.7480	2	2
1	2	2	66.614	66.659	0.11	2.6877	2	2
0	1	8	68.676	68.693	0.04	2.6093	7	12
3	0	0	73.542	73.634	0.24	2.4421	33	16
2	2	0	85.434	85.485	0.15	2.1149	13	12
0	3	6	88.642	88.620	0.06	2.0420	9	10
4	1	0	115.211	115.241	0.11	1.5987	16	15
2	3	5	117.266	117.192	0.27	1.5731	1	1
0	4	8	120.777	120.834	0.22	1.5315	5	20
2	0	14	127.082	127.097	0.06	1.4629	10	8

a) Intensity standardizes on 100 for the strongest reflection within the angular range 28.87 ° ≤ 4θ ≤ 127.092°.

Tabel B1.1.3 Indexing of the Guinier photograph of $Re_3[Si_2O(PO_4)_6]$ with the observed and calculated 4θ-values. $\Delta = |\sin^2\theta_{calc} - \sin^2\theta_{obs}| \cdot 1000$.

h	*k*	*l*	$4\theta_{calc}$	$4\theta_{obs}$	*Δ*	*d- calc.* (Å)	I_{calc} [a)]	I_{obs}
0	0	3	20.344	20.1012	0.19	8.6884	56	50
1	0	1	25.846	25.6459	0.19	6.8445	100	100
0	1	2	28.406	28.2234	0.20	6.2304	3	3
0	0	6	40.851	40.7939	0.20	4.3442	2	3
0	1	5	42.263	42.1938	0.09	4.2007	72	35
1	1	0	43.363	43.3013	0.11	4.0954	71	90
0	2	1	50.643	50.6229	0.10	3.5143	7	6
1	0	7	54.043	54.0678	0.40	3.2970	9	7
0	2	4	57.261	57.3191	0.50	3.1152	3	2
1	1	6	59.919	59.9764	0.12	2.9800	43	60
2	1	4	72.396	72.4766	0.12	2.4794	5	6
1	0	10	73.402	73.3858	0.21	2.4466	3	3
3	0	0	76.047	76.0522	0.01	2.3645	24	25
0	1	12	83.079	83.1138	0.10	2.1721	4	4
0	2	10	86.056	86.0524	0.01	2.1003	3	3
3	0	6	87.082	87.2073	0.38	2.0768	13	12
2	2	0	88.384	88.4713	0.27	2.0477	9	8
2	0	11	92.050	90.5705	0.26	1.9703	5	5
1	1	12	94.663	94.7356	0.23	1.9189	8	6
3	1	5	98.952	99.0253	0.24	1.8406	10	20
0	3	12	115.141	115.1283	0.05	1.5996	6	7
1	0	16	116.083	116.0078	0.28	1.5877	7	6
3	2	4	116.800	116.7981	0.01	1.5789	2	3
1	3	10	117.500	117.4303	0.26	1.5703	3	4
0	1	16	125.411	125.4123	0.00	1.4804	7	15

a) Intensity standardizes on 100 for the strongest reflection within the angular range $20.34° \leq 4\theta \leq 125.41°$.

Table B1.2.1 Anisotropic displacement parameters for $NaRe_2(PO_4)_3$ in $Å^2$.

atom	*U*11	*U*22	*U*33	*U*12	*U*13	*U*23
Na1	0.0417(15)	0.0417(15)	0.0074(13)	0.0208(8)	0.00000	0.00000
Na2	0.0505(19)	0.0505(19)	0.0112(15)	0.0253(9)	0.00000	0.00000
Re1	0.00604(6)	0.00604(6)	0.00542(8)	0.00302(3)	0.00000	0.00000
Re2	0.00622(6)	0.00622(6)	0.00587(8)	0.00311(3)	0.00000	0.00000
P1	0.0062(3)	0.0068(3)	0.0068(3)	0.0031(3)	0.0003(2)	0.0010(2)
O1	0.0170(12)	0.0187(12)	0.0157(10)	0.011(1)	0.0018(9)	0.0088(9)
O2	0.0051(9)	0.0095(9)	0.0122(9)	0.0014(7)	0.0006(7)	0.0021(7)
O3	0.0094(9)	0.0112(10)	0.0155(10)	0.0034(8)	-0.0008(7)	-0.0038(8)
O4	0.0125(11)	0.0155(11)	0.0142(10)	0.0063(9)	-0.0040(8)	0.0019(9)

Table B1.2.2 Anisotropic displacement parameters for $Re^{IV}{}_3[Si^t{}_2O(PO_4)_6]$ in $Å^2$.

atom	*U*11	*U*22	*U*33	*U*12	*U*13	*U*23
Re1	0.0110(3)	0.0110(3)	0.0092(3)	0.0055(1)	0.00000	0.00000
Re2	0.0101(2)	0.0101(2)	0.0118(3)	0.0050(1)	0.00000	0.00000
Si1	0.013(1)	0.013(1)	0.012(2)	0.0067(6)	0.00000	0.00000
P	0.011(1)	0.012(1)	0.0127(9)	0.0065(8)	-0.0001(7)	0.0009(7)
O2	0.023(4)	0.025(4)	0.018(3)	0.017(3)	0.005(3)	0.003(3)
O3	0.016(3)	0.016(3)	0.016(3)	0.005(3)	0.000(2)	0.000(2)
O4	0.019(3)	0.011(3)	0.020(3)	0.006(3)	0.003(2)	0.002(2)
O5	0.020(3)	0.015(3)	0.020(3)	0.010(3)	-0.001(2)	-0.001(2)

Table B1.2.3 Anisotropic displacement parameters for $(V_{0.83}Re_{0.17})O_2$ in $Å^2$.

atom	*U*11	*U*22	*U*33	*U*12	*U*13	*U*23
V1	0.0092(2)	0.0191(5)	0.0094(5)	0	0.004(9)	0
RE1	0.0092(2)	0.0191(5)	0.0094(5)	0	0.004(9)	0
V2	0.00797(2)	0.0214(5)	0.0086(4)	0	0.001(7)	0
RE2	0.00797(2)	0.0214(5)	0.0086(4)	0	0.001(7)	0
O1	0.00746(9)	0.0132(10)	0.0088(8)	0	0.0013(2)	0
O2	0.00719(8)	0.0144(10)	0.0089(8)	0	0.0001(2)	0

16.B2 Rhenium(V) oxidepyrophosphate

Tabel B2.1. Indexing of the Guinier photograph of $Re_2O_3(P_2O_7)$ with the observed and calculated 4θ-values. $\Delta = |\sin^2\theta_{calc} - \sin^2\theta_{obs}| \cdot 1000$.

h	*k*	*l*	$4\theta_{calc}$	$4\theta_{obs}$	*Δ*	*d-calc.* (Å)	I_{calc} [a)]	I_{obs}
1	1	0	20.066	20.093	0.02	8.808	100	70
2	0	0	28.908	28.91	0.00	6.122	10	6
1	1	-1	39.522	39.5	0.03	4.488	1	2
2	2	0	40.288	40.261	0.04	4.404	2	1
0	2	1	44.087	44.115	0.05	4.028	79	100
3	1	0	45.736	45.727	0.02	3.885	39	60
2	2	-1	52.926	52.845	0.16	3.365	4	4
1	3	-1	56.212	56.159	0.11	3.172	14	50
3	1	1	57.23	57.26	0.06	3.116	5	8
4	0	0	58.29	58.231	0.12	3.061	21	20
3	3	0	60.833	60.854	0.05	2.936	1	1
2	4	0	63.516	63.568	0.12	2.815	1	1
0	4	1	66.068	66.071	0.01	2.709	6	10
0	0	2	68.688	68.655	0.08	2.608	12	16
3	3	-1	70.081	70.057	0.06	2.558	18	40
1	1	2	71.73	71.659	0.18	2.501	3	3
1	5	0	72.276	72.26	0.04	2.483	6	5
2	4	1	72.447	72.47	0.06	2.477	1	1
4	4	0	81.893	81.884	0.03	2.202	1	1
3	1	2	83.313	83.286	0.08	2.166	5	5
3	5	0	83.803	83.787	0.05	2.154	7	6
0	6	0	85.497	85.529	0.10	2.113	4	3
6	0	0	88.693	88.704	0.04	2.04	5	5
4	4	1	89.239	89.175	0.20	2.029	2	2
0	4	2	89.921	89.896	0.08	2.014	8	6
4	0	2	91.282	91.289	0.02	1.986	3	3
0	6	1	92.62	92.651	0.10	1.958	2	1
6	2	-1	100.125	100.154	0.10	1.82	6	7
1	5	2	101.413	101.426	0.04	1.798	6	6
4	6	0	105.149	105.123	0.09	1.739	4	3
7	1	0	105.56	105.543	0.06	1.732	5	3
6	4	0	106.681	106.645	0.13	1.716	3	4
1	7	1	108.122	108.128	0.02	1.694	2	2
4	4	2	108.946	108.98	0.12	1.683	2	2
0	2	3	109.348	109.36	0.05	1.677	8	7
3	5	2	110.495	110.503	0.03	1.661	6	6
7	1	1	111.697	111.775	0.28	1.644	1	1
6	4	1	112.779	112.707	0.26	1.63	2	2
2	2	-3	113.745	113.769	0.09	1.617	1	1
6	0	2	114.505	114.45	0.20	1.607	2	2
1	3	3	115.521	115.512	0.03	1.594	4	5
3	1	3	116.089	116.143	0.20	1.587	1	1
3	7	1	116.846	116.825	0.08	1.578	4	3
7	3	1	119.689	119.74	0.19	1.544	5	

[a)] Intensity standardizes on 100 for the strongest reflection within the angular range $20.067° \leq 4\theta \leq 119.69°$.

Table B2.2 Anisotropic displacement parameters for $Re^{V}_2O_3(P_2O_7)$ ($Å^2$).

atom	*U*11	*U*22	*U*33	*U*12	*U*13	*U*23
Re1	0.00683(14)	0.00625(14)	0.00713(14)	0.00023(9)	-.00026(9)	0.00007(9)
P1	0.0084(7)	0.0077(7)	0.0080(7)	-0.0015(6)	0.0006(6)	-0.0013(6)
O1	0.012(2)	0.009(2)	0.008(2)	-.0001(17)	0.0005(16)	0.0029(16)
O2	0.006(3)	0.006(3)	0.012(3)	0.00000	0.000(2)	0.00000
O3	0.015(2)	0.010(2)	0.010(2)	-.0027(17)	0.0024(18)	0.0057(17)
O4	0.007(2)	0.008(2)	0.019(2)	-.0028(16)	0.0004(18)	-.0050(17)
O5	0.021(2)	0.014(2)	0.016(2)	-.0032(19)	-.0002(19)	-.0062(18)
O6	0.008(3)	0.011(3)	0.015(3)	0.00000	0.001(2)	0.00000

16.B3 Rhenium(VI) oxidephosphate

Tabel B3.1 Indexing of the Guinier photograph $Re_2O_3(PO_4)_2$ with the observed and calculated 4θ-values. $\Delta = |\sin^2\theta_{calc} - \sin^2\theta_{obs}| \cdot 1000$.

h	***k***	***l***	$4\theta_{calc}$	$4\theta_{obs}$	Δ	***d-calc***. (Å)	I_{calc} [a)]	I_{obs}
0	1	2	32.468	32.478	0.01	5.455	17	15
1	1	0	36.18	36.206	0.04	4.899	36	60
1	0	2	36.485	36.506	0.03	4.858	33	55
1	1	1	38.013	38.075	0.09	4.665	92	90
0	1	3	41.644	41.704	0.09	4.262	20	20
1	1	2	43.062	43.103	0.07	4.123	87	92
0	2	0	45.584	45.602	0.03	3.898	1	1
0	0	4	46.557	46.582	0.04	3.817	56	70
0	2	1	47.066	47.081	0.03	3.777	38	40
1	1	3	50.413	50.47	0.11	3.530	9	7
0	2	2	51.271	51.31	0.07	3.472	100	95
0	1	4	51.927	51.949	0.04	3.428	41	40
1	0	4	54.583	54.618	0.07	3.264	7	5
1	2	1	55.022	55.088	0.13	3.239	2	1
2	0	0	56.628	56.647	0.04	3.149	94	100
0	2	3	57.643	57.617	0.05	3.095	5	5
1	1	4	59.277	59.266	0.02	3.011	24	20
0	1	5	62.859	62.885	0.06	2.843	14	12
1	2	3	64.395	64.394	0.00	2.777	10	10
0	2	4	65.612	65.624	0.03	2.727	1	1
1	1	5	69.152	69.172	0.05	2.591	4	4
2	1	3	70.815	70.802	0.03	2.532	5	4
1	2	4	71.691	71.751	0.16	2.503	37	30
0	3	2	72.979	72.981	0.0	2.460	3	3
2	0	4	73.939	73.961	0.06	2.429	17	20
0	1	6	74.251	74.29	0.1	2.419	5	5
1	3	0	74.802	74.8	0.0	2.402	21	25
1	3	1	75.756	75.8	0.12	2.373	4	5
1	0	6	76.202	76.2	0.01	2.359	20	20
2	2	2	77.125	77.129	0.01	2.332	31	20
2	1	4	77.582	77.599	0.05	2.319	17	15
1	2	5	80.22	80.258	0.11	2.246	10	12
2	2	3	81.689	81.748	0.17	2.207	3	3
1	3	3	83.059	83.057	0.01	2.172	5	5
0	2	6	84.75	84.746	0.01	2.131	5	5
2	1	5	85.615	85.636	0.06	2.110	7	6
0	1	7	86.031	86.056	0.08	2.100	9	8
2	2	4	87.747	87.705	0.13	2.061	1	1
1	3	4	89.041	89.065	0.07	2.033	21	15
3	1	0	89.319	89.365	0.14	2.027	6	6
3	1	1	90.146	90.164	0.06	2.009	17	20
0	3	5	91.608	91.644	0.11	1.979	2	2
3	1	2	92.591	92.574	0.05	1.959	21	25
0	4	0	93.108	93.123	0.05	1.949	4	4
0	4	1	93.908	93.883	0.08	1.933	8	7

2	1	6	94.675	94.693	0.06	1.918	2	2
2	2	5	95.079	95.113	0.11	1.911	1	1
0	4	2	96.279	96.302	0.08	1.888	4	3
3	1	3	96.558	96.512	0.15	1.883	5	5
2	3	3	97.57	97.532	0.13	1.865	4	3
0	1	8	98.183	98.202	0.06	1.854	12	10
3	0	4	99.006	99.011	0.02	1.839	1	1
0	3	6	100.245	100.281	0.12	1.818	23	18
1	4	2	100.802	100.781	0.07	1.809	4	4
3	1	4	101.916	101.93	0.05	1.790	8	7
1	1	8	102.644	102.65	0.02	1.778	3	3
2	2	6	103.497	103.45	0.16	1.765	3	3
2	1	7	104.599	104.549	0.17	1.747	6	5
0	4	4	105.36	105.309	0.18	1.736	5	5
3	1	5	108.522	108.528	0.02	1.689	2	2
2	3	5	109.453	109.458	0.02	1.675	1	2
1	4	4	109.611	109.668	0.20	1.673	3	3
3	2	4	110.315	110.267	0.17	1.663	19	8
1	2	8	111.004	110.987	0.06	1.654	29	20
3	3	0	112.561	112.507	0.20	1.633	12	10
3	3	1	113.26	113.306	0.17	1.623	3	4
3	0	6	113.588	113.606	0.07	1.619	13	12
1	1	9	114.844	114.796	0.18	1.603	2	2
2	1	8	115.283	115.256	0.10	1.597	10	8
1	4	5	115.913	115.896	0.06	1.589	8	10
3	2	5	116.592	116.655	0.24	1.581	4	3
2	3	6	117.133	117.125	0.03	1.574	20	25
3	3	3	118.761	118.725	0.14	1.555	3	3
1	2	9	122.644	122.623	0.08	1.510	5	5
1	4	6	123.334	123.343	0.04	1.502	9	8
0	1	10	123.712	123.723	0.04	1.498	2	2
1	5	2	125.003	124.993	0.04	1.484	27	20

[a)]Intensity standardizes on 100 for the strongest reflection within the range of the angle $32.468° \leq 4\theta \leq 125.003°$.

Table B3.2 Anisotropic displacement parameters for $Re^{VI}_2O_3(PO_4)_2$ ($Å^2$).

atom	***U*11**	***U*22**	***U*33**	***U*12**	***U*13**	***U*23**
Re1	0.0155(2)	0.0053(2)	0.0047 (2)	0.00000	0.00000	0.0006(1)
Re2	0.0105(2)	0.0054(2)	0.0046(2)	0.00000	0.00000	-.0005(1)
P1	0.011(1)	0.0066(9)	0.0058(8)	0.00000	0.00000	0.0015(7)
P2	0.0086(9)	0.0067(8)	0.0039(8)	0.00000	0.00000	0.0006(7)
O1	0.041(5)	0.009(3)	0.012(3)	0.00000	0.00000	0.003(2)
O2	0.017(3)	0.004(2)	0.008(3)	0.00000	0.00000	0.001(2)
O3	0.019(3)	0.004(3)	0.013(3)	0.00000	0.00000	0.001(2)
O4	0.028(4)	0.007(3)	0.006(3)	0.00000	0.00000	0.001(2)
O5	0.017(3)	0.016(3)	0.011(3)	0.00000	0.00000	0.002(2)
O6	0.036(4)	0.008(3)	0.003(3)	0.00000	0.00000	0.000(2)
O7	0.106(9)	0.002(3)	0.012(3)	0.00000	0.00000	-.004(2)
O8	0.013(2)	0.016(2)	0.013(2)	-0.005(5)	0.000(2)	0.004(2)
O9	0.013(3)	0.050(4)	0.026(3)	0.012(2)	0.007(2)	0.024(3)

16.B4 Rhenium(VII) oxidephosphates

Tabel B4.1 Indexing of the Guinier photograph of $ReO_2(PO_4)$ with the observed and calculated 4θ-values.

h	***k***	***l***	$4\theta_{calc}$	$4\theta_{obs}$	Δ	***d-calc.*** (Å)	I_{calc} [a)]
1	1	1	25.60	25.27	6.909	49.9	75
1	1	2	30.21	29.92	5.860	78.2	107
1	1	-4	41.68	41.35	4.259	1000	2345
0	2	0	42.21	41.86	4.207	744.4	1050
3	1	0	42.63	42.33	4.084	42.63	2196
2	0	4	43.49	43.13	4.084	754.0	1376
0	2	3	49.59	48.64	3.588	10.0	77
2	2	1	50.00	49.65	3.559	87.0	148
4	0	-4	58.95	58.76	3.028	484.8	2085
2	2	4	60.97	60.54	2.930	469.3	754
2	2	-5	64.74	64.34	2.763	53.0	142
3	1	6	68.83	68.83	2.590	25.3	39
2	0	-8	72.70	72.43	2.469	136.2	372
4	2	-4	73.07	72.77	2.458	233.0	620
1	3	4	73.65	73.15	2.439	215.0	343
3	3	0	74.22	73.83	2.420	283.0	386
1	1	8	74.64	74.25	2.406	165.0	281
6	0	0	74.99	74.76	2.397	55.0	158
5	1	4	76.33	75.95	2.356	209.0	327
3	3	4	83.25	82.76	2.168	18.0	30
3	1	8	84.15	83.65	2.146	21.0	69
2	2	-8	84.82	84.45	2.129	116.0	235
0	4	0	85.93	85.34	2.103	74.0	75
4	2	6	86.23	86.57	2.096	20.2	257
4	0	8	88.66	88.26	2.042	77.7	125
5	1	-8	94.51	94.36	1.922	183.7	641
7	1	-4	95.91	95.75	1.896	156.0	625
1	3	8	97.23	96.73	1.871	98.4	270
5	3	4	98.60	98.64	1.847	136.0	175
4	4	-4	105.93	105.45	1.727	65.0	64
5	3	-8	114.00	113.66	1.614	102.0	296

a) Intensity standardizes on 100 for the strongest reflection within the range of the angle $25.27° \leq 4\theta \leq 113.66°$.

Table B4.2 Anisotropic displacement parameters for $Re^{VII}O_2(PO_4)_2$ ($Å^2$).

atom	*U*11	*U*22	*U*33	*U*12	*U*13	*U*23
Re1	0.00798(5)	0.00467(5)	0.00745(5)	-0.00039(4)	0.00147(4)	-0.00011(4)
Re2	0.00773(6)	0.00460(6)	0.00731(5)	-0.00040(4)	0.00120(4)	0.00005(3)
Re3	0.00784(6)	0.00537(6)	0.00656(5)	-0.00055(4)	0.00101(4)	-0.00021(3)
P1	0.0080(3)	0.0053(4)	0.0070(3)	0.0003(3)	0.0009(3)	0.0003(3)
P2	0.0085(4)	0.0057(4)	0.0074(3)	-0.0009(3)	0.0014(3)	-0.0004(3)
P3	0.0080(3)	0.0059(4)	0.0070(3)	0.0005(3)	0.0009(3)	0.0003(3)
O1	0.011(1)	0.007(1)	0.001(1)	-0.0017(8)	0.0032(8)	0.0005(8)
O2	0.013(1)	0.007(1)	0.008(1)	0.0008(9)	-0.0011(8)	0.0021(8)
O3	0.009(1)	0.013(1)	0.00921)	0.0024(9)	0.0014(8)	-0.0015(9)
O4	0.012(1)	0.007(1)	0.010(1)	-0.0008(8)	0.0044(8)	0.0010(8)
O5	0.01(1)	0.0125(1)	0.001(1)	0.0014(9)	0.0021(8)	0.0002(9)
O6	0.0094(1)	0.001(1)	0.011(1)	-0.0009(9)	0.0035(8)	-0.0005(9)
O7	0.007(1)	0.012(1)	0.009(1)	-0.0020(9)	0.0010(8)	0.0001(8)
O8	0.012(1)	0.006(1)	0.011(1)	0.0006(8)	-0.0004(9)	0.0011(8)
O9	0.012(1)	0.006(1)	0.012(1)	0.0026(8)	0.0025(9)	0.0035(8)
O10	0.013(1)	0.006(1)	0.010(1)	-0.0019(9)	0.0020(9)	-0.0012(8)
O11	0.011(1)	0.012(1)	0.008(1)	-0.0020(9)	-0.0006(8)	-0.0003(9)
O12	0.010(1)	0.014(1)	0.009(1)	0.0021(9)	-0.0011(8)	-0.0010(9)
O13	0.0112(1)	0.009(1)	0.008(1)	0.0020(9)	-0.0016(8)	0.0001(8)
O14	0.020(2)	0.010 (1)	0.011(1)	-0.002(1)	0.001(1)	0.0017(9)
O15	0.015(1)	0.010(1)	0.012(1)	-0.003(1)	-0.0004(9)	-0.0032(9)
O16	0.015(1)	0.013(1)	0.016(1)	0.002(1)	0.006(1)	0.001(1)
O17	0.015(1)	0.013(1)	0.015(1)	0.003(1)	0.004(1)	0.002(1)
O18	0.015(1)	0.014(1)	0.013(1)	-0.003(1)	0.001(1)	-0.0038(1)

Tabel B4.3 Indexing of the Guinier photograph $(Re_2O_5)Si^{\circ}{}_2[Si^{t}{}_2O(PO_4)_6]$ with the observed and calculated 4θ-values. $\Delta = |\sin^2\theta_{calc} - \sin^2\theta_{obs}| \cdot 1000$.

h	***k***	***l***	$4\theta_{calc}$	$4\theta_{obs}$	***Δ***	***d-calc.*** (Å)	I_{calc} [a)]	I_{obs}
1	1	0	26.641	26.18	0.46	6.641	8	5
1	0	0	27.128	27.071	0.06	6.522	100	100
1	0	1	27.591	27.541	0.05	6.413	59	60
1	1	1	28.324	28.341	0.02	6.248	53	58
0	1	-1	30.092	30.082	0.01	5.883	16	12
0	1	1	32.251	32.193	0.07	5.491	13	10
0	0	2	34.353	34.303	0.06	5.158	4	4
1	0	-1	36.108	36.094	0.02	4.909	28	20
1	0	2	37.153	37.104	0.07	4.772	11	8
1	1	2	38.593	38.505	0.13	4.595	23	18
0	1	-2	41.608	41.515	0.14	4.266	11	12
1	2	0	45.335	45.276	0.10	3.919	17	40
1	-1	1	45.745	45.706	0.07	3.884	18	15
1	-1	0	46.207	46.216	0.01	3.846	2	1
1	1	-2	48.105	48.066	0.07	3.696	10	8
2	1	2	49.761	49.766	0.01	3.575	28	35
1	2	-1	49.955	49.936	0.03	3.561	37	40
1	0	3	51.064	51.076	0.02	3.485	1	1
0	0	3	51.775	51.706	0.13	3.438	17	15
0	2	0	52.377	52.386	0.02	3.399	4	3
2	2	1	52.582	52.576	0.01	3.386	7	6
1	1	3	52.794	52.726	0.13	3.373	15	20
0	2	-1	53.936	53.906	0.06	3.303	14	20
1	2	2	54.65	54.626	0.05	3.261	18	15
2	1	-1	54.986	54.976	0.02	3.241	10	8
2	0	2	55.592	55.566	0.05	3.206	2	2
0	1	-3	56.332	56.286	0.09	3.165	12	11
0	2	1	56.441	56.456	0.03	3.159	10	12
2	1	3	59.246	59.206	0.09	3.013	9	8
1	2	-2	59.57	59.546	0.05	2.997	9	8
0	1	3	59.916	59.926	0.02	2.98	4	5
0	2	-2	60.718	60.726	0.02	2.941	16	20
1	-1	3	61.898	61.916	0.04	2.886	19	12
1	-1	-2	63.632	63.656	0.05	2.81	8	6
0	2	2	65.164	65.175	0.03	2.745	2	1
2	2	3	66.139	66.145	0.01	2.706	8	6
2	-1	1	69.581	69.574	0.02	2.576	2	1
1	-2	1	69.777	69.784	0.02	2.569	2	1
2	3	0	70.356	70.374	0.05	2.548	5	4
1	-2	0	70.596	70.594	0.01	2.54	8	7
3	1	2	70.871	70.844	0.07	2.531	7	8
2	-1	0	71.911	71.904	0.02	2.495	1	1
3	1	0	73.113	73.173	0.16	2.455	3	3
1	-2	2	73.343	73.343	0.00	2.448	3	3
2	3	2	74.054	74.063	0.02	2.425	6	5
1	-1	4	75.197	75.163	0.09	2.39	5	6
2	0	4	75.331	75.243	0.23	2.386	3	3
1	-2	-1	75.676	75.713	0.10	2.375	2	2

3	1	3	76.174	76.132	0.11	2.36	2	2
0	1	4	76.408	76.352	0.15	2.353	2	1
3	2	3	77.032	77.022	0.03	2.335	7	6
1	3	2	77.169	77.232	0.17	2.331	2	1
2	-1	3	77.865	77.782	0.23	2.311	1	1
2	-1	-1	78.317	78.342	0.07	2.298	2	3
3	3	1	79.346	79.391	0.12	2.269	8	20
0	3	-1	80.101	80.111	0.03	2.249	2	2
2	1	-3	80.691	80.661	0.09	2.233	4	4
3	3	2	81.206	81.25	0.13	2.220	1	2
3	3	0	81.448	81.46	0.03	2.213	2	1
2	3	3	81.88	81.89	0.03	2.202	6	8
0	3	1	82.77	82.78	0.03	2.179	1	1
1	-2	-2	84.36	84.389	0.09	2.140	2	1
3	2	4	86.243	86.288	0.14	2.096	5	2
2	0	-3	86.742	86.758	0.05	2.084	3	2
3	3	3	86.817	86.888	0.21	2.082	4	4
2	-1	-2	88.051	88.067	0.05	2.055	2	3
1	3	-3	89.05	88.957	0.29	2.033	3	4
0	1	-5	89.814	89.846	0.10	2.016	1	3
3	0	-1	89.977	89.976	0.00	2.013	7	15
2	-2	1	92.186	92.215	0.09	1.967	2	2
0	3	-3	92.507	92.445	0.20	1.961	5	6
2	2	5	92.698	92.685	0.04	1.957	6	4
2	-2	0	94.440	94.413	0.090	1.923	3	3
4	1	2	96.394	96.402	0.03	1.886	3	3
4	1	1	97.129	97.132	0.01	1.873	4	5
1	4	-1	97.875	97.801	0.24	1.859	2	3
1	1	-5	98.003	97.931	0.24	1.857	3	2
3	4	2	98.24	98.181	0.19	1.853	1	1
1	-3	2	98.589	98.601	0.04	1.847	2	3
0	3	3	99.534	99.53	0.01	1.83	5	7
3	0	-2	99.936	99.92	0.05	1.823	3	4

[a)]Intensity standardizes on 100 for the strongest reflection within the range of the angle $26.18° \leq 4\theta \leq 99.92°$.

Table B4.4 Anisotropic displacement parameters for $(Re^{VII}_2O_5)Si^{o}_2[Si^{t}_2O(PO_4)_6]$ ($Å^2$).

atom	*U*11	*U*22	*U*33	*U*12	*U*13	*U*23
Re1	0.0084(4)	0.0079(4)	0.0101(4)	-0.0031(3)	-0.0027(3)	0.0010(2)
Si1	0.004(2)	0.004(2)	0.009(2)	-0.001(2)	-0.002(2)	-0.0001(2)
Si2	0.007(2)	0.008(2)	0.010(2)	-0.003(2)	-0.005(2)	0.002(12)
P1	0.006(2)	0.005(6)	0.010(2)	-0.001(2)	-0.004(2)	0.001(2)
P2	0.006(6)	0.007(2)	0.011(2)	-0.002(17)	-0.004(2)	0.001(2)
P3	0.008(2)	0.006(2)	0.010(2)	-0.003(2)	-0.003(2)	0.002(2)
O1	0.009(8)	0.018(1)	0.010(9)	-0.009(8)	0.002(7)	0.004(7)
O2	0.017(9)	0.015(9)	0.015(9)	-0.009(8)	-0.009(8)	0.004(7)
O3	0.008(6)	0.012(6)	0.010(6)	-0.003(5)	-0.004(5)	0.002(5)
O4	0.010(6)	0.015(6)	0.011(6)	-0.011(5)	-0.003(5)	0.005(5)
O5	0.010(6)	0.010(6)	0.010(6)	0.000(5)	-0.004(5)	-0.001(5)
O6	0.009(6)	0.010(6)	0.010(6)	-0.004(5)	-0.005(5)	0.001(5)
O7	0.005(6)	0.006(6)	0.016(6)	-0.003(5)	0.003(5)	-0.004(5)
O8	0.003(5)	0.010(6)	0.013(6)	-0.003(5)	-0.003(5)	0.000(5)
O9	0.005(6)	0.008(6)	0.016(6)	-0.003(5)	-0.003(5)	0.002(5)
O10	0.019(7)	0.006(6)	0.022(7)	-0.007(6)	-0.012(6)	0.006(5)
O11	0.007(6)	0.010(6)	0.014(6)	-0.003(5)	0.001(5)	-0.006(5)
O12	0.010(6)	0.009(6)	0.008(6)	-0.003(5)	-0.002(5)	0.000(5)

16.C1 α-Vanadyl(V) rhenate

Table C1.1 Details concerning data collection, structure determination of α-$VO(ReO_4)_2$.

crystal data	
chemical formula	α-$VO(ReO_4)_2$
crystal system	orthorhombic
space group	*Pnma* (No. 62)
a / Å	8.1240(4)
b / Å	9.2751(6)
c / Å	36.840(2)
V / Å^3	2776.0(3)
$\tilde{\mu}$ / mm^{-1}	47.353
$D_{X\text{-}ray}$ / g·cm^{-3}	6.524
colour	turky
crystal shape	rectangular
size /mm^3	0.05×0.04×0.01
F(000)	4641
data collection	
Nonius κ-CCD diffractometer, Mo-Kα-radiation, λ = 0.71073Å, graphite-monochromator	
temperature / K	123
scan range θ / °	$2.91 \le \theta \le 30.034$
	$-11 \le h \le 9$
	$-11 \le k \le 13$
	$-51 \le l \le 51$
absorption correction	multiscans [115]
structure refinement	
software	SHELX97 [105]
measured reflections	40584
ind. reflections	2762. 1659 with $\lvert F_o \rvert > 4\sigma(F_o)$
parameter; Goof	230; 1.085
residuals	
R_{int}	0.1069
R_1[a)]	0.1038
wR_2[b)]	0.2534
weighting scheme	A = 0.058; B = 1023.6332
residual electron density	
$\Delta\rho_{max}$ / Å^{-3}	4.32 (close to Re2
$\Delta\rho_{min}$ / Å^{-3}	-6.15 (close to Re2)

[a)] $R_1 = \Sigma||F_o| - |F_c|| / |F_o|$, $F_o^2 \ge 2\sigma(F_o^2)$

[b)] $wR_2 = 1 / [\sigma^2(F_o^2) + (A \cdot P)^2 + B \cdot P]$; $P = (F_o^2 + 2F_c^2) / 3$

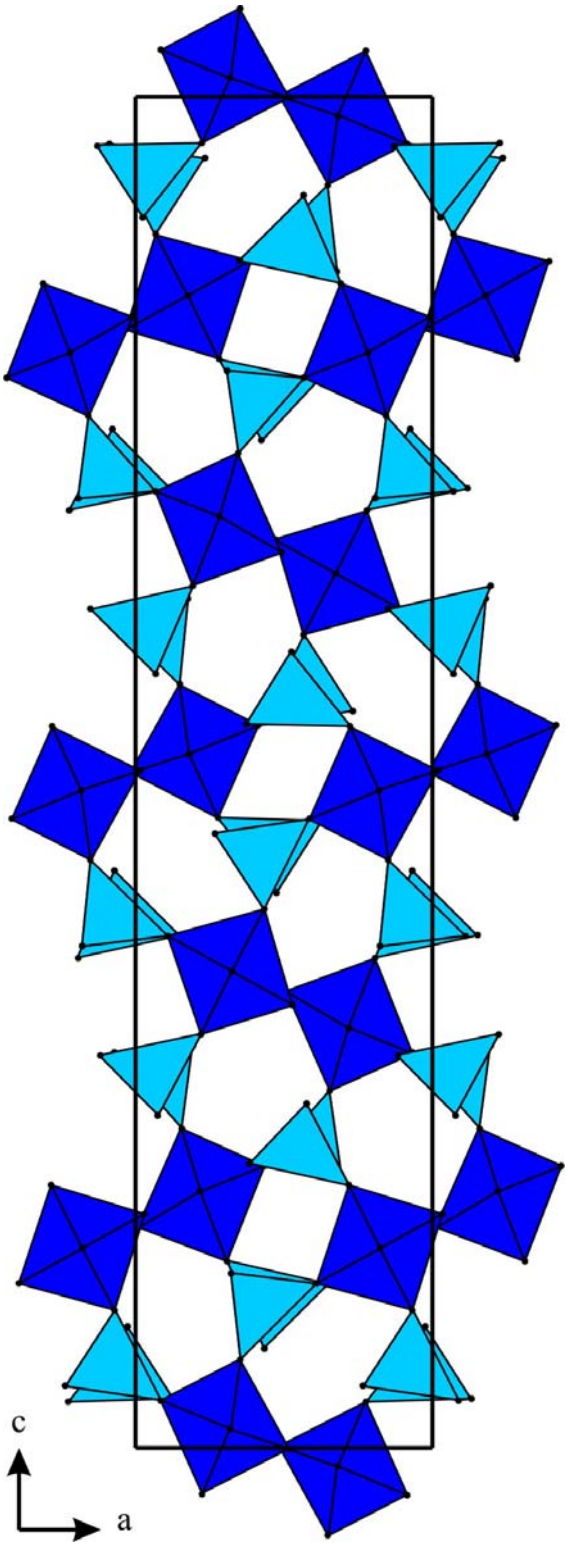

Figure C1.1 Crystal structure of α-$VO(ReO_4)_2$. [VO_6] octahedral in blue and [ReO_4] tetrahedral in ice blue (Diamond version 3.2c [138]).

Table C1.2 Atomic coordinates and isotropic displacement parameters of supercell of α-$VO(ReO_4)_2$.

atom	wyck.	site	*x*	*y*	*z*	U_{eq} /Å$^{2a)}$
Re1	4*c*	.*m*.	0.4586(3)	3/4	0.10092(6)	0.0235(7)
Re2	4*c*	.*m*.	0.4122(2)	1/4	0.11186(6)	0.0110(6)
Re3	4*c*	.*m*.	0.5594(3)	1/4	0.22796(6)	0.0158(7)
Re4	4*c*	.*m*.	0.6199(3)	3/4	0.22068(6)	0.0135(6)
Re5	4*c*	.*m*.	0.8933(4)	1/4	0.05555(7)	0.0337(8)
Re6	4*c*	.*m*.	0.9637(3)	3/4	0.06316(7)	0.0204(7)
V1	4*c*	.*m*.	0.1776(12)	3/4	0.1815(3)	0.0153(2)
V2	4*c*	.*m*.	0.8608(10)	1/4	0.1530(3)	0.014(2)
V3	4*c*	.*m*.	0.6644(19)	3/4	-0.0115(3)	0.0392(4)
O1	4*c*	.*m*.	0.932(4)	1/4	0.1018(9)	0.0106(8)
O2	8*d*	1	0.974(3)	0.602(3)	0.0893(8)	0.0148(6)
O3	4*c*	.*m*.	0.777(4)	3/4	0.0341(9)	0.012(8)
O4	4*c*	.*m*.	0.650(5)	3/4	0.1211(11)	0.023(10)
O5	4*c*	.m.	1.128(7)	3/4	0.0361(12)	0.051(16)
O6	8*d*	1	0.824(5)	0.466(4)	0.1474(11)	0.050(11)
O7	4*c*	.*m*.	1.031(4)	1/4	0.1726(9)	0.0180(10)
O8	8*d*	1	0.681(6)	0.535(4)	-.0138(11)	0.0074(15)
O9	8*d*	1	0.577(5)	0.400(3)	0.2542(9)	0.049(10)
O10	8*d*	1	0.431(5)	0.605(5)	0.0732(12)	0.075(15)
O11	4*c*	.*m*.	0.351(8)	1/4	0.0652(13)	0.058(14)
O12	8*d*	1	0.322(5)	0.401(5)	0.1289(14)	0.0568(5)
O13	4*c*	.*m*.	0.009(5)	3/4	0.1627(14)	0.09(3)
O14	4*c*	.*m*.	0.655(9)	3/4	0.2638(14)	0.06(2)
O15	8*d*	1	0.767(6)	0.389(5)	0.0455(11)	0.074(14)
O16	8*d*	1	0.218(6)	0.534(4)	0.1896(14)	0.073(15)
O17	4*c*	.*m*.	0.720(7)	1/4	0.1941(11)	0.034(13)
O18	4*c*	.*m*.	0.308(7)	3/4	0.138(3)	0.15(5)
O19	4*c*	.*m*.	0.611(5)	1/4	0.1215(19)	0.10(3)
O20	4*c*	.*m*.	0.483(7)	3/4	0.0007(12)	0.062(19)
O21	4*c*	.*m*.	1.086(10)	1/4	0.0349(15)	0.08(2)
O22	8*d*	1	0.431(9)	0.710(4)	0.208(2)	0.16(4)
O23	4*c*	.*m*.	0.383(8)	1/4	0.210(6)	0.35(14)
O24	8*d*	1	0.692(7)	0.602(4)	0.2027(13)	0.099(21)

[a)] $U_{eq} = (⅓)\Sigma_i\Sigma_j U_{ij} a_i^* a_j^* \mathbf{a}_i \cdot \mathbf{a}_j$

Table C1.3 α-$VO(ReO_4)_2$. Selected interatomic distances (Å) and estimated standard deviations in parentheses.

d(V1-O13)	1.54(5)	*d*(V2-O7)	1.56(3)	*d*(V3-O20)	1.54(6)
d(V1-O18)	1.94(11)	*d*(V2-$O17_t$)	1.90(4)	*d*(V3-O3)	1.91(4)
d(V1-O14)	2.02(5)	*d*(V2-O1)	1.97(3)	*d*(V3-O11)	1.98(5)
d(V1-O16)	2.05(4)	*d*(V2-O6)	2.04(4)	*d*(V3-O8)	2.00(3)
d(V1-O16)	2.05(4)	*d*(V2-O6)	2.04(4)	*d*(V3-O8)	2.00(3)
d(V1-O22)	2.31(6)	*d*(V2-O19)	2.33(5)	*d*(V3-O21)	2.21(8)
d(Re1-O10)	1.70(5)	*d*(Re2-O19)	1.66(5)	*d*(Re3-O23)	1.59(8)
d(Re1-O10)	1.70(5)	*d*(Re2-O12)	1.70(4)	*d*(Re3-O9)	1.70(3)
d(Re1-O4)	1.72(4)	*d*(Re2-O12)	1.70(4)	*d*(Re3-O9)	1.70(3)
d(Re1-O18)	1.82(10)	*d*(Re2-O11)	1.79(6)	*d*(R23-O17)	1.81(4)
d(Re4-O22)	1.65(6)	*d*(Re5-O15)	1.69(5)	*d*(Re6-O5)	1.66(4)
d(Re4-O22)	1.65(6)	*d*(Re5-O15)	1.69(5)	*d*(Re6-O2)	1.68(3)
d(Re4-O14)	1.61(5)	*d*(Re5-O1)	1.73(3)	*d*(Re3-O2)	1.68(3)
d(Re4-O24)	1.63(3)	*d*(Re5-O21)	1.74(8)	*d*(R6-O3)	1.85(4)

Table C1.4 Anisotropic displacement parameters (Å^2) of α-$VO(ReO_4)_2$.

Atom	U_{11}	U_{22}	U_{33}	U_{12}	U_{13}	U_{23}
Re1	0.0298(15)	0.0355(18)	0.0051(9)	0.00000	-0.0004(8)	0.00000
Re2	0.0085(11)	0.0165(14)	0.0079(8)	0.00000	-0.0004(7)	0.00000
Re3	0.0136(12)	0.0266(16)	0.0071(9)	0.00000	0.0072(8)	0.00000
Re4	0.0178(12)	0.0130(14)	0.0098(9)	0.00000	0.0060(8)	0.00000
Re5	0.0482(18)	0.043(2)	0.0096(11)	0.00000	0.0064(10)	0.00000
Re6	0.0206(14)	0.0179(15)	0.0227(11)	0.00000	0.0073(10)	0.00000
V1	0.031(6)	0.001(5)	0.013(4)	0.00000	-0.018(4)	0.00000
V2	0.000(4)	0.028(6)	0.015(4)	0.00000	0.005(3)	0.00000
V3	0.092(10)	0.019(7)	0.007(5)	0.00000	-0.012(6)	0.00000
O1	0.000(16)	0.03(2)	0.004(14)	0.00000	0.001(12)	0.00000
O2	0.007(13)	0.000(14)	0.038(17)	0.013(11)	-0.004(11)	0.004(13)
O3	0.02(2)	0.01(2)	0.003(15)	0.00000	0.015(13)	0.00000
O4	0.03(2)	0.03(3)	0.012(18)	0.00000	-0.008(17)	0.00000
O5	0.06(3)	0.08(5)	0.01(2)	0.00000	0.04(2)	0.00000
O6	0.07(2)	0.03(2)	0.05(2)	0.02(2)	0.05(2)	0.03(2)
O7	0.02(2)	0.04(3)	0.000(14)	0.00000	-0.010(13)	0.00000
O8	0.17(4)	0.000(17)	0.04(2)	-0.02(2)	-0.08(3)	0.014(17)
O9	0.13(3)	0.000(16)	0.024(16)	0.007(19)	0.019(19)	-0.032(14)
O10	0.09(3)	0.08(4)	0.06(3)	-0.04(3)	-0.06(2)	0.02(2)
O11	0.13(5)	0.03(3)	0.01(2)	0.00000	0.05(3)	0.00000
O12	0.08(3)	0.07(3)	0.07(4)	0.06(3)	0.03(3)	-0.02(3)
O13	0.00(2)	0.24(9)	0.03(3)	0.00000	0.027(19)	0.00000
O14	0.15(6)	0.00(3)	0.01(2)	0.00000	-0.02(3)	0.00000
O15	0.12(4)	0.08(3)	0.023(19)	0.00(3)	-0.04(2)	-0.01(2)
O16	0.16(4)	0.00(2)	0.06(3)	0.02(2)	0.01(3)	0.00(2)
O17	0.10(4)	0.00(2)	0.004(17)	0.00000	0.02(2)	0.00000
O18	0.00(3)	0.16(9)	0.28(16)	0.00000	0.01(5)	0.00000
O19	0.00(2)	0.27(11)	0.05(4)	0.00000	0.00(2)	0.00000
O20	0.07(4)	0.12(6)	0.000(18)	0.00000	-0.01(2)	0.00000
O21	0.21(8)	0.00(3)	0.02(3)	0.00000	0.02(4)	0.00000
O22	0.18(7)	0.02(3)	0.28(10)	-0.01(3)	-0.11(7)	0.05(3)
O23	0.02(4)	0.02(4)	1.0(4)	0.00000	-0.17(10)	0.00000
O24	0.22(5)	0.00(2)	0.07(3)	0.01(3)	0.12(4)	-0.02(2)

17 References

[1] A. Durif, *Crystal Chemistry of Condensed Phosphates*, Plenum Press, New York, **1995**.

[2] R. Glaum, *Neue Untersuchungen an wasserfreien Phosphaten der Übergangsmetalle*, Thesis of Habilitation, Univ. of Gießen **1999**. URL: http://bibd.uni-giessen.de/ghtm/1999/uni/h990001.htm

[3] A. Schnabel, J. Kretschmer, R. Glaum, *unpublished work*, Univ. of Bonn, **2011**.

[4] G. Bergerhoff, I. D. Brown, *Crystallographic Databases*, (Eds.: F. H. Allen, G. Bergerhoff, R. Sievers), Chester, International Union of Crystallography, **1987**.

[5] G. Bergerhoff, M. Berndt, K. Brandenburg, T. Degen, *Acta Crystallogr.* **1999**, *B55*, 147.

[6] Yu. E. Gorbunova, S. A. Linde, *Dokl. Akad. Nauk SSSR* **1979**, *245*, 584.

[7] L. O. Hagman, P. Kierkegaard, *Acta Chem. Scand*. **1968**, *22*, 1822.

[8] I. Tordjman, R. Masse, J. C. Guitel, *Z. Kristallogr*. **1974**, *139*, 103.

[9] A. K. Padhi, K. S. Nanjundaswamy, J. B. Goodenough, *Electrochemical Society Meeting Abstracts*, 96-1, May, **1996**, 73.

[10] Y. Si, H. R. Kunz, J. M. Fenton, *J. Electrochem. Soc*. **2004**, *151*, 623.

[11] P. M. Forster, J. Eckert, JS. Chang, SE. Park, G. Férey, A. K. Cheetham, *J. Am. Chem. Soc.* **2003**, *125*, 1309.

[12] R. Glaum, R. Gruehn, *Z. Allg. Anorg. Chem.* **1990**, *580*, 78.

[13] F. Reinauer, R. Glaum, *Acta Crystallogr*. **1998**, *B54*, 722.

[14] M. Schöneborn, R. Glaum, *J. Solid State Chem*. **2008**, *181*, 1367.

[15] E. Benser, T. Droß, H. Hibst, R. Glaum, *Chem. Mater.* **2007**, *19*, 4341.

[16] T. Droß, *Ph. D. Thesis*, Univ. of Bonn, **2002**. URL: http://hss.ulb.uni-bonn.de/diss_online/math_nat_fak/2004/dross_thomas/index.htm

[17] U. Kaiser, *Ph. D. Thesis*, Univ. of Gießen, **1996**.

[18] A. Schmidt, *Ph. D. Thesis*, Univ. of Gießen, **2002**.

[19] M. Lenz, *Ph. D. Thesis*, Univ. of Gießen, **1995**.

[20] H. Mathis, R. Glaum, R. Gruehn, *Acta Chem. Scand*. **1991**, *45*, 781.

[21] M. Gerk, *Ph. D. Thesis*, Univ. of Gießen, **1996**.

[22] C. Gleitzer, *Eur. J. Solid State Inorg. Chem.* **1991**, *28*, 77.

[23] D. Özalp, *Ph. D. Thesis*, Univ. of Gießen, **1993**.

[24] P. Kierkegaard, *Arkiv Kemi.* **1962**, *19*, 1.

[25] S. E. Lister, A. Soleilhavoup, R. L. Withers, P. Hodgkinson, J. S. O. Evans, *Inorg. Chem.* **2010**, *49*, 2290.

[26] P. Kierkegaard, *Arkiv Kemi*. **1961**, *18*, 521.

[27] P. Kierkegaard, J. M. Longo, *Acta Chem. Scand*. **1970**, *24*, 427.

[28] G. Costentin, A. Leclaire, M. M. Borel, A. Grandin, B. Raveau, *Z. Kristallogr*. **1992**, *201*, 53.

[29] S. E. Lister, I. R. Evans, J. S. O. Evans, *Inorg. Chem.* **2009**, *48*, 9271.

[30] V. V. Lisnyak, N. V. Stus', P. Popovich, D. A. Stratiychuk, Ya. Filinchuk, V. M. Davydov, *J. Alloys Compd*. **2003**, *360*, 81.

[31] A. Leclaire, M. M. Borel, A. Grandin, B. Raveau, *Eur. J. Solid State Inorg. Chem*. **1988**, *25*, 323.

[32] I. M. Watson, M. M. Borel, J. Chardon, A. Leclaire, *J. Solid State Chem.* **1994**, *111*, 253.

[33] S. T. Norberg, G. Svensson, J. Albertsson, *Acta Crystallogr.* **2001**, *C57*, 225.

[34] A. Magnéli, *Acta Chem. Scand*. **1957**, *11*, 28.

[35] W. Jeitschko, A. W. Sleight, *J. Solid State Chem.* **1972**, *4,* 324.

[36] K. Meisel, *Z. Anorg. Allg. Chem*. **1932**, *207,* 121.

[37] T. Hartmann, H. Ehrenberg, G. Miehe, T. Buhrmester, G. Wltschek, J Galy, H. Fuess, *J. Solid State Chem*. **2001**, *160*, 317.

[38] B. Krebs, A. Müller, H. H. Beyer, *Inorg. Chem*. **1969**, *8*, 436.

[39] A. J. Edwards, G. R. Jones, *Chem. Comm*. **1967**, 462.

[40] A. J. Edwards, *J. Chem. Soc. Dalton Trans*. **1972**, 582.

[41] J. Supeł, R. Marx, K. Seppelt, *Z. Anorg. Allg. Chem.* **2005**, *631*, 2979.

[42] J. Supeł, K. Seppelt, *Angew. Chem. Intl. Ed.* **2006**, *45*, 4675.

[43] C. Ujica, D. Gutierrez, J. Llanos, R. Cardoso, *J. Alloys Compd*. **2000**, *307*, 127.

[44] W. Jeitschko, D. H. Heumannskaemper, M. S. Schriewer-Pöttgen, U. C. Rodewald, *J. Solid State Chem*. **1999**, *147*, 218.

[45] R. J. Cava, A. Santoro, D. W. Murphy, S. M. Zahurak, R. S. Roth, *Solid State Ionic* **1981**, *5*, 323.

[46] D. Mikhailova, H. Ehrenberg, D. Trots, G. Brey, S. Oswald, H. Fuess, *J. Solid State Chem.* **2009**, *182*, 1506.

[47] W. Baur, W. Joswig, G. Pieper, D. Kassner, *J. Solid State Chem*. **1992**, *99*, 207.

[48] A. R. P. Smith, A. K. Cheetham, *J. Solid State Chem*. **1979**, *30*, 345.

[49] M. Wakeshima, Y. Hinatsu, *J. Solid State Chem*. **2006**, *179*, 3575.

[50] R. J. Cava, A. Santoro, D. W. Murphy, S. M. Zahurak, R. S. Roth, *J. Solid State Chem.* **1982**, *42*, 251.

[51] P. C. Donohue, J. M. Longo, R. D. Rosenstein, L. Katz, *Inorg. Chem*. **1965**, *4*, 1152.

[52] K. G. Bramnik, H. Ehrenberg, S. Buhre, H. Fuess, *Acta Crystallogr.* **2005**, *B61*, 246.

[53] A. K. Cheetham, D. M. Thomas, *J. Solid State Chem*. **1987**, *71*, 61.

[54] G. J. Kruger, E. C. Reynhardt, *Acta Crystallogr.* **1978**, *B34*, 259.

[55] T. Betz, R. Hoppe, *Z. Anorg. Allg. Chem*. **1983**, *500*, 23.

[56] A. Atzesdorfer, K. J. Range, *Z. Naturforsch.* **1995**, *B50,* 1417.

[57] B. Krebs, K. Hasse, *Acta Crystallogr*. **1976**, *32*, 1334.

[58] P. Roegner, K. J. Range, *Z. Naturforsch.* **1993**, *B48*, 233.

[59] P. Roegner, K. J. Range, *Z. Naturforsch.* **1993**, *B48*, 685.

[60] D. Mikhailova, H. Ehrenberg, H. Fuess, *J. Solid State Chem*. **2006**, *179*, 2004.

[61] J. Beintema, *Z. Kristallogr*. **1937**, *97*, 300.

[62] D. Yu. Naumov, A. V. Virovets, S. V. Korenev, A. I. Gubanov, *Acta Crystallogr*. **1999**, *C55*, 1.

[63] A. Butz, G. Miehe, H. Paulus, P. Strauss, H. Fuess, *J. Solid State Chem*. **1998**, *138*, 232.

[64] J. P. Picard, G. Baud, J. P. Besse, R. Chevalier, M. Gasperin, *J. Less-Comm. Met.* **1984**, *96*, 171.

[65] H. A. Mons, M. S. Schriewer, W. Jeitschko, *J. Solid State Chem*. **1992**, *99*, 149.

[66] G. Baud, J. Besse, R. Chevalier, M. Gasperin, *J. Solid State Chem*. **1979**, *29*, 267.

[67] W. Jeitschko, D. H. Heumannskaemper, U. C. Rodewald, M. S. Schriewer-Pöttgen, *Z. Anorg. Allg. Chem.* **2000**, *626*, 80.

[68] J. P. Besse, M. Bolte, G. Baud, R. Chevalier, *Acta Crystallogr.* **1976**, *B32*, 3045.

[69] C. Mujica, K. Peters, E. M. Peters, H. G. Z. Schnering, Z. *Kristallogr.* **2000**, *215*, 3.

[70] W. Freundlich, M.-R. Lee, *C. R. Acad. Sci. Paris* **1967**, *264,* 704.

[71] B. Bastide, R. Enjalbert, H. Fuess, J. Galy, *Solid State Sci*. **2000**, *2*, 545.

[72] I. Schulz, *Z. Allg. Anorg. Chem.* 1**955**, *281*, 99.

[73] P. Kierkegaard, *Acta Chem. Scand.* **1960**, *14*, 657.

[74] P. Kierkegaard, S. Asbrink, *Acta Chem. Scand*. **1964**, *18*, 2329.

[75] M. Hanawa, H. Imoto, *J. Solid State Chem.* **1999**, *144*, 325.

[76] P. Kierkegaard, *Acta Chem. Scand*. **1958**, *12*, 1715.

[77] S. L. Wang, C. C. Wang, K. H. Lii, *J. Solid State Chem*. **1989**, *82,* 298.

[78] A. Leclaire, J. Chardon, B. Raveau, *J. Solid State Chem.* **2000**, *155,* 112.

[79] V. V. Lisnyak, N. V. Stus', N. S. Slobodyanik, N. M. Belyavina, V. Ya. Markiv, *J. Alloys Compd*. **2000**, *309*, 83.

[80] P. Roussel, P. Labbé, D. Groult, *Acta Crystallogr*. **2000**, *B56*, 317.

[81] E. Banks, R. Sacks, *Mater. Res. Bull*. **1982**, *17*, 1053.

[82] K. Popa, V. Brandel, A. Cecal, *Rev. Roumaine de Chem.* **2001**, *46,* 509.

[83] V. V. Lisnyak, N. V. Stus, D. A. Stratiichuk, N. M. Belyavina, V. Ya. Markiv, *Phosphorus, Sulfur Silicon Relat. Elem*. **2008**, *183*, 2248.

[84] H. Schäfer, *Z. Anorg. Allg. Chem*. **1973**, *400*, 253.

[85] H. Schäfer, *Chemische Transportreaktionen*, Verlag Chemie, Weinheim, **1962**.

[86] P. W. Atkins, *Physikalische Chemie*, 3. Auflage, Spektrum Akademischer Verlag, **1993**.

[87] I. Müller, *A History of Thermodynamics - the Doctrine of Energy and Entropy*, Springer-Verlag, **2007**.

[88] G. Schmidt, R. Gruehn, *J. Crystal Growth.* **1982**, *57*, 585.

[89] W. H. Bragg, W. L. Bragg. *Proc. Royal Soc. (London)*, **1913**, *A88*, 428.

[90] Y. Amemiya, J. Miyahara, *Nature* **1988**, *336*, 89.

[91] Programm AIDA: Advanced Image Data Analyser (AIDA). Version 2,2, Raytest-Isotopenmeßgeräte GmbH, **1999**.

[92] Origin 6.1G, OriginLab Corporation, **1991** – **2000**.

[93] ICSD-Database FIZ/NIST; Fachinformationszentrum Karlsruhe, National Institute of Standards and Technology, Geithersburg, USA, Vers. 1.4.4, **2008**.

[94] K. Yvon, W. Jeitschko, E. Parté, *J. Appl. Crystallogr.* **1977**, *10*, 73.

[95] G. Meyer, J. Soose: „SOS-Programme zur Auswertung von Guinier-Aufnahmen“, *Staatsexamensarbeit*, Univ. of Gießen, **1980**.

[96] P. E. Werner, *Z. Kristallogr.* **1964**, *120*, 375.

[97] P. E. Werner, L. Eriksson, M. Westdahl, *J. Appl. Cryst.* **1985**, *18*, 367.

[98] A. Boutlif, D. Louër, *J. Appl. Cryst.* **1991**, *24*, 987.

[99] J. Visser, *J. Appl. Cryst*. **1966**, *2*, 89.

[100] J. R. Carvajal, T. Roisnel: „FullProf98 and WinPLOTR: New Windows 95/NT Applications for Diffraction, Commission For Powder Diffraction", International Union for Crystallography, Newsletter N°20, **1998**.

[101] P. M. de Wolf, *J. Appl. Cryst.* **1957**, 10, 590.

[102] W. Massa, *Kristallstrukturbestimmung*, 3. Auflage, Teubner Verlag, **2002**.

[103] G. M. Sheldrick: "*SHELXS-97: Program for Crystal Structure Solution*", Univ. of Göttingen, **1997**.

[104] L. Palatinus and G. Chapuis, *J. Appl. Cryst.* **2007**, *40*, 786.

[105] G. M. Sheldrick, SHELXl-97-A Program for crystal structure refinement, Univ. of Goettingen, **1997**.

[106] A. L. Patterson, *Phys. Rev.* **1934**, *46*, 372.

[107] A. L. Patterson, *Z. Kristallogr.* **1935**, *A90*, 517.

[108] D. Sayre, *Acta Crystallogr.* **1952**, *5*, 60.

[109] H. Hauptman, *J. Acta Crystallogr.* **1950**, *3*, 181.

[110] J. Karlé, H. Hauptmann, *Acta Crystallogr.* **1952**, *10*, 267".

[111] G. Oszla´nyi, A. Su¨to, *Acta Cryst.* **2004**, *A60*, 134.

[112] L. Palatinus, *Acta Cryst.* **2004**, *A60*, 604.

[113] J. Karle, H. Hauptman, *Acta Crystallogr.* **1956***, 9,* 635.

[114] L. Palatinus and G. Chapuis, *J. Appl. Cryst.* **2007**, *40*, 786.

[115] R. H. Blessing, *Acta Crystallogr.* **1995**, *A51*, 33.

[116] L. Reimer, *Scanning Electron Microscop*, Springer-Verlag, Berlin, **1983**.

[117] D. Newbury, *Advanced Scanning Electron Microscopy and X-ray Microanalysis*, Plenum Press, New York, **1987**.

[118] Bedienungsanleitung, *PVSUPQ (EDAX-Analysensystem)*, Philips, Eindhoven, Netherland, **1986**.

[119] E. R. Andrew, E. Szczesniak, *Prog. Nucl. Magn. Reson. Spectrosc.* **1995**, *28*, 11.

[120] B. Wrackmeyer, *Chem. unserer Zeit*, **1988**, *22*, 100.

[121] E. Krausz, *Aust. J. Chem*. **1993**, *46*, 1041.

[122] E. Krausz, *AOS news* **1998**, *12*, 21.

[123] J. Weidlein, U. Müller, K. Dehnike, *Schwingungsspektroskopie*, 2. überarbeitete Auflage, Georg Thieme Verlag, Stuttgart, **1988**.

[124] K. Nakamoto, *Infrared and Raman Spectra of Inorganic and Coordination Compounds*, Third Edition, Wiley Interscience, John Wiley & Sons, New York, USA, **1978**.

[125] H. Oppermann, *Z. Anorg. Allg. Chem*. **1985**, *523*, 135.

[126] M. Binnewies, R. Glaum, M. Schmidt, P. Schmidt, *Chemische Transportreaktionen*, **2011**.

[127] G. R. Levi, G. Peyronel, *Z. Kristallogr. Kristallgeom. Kristallphys. Kristallchem*. **1935**, *92*, 190.

[128] R. C. Haushalter, L. A. Mundi*, Chem. Mater.* **1992**, *4,* 31.

[129] S. E. Lister, V. J. Rixom, J. S. O. Evans, *Chem. Mater.* **2010**, *22*, 5279.

[130] R. Gopal, C. Calvo, *J. Solid State Chem.* **1972**, *5*, 432.

[131] H. Schäfer, *J. Cryst. Growth* **1971**, *9*, 17.

[132] H. Oppermann, *Z. Allg. Anorg. Chem.* **1971**, *383*, 285.

[133] D. W. Muenow, O. M. Uy, J. L. Margrave, *J. Inorg. Nucl. Chem.* **1970**, *32*, 3459.

[134] R, Gruehn, R. Glaum, *Angew. Chem*. **2000**, *112*, 706; *Angew. Chem. Intl. Ed*. **2000**, *39*, 692.

[135] L. J. Farrugia*, J. Appl. Cryst*. **1990**, *70*, 837.

(136) R. Hundt, "*KPLOT*", Version 9.0, Univ. of Bonn, **2005**.

[137] G. M. sheldrick, *Acta Crystallogr.* **1990**, *A46*, 467.

[138] K. Brandenburg, *DIAMOND* - Crystal and Molecular Structure Visualization. Crystal Impact, GbR, Bonn, Vers. 3.2c, **2009**.

[139] G. W. Stinton, M. R. Hampson, J. S. O. Evans, *Inorg. Chem.* **2006**, *45*, 4352.

[140] H. Birkedal, A. M. K. Andersen, A. Arakcheeva, G. Chapuis, P. Norby, P. Pattison, *Inorg. Chem.* **2006**, *45*, 4346.

[141] A. Guesdon, A. Leclaire, M. M. Borel, A. Grandin, B. Raveau, *Acta Crystallogr.* **1994**, *C50*, 1852.

[142] A. Guesdon, M. M. Borel, A. Grandin, A. Leclaire, B. Raveau, *Acta Crystallogr.* **1993**, *C49*, 1877.

[143] J. J. Zah-Letho, S. Oyetola, A. Verbaere, F. Taulelle, Y. Piffard, *Eur. J. Solid State Inorg. Chem.* **1994**, *31*, 1009.

[144] L. Lezama, J. M. Rojo, J. L. Pizarro, M. I. Arriortua, T. Rojo, *Solid State Ionics*, **1993**, *63*, 657.

[145] H. B. Gray, C. R. Hare, *Inorg. Chem.* **1962**, *1*, 363.

[146] C. J. Ballhausen, H. B. Gray, *Inorg. Chem.* **1962**, *1*, 111.

[147] R. Glaum, W. Hoffbauer, J. Schmidt auf der Grünne, *unpublished result*, Univ. Bonn. **2005**.

[148] H. Schäfer, T. Grofe, M. Trenkel, *J. Solid. State Chem*. **1973**, *8*, 14.

[149] E. Milke, M. Binnewies, M. S. Islam, R. Glaum, *unpublished results*, **2010**.

[150] P. Kierkegaard, *Arkiv Kemi.* **1962**, *19*, 51.

[151] BASREADER V. 2.26, Program for Windows, Raytest Isotopenmessgeräte GmbH, Straubenhard/Germany, **1999**.

[152] I. Tanaka, M. Yao, M. Suzuki, K. Hikichi, *J. Appl. Cryst.* **1990**, *23*, 334.

[153] K. Maaß, R. Glaum, R. Gruehn, *Z. Anorg. Allg. Chem*. **2002**, *628*, 1663.

[154] A. F. Christiansen, H. Fjellvag, A. Kjekshus, B. Klewe, *J. Chem. Soc., Dalton Trans.* **2001**, 806.

[155] P. Kierkegaard, *Arkiv. Kemi.* **1962**, *18*, 553.

[156] F. A. Cotton, S. M. Morehouse, J. S. Wood, *Inorg. Chem.* **1964***, 3,* 1603.

[157] C. Sanchez, J. Livage, J. P. Launay, M. Fournier, Y. Jeannin, *J. Am. Chem. Soc.* **1982**, *104*, 3194.

[158] J. M. Fruchart, G. Herve, J. P. Launay, R. Massart, *J. Inorg. Nucl. Chem.* **1976**, *38*, 127.

[159] P. Kierkegaard, *Arkiv. Kemi.* **1962**, *19*, 4.

[160] R. Rühl, U. Flörke, W. Jeitschko, *J. Solid State Chem*. **1984**, *53*, 55.

[161] S. V. Orishchin, V. S. Babizhet'sky, Yu. B. Kuz'ma, *Neorg. Mater.* **1998**, *34*, 1455.

[162] R. Rühl, W. Jeitschko, *Z. Anorg. Allg. Chem*. **1980**, *466*, 171.

[163] R. Rühl, W. Jeitschko, *Inorg. Chem*. **1982**, *21*, 1886.

[164] R. Rühl, W. Jeitschko, *Acta Crystallogr.* **1982**, *B38*, 2784.

[165] W. Jeitschko, R. Ruehl, *Acta Crystallogr*. **1979**, *B35*, 1953.

[166] F. A. Cotton, G. Wilkinson, *Advanced Inorganic Chemistry*, Intersceince, New York, **1980**.

[167] W. L. Hill, G. Faust, S. B. Hendricks, *J. Am. Chem. Soc.* **1943**, *65*, 794.

[168] J. R. van Wazer, *Phosphorus and its compounds*, Interscience, New York, **1988**.

[169] B. D. sharma, *Inorg. Chem.* **1987**, *26*, 454.

[170] M. Jansen, M. Möbs, *Inorg. Chem.* **1984**, *23*, 4486.

[171] M. Jansen, M. Voss, *Angew. Chem.* **1981**, *93.*120.

[172] K. H. Jost, *Acta Crystallogr*. **1966**, *21*, 34.

[173] K. H. Jost, *Acta Crystallogr*. **1964**, *17*, 1593.

[174] E. Tillmanns, W. Gebert, W. H. Baur, *J. Solid State Chem.* **1973**, *7*, 69.

[175] N. Khosrovani, V. C. Korthuis, A.W. Sleight, T. Vogt, *Inorg. Chem.* **1996**, *35*, 485.

[176] K. M. White, P. L. Lee, P. J. Chupas, K. W. Chapman, E. A. Payzant, *Chem. Mater.* **2008**, *20*, 3728.

[177] A. Cabeza, M. A. G. Aranda, F. M. Cantero, D. Lozano, M. Martinez-Lara, S. Bruque, *J. Solid State Chem.* **1996**, *121*, 181.

[178] C. H. Huang, O. Knop, D. A. Othen, F. W. D. Woodhams, R. A. Howie, *Canad. J. Chem.* **1975**, *53*, 79.

[179] A. Burdese, M. L. Borlera, *Ricerca Scientifica*, **1960**, *30*, 1343.

[180] S. T. Norberg, G. Svensson, J. Albertsson, *Acta Crystallogr.* **2001**, *C57*, 225.

[181] D. M. Poojary, R. B. Borade, F. L. Campbell, A. Clearfield, *J. Solid State Chem.* **1994**, *112*, 106.

[182] K. F. Hesse, *Acta Crystallogr.* **1979**, *B35*, 724.

[183] U. Kaiser, R. Glaum, *Z. Anorg. Allg. Chem*. **1994**, *620*, 1755.

[184] B. Wellmann, F. Liebau, *J. Less-Common Met.* **1981**, *77*, 31.

[185] J. C. Eisenstein, *J. Chem. Phys.* **1961**, *34*, 1628.

[186] Chr. K, Jørgensen, *Z. Naturforsch.* **1965**, *20a*, 65.

[187] P. B. Dorain, R, G. Wheeler, *J. Chem. Phys.* **1966**, *45*, 1172.

[188] A. R. Reinberg, S. G. Parker, *Phys. Rev.* **1970**, *B1,* 2085.

[189] J. C. Collingwood, S. B. Piepho, R. W. Schwartz, P. A. Dobosh, J. R. Dickinson, P. N. Schatz, *Molec. Phys.* **1975**, *29*, 793.

[190] D. R. Gamelin, H. U. Güdel, *Inorg. Chem.* **1999**, *38*, 5154.

[191] N. Khosrovani, A. W. Sleight, T. Vogt, *J. Solid State Chem.* **1997**, *132*, 355.

[192] C. Turquat, C. Muller, E. Nigrelli, C. Leroux, J. L. Soubeyroux, G. Nihoul, *Eur. Phys. J. Appl. Phys*. **2000**, *10*, 15.

[193] S. Mondet, A. Rimsky, J. Borene, W. Freundlich, *Comptes rendus, Serie C*, **1968**, *266*, 1145.

[194] A. Aatiq, M. Menetrier, L. Croguennec, E. Suard, C. Delmas, *J. Mater. Chem.* **2002**, *12*, 2971.

[195] Yu. A. Ivanov, E. L. Belokoneva, Yu. K. Egorov-Tismenko, N. V. Simonov, *Dokl. Akad. Nauk SSSR* **1980**, *252*, 1122.

[196] E. S. Lunezheva, B. A. Maksimov, O. K. Mel'nikov, *Kristallografiya* **1989**, *34*, 1119.

[197] R. Duhlev, *Acta Crystallogr.* **1994**, *C50*, 1525.

[198] R. M. Hazen, D. C. Palmer, L. W. Finger, G. D. Stucky, W. T. A. Harrison, T. E. Gier, *J. Phys. Condens. Matter*. **1994**, *6*, 1333.

[199] E. M. McCarron, J. C. Calabrese, M. A. Subramanian, *Mater. Res. Bull.* **1987**, *22*, 1421.

[200] M. Alami, R. Brochu, J. L.Soubeyroux, G. le Flem Gravereau, P. Hagenmuller, *J. Solid State Chem.* **1991**, *90*, 185.

[201] R. Brochu, M. Louer, M. Alami, M. Alqaraoui, D. Louer, *Mater. Res. Bull.* **1997**, *32*, 113.

[202] M. P. Carrasco, M. C. Guillem, J. Alamo, *Mater. Res. Bull.* **1993**, *28*, 793.

[203] D. Petit, P. Colomban, G. Collin, J. P. Boilot, *Mater. Res. Bull.* **1986**, *21*, 365.

[204] H. Kohler, H. Schulz, *Mater. Res. Bull*. **1986**, *21*, 23.

[205] E. R. Gobechiya, Yu. K. Kabalov, V. I. Pet'kov, M. V. Sukhanov, *Kristallografiya* **2004**, *49(N),* 829.

[206] I. Bussereau, M. S. Belkhiria, P. Gravereau, A. Boireau, J. L. Soubeyroux, R. Olazcuaga, G. Le. Flem, *Acta Crystallogr.* **1992**, *C48*, 1741.

[207] A. Leclaire, M. M. Borel, A. Grandin, B. Raveau, *Acta Crystallogr.* **1989**, *C45*, 699.

[208] K.-H. Lii, J. J. Chen, S. -L. Wang, *J. Solid State Chem.* **1989**, *78*, 93.

[209] J. Alamo, J. L. Rodrigo, *Mater. Res. Bull.* **1992**, *27*, 1091.

[210] A. Serghini, R. Brochu, R. Olazcuaga, P. Gravereau, *Mater. Lett*. **1995**, *22*, 149.

[211] E. R. Gobechiya, Yu. K. Kabalov, S. V. Tomilin, A. N. Lukinykh, A. A. Lizin, A. I. Orlova, *Crystallogr. Rep*. **2005**, *50,* 374.

[212] J. Galy, G. Miehe, *Solid State Sci.* **1999**, *1*, 433.

[213] F. Chen, Q. Shen, J. M. Schoenung, L. Zhang, *J. Am. Ceram. Soc.* **2008**, *91*, 3173.

[214] M. Schöneborn, *Ph. D. Thesis*, University of Bonn, **2008**. URL:http://hss.ulb.uni-bonn.de/diss_online/math_nat_fak/2008/schoeneborn_marcos/index.htm

[215] K. Panagiotidis , R. Glaum, W. Hoffbauer, J. Weber, J. Schmedt auf der Günne, *Z. Anorg. Allg. Chem.* **2008**, *634*, 2922.

[216] A. Kostencki, *Ph. D. thesis*, Univ. of Gießen, **1997**.

[217] A. N. Lazarev, V. S. Aksel'rod*, Opt. Spektrosk,* **1960**, *9*, 360.

[218] C. H. Huang, O. Knop, D. A. Othen, F. W. D. Woodhams, R. A. Howie, *Can. J. Chem.* **1975**, *53*, 79.

[219] L. O. Hagman, P. Kierkegaard, *Acta Chem. Scand.* **1968**, *22*, 1822.

[220] M. Schöneborn, R. Glaum, *Z. Anorg. Allg. Chem.* **2008**, *634*, 1843.

[221] G. Amonoff, *Z. Kristallogr.* **1923**, *58*, 203.

(222) H. Mayer, *Monatsh. Chem*. **1974**, *46*, 105.

[223] H. Mayer, H. Voellenkle, *Monatsh. Chem.* **1972**, *103*, 1560.

[224] F. Liebau, *Acta. Cryst.* **1961**, *14*, 1103.

[225] A. F. Reid, C. Li, A. E. Ringwood, *J. Solid State Chem.* **1977**, *20*, 219.

[226] W. H. Zachariasen, *Z. Kristallogr.* **1930**, *73*, 1.

[227] M. Schöneborn, W. Hoffbauer, J. Schmedt auf der Günne, R. Glaum, *Z. Naturforsch.* **2006**, *61b*, 741.

[228] K. G. Bramnik, H. Ehrenberg, R. Teissmann, H. Fuess, E. Morán, *Z. Kristallogr*. **2003**, *218*, 455.

[229] D. S. McClure*, Solid State Phys.* **1959**, *9*, 399.

[230] R. K. Yoo, S. C. Lee, B. A. Kozikowski, T. A. Keiderling, *Chem. Phys.* **1987**, *117*, 237.

[231] C. K. Jørgensen, R. Pappalardo, H. H. Schmidtke, *J. Chem. Phys.* **1963**, *39*, 1422.

[232] D. E. Richardson, *J. Chem. Educ*. **1993**, *70*, 372.

[233] B. N. Figgis, M. A. Hitchman, *Ligand Field Theory and Its Applications*, Wiley-VCH, New York, **2000**.

[234] R. Glaum, M. Hitchman, *Aust. J. Chem.* **1996**, *49*, 1221.

[235] M. Gerloch, *Cam. Univ. Press,* **1983**.

[236] D. Reinen, M. Atanasov, S. L. Lee, *Coord. Chem. Rev*. **1998**, *175*, 91.

[237] H. Thauern, R. Galum, *Inorg. Chem*. **2007**, *46*, 2057.

[238] J. M. Longo, P. Kierkegaard, *Acta Chem. Scand.* **1966**, *20*, 72.

[239] T. G. Amos, A. Yokochi, A. W. Sleight, *J. Solid State Chem.* **1998**, *141*, 303.

[240] U. Kaiser, G. Schmidt, R. Glaum, R. Gruehn, *Z. Anor. Allg. Chem.* **1992**, *607*, 13.

[241] D. L. Serra, S. -J. Hwu, *Acta Crystallogr.* **1992**, *C48*, 733.

[242] T. G. Amos, A. W. Sleight, *J. Solid State Chem*. **2001**, *160*, 230.

[243] V. P. Nicolaev, G. G. Sadikov, A. V. Lavrov, M. A. Porai-Koshits, *Izv. Akad. Nauk SSSR, Neorg. Mater.* **1986**, *22*, 1364.

[244] J. J. Zah-Letho, A. Jouanneaux, A. N. Fitch, A.Verbaere, M. Tournoux, *Eur. J Solid State Inorg. Chem.* **1992**, *29*, 1309.

[245] J. J. Zah-Letho, A. Verbaere, A. Jouanneaux, F. Taulelle, Y. Piffard, M. Tournoux, *J. Solid State Chem.* **1995**, *116*, 335.

[246] R. S. Roth, A. D. Wadsley, S. Andersson, *Acta Crystallogr*. **1965**, *18*, 643.

[247] M. Tachez, F. Theobald, E. Bordes, *J. Solid State Chem.* **1981**, *40,* 280.

[248] B. Jordan, C. Calvo, *Canad. J. Chem.* **1973**, *51*, 2621.

[249] E. Bordes, P. Courtine, *J. Chem. Soc. Chem. Commun.* **1985**, 294.

[250] S. C. Lim, J. T. Vaughey, W. T. A. Harrison, L. L. Dussac, A. J. Jacobson, J. W. Johnson, *Solid State Ionics* **1996**, *84*, 219.

[251] F. Girgsdies, T. Ressler, R. Schlögl, W.-S. Dong, K. K. Bartley, G. J. Hutchings, *Solid State Sci*. **2006**, *8*, 807.

[252] P. Amorosós, M. D. Marcos, M. Roca, J. Alamo, A. Beltrán- Porter, D. Beltrán-Porter, *J. Phys. Chem. Solids* **2001**, *62*, 1393.

[253] J. M. Longo, J. W. Pierce, J. A. Kafalas, *Mater. Res. Bull.* **1971**, *6*, 1157.

[254] H. Chahboun, D. Groult, M. Hervieu, B. Raveau, *J. Solid State Chem.* **1986**, *65*, 331.

[255] M. Goreaud, P. H. Labbe, B. Raveau, *J. Solid State Chem.* **1985**, *56*, 41.

[256] H. L. Cuthbert, J. E. Greedan, L. Cranswick, *J. Solid State Chem.* **2006**, *179*, 1938.

[257] E. V. Murashova, N. N. Chudinova, *Kristallografiya* **1994**, *39*, 145.

[258] S. N. Achary, S. J. Patwe, A. K. Tyagi, *J. Alloys Compd.* **2008**, *461*, 474.

[259] E. Dowty, *ATOMS for Windows. V.6.3,* Shape Software, Kingsport, **2007**.

[260] R. Ya. Mel'nikova, V. V. Pechkovskii, E. D. Dzyuba, I. E. Malashonok, Atlas of *Infrared Spectra of Phosphates, Aca*demy of Science SSSR, Moskow, **1985**.

[261] M. Ishi, T. Tanaka, T. Akahane, N. Tsuda, *J. Phys. Soc. Jpn.* **1976**, *41*, 908.

[262] B. Krebs, A. Müller, *Z. Naturforsch.* **1968**, *23b*, 415.

[263] A. Leclaire, M. M. Borel, J. Chardon, B. Raveau, *J. Solid State Chem.* **1997**, *128*, 191.

[264] G. Andersson, A. Magneli, *Acta Chem. Scand*. **1950**, *4*, 793.

[265] E. Salje, *Acta Crystallogr.* **1977**, *B33*, 574.

[266] A. J. Edwards, B. R. Steventon, *J. Chem. Soc.* **1968**, *A1968,* 2503.

[267] J. C. Taylor, A. B. Waugh, *J. Chem. Soc. Dalton Trans.* **1980**, *1980*, 2006.

[268] A. J. Edwards, G. R. Jones, *J. Chem. Soc.* **1968**, *A1968,* 2074.

[269] H. Hess, H. Hartung, *Z. Anorg. Allg. Chem.* **1966**, *344*, 157.

[270] W. Klemm, *Magnetochemie*, Akademische Verlagsgesellschaft, Leipzig, **1936**.

[271] W. Klemm, *Z. Anorg. Allg. Chem.* **1941**, *246*, 347.

[272] A. Weiss, H. Witte, *Magnetochemie*, Verlag Chemie, Weinheim, **1973**.

[273] Hk. Müller-Buschbaum, *Z. Anorg. Allg. Chem.* **2007**, *633*, 2491.

[274] A. R. Middleton, A. F. Masters, G. Wilkinson, *J. Chem. Soc. Dalton trans.* **1979**, 542.

[275] R. Glaum, R. Gruehn, *Z. Kristallogr.* **1992**, *198*, 41.

[276] R. Glaum, R. Gruehn, *Z. Kristallogr.* **1989**, *186*, 91.

[277] R. Glaum, A. Schmidt, *Z. Anorg. Allg. Chem.* **1997**, *623*, 1672.

[278] E. Hammer, R. Glaum, W. Hermes, R. Pöttgen, *Z. Anorg. Allg. Chem.* **2011**, submitted.

[279] R. Glaum, M. Walter-Peter, D. Özalp, R. Gruehn, *Z. Anorg. Allg. Chem.* **1991**, *601*, 145.

[280] L. Palatinus, M. Dusek, R. Glaum, B. El Bali, *Acta Crystallogr.* **2006**, *B62*, 556.

[281] M. S. Islam, R. Glaum, *Z. Anorg. Allg. Chem.* **2009**, *635*, 1008.

[282] M. S. Islam, R. Glaum, *Z. Anorg. Allg. Chem.* **2010**, *636*, 144.

[283] H. Lux, *Z. Elektrochem.* **1939**, *45*, 303.

[284] H. Flood, T. Förland, *Acta Chem. Scand.* **1947**, *1*, 592.

[285] S. Stølen, T. Grande, *Chemical Thermodynamics of Materials - Macroscopic and Microscopic Aspects*, John Wiley & Sons Ltd, Chichester **2004**.

[286] W. T. Smith, L. E. Line, W. A. Bell, *J. Am. Chem. Soc.* **1952**, *74*, 4964.

[287] O. S. Glemser, A. Müller, H. Schwarzkopf, *Z. Allg. Anorg. Chem.* **1964**, *334*, 21.

[288] I. Barin, *Thermochemical Data of Pure Substances,* 2nd ed., Verlag Chemie, Weinheim **1992**.

[289] H. Schäfer, V. P. Orlovskii, M. Wiemeyer, *Z. Anorg. Allg. Chem.* **1972**, *390*, 13.

[290] O. Knacke, O. Kubaschewski, K. Hesselmann, *Thermochemical Properties of Inorganic Substances,* Springer, Berlin **1991**.

[291] H. P. A. Mercier, G. J. Schrobilgen, *Inorg. Chem.* **1993***, 32,* 145.

[292] J. Supel, U. Abram, A. Hagenbach, K. Seppelt, *Inorg. Chem*. **2007**, *46,* 5591.

[293] R. Bougon, B. Buu, K. Seppelt, *Chem. Ber.* **1993**, *126*, 1331.

[294] K. Panagiotidis, R. Glaum, W. Hoffbauer, J. Weber, J. Schmedt auf der Günne, *Z. Anorg. Allg. Chem*, **2008**, *634*, 2922.

[295] G. L. Turner, K. A. Smith, R. J. Kirkpatrick, E. Oldfield, *J. Magn. Reson.* **1986**, *70*, 408.

[296] S. Hayashi, K. Hayamizu, *Bull. Chem. Soc. Jpn.* **1989**, *62*, 3061.

[297] C. Lejeune, C. Coelho, L. Bonhhomme-Coury, T. AzÏs, J. Maquet, C. Bonhhomme, *Solid State Nucl. Magn. Reson*. **2005**, *27*, 242.

[298] C. Coelho, T. Azaïs, L. Bonhomme-Coury, G. Laurent, C. Bonhomme, *Inorg. Chem.* **2007**, *46*, 1379.

[299] M. S. Ram, J. T. Hupp, *Inorg. Chem.* **1991**, *30*, 130.

[300] I. R. Beattie, T. R. Gilson, P. J. Jones, *Inorg. Chem.* **1996**, *35*, 1301.

[301] R. Schlögl in N. Mizuno (ed.), *Modern Oxidation Catalysis*, Wiley-VCH, Weinheim, **2009**.

The present work has been carried out within Jun. 2007 to Sept. 2011 in the Institute of Inorganic Chemistry in Rheinische Friedrich-Wilhelms-Universität Bonn under the supervision of Prof. Dr. Robert Glaum.

My deepest gratitude is to my Supervisor, Prof. Dr. Robert Glaum. I have been amazingly fortunate to have an advisor who gave me the freedom to explore on my own, and at the same time the guidance to recover when my steps faltered. Prof. Glaum taught me how to question thoughts and express ideas. His insightful comments and constructive criticisms at different stages of my research were thought-provoking and they helped me focus my idea. His patience and support helped me overcome many crisis situations and finish this dissertation.

I am profoundly grateful to German Academic Exchange Service (DAAD) for my PhD scholarship. I am indebted to Deutsche Forschungsgemeinschaft (DFG) and UMICORE for the financial support for chemicals.

I would be grateful to Dr. Jörg Daniels, Dipl. Chem. Axel Pelka and Dr**.** Gregor Schnakenburg for X-ray single-crystal data collections. I am also thankful to Volker Dittrich and Markus Stichnote for the single-crystal UV/Vis/NIR data collections. Miss Bärbel Knopp and Volker Bendisch are thanked for the photographs of the crystals.

My special thanks go to Dr. Reinhard K. Kremer (Max-Planck-Institute Solid state Research, MPIFKT Stuttgart) and Prof. Rainer Pöttgen (Institut für Anorganische und Analytische Chemie, Uni Münster) for magnetic measurements.

I would like to thank my ACF students Ina Krieger, Tobias Dahmen and Alexander Leiendecker for their contributions for the some experiments during their practical periods.

It is a great pleasure for me to thank my former and current colleagues, Dr. Ernst Benser, Dr. Marcos Schöneborn, Dr. Christian Litterscheid, Dr. Kosta Panagiotidis, Dr. Eva Maria Hammer, Michael Funke, Sven Titlbach, Emma Mosymow, Katharina Gerber, Subrata Chandra Roy, Anke Scnabel, Anna Bronova, Tobias Freers and Prof. Dr Aftab Ali Shaikh for their assistance and cooperation to maintain a nice working environment in the group.

I would like to thank my Master thesis supervisor Prof. Dr. Altaf Hussain (Dept. of Chemistry, University of Dhaka), my uncle Md. Amir Hossain and unty Mrs. Akhlima Khanam who have a great contribution to my academic career.

Most importantly, none of this would have been possible without the love and patience of my parents, wife, brother and sisters. My immediate family to whom this dissertation is dedicated to, has been a constant source of love, support and strength all these years.

PUBLICATIONS

1 "The First Phosphates of a Heptavalent Metal: Rhenium(VII)-oxidephosphate and Di-Rhenium(VII)-Pentaoxide-Silicon-Silicophosphate." Saiful M. Islam, Robert Glaum, Axel Pelka, Jörg Daniels, Wilfried Hoffbauer, *Inorg. Chem*. **2010**, submitted.

2 "Rhenium(V)-oxidepyrophosphate $Re_2O_3(P_2O_7)$." Saiful, M. Islam, Robert. Glaum, *Z. Anorg. Allg. Chem.* **2010**, *636*, 144.

3 "Rhenium(VI)-oxidephosphate: Chemical Vapour Transport, Crystal Structure, UV/visible Spectrum and Magnetic Behaviour." Saiful, M. Islam, Robert Glaum, *Z. Anorg. Allg. Chem.* **2009**, *635*, 1008.

PRESENTATION (Poster)

1 New Phosphates of Rhenium, European Conference on Solid State Chemistry, 20-23.09.2009. Münster, Germany.

PRESENTATIONS (Oral)

2 New phosphates of Rhenium and Molybdenum, Department of Chemistry, University of Dhaka, Bangladesh, **8.04.2010**.

3 Anhydrous Phosphates of Molybdenum and Rhenium, Institute of Inorganic Chemistry, University of Bonn, Germany, **5.02.2009**.

I, Muhammad Saiful Islam declare that this research work has been done by myself and no other outer help was taken. I also ensure that necessary references were given regarding the compounds as well as scientific discussions.